# DESIGN AND SYNTHESIS OF BIMETALLIC CATALYSTS FOR VARIOUS ENVIRONMENTALLY BENIGN ORGANIC TRANSFORMATIONS

#### **A THESIS**

Submitted in partial fulfilment of the requirements for the award of the degree

of

#### **DOCTOR OF PHILOSOPHY**

By

#### **NEHA CHOUDHARY**



### DEPARTMENT OF CHEMISTRY INDIAN INSTITUTE OF TECHNOLOGY INDORE JULY 2023



### INDIAN INSTITUTE OF TECHNOLOGY INDORE

#### CANDIDATE'S DECLARATION

AND SYNTHESIS OF BIMETALLIC CATALYSTS FOR VARIOUS ENVIRONMENTALLY BENIGN ORGANIC TRANSFORMATIONS in the partial fulfilment of the requirements for the award of the degree of DOCTOR OF PHILOSOPHY and submitted in the DEPARTMENT OF CHEMISTRY, INDIAN INSTITUTE OF TECHNOLOGY INDORE, is an authentic record of my own work carried out during the time period from July 2018 to July 2023 under the supervision of Dr. Shaikh M. Mobin, Professor, Department of Chemistry, Indian Institute of Technology Indore.

The matter presented in this thesis has not been submitted by me for the award of any other degree of this or any other institute.

Ueta 06.07.2023

Signature of the student with date (NEHA CHOUDHARY)

This is to certify that the above statement made by the candidate is correct to the best of my/our knowledge.

M. Shaith 06.07.2023

Signature of Thesis Supervisor with date

(Dr. SHAIKH M. MOBIN)

NEHA CHOUDHARY has successfully given his/her Ph.D. Oral Examination held on 1st September 2023.

Signature of Thesis Supervisor with date

(Prof. SHAIKH M. MOBIN)

#### **ACKNOWLEDGEMENTS**

I would like to express my sincere gratitude to my supervisor Prof. Shaikh M. Mobin for his valuable guidance and constant support through my Ph.D. journey. I want to thank him for providing research facilities with freedom to work independently to develop new the research ideas. He always encouraged me to come out of my comfort zone and said go ahead to try new things. I specially thank him for his quick response and efforts to publish the work on time in reputed journals. Also, I sincerely want to thank him for providing opportunities to present my work in various national and international conferences. The scope provided by him to develop my own research goals and to participate in projects within the lab have been helpful in my growth through the last five years.

I also thank my PSPC members, Prof. Sampak Samanta and Prof. Saríka Jalan, for their constructive suggestions and comments to improve the work. I would like to thank Prof. Pratibha Sharma who motivated me to join Ph.D. at III-Indore.

I extend my thanks to all the faculties, staff members and technicians at the Department of Chemistry, IIT Indore, for their guidance and support during my course work, department-related activities, and documentations. I am grateful to the staff members at SIC, Mr. Kinny, Mr. Ghanshyam, Mr. Nitin, Mr. Ravindra for their help to perform various characterizations. I am also thankful to SAIF, IIT-Bombay, ACMS, IIT-Kanpur, MRC, MNIT-Jaipur,

IIC, IIT-Roorkee, CIF, IIT-GN, IISER Bhopal for providing characterization facilities.

I am deeply grateful to our computational collaborator Prof. Giannis Mpourmpakis, University of Pittsburgh, USA, and his student Ms. Mona Abdelgaid for performing DFT calculations for exploring the mechanism. I extend my thanks to Prof. Jeffrey T. Miller Purdue University, USA and Prof. Abhaya Datye, University of New Mexico, USA for performing characterizations and for their guidance throughout the collaborative work.

I also thank UGC, India, for providing research fellowship. I also thank SERB, CSIR and BRNS for providing financial support for travel to present my thesis work in conferences.

I would like to extend my sincere thanks to all my current and past lab members for their warm support during these years. I would like to specially thank Dr. Topi, Dr. Shagufi and Ms. Puja who guided and helped me in shaping my research goals like a sister in my initial years. I would like to thank my other group members Dr. Sanjay, Dr. Anoop Gupta, Dr. Ajeet, Dr. Prakash, Dr. Vinay, Dr. Mohit, Dr. Khursheed, Dr. Kaushik, Dr. Richa, Dr. Navpreet, Dr. Pranav, Dr. Nabeela, Dr. Kamal, Dr. Viresh, Dr. Diptangshu, Mr. Ravinder, Ms. Nirmiti, Mr. Nissar, Mr. Praveen, Mr. Zahir, Mr. Rakesh, Ms. Priya, Ms. Vinita, Mr. Debashish and Mr. Kapil for their suggestions during my work.

I want to offer special thanks to my friends Mr. Sandeep, Ms. Ekta, Mr. Shivendu, Ms. Nida, Mr. Deepak for their support during my Ph.D. journey. They were always behind to support me and gave valuable suggestions throughout. A special

thanks to Mr. Navdeep Srivastava for always motivating me and giving mental support during this five-year journey. Without his support this journey won't be possible. He was always there in my hard time and motivated me to keep going. Finally, I would like to thank my parents who has unconditionally supported me and allowed me to pursue my career despite all hurdles. My mother Mrs. Nirmala and my father Mr. Babulal Choudhary always encouraged me to be independent and go for further studies. They have given me enough freedom to take my decisions and motivated me to keep going. Words are not enough to explain their contribution in this journey and in my life. I owe them a lot. Lastly, I extend my sincere gratitude to everyone who has directly or indirectly contributed to my educational life.

#### **NEHA CHOUDHARY**

Dedicated to my family

#### **ABSTRACT**

The investigation embodied in the thesis entitled "DESIGN AND SYNTHESIS OF BIMETALLIC CATALYSTS FOR VARIOUS ENVIRONMENTALLY BENIGN ORGANIC

**TRANSFORMATIONS**" was initiated in July 2018 in the Department of Chemistry, Indian Institute of Technology Indore. The objectives of this thesis are synthesizing recyclable, bimetallic catalysts i.e., nanocatalysts and single atom catalysts for various organic transformations like hydrogenation, carboxylation, and CO<sub>2</sub> fixation reactions. The focal points of the thesis are as follows-

- 1) Synthesis and characterization of Zn-Cu supported on mesoporous silica MCM-41 (ZnO-Cu(OH)Cl/MCM-41) for transfer hydrogenation of ketones with water as solvent and NaBH<sub>4</sub> as reducing agent.
- 2) Bimetallic CoNi nanoflowers for reduction of terminal alkynes into alkanes using hydrazine hydrate as reducing agent and ethanol as solvent.
- 3) Bimetallic CuNi-12 nanoparticles with 1:2 molar ratio of Cu:Ni for hydrogenation of biomass derived furfural, cinnamaldehyde and 5-hydroxy methyl furfural (HMF) into corresponding alcohols using 2-propanol as hydrogen source, KOH as base.
- 4) Bimetallic CuNi-11 nanocatalyst (Cu:Ni = 1:1 molar ratio) for carboxylation of benzene to benzoic acid with solvent-free condition and HCOOH as carboxylating agent.
- 5) Co doped ZrO<sub>2</sub> single atom catalysts for chemical fixation of CO<sub>2</sub> into epoxides to cyclic carbonates with solvent free conditions.

This thesis includes seven chapters, and it starts with the general introduction of heterogeneous catalysis with focusing on nanoparticles and single atom catalysts strategies (**Chapter 1**), followed by synthesis of supported nanocatalyst (**Chapter 2**) for hydrogenation reactions, followed by utilization of bimetallic nanocatalysts hydrogenation of terminal alkynes (**Chapter 3**), hydrogenation of biomass derived furfural (**Chapter 4**), carboxylation of arenes (**Chapter 5**), and further synthesis of single atom catalysts for CO<sub>2</sub> fixation reaction (**Chapter 6**). Finally, thesis concludes with the future perspective specially focusing further utilization of nanocatalysts and developing new strategies of synthesis of SACs (**Chapter 7**). The contents of each chapter included in the thesis are discussed as follows:

Chapter 1 includes the general introduction of catalysis, types of catalysis i.e., homogeneous, and heterogeneous catalysis and their advantages and disadvantages with focusing on heterogeneous catalyst i.e., nanoparticles and single atom catalysts. This is followed by a brief discussion on the tuning of the properties of nanoparticles as catalysts and their applications in various organic transformation reactions such as hydrogenation of ketones, aldehydes, and terminal alkynes. Furthermore, the single atom catalysts and their synthetic strategies, characterization techniques and their applications.

In **Chapter 2**, the MCM-41 supported ZnO-Cu(OH)Cl nanocatalyst was synthesized via facile wet impregnation method at room temperature and characterized via various techniques like powder X-ray diffraction (PXRD), thermogravimetric analysis (TGA). Morphological studies were performed by Scanning electron microscopy (SEM), Transmission electron microscopy (TEM). The above studies revealed the incorporation of metal species into the pores of MCM-41, leading to decrease in surface area of the nanoparticles found to be 239.079 m<sup>2</sup>/g. As synthesized catalysts showed high catalytic activity towards 19 ketone substrates using NaBH<sub>4</sub> as reducing agent, water as a solvent and within 45 minutes at 40 °C, the

acetophenone (model substrate) converted 100% with 100% selectivity and recyclable up to six cycles. Hence, ZnO-Cu(OH)Cl/MCM-41 nanoparticles with 2.46 wt% zinc and 6.39 wt% copper were deciphered as an active catalyst for the reduction of ketones without using any gaseous hydrogen source making it highly efficient and, environmentally and economically benign.

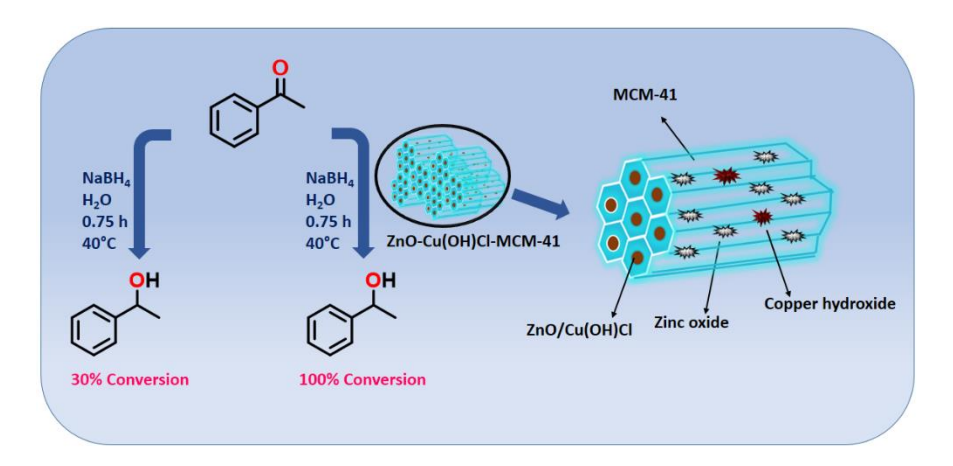


**Figure 1.** Schematic representation of hydrogenation of ketones using ZnO-Cu(OH)Cl/MCM-41 nanocatalyst.

In **Chapter 3**, bimetallic CoNi nanoflowers developed via facile liquid-phase reduction method. The catalyst has flower like morphology confirmed by HR-TEM and SEM. The nanoflower utilized for hydrogenation of terminal alkynes (15 substrates) using hydrazine hydrate as hydrogen source at 80 °C. The heterometallic nanoflower exhibited 100% conversion with ~100% selectivity towards alkane products (15 substrates). CoNi nanoflowers are magnetically separable and recyclable up to six cycles.

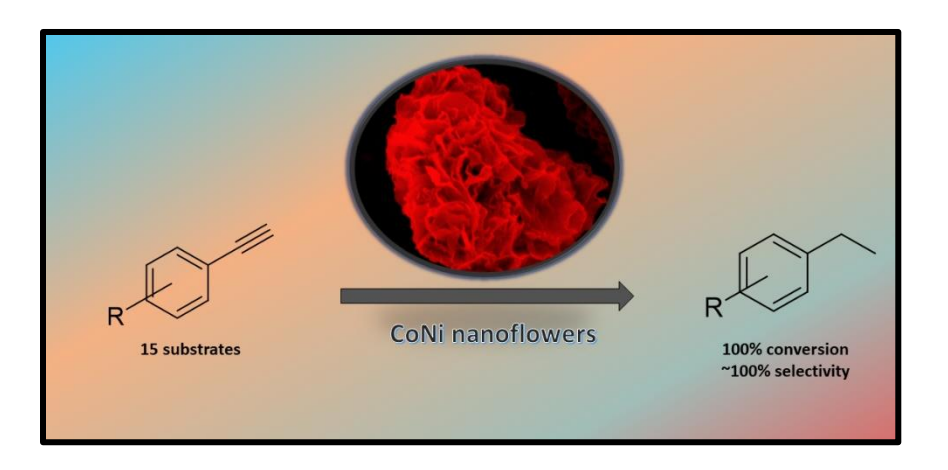


**Figure 2.** Schematic representation of hydrogenation of terminal alkynes into alkanes.

In Chapter 4, magnetic CuNi-12 nanocatalyst (Cu:Ni = 1:2 molar ratio) was synthesized via a liquid-phase reduction method and utilized for the efficient and selective hydrogenation of biomass-derived aldehydes and ketones with 2-propanol as hydrogen source and KOH as base. As synthesized nanocatalyst have flakes like morphology confirmed by SEM and HR-TEM analysis. The synergistic effect between copper and nickel metal enhanced the catalytic activity and selectivity. Biomass derived alcohol i.e., furfural, cinnamaldehyde, 5-hydroxy methyl furfural were utilized as substrate and converted into alcohol with 100 % conversion and selectivity. Bimetallic nanocatalyst CuNi-12 having high surface area and it is reusable, magnetically separable, and recyclable up to seven cycles. This approach of catalytic conversion of biomass-derived aldehydes is sustainable and can be implemented for chemical industries.

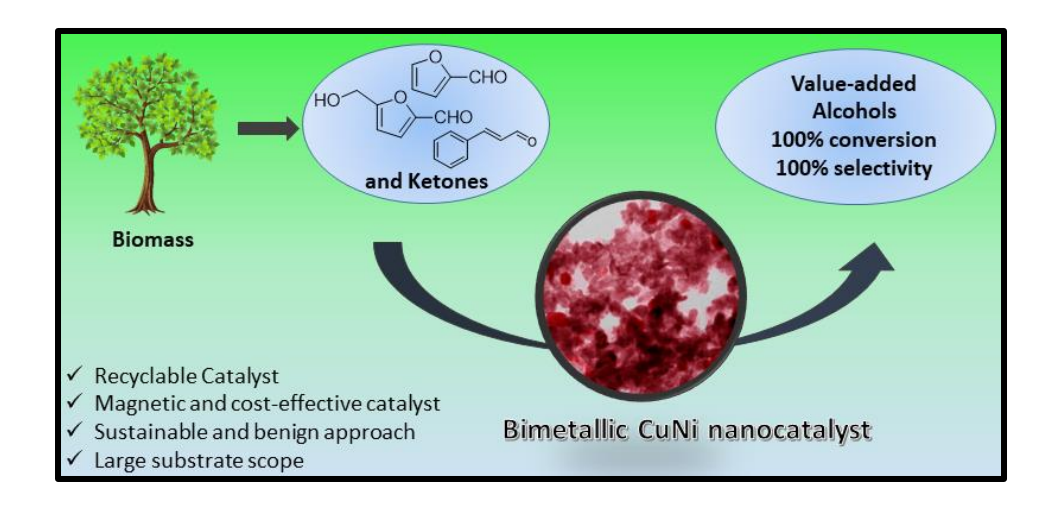


**Figure 3.** Biomass derived aldehydes conversion into alcohol using CuNi-12 nanocatalyst.

In **Chapter 5**, bimetallic CuNi-11 nanocatalyst with 1:1 molar ratio via liquid-phase reduction method and used for carboxylation of benzene with formic acid with 100% conversion and 100% selectivity. The catalyst was characterized by SEM and TEM which confirm the flakes like morphology and BET analysis confirm the high surface area of 58.99 m²/g with recyclability up to six cycles. The catalytic reaction mechanism was analysed using Density Functional Theory (DFT) calculations which demonstrate that the mechanistic pathway involves benzene and formic acid C-H bond activation, benzoic acid and H₂ formation with the benzene C-H activation being the rate-determining step. Further, the bimetallic CuNi-11 nanocatalyst exhibits an activator-, additive- and solvent-free carboxylation of benzene with magnetically separable, recyclable approach. Overall, our work contributes to introducing sustainable and environmentally friendly carboxylation routes of arenes with a new mechanistic approach.

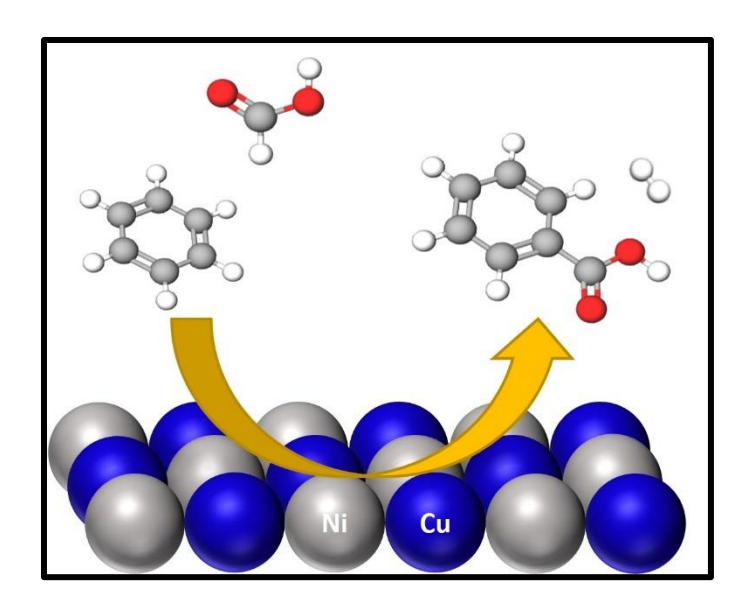


**Figure 4.** Carboxylation of benzene to benzoic acid using formic acid and CuNi-11 nanocatalyst.

In **Chapter 6**, Cobalt doped ZrO<sub>2</sub> was synthesized and utilized for CO<sub>2</sub> fixation of epoxides. The synthesized Co/ZrO<sub>2</sub> catalyst was characterized by EXAFS and STEM to confirm the presence of isolated Co<sup>+2</sup> on the ZrO<sub>2</sub> support. The STEM-EDS data showed uniform distribution of Co over the surface of the ZrO<sub>2</sub> support. The catalytic results revealed the Co active sites on ZrO<sub>2</sub> enhance catalytic performance and provide 100% conversion with 100% selectivity towards carbonate products in the presence of trace amounts of tetrabutylammonium bromide (TBAB). The catalyst is readily regenerated and recycled. When undoped ZrO<sub>2</sub> and Co<sub>3</sub>O<sub>4</sub> impregnated ZrO<sub>2</sub> catalyst was utilized for comparison, less than 50% conversion of epoxides was obtained. The single atom catalyst (SAC) showed a broad substrate scope, solvent-free reaction and higher catalytic activity and selectivity.

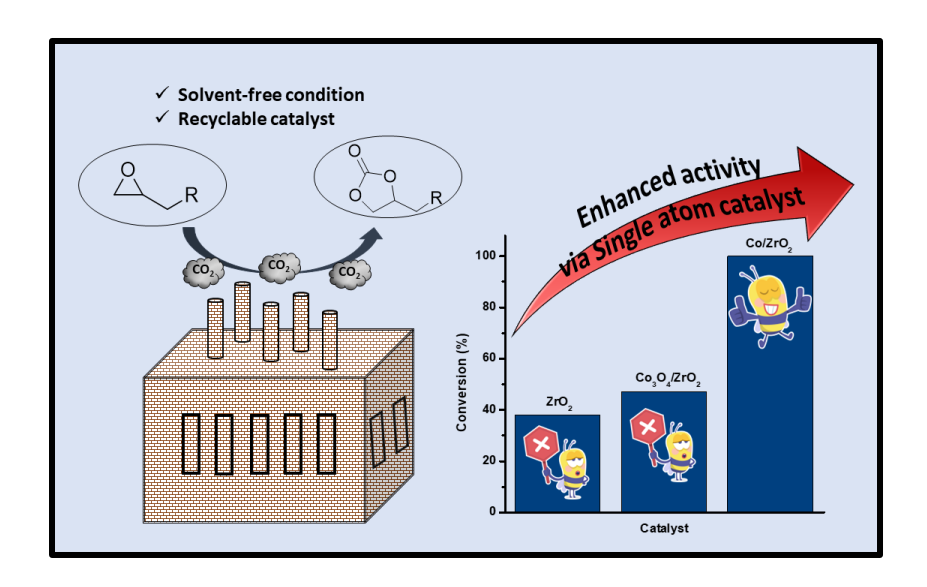


Figure 5. CO<sub>2</sub> fixation into cyclic carbonates using Co doped ZrO<sub>2</sub> SACs.

**Chapter** 7 includes the outline of the future perspective of the work.

#### LIST OF PUBLICATIONS

- 1) **Choudhary, N.**, Ghosh, T., and Mobin, S. M.; Ketone Hydrogenation by Using ZnO–Cu(OH)Cl/MCM-41 with a Splash of Water: An Environmentally Benign Approach. *Chem. Asian J.*, **2020**, *15* (8), 1339–1348.
- 2) **Choudhary, N.**, Abdelgaid, M., Mpourmpakis, G., and Mobin, S. M.; CuNi bimetallic nanocatalyst enables sustainable direct carboxylation reactions. *Mol. Catal.*, 2022, *530*, 112620.
- 3) **Choudhary, N.,** Kumar, V., Mobin, S. M.; Bimetallic CoNi nanoflowers for catalytic transfer hydrogenation of terminal alkynes. *Chem. Select*, **2022**, *7*(*37*), e202202501.
- 4) **Choudhary, N.,** Mobin, S. M. Conversion of Biomass-Derived Aldehydes Using Environmentally Benign CuNi Nanocatalyst. *Asian J. Org. Chem,* **2023,** *12* (2), e202200626.
- 5) **Choudhary, N.**, Jiang, S.; Pham, H., Datye, A, Miller, J. T. Mobin, S. M; Precisely designed cobalt single atom on ZrO<sub>2</sub> support for chemical CO<sub>2</sub> fixation (*Manuscript submitted*)
- 6) Chandra, P., Ghosh, T., **Choudhary, N.**, Mohammad, A., and Mobin, S. M.; Recent advancement in oxidation or acceptorless dehydrogenation of alcohols to valorised products using manganese-based catalysts. *Coord. Chem. Rev.*, **2020**, *411*, 213241.
- 7) Ghosh, T., **Choudhary**, **N**., Mobin, S. M. Design and Synthesis of silver decorated Fe<sub>3</sub>O<sub>4</sub> @ Fe doped CeO<sub>2</sub> core @ shell ternary composite as highly efficient Nano catalyst for selective oxidation of alkenes. *Chem. Select*, **2020**, *5*, 9601-9606.
- 8) Singh, A., **Choudhary, N.**, Mathur, P., Mobin S. M. Cubane Ru<sub>4</sub>(CO)<sub>8</sub> cluster containing 4 pyridine-methanol ligands as a highly efficient

- photoelectrocatalyst for oxygen evolution reaction from water. *J. Organomet. Chem.*, **2021**, *940*, 121769.
- 9) Chandra, P., **Choudhary, N.**, Lahiri, G. K., Maiti, D., Mobin S. M.; Copper mediated chemo-and stereoselective cyanation reactions, *Asian J. Org. Chem.*, **2021**, *10* (8), 1897–1937.
- 10) Chandra, P.; **Choudhary, N**.; Mobin, S. M. The Game between Molecular Photoredox Catalysis and Hydrogen: The Golden Age of Hydrogen Budge. *Molecular Catalysis* **2023**, *537*, 112921.
- 11) Chandra, P.; **Choudhary, N.;** Lahiri, G.; Maiti, D.; Shaikh, M. Modern Trends in the Copper-Catalyzed Synthesis of Sulfonamide. 2022. https://doi.org/10.21203/rs.3.rs-2046804/v1.
- 12) Choudhary, N., Hussain, N., Mobin, S. M; Insights on effect of different electrolytes on electrochemical performance of CoNi nanoflower based supercapacitor. Just Accepted, *Energy Technology*, 2300521. <a href="https://doi.org/10.1002/ente.202300521">https://doi.org/10.1002/ente.202300521</a>.
- 13) **Choudhary, N.,** Hussain, N., Kallayi, N., Mobin, S. M; Electrospun Copper-Lanthanide carbon nanofibers for efficient oxygen evolution reaction (*Manuscript under preparation*)

#### Conferences/Workshop/Oral/Poster presentation

#### **Oral presentation**

- 1. "*In-House Symposium CHEM-2020*" organized by Department of Chemistry, IIT-Indore, India on February 28, 2020.
- 2. "7<sup>th</sup> International Conference on Advanced Nanomaterials and Nanotechnology (ICANN-2021)" organized by Centre for Nanotechnology at the Indian Institute of Technology Guwahati (IITG), India on December 14-17, 2021.

3. "Frontiers in Organometallic and catalysis (FOMC-2021) conference, organized by Department of Chemistry, MNIT-Jaipur, India on January 20-22, 2021.

#### **Poster presentation**

- 4. "Advances in Catalysis for Energy and Environment (CACEE -2022) & CO<sub>2</sub> India Network 1st Annual Meet" organized by Tata Institute of Fundamental Research (TIFR), Mumbai, India on October 31-November 4, 2022.
- 5. 19th International Conference on "Modern Trends in Inorganic Chemistry (MTIC XIX)- 2022" organized by Department of Chemistry, Banaras Hindu University, Varanasi on December 15-17, 2022.
- 6. RSC Symposium on "*Materials Science Towards New Horizons-2023*" organized by Department of Chemistry, IIT-Indore on January 19-20, 2023.
- 7. Presented poster in #RSCPoster twitter conference-2023 on February 28-March 1, 2023.

#### Webinar/workshops attended

- 8. Attended certified online course on Coursera "Nanotechnology and Nanosensors" organized by Technion Israel Institute of Technology, Israel in 2020
- 9. Attended certified online course on Coursera "Nanotechnology: A Maker's Choice" organized by Duke University, NC State University and The University of North Carolina, US at Chapel Hill in 2020.
- 10. Attended certified online course on Coursera "Introduction to Chemistry: Structures and solutions" organized by Duke University, US in 2020.
- 11. Attended certified online course on Coursera "Introduction to Molecular Spectroscopy" organized by The University of Manchester, United Kingdom in 2020.

#### **TABLE OF CONTENTS**

LIST OF SCHEMES	xxvi
LIST OF FIGURES	xxvii-xxx
LIST OF TABLES	xxxi-xxxii
ACRONYMS	xxxii-xxxiv

#### Chapter 1

#### Introduction

1.1.	Bimetallic nanocatalysts	1-8
1.2.	Single atom catalysts	8-15
1.3.	Scope of present work	15-17
1 4	References	17-22

#### **Chapter 2**

## Ketone Hydrogenation by using ZnO-Cu(OH)Cl/MCM-41 with a Splash of Water: an Environmentally Benign Approach

2.1.	Introduction	23-25
2.2.	Experimental	25-26
2.3.	Results and discussion	26-45
2.4.	Conclusions	46
2.5	GCMS spectra of all products	46-52
2.6.	References	53-59

#### **Chapter 3**

#### Bimetallic CoNi Nanoflowers for Catalytic Transfer Hydrogenation of Terminal Alkynes

3.1.	Introduction	60-62
3.2.	Experimental	62-63
3.3.	Results and discussion	63-79
3.4.	Conclusions	<b>79</b>
3.5	GCMS spectra of all products	80-84
3.6.	References	85-91

#### **Chapter 4**

#### Conversion of Biomass-Derived Aldehydes using Environmentally Benign CuNi nanocatalyst

4.1.	Introduction	92-94
4.2.	Experimental	94-96
4.3.	Results and discussion	96-114
4.4.	Conclusions	115
4.5	GCMS spectra of all products	115-122
4.6.	References	123-129

#### **Chapter 5**

#### CuNi Bimetallic Nanocatalyst Enables Sustainable Direct Carboxylation Reactions

5.1.	Introduction	130-132
5.2.	Experimental	133-136
5.3.	Results and discussion	137-158
5.4.	Conclusions	158

5.5.	GCMS spectra of all products	159-162
5.6.	<sup>1</sup> H and <sup>13</sup> C-NMR data	162-171
5.7.	References	172-181
Chapte	er 6	
Preciso	ely Designed Cobalt Single Atom on ZrO <sub>2</sub> St	upport for
Chemi	cal CO <sub>2</sub> Fixation	
6.1.	Introduction	182-184
6.2.	Experimental section	185-187
6.3.	Results and discussion	187-208
6.4.	Conclusions	210
6.5.	<sup>1</sup> H and <sup>13</sup> C-NMR data	210-224
6.6.	References	223-232
Chapte	er 7	

233-234

235-236

**Conclusions and Future Outlook** 

APPENDIX 1

#### LIST OF SCHEMES

Scheme 1.1	Reaction scheme for the transfer hydrogenation of ketone to alcohol	7
Scheme 1.2	Reaction scheme for the transfer hydrogenation	8
Scheme 1.3	of terminal alkynes to alkanes Reaction scheme for the transfer hydrogenation of aldehydes to alcohol	8
Scheme 1.4	Reaction scheme for the carboxylation of benzene to benzoic acid	8
Scheme 1.5 Scheme 2.1	CO <sub>2</sub> fixation reaction into epoxides sing SACs Synthesis of nanoparticle ZnO-Cu(OH)Cl/MCM- 41.	15 26
Scheme 2.2	General catalytic transfer hydrogenation of substituted acetophenones and heterocyclic ketones	34
Scheme 3.1	Schematic representation of the synthesis of bimetallic CoNi nanoflower	64
Scheme 3.2	General catalytic scheme of phenyl acetylene using bimetallic CoNi nanoflower	69
Scheme 3.3	General catalytic scheme of substituted phenyl acetylene and heterocyclic alkynes by using bimetallic CoNi nanoflower	73
Scheme 3.4	Plausible mechanism of catalytic hydrogenation of alkynes into alkanes	76
Scheme 4.1	Schematic representation of the synthesis of CuNi-12 nanocatalyst.	96
Scheme 4.2	General catalytic conversion of biomass-derived aldehydes and ketones using CuNi-12 bimetallic nanocatalyst.	107
Scheme 4.3	A plausible mechanism of hydrogenation of furfural into furfuryl alcohol	110
Scheme 5.1	Schematic representation of the synthesis of CuNi-11 nanocatalyst	137
Scheme 5.2	Catalytic conversion reaction scheme of substituted benzene to corresponding benzoic acids using CuNi-11 nanocatalyst	150
Scheme 5.3	Plausible mechanism of benzene carboxylation with formic acid on bimetallic nanoparticles	155
Scheme 6.1	Schematic representation of the synthesis of Co/ZrO <sub>2</sub> catalyst	188
Scheme 6.2	General catalytic reaction of cycloaddition of CO <sub>2</sub> to epoxides	204

Scheme 6.3 A plausible mechanism of CO<sub>2</sub> fixation of epoxides into cyclic carbonates

#### LIST OF FIGURES

Figure 1.1	Major highlights of nanocatalysts.	01
Figure 1.2	Representation of bimetallic alloys and	02
	intermetallics	
Figure 1.3	Comparative results of monometallic and bimetallic	04
	catalyst for deoxygenation reaction	
Figure 1.4	Representation of (a) supported	05
	nanocatalyst and (b) modified nanocatalyst	
Figure 1.5	Bimetallic catalyst separations using external	06
	magnet	
Figure 1.6	Applications of supported and unsupported	07
	nanoparticles in catalysis	
Figure 1.7	Comparative geometrical and electronic structures	09
	of nanoparticles, cluster, and single atom catalyst	
Figure 1.8	The effects of support on stabilizing single atoms	10
Figure 1.9	Different types of SACs are illustrated by	11
	schematic diagrams	
Figure 1.10	Characterization techniques for analyzing single	13
	atom catalysis	
Figure 1.11	Chemoselectivity pattern from nanocatalysts to	14
	single atom catalysts	
Figure 2.1	PXRD measurement data of ZnO-	27
	Cu(OH)Cl/MCM-41	
Figure 2.2	FT-IR spectra of ZnO-Cu(OH)Cl/MCM-41	28
Figure 2.3	TG analysis of ZnO-Cu(OH)Cl/MCM-41	28
Figure 2.4	SEM analysis of ZnO-Cu(OH)Cl/MCM-41	30
Figure 2.5	(A) Mapping, (B) Zn, (C) Cu, (D) Si, (E) O	30
	elemental analysis of ZnO-Cu(OH)Cl/MCM-41	
Figure 2.6	HR-TEM analysis of ZnO-Cu(OH)Cl/MCM-41	31
Figure 2.7	N <sub>2</sub> adsorption-desorption studies for surface area	32
	(A) and pore size (B) measurement.	
Figure 2.8	XPS analysis for ZnO-Cu(OH)Cl/MCM-41 (A) Zn	33
	2p, (B) Cu 2p and (C) O 1s.	
Figure 2.9	Plausible Mechanism of reduction of ketone using	43
	NaBH <sub>4</sub> , water and catalyst	
Figure 2.10	Kinetic study of the conversion of acetophenone to	44
	1- Phenyl ethanol.	
Figure 2.11	Recycle study of the catalyst for conversion of	45
<b>T</b>	acetophenone to 1- Phenyl ethanol.	
Figure 3.1	(A) XRD pattern and (B) TGA curve of bimetallic	64
	CoNi nanoflower.	
Figure 3.2	N <sub>2</sub> adsorption desorption study for (A) surface area	65
	(B) pore size distribution.	

Figure 3.3	SEM images of bimetallic CoNi nanoflower	66
Figure 3.4	HR-TEM images of bimetallic CoNi nanoflower	67
Figure 3.5	Hysteresis loop of bimetallic CoNi nanoflower at	67
	room temperature	
Figure 3.6	XPS analysis of CoNi nanoflower for (A) Co 2p	68
	(B) Ni 2p, and (C) survey scan.	
Figure 3.7	Effect of different catalyst on hydrogenation of	70
	phenyl acetylene	
Figure 3.8	Effect of (A) catalyst amount (B) hydrazine hydrate	71
	amount (C) substrate amount (D) solvent and (E)	
T: 2.0	temperature on hydrogenation of phenyl acetylene	
Figure 3.9	(A) Kinetic study of conversion of phenyl acetylene	77
	into ethyl benzene and (B) recycle study of the	
	catalyst for hydrogenation reaction of phenyl	
Figure 3.10	acetylene X-ray photoelectron spectroscopy analysis of (A)	78
rigure 3.10	Co 2p, (B) Ni 2p and (C) survey scan of recovered	70
	CoNi nanoflowers	
Figure 3.11	FE-SEM analysis of recycled CoNi nanoflower	79
Figure 4.1	(A) PXRD and (B) thermogravimetric analysis of	97
	bimetallic CuNi-12 nanocatalyst.	
Figure 4.2	N <sub>2</sub> adsorption-desorption study for (A) surface area	98
S	and (B) Pore size distribution of bimetallic CuNi-	
	12 nanocatalyst.	
Figure 4.3	FE-SEM images and Elemental analysis of	99
	bimetallic CuNi-12 nanocatalyst.	
Figure 4.4	HR-TEM images of bimetallic CuNi-12	100
	nanocatalyst and Selective area electron diffraction	
	(SAED) pattern at 2 1/nm.	
Figure 4.5	Hysteresis loop for magnetic properties of	101
	bimetallic CuNi-12 nanocatalyst at room	
Figure 4.6	temperature.	102
Figure 4.6	XPS analysis of fresh bimetallic CuNi-12	102
	nanocatalysts (A) Cu 2p, (B) Ni 2p, (C) O 1s and (D) survey scan.	
Figure 4.7	Screening of catalyst on the hydrogenation of	103
riguit 4.7	furfural into furfuryl alcohol	103
Figure 4.8	Effect of catalyst amount loading, hydrogen source	104
rigure no	with different base and base amount on conversion	101
	of furfural	
Figure 4.9	Kinetic study and (B) Recycle study of bimetallic	113
<b>6</b>	CuNi-12 nanocatalyst for conversion of furfural.	
Figure 4.10	XPS spectra of (A) Cu 2p element (B) Ni 2p	114
Ü	element of spent CuNi-12 nanocatalyst.	

Figure 5.1	PXRD analysis of all synthesized nanocatalysts (i)	138
	CuNi-11, (ii) Cu, (iii) Ni, (iv) CuNi-12, (v) CuNi-	
	21	
Figure 5.2	(A) PXRD spectra and (B) thermogravimetric	139
	analysis of CuNi-11 nanocatalyst.	
Figure 5.3	FT-IR spectrum of bimetallic CuNi-11	140
	nanocatalyst.	
Figure 5.4	(A) N <sub>2</sub> adsorption-desorption (B) CO <sub>2</sub> adsorption-	141
	desorption (C) BJH pore-size distribution isotherm	
	of CuNi-11 nanocatalyst	
Figure 5.5	SEM images of CuN-11 nanoflower, EDX pattern	142
	and elemental mapping	
Figure 5.6	TEM images of CuNi-11 nanocatalyst and SAED	142
	pattern.	
Figure 5.7	Magnetic hysteresis curve of CuNi-11 nanoparticle	143
Figure 5.8	XPS spectra of synthesized CuNi-11 nanocatalyst.	144
Figure 5.9	XPS spectra of recovered CuNi-11 nanocatalyst.	145
Figure 5.10	Effect of different catalysts on the conversion of	146
	benzene to benzoic acid.	
Figure 5.11	Effect of temperature on the carboxylation reaction	149
	of benzene	
Figure 5.12	(A) Kinetic study and (B) Catalyst reusability of the	152
	carboxylation reaction of benzene for all the cyclic	
	runs.	
Figure 5.13	FE-SEM images of recovered CuNi-11	153
	nanocatalyst	
Figure 5.14	FT-IR spectra of isolated benzoic acid after	154
	reaction.	
Figure 5.15	Labelling experiment with benzene-d6	154
Figure 5.16	Potential energy surface of direct carboxylation of	157
	benzene to benzoic acid on close-packed fcc (111)	
	CuNi-11 bimetallic surface	
Figure 5.17	Potential energy surface of direct carboxylation of	158
	benzene to benzoic acid on close-packed fcc (111)	
	CuNi-11 bimetallic surface on the gas phase and in	
	the presence of formic acid, and benzene as the	
	solvation medium.	
Figure 6.1	PXRD of Co/ZrO <sub>2</sub> single atom catalyst, Co <sub>3</sub> O <sub>4</sub>	189
	supported on ZrO <sub>2</sub> and undoped ZrO <sub>2</sub> and (B)	
	shifting of (101) plane of $ZrO_2$ with doping of	
T1	cobalt.	100
Figure 6.2	Thermogravimetric analysis of Co/ZrO <sub>2</sub> single	190
T' (C	atom catalyst	100
Figure 6.3	N <sub>2</sub> adsorption-desorption study for (A) surface area	190
	and (B) Pore size distribution of Co/ZrO <sub>2</sub> single	
	atom catalyst	

Figure 6.4	N <sub>2</sub> adsorption-desorption study for (A-C) surface	191
O	area and (B-D) Pore size distribution of undoped	
	ZrO <sub>2</sub> and Co <sub>3</sub> O <sub>4</sub> /ZrO <sub>2</sub> catalyst	
Figure 6.5	(A-B) STEM images in ABF mode and (C-D)	192
C	STEM images in ADF mode of Co/ZO <sub>2</sub> single atom	
	catalyst.	
Figure 6.6	STEM mapping of Zirconium, Cobalt, and Oxygen	193
C	element of Co doped ZrO <sub>2</sub> catalyst at different	
	regions at higher magnifications	
Figure 6.7	HR-TEM images of single atom Co/ZrO <sub>2</sub> catalyst	194
O	at (A-B) 5 nm, (C) Elemental mapping and (D)	
	EDS spectra (inset SAED pattern)	
Figure 6.8	FE-SEM mapping and elemental analysis of	194
S	Zirconium, Cobalt, and Oxygen of Co doped ZrO <sub>2</sub>	
	catalyst	
Figure 6.9	(A-B) STEM images of impregnated Co <sub>3</sub> O <sub>4</sub> /ZrO <sub>2</sub>	195
S	catalyst at different magnifications with elemental	
	analysis	
Figure 6.10	STEM mapping of Zirconium, Cobalt, and Oxygen	196
S	element of Co <sub>3</sub> O <sub>4</sub> impregnated ZrO <sub>2</sub>	
Figure 6.11	(A) Co K-edge XANES spectrum of Co/ZrO <sub>2</sub>	197
G	single atom catalyst, Co <sub>3</sub> O <sub>4</sub> /ZrO <sub>2</sub> impregnated	
	catalyst along with Co foil (black) as references and	
	(B) Fourier transform of Co K-edge EXAFS	
	spectra of Co/ZrO <sub>2</sub> single atom catalyst	
Figure 6.12	Fourier transform of Co K-edge EXAFS spectra of	198
	(A) Co/ZrO <sub>2</sub> single atom catalyst, (B) Co <sub>3</sub> O <sub>4</sub> /ZrO <sub>2</sub>	
	catalyst and (C-D) Fourier transform of Co K-edge	
	EXAFS spectra with corresponding fitting in R-	
	space.	
Figure 6.13	XPS analysis of fresh single atom Co/ZrO <sub>2</sub> catalyst	200
Figure 6.14	Catalytic optimization of CO <sub>2</sub> fixation reaction at	202
_	various reaction conditions.	
Figure 6.15	Effect of different catalysts on CO <sub>2</sub> fixation of	203
_	epichlorohydrin	
Figure 6.16	Catalyst reusability of the CO <sub>2</sub> fixation in	207
	epichlorohydrin for all the cyclic runs	

#### LIST OF TABLES

Table 2.1	Effect of solvents on the formation of 1-Phenyl ethanol	34
Table 2.2	Time optimization for reduction of acetophenone to 1-Phenyl ethanol	35
Table 2.3	Reducing agent amount loading for reduction of acetophenone	35
Table 2.4	Substrate amount loading for reduction of acetophenone to 1-Phenyl ethanol	36
Table 2.5	Catalyst screening for the reduction of acetophenone to 1-Phenyl ethanol	37
Table 2.6	Substrate scope for reduction of ketones to corresponding alcohols	38
Table 2.7	Comparison of ZnO-Cu(OH)Cl/MCM-41 and some previously reported work of hydrogenation	41
Table 2.8	ICP-AES data of catalyst ZnO-Cu(OH)Cl/MCM-41 after catalysis	44
Table 3.1	Effect of reducing agent on hydrogenation of phenyl acetylene	72
Table 3.2	Substrate scope of hydrogenation of alkynes into alkanes	73
Table 3.3	Comparison of hydrogenation of alkynes using bimetallic CoNi with some previous reports	75
Table 3.4	ICP-AES analysis of reaction mixture for leaching of CoNi nanoflower.	79
Table 4.1	Substrate scope of hydrogenation of aldehydes and ketones into alcohols	107
Table 4.2	Comparison of present work with some previously reported work	111
Table 4.3	ICP-AES analysis data of CuNi-12 nanocatalyst for hydrogenation reaction	114
Table 5.1	Effect of solvent on the conversion of benzene into benzoic acid	147
Table 5.2	Effect of amount of formic acid on carboxylation of benzene	148
Table 5.3	Effect of substrate amount on carboxylation reaction of benzene	148
Table 5.4	Effect of catalyst amount loading on carboxylation of benzene	149
Table 5.5	Carboxylation of selected substituted arenes into their corresponding acids	151
Table 5.6	ICP-OES analysis of reaction mixture for leaching of the himetallic CuNi-11 panocatalyst	152

Table 6.1	Co K-edge first shell EXAFS fitting results for	199
	Co/ZrO <sub>2</sub> , Co <sub>3</sub> O <sub>4</sub> /ZrO <sub>2</sub> and reference Co foil	
<b>Table 6.2</b>	Substrate scope on CO <sub>2</sub> fixation of epichlorohydrin	204
Table 6.3	ICP-AES analysis for leaching of Co doped single	207
	atom catalyst	
<b>Table 6.4</b>	Comparative results of some earlier reported single-	209
	atom catalysts	

#### **ACRONYMS**

PXRD	Powder X-Ray Diffraction
FE-SEM	Field-Emission Scanning Electron Microscope
BET	Brunauer–Emmett–Teller
HR-TEM	High Resolution Transmission Electron Microscope
FT-IR	Fourier-Transform Infrared
TGA	Thermogravimetric Analysis
EELS	Electron Energy-Loss Spectroscopy
EXAFS	Extended X-Ray Absorption Fine Structure
AC-STEM	Aberration-Corrected Scanning Tunneling Electron Microscopy
EDX	Energy Dispersive X-Ray
XANES	X-Ray Absorption Near-Edge Structure
HAADF	High-Angle Annular Dark-Field
XPS	X-Ray Photoelectron Spectroscopy
VSM	Vibrating Sample Magnetometry
ICP-AES	Inductively Coupled Plasma Atomic Emission Spectroscopy
ICP-MS	Inductively Coupled Plasma Mass Spectroscopy
ABF	Annular Bright Field
ADF	Annular Dark Field
PBE	Perdew-Burke-Ernzerhof

NPs	Nanoparticles
MOFs	Metal Organic Frameworks
DFT	Density Functional Theory
SACs	Single Atom Catalysts
ZnO	Zinc Oxide
CO	Carbon Mono Oxide
$CO_2$	Carbon Dioxide
КОН	Potassium Hydroxide
KBr	Potassium Bromide
CTAB	Cetyl Trimethyl Ammonium Bromide
NaOH	Sodium Hydroxide
MCM-41	Mobil Composition Of Matter No. 41
DCC	N,N'-Dicyclohexylcarbodiimide
TBAB	Tetrabutylammonium Bromide
TBAF	Tetrabutylammonium Chloride
TBAI	Tetrabutylammonium Iodide
DMAP	4-(Dimethylamino)Pyridine
MeOH	Methanol
SAED	Selective Area Electron Diffraction
DCM	Dichloromethane
ACN	Acetonitrile
FCC	Face Centered Cubic
$DMSO-d_6$	Deuterated Dimethyl Sulfoxide
CDCl <sub>3</sub>	Deuterated Chloroform
MeOH-d <sub>4</sub>	Deuterated Methanol
$C_6D_6$	Deuterated Benzene
RT	Room Temperature
$^{\circ}\mathrm{C}$	Degree Celsius

xxxi

o Degree

K Kelvin

pH Potential Of Hydrogen

min Minutes

h Hour

nm Nanometer

μm Mircometer

mmol Millimole

Conv. Conversion

Sel. Selectivity

a.u. Arbitrary Unit

eV Electron Volt

GC-MS Gas Chromatography–Mass Spectrometry

NMR Nuclear Magnetic Resonance

JCPDS Joint Committee on Powder Diffraction Standards

#### **CHAPTER 1**

#### Introduction

Heterogeneous catalysts i.e. metal nanoparticles, single-atom catalysts (SACs), metal oxide supported catalysts, metal organic frameworks (MOFs) etc has different phases from the reaction mixture and owing to this, it is stable in the reaction medium and easily recoverable and recyclable from the reaction mixture.[1,2] Nanoparticles are best suitable catalysts as they have high surface area, low preparation cost, reusability, and easy synthesis process (**Figure 1.1**).[3]

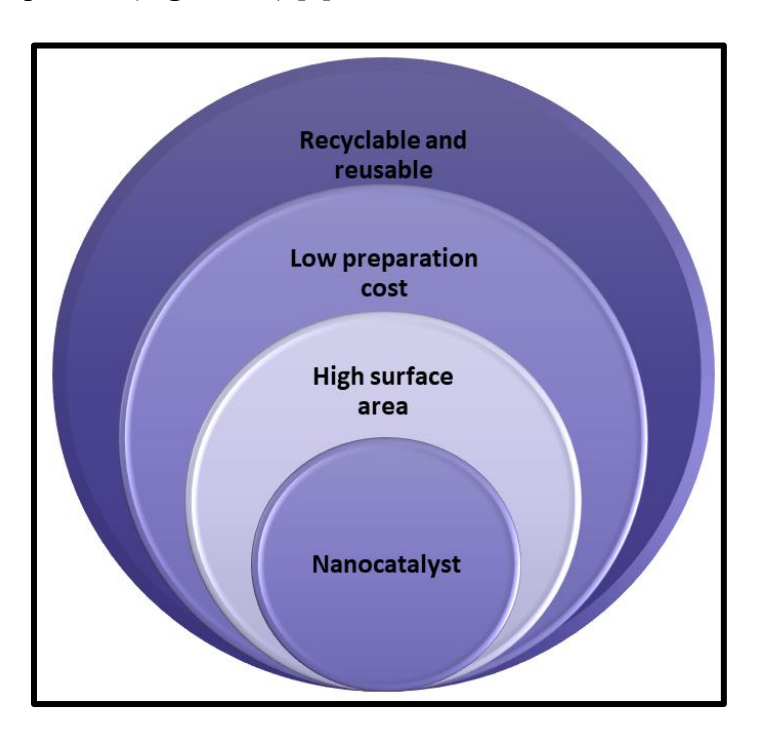
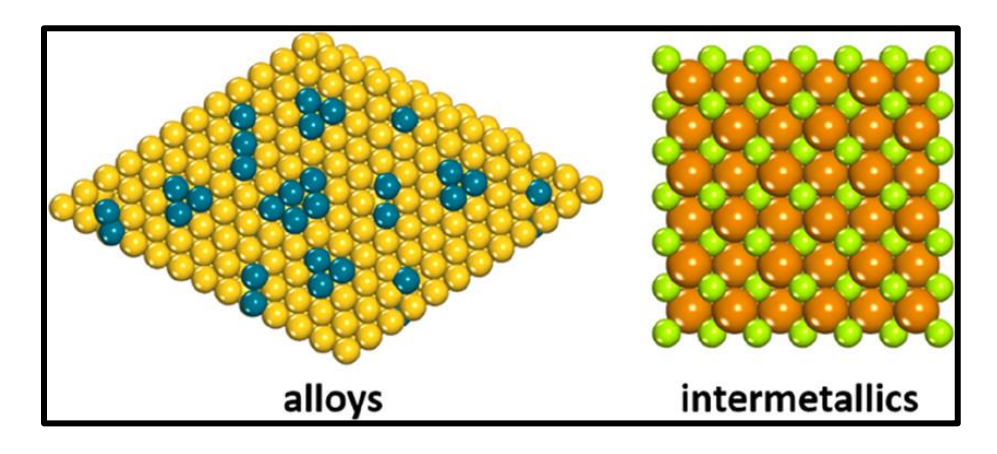


Figure 1.1. Major highlights of nanocatalysts.

#### 1.1. Bimetallic nanocatalysts

Bimetallic nanomaterials proved to be multifunctional materials and discovered to enhance the chemical, magnetic, electrical, and biological activities owing to the synergistic effect between existing metal components (**Figure 1.2**).[4–6] Bimetallic nanostructures are becoming a prominent

class of metal nanomaterials owing to their extraordinary properties that are beneficial in numerous fields of science and technology. Alloying high-cost noble metals with low-cost metals reduce the total preparation cost and made the process economic and showed excellent catalytic activity for various organic transformations.



**Figure 1.2.** Representation of bimetallic alloys and intermetallics [7]

To achieve optimal activity for the desired functions, their dual metal composition and configuration can be adjusted. In bimetallic systems, the elemental ratio and atom arrangement are important parameters to tune their properties for the desired application or activity. Bimetallic nanoparticles can control the corrosion and leaching of metals which plays an important role in catalyst deactivation in bulk scale reactions.[8]

The bimetallic nanoparticles show excellent efficiency and catalytic activity than their monometallic nanoparticles for various organic transformation reactions i.e. hydrogenation, dehydrogenation, methanol production, Suzuki coupling, C-N cross coupling etc.[9–12] Modifying the nanoparticle by introducing some metals can enhance the selectivity like Lindlar catalyst Pd/CaCO<sub>3</sub>-Pb.[7,13] Cheephat et al.[14] compared the catalytic activity of monometallic and bimetallic catalytic systems for partial oxidation of methane and they observed that bimetallic Re over Ni supported on Al<sub>2</sub>O<sub>3</sub> showed superior catalytic activity than their monometallic Ni, Rh, Re supported on Al<sub>2</sub>O<sub>3</sub> catalyst. The introduction of

Re drastically promote the reaction synergistically. Furthermore, Goulas et al.[15] reported that selectivity can be tuned by using supported materials with bimetallic system. The support material affected the catalytic activity of PdCu alloy catalyst for (de-)hydrogenation and decarbonlylation reactions. Pd and Cu alloying is the main factor for the increased selectivity towards (de)hydrogenation.

Iriondo et al.[16] compared the catalytic activity of monometallic Ni, Pt and bimetallic PtNi catalysts supported on  $\gamma$ -Al<sub>2</sub>O<sub>3</sub> and La<sub>2</sub>O<sub>3</sub>-modified  $\gamma$ -Al<sub>2</sub>O<sub>3</sub>. Among all catalysts, bimetallic PtNi showed higher catalytic activity. However, La<sub>2</sub>O<sub>3</sub> as support showed the conversion of glycerol towards lighter gaseous product. The study reveals the importance of supported material which enhances catalytic activity. Additionally, Seemala et al.[17] explored and compared the catalytic activity, product selectivity and catalyst stability of supported bimetallic CuNi catalyst with monometallic supported catalysts. Also, they have studied the effect of supported material with CuNi bimetallic nanoparticles with varying the Ni loading for the conversion of furfural to 2-Methylfuran. They have observed that both supports enhance the catalytic activity for furfural conversion. However, Al<sub>2</sub>O<sub>3</sub> promoted hydrogenation of furan ring to furfuryl alcohol and tetrahydrofurfuryl alcohol whereas TiO<sub>2</sub> promoted carbonyl hydrogenolysis to form methyl furan.

Moreover, Robinson et al.[18] reported the enhanced hydrodeoxygenation of *m*-Cresol using supported Pt-Mo/Al<sub>2</sub>O<sub>3</sub> bimetallic system over monometallic Pt/Al<sub>2</sub>O<sub>3</sub> catalyst. Using Mo with Pt reduce the overall cost of the catalyst with enhanced catalytic activity. They have explored the mechanism using DFT studies and observed that Mo sites in the Pt surface increased the interaction between oxygen and *m*-Cresol (**Figure 1.3**).[18]

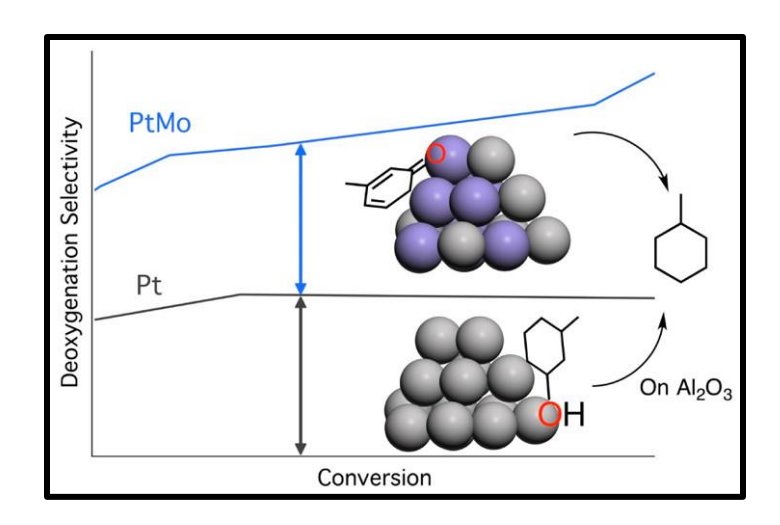


**Figure 1.3.** Comparative results of monometallic and bimetallic catalyst for deoxygenation reaction.[18]

Bimetallic catalysts with supported materials showed promoted catalytic activity. Supported materials stabilize the structure and enhance interaction between reactant and provides high surface area. Enhanced catalytic activity and selectivity could be accomplished by taking advantage of the special metal-support interactions between the metal nanoparticles and the supporting materials.[19,20] Porous supported materials can provide internal and external both surface to substrate to react further which leads to increase in catalytic activity.[21,22] Hence, modification in bimetallic nanomaterials using supported material or metal oxides with high surface area is a better approach. The use of support to the metal nanoparticles not only increase the surface area but also stabilize the nanoparticles by preventing agglomeration of nanoparticles.[3,7,20] Scheuermann et al. observed that the doping of oxide materials alter the shape and electronic properties of supported metal particles as well as facilitate the gas adsorption and enhance the catalytic performance (Figure 1.4).[23] Additionally, C, N, F, B-doped carbon supports showed superior catalytic activity over undoped material due to synergistic effect and also creates acidic or basic sites on the catalyst surface.[24–26]



**Figure 1.4.** Representation of (a) supported nanocatalyst and (b) modified nanocatalyst.[7]

Furthermore, in bimetallic catalysts magnetic properties can be introduced by alloying one nonmagnetic metal with magnetic metal. Alloying Fe, Mn, Co, Ni metals with precious metals can introduce magnetic properties. [27–29] Magnetic properties in the field of catalytic applications are highly desirable due to easy recoverability and recyclability from the reaction mixture using external magnet (**Figure 1.5**).[30,31] The easy recovery of the catalyst makes them suitable for industrial applications. In a review article, Zhang et al. discussed about various catalytic applications of magnetic nanomaterials i.e., hydrogenation reaction, Suzuki–Miyaura reaction, oxidation reaction, chiral catalysis, enzyme catalysis, photocatalysis, electrocatalysis, and photoelectrochemical catalysis.[32]

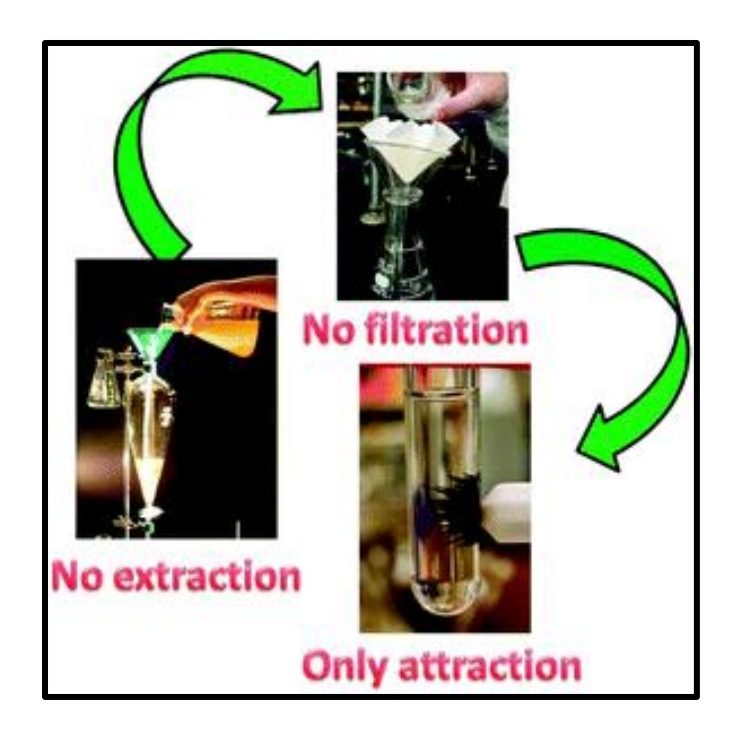


**Figure 1.5.** Bimetallic catalyst separations using external magnet.[31]

Hence, the use of bimetallic nanoparticles for catalytic application is getting attention of scientific community owing to their above properties and it is easy to tune their properties according to reaction requirement for desired product selectivity.

# 1.1.1. Applications in catalysis

Nanoparticles as catalysts or nanocatalysts have been widely utilized for various catalytic applications i.e., photochemically, thermally, electrochemically. The use of nanocatalysts gave a new approach to catalytic applications. As discussed in above section, nanocatalysts include core-shell, metal oxides, carbon-based materials, supported nanomaterials etc have great importance in catalysis. Specifically, transition metal based catalysts are preferable due to their high abundance. Since ages, Pd, Co, Ni, Ru, Fe, Cu, Rh etc have been reported for various catalytic reactions due to their outstanding properties as shown in Figure 1.6. First row transition metal nanoparticles of Cu, Ni, Co, Zn showed excellent activity for hydrogenation reactions. These metal oxides were extensively explored for

hydrogenation reactions due to their redox properties, low cost, and low sensitivity.

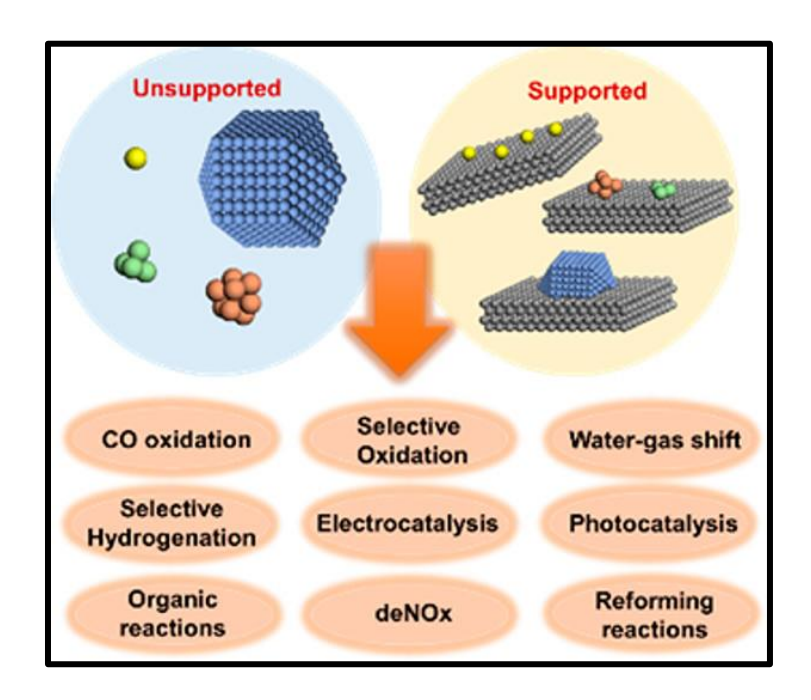


**Figure 1.6.** Applications of supported and unsupported nanoparticles in catalysis.[33]

For examples, Dragoi et al. reported Ni supported on mesoporous silica for transfer hydrogenation of acetophenone using 2-propanol with base as solvent at 80 °C (**Scheme 1.1**). [34]

$$R_2$$
 $Ni@mSiO_2$ 
 $R_1$ 
 $NaOH, i-PrOH$ 
 $R_1$ 

**Scheme 1.1** Reaction scheme for the transfer hydrogenation of ketone to alcohol.

Furthermore, bimetallic Rh<sub>4</sub>Co nanocatalyst was reported for hydrogenation of terminal alkynes and alkenes using hydrazine hydrate and 60 °C temperatures.[35] The reaction was performed with 19 substrate and it showed food to excellent yield (Scheme 1.2).

**Scheme 1.2**. Reaction scheme for the transfer hydrogenation of terminal alkynes to alkanes.

Additionally, transfer hydrogenation of aldehydes and ketones were reported using Pd nanoparticles on graphene oxide using 2-propanol and KOH as base at 80 °C. The catalyst showed good to moderate yield (**Scheme 1.3**).[36]

$$R_1$$
  $GO-Se-Pd$   $R_1$   $R_1$   $R_1$   $R_1$   $R_2$   $R_3$   $R_4$   $R_4$   $R_5$   $R_5$ 

**Scheme 1.3.** Reaction scheme for the transfer hydrogenation of aldehydes to alcohol.

Furthermore, the carboxylation of arenes were reported generally using CO<sub>2</sub> high pressure or CO toxic gas with oxidizing agent with high cost Pd catalyst. Pd acetate as catalyst has been utilized for carboxylation of aryl halide with HCOOH and DCC as additive with xantphos (**Scheme 1.4**). In this reaction triethyl amine and DMF used as solvent at 100 °C.[37]

**Scheme 1.4.** Reaction scheme for the carboxylation of benzene to benzoic acid.

# 1.2. Single atom catalysts (SACs) as heterogeneous catalysts

Single-atom catalysts (SACs) where each metal atom present on metal oxide support in isolated form, emerged as outstanding alternative in

heterogenous catalysis (**Figure 1.7**).[38] They have properties of both homogeneous and heterogeneous catalysts i.e. high exposure of active sites, easy recovery and good recyclability.[39,40] The SACs have high catalytic activity due to presence of isolated atoms as active sites over other supported metal systems.[7]

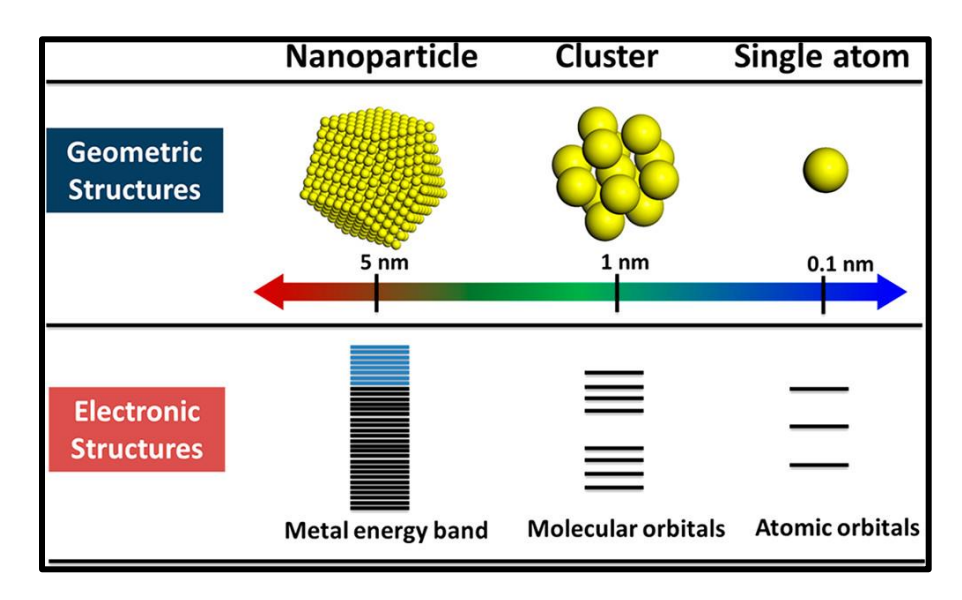


**Figure 1.7.** Comparative geometrical and electronic structures of nanoparticles, cluster, and single atom catalyst.[33]

Initially, SACs named as isolated atom or single site catalysts where metal atoms presented isolated on metal oxide support.[38,41] Later, with the advancement of characterization techniques contributed to the research on single-atom catalysts. Thanks to the technology to develop the microscopic and spectroscopic techniques i.e., high resolution transmission electron microscope (HR-TEM), and aberration-corrected scanning tunneling electron microscopy (AC-STEM), electron energy-loss spectroscopy (EELS), energy dispersive X-ray (EDX), X-ray absorption near-edge structure (XANES) and extended X-ray absorption fine structure (EXAFS) through which we can observe the subnanoclusters and atoms in the catalysts.[40,42]

However, the main challenge is to synthesize these SACs in large scale because due to their high surface energy, single-atom sites are prone to sintering and aggregating into thermodynamically stable nanoclusters. Sintering can be avoided by incorporating suitable supports to enhance the local coordination environment, electrical characteristics, and strong metal-support interactions. As the size decreases from bulk to atomic level, the surface free energy increases due to which capacity of metal sites interaction with the support and adsorbates increases (**Figure 1.8**). Although a variety of potential SACs with affordable supports are emerging as attractive candidates for heterogeneous catalysis, it is still unclear what the true functions and crucial components of supports are in determining the catalytic properties of these SACs.

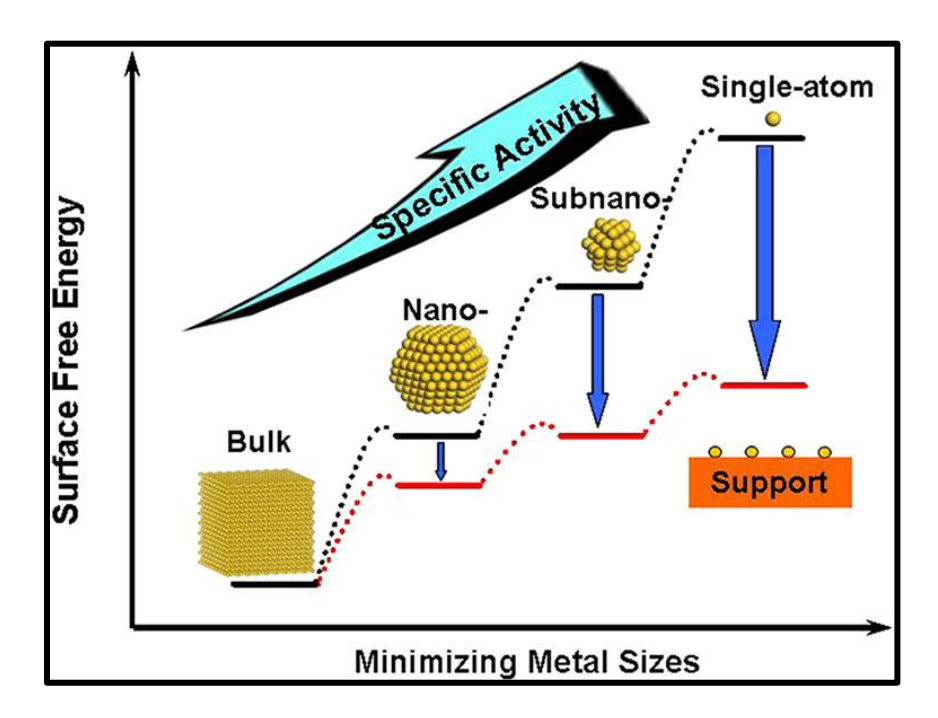


**Figure 1.8.** The effects of support on stabilizing single atoms and changes in surface free energy and specific activity per metal atom with metal particle size.[43]

## 1.2.1. Synthesis strategies

The most common strategies for atom stabilization over the support include doping, taking advantage of defects, and spatial confinement (**Figure 1.9**).

1) Doping of heteroatom provides endless opportunity for tuning the coordination sites because the doping of element creates isomorphous substitution in lattice. Single atoms can bind effectively to dopants which have lone pairs of electrons i.e., N, O, S. Additionally, doping of element generates surface defects which help single atoms to stabilize on support. Specifically, doping in carbon based materials shows excellent properties due to electron donating and accepting sites.[44,45] Nitrogen containing materials not only enhances the stabilization of metals but also prevents their aggregation and leaching.[46]

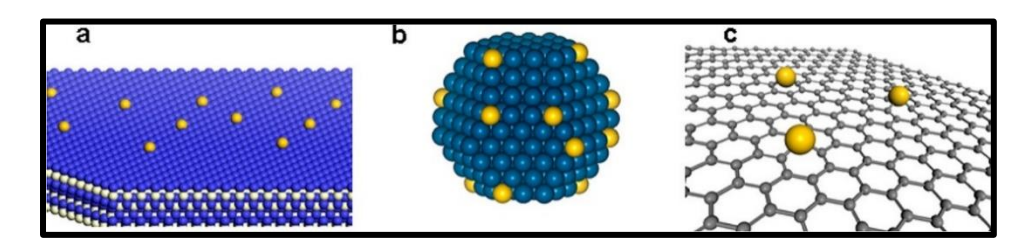


**Figure 1.9.** Different types of SACs are illustrated by schematic diagrams: (A) Metal single atoms anchored to graphene, (B) metal surfaces, and (C) metal oxides, respectively.[43]

- 2) Defects on the surface of the support facilitate the modification in electronic and surface morphology by creating unsaturated coordination sites and showed enhance catalytic properties for electrocatalysis and photocatalysis. Metal oxides such as ZrO<sub>2</sub>, TiO<sub>2</sub>, CeO<sub>2</sub> and Al<sub>2</sub>O<sub>3</sub> have defects on their surface when used as support and this is most promising approach to stabilize the SACs. These type of SACs are highly stable at higher temperature.[40]
- 3) Spatial confinement strategies are applicable in case of porous supports like zeolites, MOFs, COFs, graphitic carbon nitride which are able to trap

the atom. In MOFs, the SACs immobilization can be done at unsaturated metal nodes or on chelating sites which was generated by organic linkers or only if the precursors are incorporated into the MOF pores.[47] However, high metal loading on low surface area leads to agglomeration of single atom which can be controlled by using high surface area support with mesoporosity.[48]

### 1.2.2. Characterization techniques

For characterizing single atom catalysts various microscopic and spectroscopic techniques have been utilized as shown in **Figure 1.10**. To check the presence of isolated atoms, the HR-TEM and AC-STEM analysis have been utilized. However, the existing tools are not enough to analyze the presence of all atoms. It has some limitations as it is dependent on atomic number Z and the acquired images are best only if the support material has lower atomic number than the isolated atoms. Moreover, high-angle annular dark-field (HAADF) is used to increase the contrast of the image. Although, EDX of SACs can confirm the element dispersion over the support by analyzing various sections of surface. Additionally, electron energy-loss spectroscopy (EELS) is analysis technique which provides the elemental analysis of low atomic numbers.

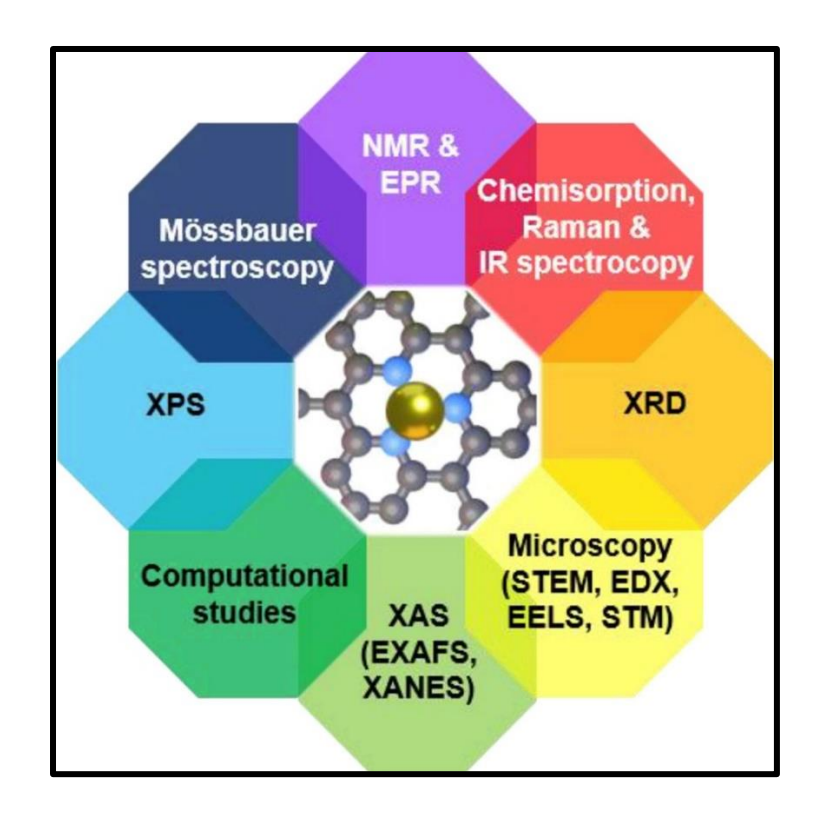


**Figure 1.10.** Characterization techniques for analyzing single atom catalysis.[46]

Furthermore, EXAFS is the technique through which the coordination number, chemical bonding, bond distance can be analyzed. EXAFS can provide the details about the local environment and geometric structure of the single atom. If the doping of the element occurred successfully onto the support, then the bond distance and chemical environment vary from the standard one, hence we can confirm the same from EXAFS. Further, XANES is also provides the local electronic structure of an atom. Additionally, XPS, XRD, *insitu* FT-IR, Raman etc are the techniques which utilizes to analyze the formation of material, element presence, binding energy etc. Furthermore, DFT calculations are also explored widely to study the surface defects, plausible structure. DFT studies are generally complement the other XAS studies to confirm the actual nature and to explore the mechanistic pathways.

# 1.2.3. Applications in catalysis

SACs have been widely explored for various catalytic reactions for thermocatalytic, photocatalytic and electrocatalytic reactions.[39,49–52] Specifically, for thermocatalysis SACs were explored for various organic transformation reactions such as biomass derived materials conversion, CO<sub>2</sub> reduction, gas sensing, water remediation, hydrogenation, hydrosilylation, hydroformylation, alkane oxidation, alcohol oxidation, C-C coupling etc.[51,52] SACs showed outstanding catalytic activity, high selectivity and maximum utilization efficiency in all cases. Furthermore, for electrocatalytic reactions, SACs showed excellent results for CO2 electroreduction (CO<sub>2</sub>RR), water-oxidation reaction, oxidation evolution reaction (OER), hydrogen evolution reaction (HER), NO<sub>x</sub> removal, N<sub>2</sub> electroreduction (NRR) etc. [53,54] Zhang et al. discussed the comparative study of the selective hydrogenation over nanocatalysts, modified nanocatalysts and SACs as shown in Figure 1.11.[7] Based on reports, they have concluded that the presence of active sites on single atom catalysts showed selectivity for hydrogenation reaction over other catalysts.

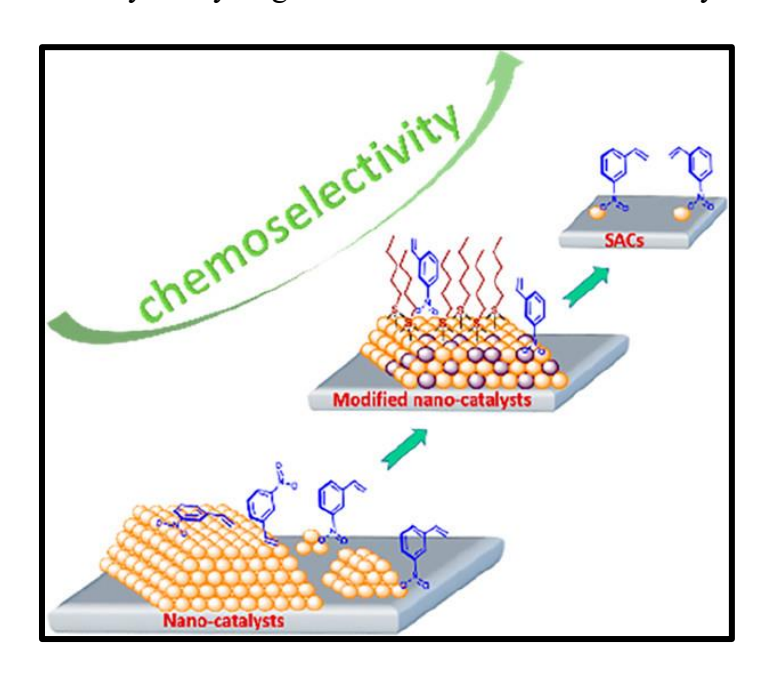


**Figure 1.11.** Chemoselectivity pattern from nanocatalysts to single atom catalysts.[7]

For CO<sub>2</sub> conversion into value added chemicals like CH<sub>4</sub>, HCOOH, MeOH etc have been extensively explored using SACs.[55,56] Mechanistic studies proved the high catalytic activity of single atom for the CO<sub>2</sub> activation and reduction. The production of methanol and hydrocarbons is highly desirable due to their use in synthesis of fuels and other fine chemicals. However, various reports were there on the synthesis of these chemicals and CO<sub>2</sub> conversion, but SACs showed greater activity compared to other materials. The side reactions during methanol or methane synthesis are the major issues during their selective production. Also, the traditional methods of CO<sub>2</sub> hydrogenation need to be improved to make it more practical. SACs pave the path for new catalytic approach by providing more active sites.

For example, SACs have been utilized for CO<sub>2</sub> fixation reaction of epoxides into cyclic carbonates. Xu et al. reported Iridium single atom supported on WO<sub>3</sub> catalyst for cycloaddition of CO<sub>2</sub>. Epichlorohydrin used as model substrate and TBAB used as co-catalyst with solvent-free conditions (Scheme 1.5).[57]

**Scheme 1.5.** CO<sub>2</sub> fixation reaction into epoxides sing SACs.

However, to make these processes more suitable for industrial applications, some efforts are required to design the catalysts to overcome the existing issues of product selectivity.

# 1.3. Scope of present work

The above discussed contain the importance of nanomaterials and single atom catalyst for catalytic reaction. The present thesis work focuses on heterogeneous catalysis using bimetallic nanocatalysts of non-noble metals i.e., Zn-Cu/MCM-41, CuNi-11, CuNi-12, CoNi and single atom catalyst

(Co/ZrO<sub>2</sub>). All catalysts were synthesized and characterized with various characterization techniques such as PXRD, TGA, BET, SEM, EDAX, HR-TEM, XPS and then utilized for various catalytic applications (hydrogenation and carboxylation reaction). All the nanocatalysts were synthesized using simple reduction method, wet-impregnation method, and liquid phase reduction methods. Furthermore, single atom catalyst was synthesized by co-precipitation method and extensively characterized via EXAFS, XANES, AC-STEM, HAADF, STEM-EDX and utilized for CO<sub>2</sub> fixation reaction into epoxides for cyclic carbonates. All results were compared with earlier results.

The main highlights of thesis work are mentioned below:

- 1) Zn-Cu supported on mesoporous silica MCM-41 (ZnO-Cu(OH)Cl/MCM-41) was synthesized via wetness-impregnation method and utilized for transfer hydrogenation of ketones with water as solvent and NaBH<sub>4</sub> as reducing agent.
- 2) Bimetallic CoNi nanoflowers were synthesized via liquid phase reduction method and utilized for reduction of terminal alkynes into alkanes using hydrazine hydrate as reducing agent and ethanol as solvent.
- 3) Bimetallic CuNi-12 nanoparticles were synthesized with 1:2 molar ratio of Cu:Ni and utilized for hydrogenation of biomass derived furfural and 5-hydroxy methyl furfural (HMF) into corresponding alcohols using 2-propanol as hydrogen source, KOH as base.
- 4) Bimetallic CuNi-11 nanoparticles were synthesized via simple reduction method with 1:1 molar ratio of Cu:Ni and utilized for carboxylation of benzene to benzoic acid with solvent-free condition and HCOOH as carboxylating agent. The reaction mechanism was explored with DFT calculations.
- 5) Co doped ZrO<sub>2</sub> single atom catalysts were synthesized and characterized via EXAFS, XANES, STEM-EDX, HAADF and the EDX data confirmed

the uniform dispersion all over the ZrO<sub>2</sub>. Also, for comparison, undoped ZrO<sub>2</sub> and impregnated Co<sub>3</sub>O<sub>4</sub>/ZrO<sub>2</sub> was also synthesized and utilized for chemical fixation of CO<sub>2</sub> and Co/ZrO<sub>2</sub> single atom catalyst showed superior catalytic activity with 100% conversion and selectivity with solvent free conditions.

#### 1.4. References

- [1] Z. Guo, B. Liu, Q. Zhang, W. Deng, Y. Wang, Y. Yang, Recent advances in heterogeneous selective oxidation catalysis for sustainable chemistry, Chem. Soc. Rev. 43 (2014) 3480–3524. https://doi.org/10.1039/C3CS60282F.
- [2] A. Balouch, A. Ali Umar, A.A. Shah, M. Mat Salleh, M. Oyama, Efficient Heterogeneous Catalytic Hydrogenation of Acetone to Isopropanol on Semihollow and Porous Palladium Nanocatalyst, ACS Appl. Mater. Interfaces. 5 (2013) 9843–9849. https://doi.org/10.1021/am403087m.
- [3] D. Astruc, Introduction: Nanoparticles in Catalysis, Chem. Rev. 120 (2020) 461–463. https://doi.org/10.1021/acs.chemrev.8b00696.
- [4] A.K. Singh, Q. Xu, Synergistic Catalysis over Bimetallic Alloy Nanoparticles, ChemCatChem. 5 (2013) 652–676. https://doi.org/10.1002/cctc.201200591.
- [5] W. Gong, C. Chen, H. Zhang, G. Wang, H. Zhao, In Situ Synthesis of Highly Dispersed Cu–Co Bimetallic Nanoparticles for Tandem Hydrogenation/Rearrangement of Bioderived Furfural in Aqueous-Phase, ACS Sustain. Chem. Eng. 6 (2018) 14919–14925. https://doi.org/10.1021/acssuschemeng.8b03418.
- [6] I. Mustieles Marin, J.M. Asensio, B. Chaudret, Bimetallic Nanoparticles Associating Noble Metals and First-Row Transition Metals in Catalysis, ACS Nano. 15 (2021) 3550–3556. https://doi.org/10.1021/acsnano.0c09744.
- [7] L. Zhang, M. Zhou, A. Wang, T. Zhang, Selective Hydrogenation over Supported Metal Catalysts: From Nanoparticles to Single Atoms, Chem. Rev. 120 (2020) 683–733. https://doi.org/10.1021/acs.chemrev.9b00230.
- [8] M. Oezaslan, M. Heggen, P. Strasser, Size-Dependent Morphology of Dealloyed Bimetallic Catalysts: Linking the Nano to the Macro Scale, J. Am. Chem. Soc. 134 (2012) 514–524. https://doi.org/10.1021/ja2088162.
- [9] M. Meng-Jung Li, S.C. Edman Tsang, Bimetallic catalysts for green methanol production via CO 2 and renewable hydrogen: a mini-review

- and prospects, Catal. Sci. Technol. 8 (2018) 3450–3464. https://doi.org/10.1039/C8CY00304A.
- [10] H.-L. Jiang, Q. Xu, Recent progress in synergistic catalysis over heterometallic nanoparticles, J. Mater. Chem. 21 (2011) 13705–13725. https://doi.org/10.1039/C1JM12020D.
- [11] M. Ali Nasseri, Z. Rezazadeh, M. Kazemnejadi, A. Allahresani, A Co–Cu bimetallic magnetic nanocatalyst with synergistic and bifunctional performance for the base-free Suzuki, Sonogashira, and C–N cross-coupling reactions in water, Dalton Trans. 49 (2020) 10645–10660. https://doi.org/10.1039/D0DT01846E.
- [12] B.D. Boruah, A. Maji, A. Misra, Synergistic effect in the heterostructure of ZnCo 2 O 4 and hydrogenated zinc oxide nanorods for high capacitive response, Nanoscale. 9 (2017) 9411–9420. https://doi.org/10.1039/C7NR01644A.
- [13] G. Vilé, N. Almora-Barrios, S. Mitchell, N. López, J. Pérez-Ramírez, From the Lindlar catalyst to supported ligand-modified palladium nanoparticles: selectivity patterns and accessibility constraints in the continuous-flow three-phase hydrogenation of acetylenic compounds, Chem. Eur. J. 20 (2014) 5926–5937.
- [14] Partial oxidation of methane over monometallic and bimetallic Ni-, Rh-, Re-based catalysts: Effects of Re addition, co-fed reactants and catalyst support, Appl. Catal. Gen. 563 (2018) 1–8. https://doi.org/10.1016/j.apcata.2018.06.032.
- [15] K. A. Goulas, Y. Song, G. R. Johnson, J. P. Chen, A. A. Gokhale, L. C. Grabow, F. Dean Toste, Selectivity tuning over monometallic and bimetallic dehydrogenation catalysts: effects of support and particle size, Catal. Sci. Technol. 8 (2018) 314–327. https://doi.org/10.1039/C7CY01306J.
- [16] A. Iriondo, J.F. Cambra, V.L. Barrio, M.B. Guemez, P.L. Arias, M.C. Sanchez-Sanchez, R.M. Navarro, J.L.G. Fierro, Glycerol liquid phase conversion over monometallic and bimetallic catalysts: Effect of metal, support type and reaction temperatures, Appl. Catal. B Environ. 106 (2011) 83–93. https://doi.org/10.1016/j.apcatb.2011.05.009.
- [17] B. Seemala, C.M. Cai, R. Kumar, C.E. Wyman, P. Christopher, Effects of Cu–Ni Bimetallic Catalyst Composition and Support on Activity, Selectivity, and Stability for Furfural Conversion to 2-Methyfuran, ACS Sustain. Chem. Eng. 6 (2018) 2152–2161. https://doi.org/10.1021/acssuschemeng.7b03572.
- [18] A. Robinson, G.A. Ferguson, J.R. Gallagher, S. Cheah, G.T. Beckham, J.A. Schaidle, J.E. Hensley, J.W. Medlin, Enhanced Hydrodeoxygenation of m-Cresol over Bimetallic Pt-Mo Catalysts through an Oxophilic Metal-Induced Tautomerization Pathway, ACS Catal. 6 (2016) 4356–4368. https://doi.org/10.1021/acscatal.6b01131.
- [19] T.W. van Deelen, C. Hernández Mejía, K.P. de Jong, Control of metalsupport interactions in heterogeneous catalysts to enhance activity and

- selectivity, Nat. Catal. 2 (2019) 955–970. https://doi.org/10.1038/s41929-019-0364-x.
- [20] C. Gao, F. Lyu, Y. Yin, Encapsulated Metal Nanoparticles for Catalysis, Chem. Rev. 121 (2021) 834–881. https://doi.org/10.1021/acs.chemrev.0c00237.
- [21] A. Lion, N. Laidani, P. Bettotti, C. Piotto, G. Pepponi, M. Barozzi, M. Scarpa, Angle resolved XPS for selective characterization of internal and external surface of porous silicon, Appl. Surf. Sci. 406 (2017) 144–149. https://doi.org/10.1016/j.apsusc.2017.02.099.
- [22] J. Kecht, A. Schlossbauer, T. Bein, Selective Functionalization of the Outer and Inner Surfaces in Mesoporous Silica Nanoparticles, Chem. Mater. 20 (2008) 7207–7214. https://doi.org/10.1021/cm801484r.
- [23] S. Schauermann, N. Nilius, S. Shaikhutdinov, H.-J. Freund, Nanoparticles for Heterogeneous Catalysis: New Mechanistic Insights, Acc. Chem. Res. 46 (2013) 1673–1681. https://doi.org/10.1021/ar300225s.
- [24] R.L. Oliveira, J. Kerstien, R. Schomäcker, A. Thomas, Pd nanoparticles confined in mesoporous N-doped carbon silica supports: a synergistic effect between catalyst and support, Catal. Sci. Technol. 10 (2020) 1385–1394. https://doi.org/10.1039/C9CY01920K.
- [25] S. Li, C. Cheng, X. Zhao, J. Schmidt, A. Thomas, Active Salt/Silica-Templated 2D Mesoporous FeCo-Nx-Carbon as Bifunctional Oxygen Electrodes for Zinc–Air Batteries, Angew. Chem. Int. Ed. 57 (2018) 1856–1862. https://doi.org/10.1002/anie.201710852.
- [26] X. Xu, Y. Li, Y. Gong, P. Zhang, H. Li, Y. Wang, Synthesis of Palladium Nanoparticles Supported on Mesoporous N-Doped Carbon and Their Catalytic Ability for Biofuel Upgrade, J. Am. Chem. Soc. 134 (2012) 16987–16990. https://doi.org/10.1021/ja308139s.
- [27] D. Wang, C. Deraedt, J. Ruiz, D. Astruc, Magnetic and Dendritic Catalysts, Acc. Chem. Res. 48 (2015) 1871–1880. https://doi.org/10.1021/acs.accounts.5b00039.
- [28] S. Khizar, N.M. Ahmad, N. Zine, N. Jaffrezic-Renault, A. Errachid-elsalhi, A. Elaissari, Magnetic Nanoparticles: From Synthesis to Theranostic Applications, ACS Appl. Nano Mater. 4 (2021) 4284–4306. https://doi.org/10.1021/acsanm.1c00852.
- [29] R.K. Sharma, M. Yadav, Y. Monga, R. Gaur, A. Adholeya, R. Zboril, R.S. Varma, M.B. Gawande, Silica-Based Magnetic Manganese Nanocatalyst Applications in the Oxidation of Organic Halides and Alcohols, ACS Sustain. Chem. Eng. 4 (2016) 1123–1130. https://doi.org/10.1021/acssuschemeng.5b01183.
- [30] P. Guardia, A. Labarta, X. Batlle, Tuning the Size, the Shape, and the Magnetic Properties of Iron Oxide Nanoparticles, J. Phys. Chem. C. 115 (2011) 390–396. https://doi.org/10.1021/jp1084982.
- [31] R.B. Nasir Baig, R. S. Varma, Magnetically retrievable catalysts for organic synthesis, Chem. Commun. 49 (2013) 752–770. https://doi.org/10.1039/C2CC35663E.

- [32] Q. Zhang, X. Yang, J. Guan, Applications of Magnetic Nanomaterials in Heterogeneous Catalysis, ACS Appl. Nano Mater. 2 (2019) 4681–4697. https://doi.org/10.1021/acsanm.9b00976.
- [33] L. Liu, A. Corma, Metal Catalysts for Heterogeneous Catalysis: From Single Atoms to Nanoclusters and Nanoparticles, Chem. Rev. 118 (2018) 4981–5079. https://doi.org/10.1021/acs.chemrev.7b00776.
- [34] H. Kweon, S. Jang, A. Bereketova, J.C. Park, K. Hyun Park, Highly dispersed Ni nanoparticles on mesoporous silica nanospheres by melt infiltration for transfer hydrogenation of aryl ketones, RSC Adv. 9 (2019) 14154–14159. https://doi.org/10.1039/C9RA01608B.
- [35] J. Lin, J. Chen, W. Su, Rhodium-Cobalt Bimetallic Nanoparticles: A Catalyst for Selective Hydrogenation of Unsaturated Carbon-Carbon Bonds with Hydrous Hydrazine, Adv. Synth. Catal. 355 (2013) 41–46. https://doi.org/10.1002/adsc.201200576.
- [36] R. Bhaskar, H. Joshi, A.K. Sharma, A.K. Singh, Reusable Catalyst for Transfer Hydrogenation of Aldehydes and Ketones Designed by Anchoring Palladium as Nanoparticles on Graphene Oxide Functionalized with Selenated Amine, ACS Appl. Mater. Interfaces. 9 (2017) 2223–2231. https://doi.org/10.1021/acsami.6b10457.
- [37] F.-P. Wu, J.-B. Peng, X. Qi, X.-F. Wu, Palladium-Catalyzed Carbonylative Transformation of Organic Halides with Formic Acid as the Coupling Partner and CO Source: Synthesis of Carboxylic Acids, J. Org. Chem. 82 (2017) 9710–9714. https://doi.org/10.1021/acs.joc.7b01808.
- [38] A. Wang, J. Li, T. Zhang, Heterogeneous single-atom catalysis, Nat. Rev. Chem. 2 (2018) 65–81. https://doi.org/10.1038/s41570-018-0010-1.
- [39] Y. Shang, X. Xu, B. Gao, S. Wang, X. Duan, Single-atom catalysis in advanced oxidation processes for environmental remediation, Chem. Soc. Rev. 50 (2021) 5281–5322. https://doi.org/10.1039/D0CS01032D.
- [40] B. Singh, M.B. Gawande, A.D. Kute, R.S. Varma, P. Fornasiero, P. McNeice, R.V. Jagadeesh, M. Beller, R. Zbořil, Single-Atom (Iron-Based) Catalysts: Synthesis and Applications, Chem. Rev. 121 (2021) 13620–13697. https://doi.org/10.1021/acs.chemrev.1c00158.
- [41] L. Gong, D. Zhang, C.-Y. Lin, Y. Zhu, Y. Shen, J. Zhang, X. Han, L. Zhang, Z. Xia, Catalytic Mechanisms and Design Principles for Single-Atom Catalysts in Highly Efficient CO2 Conversion, Adv. Energy Mater. 9 (2019) 1902625. https://doi.org/10.1002/aenm.201902625.
- [42] Y. Kwon, T.Y. Kim, G. Kwon, J. Yi, H. Lee, Selective Activation of Methane on Single-Atom Catalyst of Rhodium Dispersed on Zirconia for Direct Conversion, J. Am. Chem. Soc. 139 (2017) 17694–17699. https://doi.org/10.1021/jacs.7b11010.

- [43] X.-F. Yang, A. Wang, B. Qiao, J. Li, J. Liu, T. Zhang, Single-Atom Catalysts: A New Frontier in Heterogeneous Catalysis, Acc. Chem. Res. 46 (2013) 1740–1748. https://doi.org/10.1021/ar300361m.
- [44] J. Li, Y. Jiang, Q. Wang, C.-Q. Xu, D. Wu, M.N. Banis, K.R. Adair, K. Doyle-Davis, D.M. Meira, Y.Z. Finfrock, W. Li, L. Zhang, T.-K. Sham, R. Li, N. Chen, M. Gu, J. Li, X. Sun, A general strategy for preparing pyrrolic-N4 type single-atom catalysts via pre-located isolated atoms, Nat. Commun. 12 (2021) 6806. https://doi.org/10.1038/s41467-021-27143-5.
- [45] J. Wan, W. Chen, C. Jia, L. Zheng, J. Dong, X. Zheng, Y. Wang, W. Yan, C. Chen, Q. Peng, D. Wang, Y. Li, Defect Effects on TiO2 Nanosheets: Stabilizing Single Atomic Site Au and Promoting Catalytic Properties, Adv. Mater. 30 (2018) 1705369. https://doi.org/10.1002/adma.201705369.
- [46] S.K. Kaiser, Z. Chen, D. Faust Akl, S. Mitchell, J. Pérez-Ramírez, Single-Atom Catalysts across the Periodic Table, Chem. Rev. 120 (2020) 11703–11809. https://doi.org/10.1021/acs.chemrev.0c00576.
- [47] X.-K. Kong, C.-L. Chen, Q.-W. Chen, Doped graphene for metal-free catalysis, Chem. Soc. Rev. 43 (2014) 2841–2857. https://doi.org/10.1039/C3CS60401B.
- [48] Y. Liu, Z. Li, Q. Yu, Y. Chen, Z. Chai, G. Zhao, S. Liu, W.-C. Cheong, Y. Pan, Q. Zhang, L. Gu, L. Zheng, Y. Wang, Y. Lu, D. Wang, C. Chen, Q. Peng, Y. Liu, L. Liu, J. Chen, Y. Li, A General Strategy for Fabricating Isolated Single Metal Atomic Site Catalysts in Y Zeolite, J. Am. Chem. Soc. 141 (2019) 9305–9311. https://doi.org/10.1021/jacs.9b02936.
- [49] Y. Xia, M. Sayed, L. Zhang, B. Cheng, J. Yu, Single-atom heterogeneous photocatalysts, Chem Catal. 1 (2021) 1173–1214. https://doi.org/10.1016/j.checat.2021.08.009.
- [50] J. Su, R. Ge, Y. Dong, F. Hao, L. Chen, Recent progress in single-atom electrocatalysts: concept, synthesis, and applications in clean energy conversion, J. Mater. Chem. A. 6 (2018) 14025–14042. https://doi.org/10.1039/C8TA04064H.
- [51] L. Liu, M. Li, F. Chen, H. Huang, Recent Advances on Single-Atom Catalysts for CO2 Reduction, Small Struct. 4 (2023) 2200188. https://doi.org/10.1002/sstr.202200188.
- [52] J. Fang, Q. Chen, Z. Li, J. Mao, Y. Li, The synthesis of single-atom catalysts for heterogeneous catalysis, Chem. Commun. 59 (2023) 2854–2868. https://doi.org/10.1039/D2CC06406E.
- [53] J. Xia, B. Wang, J. Di, Y. Li, S.-Z. Yang, H. Li, S. Guo, Construction of single-atom catalysts for electro-, photo- and photoelectro-catalytic applications: State-of-the-art, opportunities, and challenges, Mater. Today. 53 (2022) 217–237. https://doi.org/10.1016/j.mattod.2021.11.022.
- [54] C.D. Koolen, W. Luo, A. Züttel, From Single Crystal to Single Atom Catalysts: Structural Factors Influencing the Performance of Metal

- Catalysts for CO2 Electroreduction, ACS Catal. 13 (2023) 948–973. https://doi.org/10.1021/acscatal.2c03842.
- [55] Y. Guo, S. Mei, K. Yuan, D.-J. Wang, H.-C. Liu, C.-H. Yan, Y.-W. Zhang, Low-Temperature CO2 Methanation over CeO2-Supported Ru Single Atoms, Nanoclusters, and Nanoparticles Competitively Tuned by Strong Metal–Support Interactions and H-Spillover Effect, ACS Catal. 8 (2018) 6203–6215. https://doi.org/10.1021/acscatal.7b04469.
- [56] Z. Fu, M. Wu, Y. Zhou, Z. Lyu, Y. Ouyang, Q. Li, J. Wang, Support-based modulation strategies in single-atom catalysts for electrochemical CO 2 reduction: graphene and conjugated macrocyclic complexes, J. Mater. Chem. A. 10 (2022) 5699–5716. https://doi.org/10.1039/D1TA09069K.
- [57] Xu et al., Strong Electronic Metal—Support Interaction between Iridium Single Atoms and a WO3 Support Promotes Highly Efficient and Robust CO2 Cycloaddition, Adv. Mater. 34 (2022) 2206991. https://doi.org/10.1002/adma.202206991.

## **CHAPTER 2**

# Ketone Hydrogenation by using ZnO-Cu(OH)Cl/MCM-41 with a Splash of Water: an Environmentally Benign Approach

#### 2.1. Introduction

Nanoparticles as a catalyst have recently attracted the attention of the scientific community because of their high selectivity, durability, recoverability with considerable economic benefits in manufacturing as an industrial commodity.[1] Metal nanoparticles as catalysts are popular owing to their high surface area properties, leading to enhanced interaction between reactant and catalyst surface, hence high activities observed even under mild conditions.[2] Nanocatalysts have applications in numerous fields such various petrochemicals, pharmaceuticals, chemicals, food processing.[3,4] The nanomaterial based on transition metals is the center of attraction because these species can be used both as a catalyst and catalyst support due to their activity and their activated surface.[5] The first row transition metals are replacing the organometallic compounds due to their high stability and low cost. Since they advantages mixture so we can say that nanoparticles bridge the gap between homogeneous heterogeneous catalysis.[6] Hence, after studying the and aforementioned advantages, we have synthesized the nanocatalyst ZnO-Cu(OH)Cl/MCM-41 nanoparticles with 2.46 wt% zinc and 6.39 wt% copper by using MCM-41 (Mobil Corporation Matter no. 41) as support for zinc and copper oxides.

From previous reports, it deduced that individually ZnO and CuO have various properties such as high electron mobility, high catalytic activity, high chemical and thermal stability and non-toxicity, easy availability in nature as well as biocompatibility,[7–9] while a hybrid Copper-Zinc oxide catalyst possess application in steam forming[10,11], methanol synthesis,[12–14] methanol reforming for

fuel cell,[15] anodic material in lithium-ion batteries[16] and CO<sub>2</sub> fixation.[17] So, we have amalgamated them together and synthesized a catalyst with zinc and copper supported on mesoporous silica MCM-41. Out of various metal nanoparticle supports reported like MnO<sub>2</sub>,[18,19] alumina,[20] graphene oxide[21] and cerium oxide[22] silica MCM-41 as support pertaining its high surface area (~1000 m<sup>2</sup>/g) and pore diameter.[23] Being a porous material, it is capable of providing more active sites to the reactant and permitting both internal and external catalysis.[24] Hence, the above properties make MCM-41 an appealing and a novel candidate to act as a support of metal nanoparticles for catalysis. The previous reports has marked efficiency of MCM-41 as support for catalysis of acetylene hydration,[25] oxidation of phenol solution,[26] hydrohalogenation chlorobenzene,[27] amination of glycerol,[28] formylation of hydrosulfurization methanation,[30] amines,[29] syngas of dibenzothiophene,[31] toluene alkylation,[32] oxidation of hydrocarbons,[33] hydrogenation,[34]<sup>-</sup>[35] and also used as drug delivery[36], etc. Herein, the catalytic transfer hydrogenation using acetophenone as model substrate was studied and the best reaction condition was optimized using ZnO-Cu(OH)Cl/MCM-41 catalyst.

The principle of 'green chemistry', focusses on non-toxicity of the reaction solvent along with recyclability and cost-effectiveness of the catalyst.[37] Water as a solvent demonstrates distinctive activity. Hence, in this work water as "green solvent" used, which is cheap, abundant, eco-friendly, and non-toxic for the reduction of ketones using synthesized nanomaterial ZnO-Cu(OH)Cl/MCM-41 nanoparticles with 2.46 wt% zinc and 6.39 wt% copper along with sodium borohydride as reducing agent. Reduction using hydrogen sources like water, methanol, isopropanol, which is known as transfer hydrogenation has attracted attention owing to its secure handling and also safety concerns.[38] Although, sodium borohydride reported for reduction of ketones and aldehydes to alcohols in organic chemistry[39] with different catalyst. As previously reported that 1-Phenyl ethanol is used as a flavouring agent, coloring agent in food additives, perfumery agent, and in pharmaceutical industries.[40] We have designed and evaluated the reduction of acetophenone to 1-Phenyl ethanol as model substrate using sodium borohydride and water as a solvent. [41,42]

## 2.2. Experimental

#### 2.2.1. Synthesis of Zn-Cu/MCM-41

Materials used for synthesizing the nanoparticles were Mesoporous Silica MCM-41, Zinc Chloride and Copper (ii) chloride (≥ 98%), Zinc Oxide nanopowder, and all reagent grade ketones, heterocyclic compounds for the catalytic reaction were purchased from Merck. For the preparation of bimetallic ZnO-Cu(OH)Cl catalyst supported on MCM-41, firstly zinc chloride (ZnCl₂) 3 g and copper chloride (CuCl₂) 0.33 g were dissolved in 90 ml deionized water with 9:1 weight% loading respectively and stir for 15 minutes. After that the aqueous solution of metal salts was added dropwise to the MCM-41 (333 mg) with continuous stirring at room temperature for 6 hours in the round bottom flask. The precipitate was then centrifuged and dried at 100 °C overnight, and hence, the synthesized catalyst named as ZnO-Cu(OH)Cl/MCM-41 nanoparticles.

#### 2.2.2. General catalytic procedure

The reduction of ketones carried out in a 15 mL culture tube with stirring at a magnetic bar stirrer at 40 °C temperature. The ketone substrate (1 mmol), reducing agent NaBH<sub>4</sub> (0.5-1 mmol), 3 mg of catalyst (ZnO-Cu(OH)Cl/MCM-41 nanoparticles with 2.46 wt% zinc and 6.39 wt% copper) and water (2 mL) stirred at 40 °C for appropriate time(0.5-4 h). After 100% conversion of the reactant, the reaction mixture was quenched with NH<sub>4</sub>Cl aqueous solution to pH = 7 and then work up with ethyl acetate and further analyzed by Shimadzu GC-MS.

#### 2.2.3. Physicochemical measurements

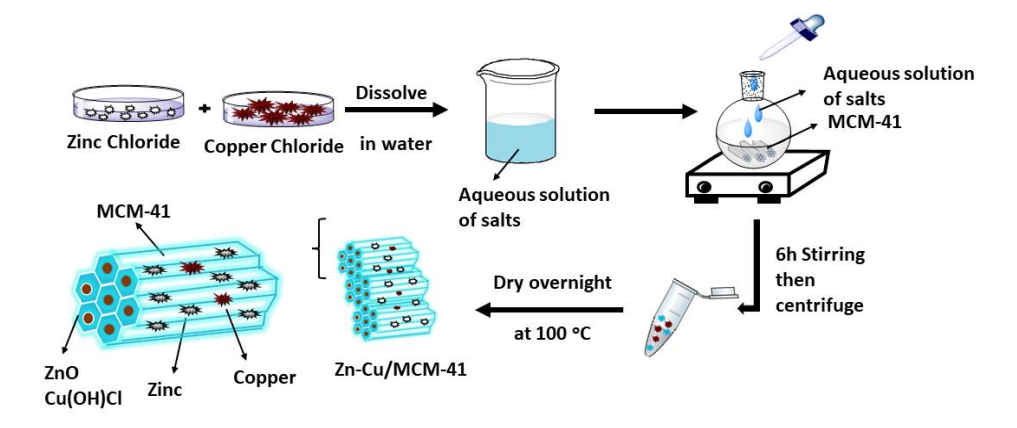
Powder x-ray diffraction (PXRD) of the nanoparticle performed using Cu Kα radiation (1.54 Å) using the Rigaku Smart Lab X-ray

diffractometer. Fourier-transform infrared spectroscopy (FT-IR) carried out using KBr pellets with a Bio-Rad FTS 3000MX instrument. For analyzing thermal stability, the thermogravimetric analysis performed using TGA 4000, Perkin Elmer using software PYRIS 6. To know the surface morphology, Scanning Electron Microscopy (FE-SEM) and Field Emission Gun-Transmission electron microscopy (HR-TEM, 300 kV) performed using Supra55 Zeiss and FEI Tecnai G2, F30 respectively. The Brunauer-Emmett-Teller (BET) surface CO<sub>2</sub> adsorption-desorption determined using  $N_2$ and measurements. XPS analysis of fresh and spent catalysts recorded using Auger Electron Spectroscopy (AES) PHI 5000 Versa Prob II, FEI Inc. Identification of the products of catalytic reactions carried out using Shimadzu GC-MS, QP2010 mass spectrometer.

#### 2.3. Results and discussion

#### 2.3.1. Characterization of nanoparticles

Synthesis of the catalyst is carried out via an incipient wetness impregnation technique as shown below in **Scheme 2.1**.



Scheme 2.1. Synthesis of ZnO-Cu(OH)Cl/MCM-41 nanoparticles.

The XRD patterns of ZnO-Cu(OH)Cl/MCM-41 nanoparticles with 2.46 wt% zinc and 6.39 wt% copper catalyst is shown in **Figure 2.1**, in which a broad peak around  $2\theta = 23^{\circ}$ , indicates amorphous behaviour of MCM-41 silica support [43]<sup>-</sup>[44] and the other diffraction peaks on  $2\theta = 16.16^{\circ}$ ,  $32.28^{\circ}$  and  $39.64^{\circ}$  representing the planes (100), (021) and (121) of Cu(OH)Cl (PDF- #51-0400) and the diffraction peak at  $32.28^{\circ}$ 

confirmed the ZnO formation and exactly matched with JCPDS No. 36-1451.[45] This revealed the formation of ZnO-Cu(OH)Cl/MCM-41 nanoparticles with 2.46 wt% zinc and 6.39 wt% copper. The average crystallite size of the ZnO-Cu(OH)Cl/MCM-41 nanoparticles obtained 29 nm by using Scherrer's equation.

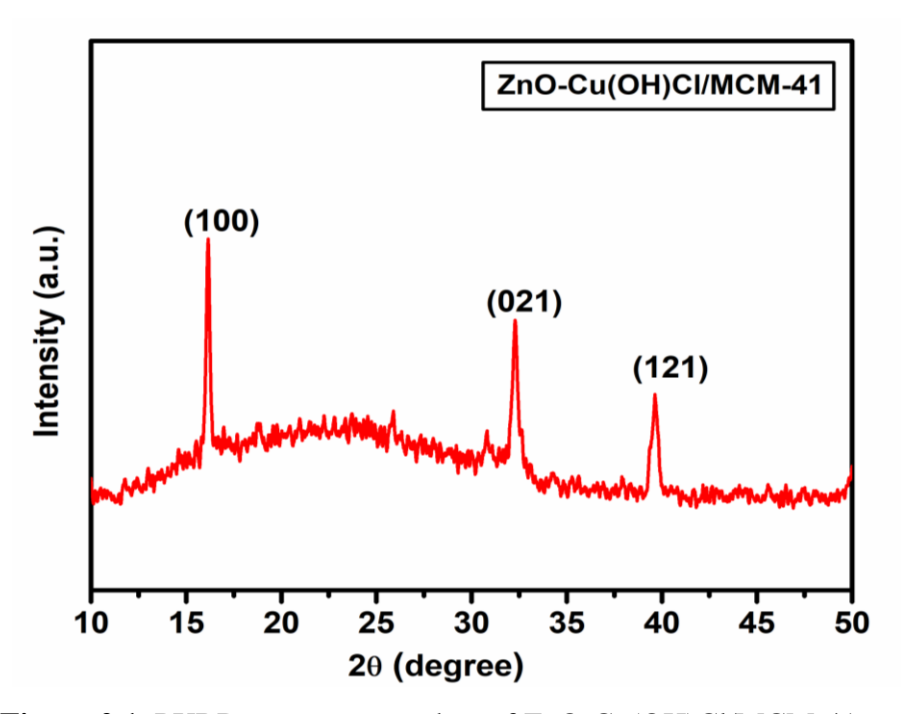


**Figure 2.1.** PXRD measurement data of ZnO-Cu(OH)Cl/MCM-41.

In the FT-IR spectrum, as shown in **Figure 2.2**, the absorption peak at 3566 cm<sup>-1</sup> assigned to the stretching vibrations of –OH bond of silanol group of surface of supported silica[26,46] and the absorption band at 1620 cm<sup>-1</sup> was because of bending vibration of H-OH bond[47], and 956 cm<sup>-1</sup> attributed to the asymmetric stretching vibration of Si-OH bond.[48,49] The absorption band at 802, 1087, and 1237 cm<sup>-1</sup> assigned to internal and external asymmetric stretching of Si-O-Si of the SiO<sub>2</sub> framework. The shift in absorption peaks was may be because of the substitution of silicon by incorporated metals zinc and copper.[27] Due to the introduction of zinc and copper the bond distance of Si-O increases and causes the smaller wavenumbers.[27]

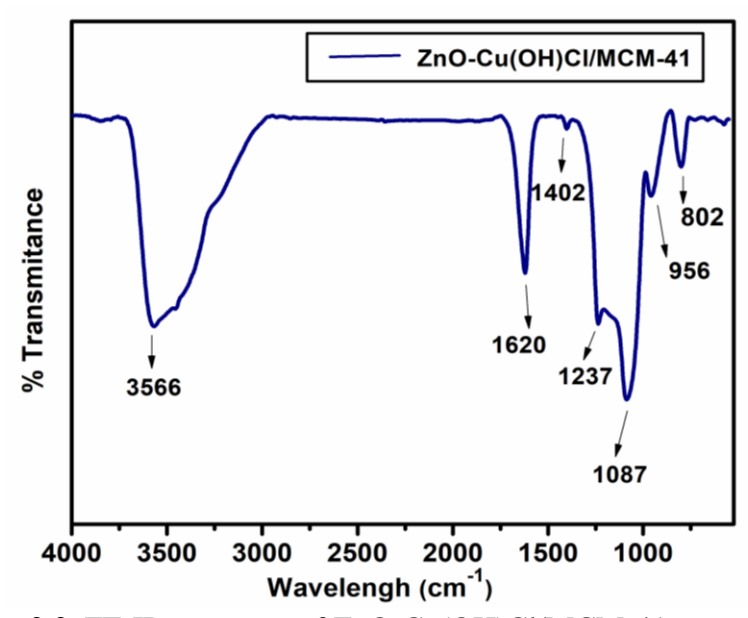


Figure 2.2. FT-IR spectrum of ZnO-Cu(OH)Cl/MCM-41.

Thermogravimetric analysis (TGA) was performed to determine the thermal stability of the catalyst (**Figure 2.3**). The major weight loss observed in three temperature regions: (i) 37 – 140 °C, (ii) 202 – 490 °C, and (iii) above 490 °C. The total weight of the sample is 4.336 mg and the weight loss in these three major regions is respectively 18.656 wt%, 8.659 wt% and 20.023 wt%. The weight loss below 140 °C might be because of the removal of adsorbed water and organic solvents. The second significant weight loss was observed because of the removal of organic species trapped inside the pores of supported silica. Beyond 490 °C, the weight loss due to the removal of hydroxyl groups linked to copper[43] and condensation of Si-OH groups of the inner surface of pores of silica.[50]

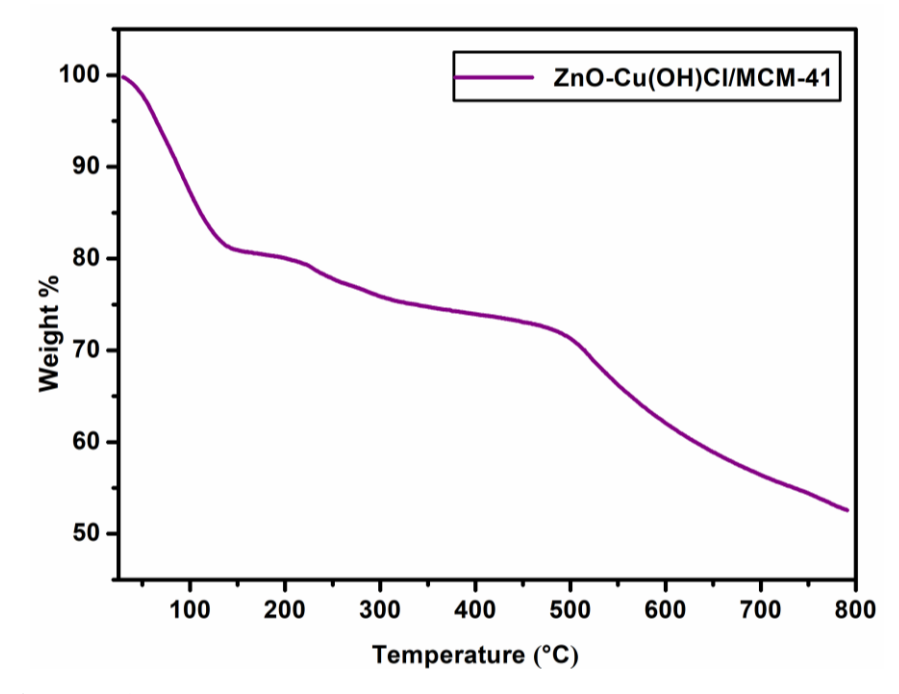
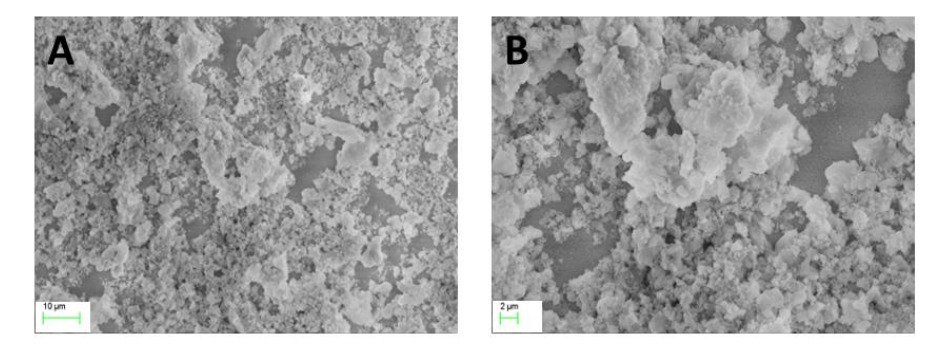
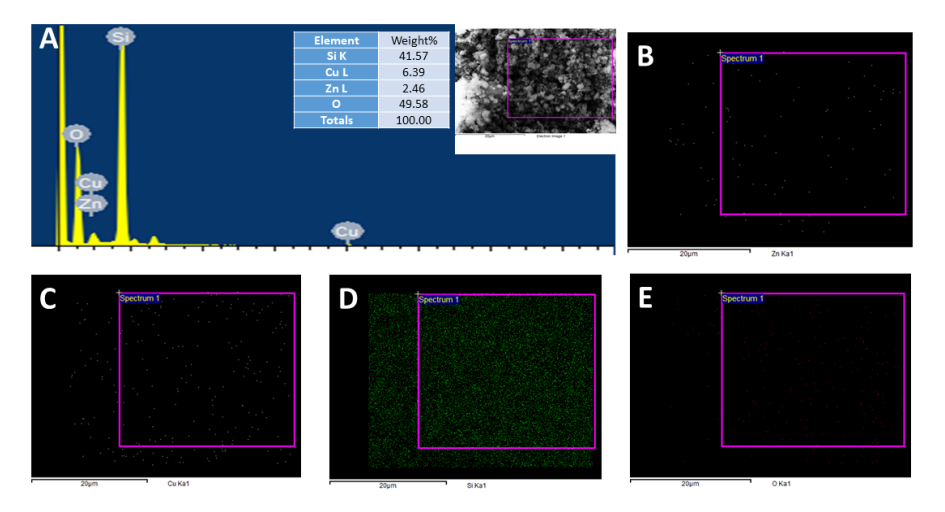


Figure 2.3. Thermogravimetric analysis of ZnO-Cu(OH)Cl/MCM-41.

SEM analysis performed to study the surface morphology and the structure of the nanoparticles, as shown in **Figure 2.4**. The presence of Zn, Cu, Si, and O elements was confirmed by EDAX and mapping (**Figure 2.5** (**A-E**)). Moreover, the EDAX spectrum for catalyst ZnO-Cu(OH)Cl/MCM-41 shows the presence of desired elements such as Zn, Cu, Si, and O with 6.39 wt% of copper and 2.46 wt% of zinc present.



**Figure 2.4.** SEM images at (**A**) 10  $\mu$ m and (**B**) 2  $\mu$ m of catalyst ZnO-Cu(OH)Cl/MCM-41.



**Figure 2.5.** (**A**) Mapping, (**B**) Zn, (**C**) Cu, (**D**) Si, (E) **O** elemental analysis of ZnO-Cu(OH)Cl/MCM-41 catalyst.

To understand the surface morphology and distribution of zinc and copper on the surface of the catalyst, the TEM experiment was performed. As shown in all images, it is confirmed that the metal nanoparticles are disseminated on the surface of MCM-41. The highly ordered hexagonal channels of MCM-41 can easily be seen in Figure **2.6(A-B)**,[33,51] and **Figure 2.6C** indicates the incorporation of metal inside further pores which corroborated adsorption/desorption study which shows the decrease in surface area of MCM-41 in ZnO-Cu(OH)Cl/MCM-41 nanoparticles with 2.46 wt% zinc and 6.39 wt% copper.[52] It is also validated that the MCM-41 is used as support for zinc and copper and after introducing the metals, there is no change in the framework of MCM-41.[48,49] As shown in Figure 2.5D, selected area electron diffraction (SAED) was performed which indicated the concentric rings which show the crystalline nature of the catalyst ZnO-Cu(OH)Cl/MCM-41 nanoparticles with 2.46 wt% zinc and 6.39 wt% copper.

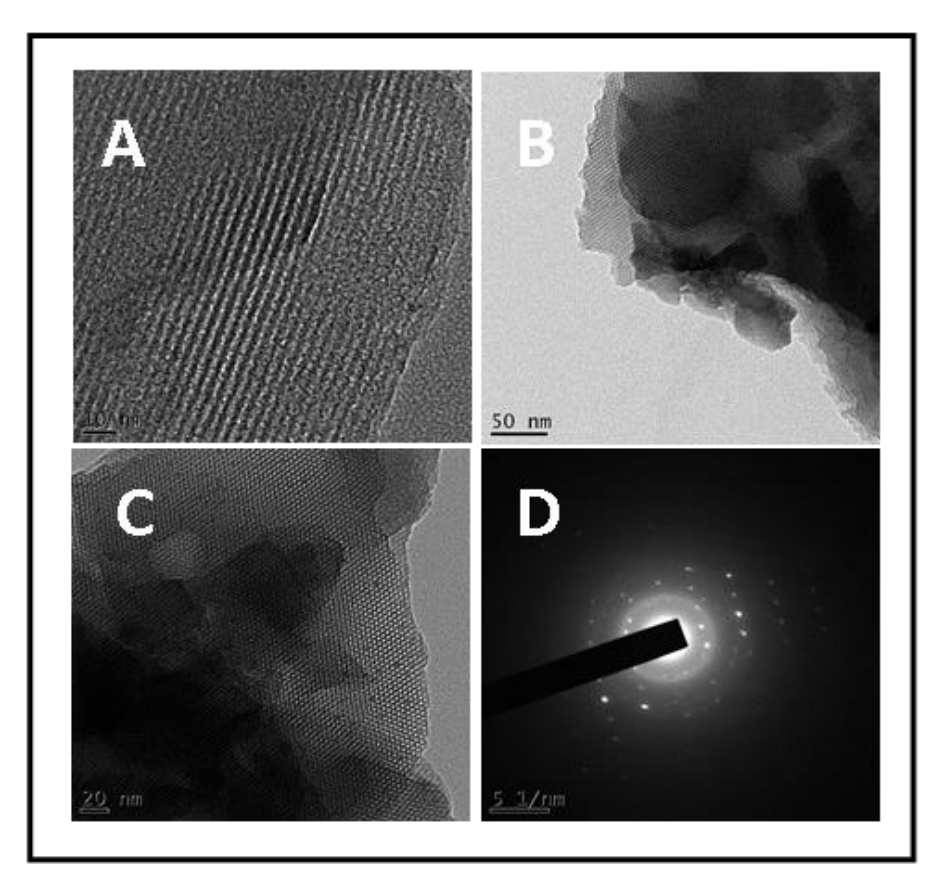


**Figure 2.6.** HR-TEM analysis of catalyst at (**A**) 10 nm, (**B**) 50 nm and (**C**) 20 nm and (**D**) SAED images of nanoparticles at 5 1/nm.

Furthermore, the pore size and surface area of the catalyst was determined by the nitrogen gas adsorption and desorption studies as shown in Figure 2.7 (A-B). The observed adsorption-desorption isotherm was type IV which indicate the mesoporous behaviour of the catalyst.[53,54] The surface area of ZnO-Cu(OH)Cl/MCM-41 nanoparticles with 2.46 wt% zinc and 6.39 wt% copper calculated with the Brunauer-Emmett-Teller (BET) equation was 239.079 m<sup>2</sup>/g, and pore volume is 0.743 cc/g and pore diameter 3.055 nm. The surface area for MCM-41 is approximate 1000 m<sup>2</sup>/g and the pore volume 0.98 cc/g and pore diameter 4 nm which decreases after incorporation of metal inside the pore of the MCM-41. Incorporation of metal species blocked the pores of the supported silica MCM-41 and reduced the specific surface area and pore volume.[55,56] The hysteresis curve indicates that the metal species distributed all over the channels of MCM-41. The metal species were not agglomerated at the opening of mesopores of MCM-41.[52]

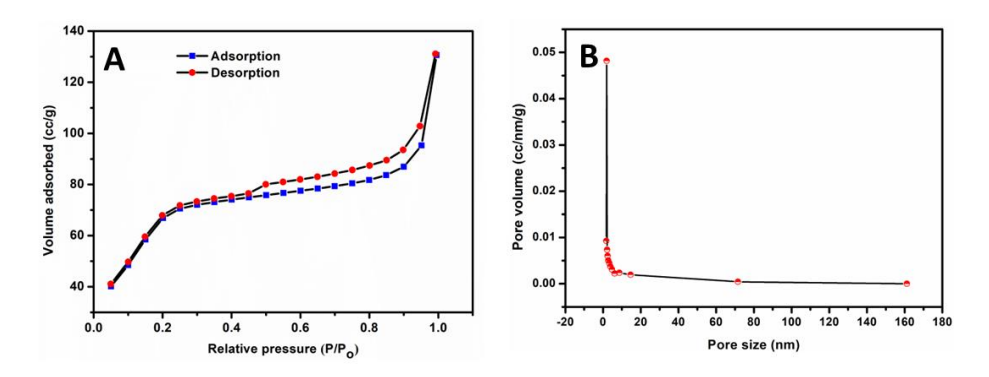


**Figure 2.7.** N<sub>2</sub> adsorption-desorption studies for (**A**) surface area and (**B**) pore size measurement.

The chemical composition and oxidation states of the prepared ZnO-Cu(OH)Cl/MCM-41 nanoparticles with 2.46 wt% zinc and 6.39 wt% copper were investigated by X-ray photoelectron spectroscopy (XPS) analysis as shown in Figure 6. The survey spectrum and high-resolution XPS of ZnO-Cu(OH)Cl/MCM-41 showed the existence of Zn, Cu and O (**Figure 2.8**). The high-resolution XPS spectra of Zn 2p reveals the binding energies of Zn  $2p_{3/2}$  at about 1020.5 eV and Zn  $2p_{1/2}$  center at 1043.7 eV, peak shape and peak separation which is ~ 23eV revealed that presence of  $2n^{2}$  in  $2n^{2}$  as shown in **Figure 2.8A**.[57,58] XPS spectra of Cu  $2p^{2}$  showed the two peaks centered at 933 eV and 953 eV were assign to Cu  $2p^{2}$  and Cu  $2p^{2}$  present in Cu(OH)Cl in where Cu is in +2 oxidation state shown in **Figure 2.8B**.[59] The O1s spectra at 530.4 eV attributed that  $2n^{2}$  ions in the ZnO lattice.[60,61]

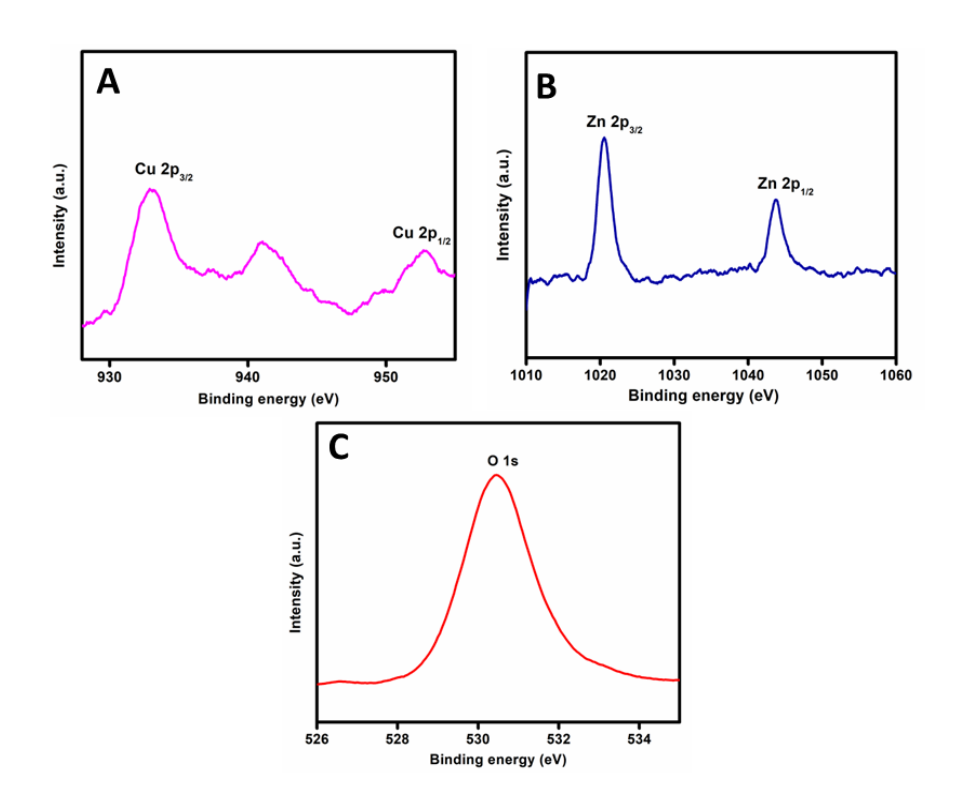


**Figure 2.8.** XPS analysis for ZnO-Cu(OH)Cl/MCM-41 (**A**) Zn 2p, (**B**) Cu 2p and (**C**) O 1s.

#### 2.3.2. Catalytic results

The catalytic transfer hydrogenation is a good choice of green chemistry to reduce the way to reduce the ketones into alcohol without using molecular hydrogen. It is a less hazardous route to reduce the ketones using cheap reducing agent sodium borohydride. The catalytic hydrogenation reaction was performed using sodium borohydride (NaBH<sub>4</sub>) as a reducing agent in the presence of green solvent "water" at 40 °C. The preliminary experiments were performed with acetophenone as model substrate. Firstly, to know the effect of solvent on the model substrate, different types of solvents such as water, methanol, acetonitrile, ethanol, and DCM were used as shown in Table **2.1**. The complete conversion of acetophenone into 1-Phenyl ethanol was observed with water, methanol, and acetonitrile in 1.5 h. The effect of solvents on the conversion of the ketone is in order of polar protic solvents < polar aprotic < non-polar solvent.[40] Solvents like water, methanol, acetonitrile have a high dielectric constant than dioxane and ethanol, which lead to high conversion and selectivity.[27]

**Table 2.1.** Effect of solvents on the formation of 1-Phenyl ethanol

Entry	Solvent	Temperature (°C)	Conversion (%)
1	$H_2O$	40	100
2	МеОН	40	100
3	CH₃CN	40	100
4	EtOH	40	87
5	Dioxane	40	49

**Reaction conditions**: Substrate (acetophenone) = 1 mmol, catalyst (ZnO-Cu(OH)Cl/MCM-41) = 3 mg, NaBH<sub>4</sub> = 0.5 mmol, time = 1.5 h, temperature = 40 °C, solvent = 2 mL.

For finalizing the solvent of the reaction, the reaction was carried out with these three solvents that are water, methanol, and acetonitrile and as a result, water gave 100% conversion and 100% selectivity within 0.75 h as shown in **Table 2.2**, so further experiments were performed using water as the solvent. The variation in conversion may be observed due to a higher dielectric constant of water than methanol and acetonitrile.[27,62]

**Table 2.2.** Time optimization for reduction of acetophenone to 1-Phenyl ethanol

Entry	Time (min)	Conversion (%)
1	15	28
2	30	46
3	45	100
4	60	100

**Reaction conditions**: Substrate (acetophenone) = 1 mmol, catalyst (ZnO-Cu(OH)Cl/MCM-41) = 3 mg,  $NaBH_4 = 0.5$  mmol,  $H_2O = 2$  mL, temperature = 40 °C, time = 15-60 min.

Furthermore, the effect of reducing agent loading was performed and observed that 0.5 mmol of NaBH<sub>4</sub> is appropriate for

complete conversion and selectivity. As shown in **Table 2.3**, when the amount of reducing agent increased from 0.4 mmol to 0.5 mmol, the conversion and selectivity 100% obtained.

**Table 2.3.** Reducing agent amount loading for reduction of acetophenone

Entry	Reducing agent (mmol)	Conversion (%)
1	0.25	28
2	0.3	40
3	0.4	54
4	0.5	100

**Reaction conditions**: Substrate (acetophenone) = 1 mmol, catalyst (ZnO-Cu(OH)Cl/MCM-41) = 3 mg,  $H_2O = 2$  mL, temperature = 40 °C, time = 0.75 h, Reducing agent = 0.25-0.5 mmol.

Also, the optimization of the substrate amount loading on the catalytic reaction was performed and observed that with increasing the loading, the reaction time increases, and conversion decrease simultaneously as shown in **Table 2.4**.

**Table 2.4.** Substrate amount loading for reduction of acetophenone to 1-Phenyl ethanol

Entry	Substrate (mmol)	Conversion (%)		
1	0.5	100		
2	1	100		
3	1.5	27		
4	2	18		

**Reaction conditions**: Substrate (acetophenone) = 0.5-2 mmol, NaBH<sub>4</sub> = 0.5 mmol, Catalyst (ZnO-Cu(OH)Cl/MCM-41) = 3 mg, H<sub>2</sub>O = 2 mL, temperature = 40 °C, time = 0.75 h.

Furthermore, to investigate the effect of Zn and Cu ions in catalytic reduction, we performed the reaction using ZnCl<sub>2</sub>, CuCl<sub>2</sub>, ZnO as catalyst (**Table 2.5**). Conversion of acetophenone to the desired product 1- phenyl ethanol was observed 100% with the catalyst ZnO-Cu(OH)Cl/MCM-41 nanoparticles with 2.46 wt% zinc and 6.39 wt% copper (3 mg amount) with 100% selectivity. Conversion with CuCl<sub>2</sub> and ZnO is 54% observed with 100% selectivity, whereas with ZnCl<sub>2</sub>, the conversion is 44% found. So far, the reaction carried out without catalyst only 30% conversion observed.

**Table 2.5.** Catalyst screening for the reduction of acetophenone to 1-Phenyl ethanol

Entry	Catalyst	Conversion (%)
1	$ZnCl_2$	44
2	CuCl <sub>2</sub>	54
3	ZnO (Purchased)	54
4	ZnO-Cu(OH)Cl/MCM-41	100
5	-	30

**Reaction conditions**: Substrate (acetophenone) = 1 mmol, different catalyst = 3 mg,  $H_2O = 2$  mL,  $NaBH_4 = 0.5$  mmol, temperature = 40 °C, time = 0.75 h.

Further, we studied the scope of the reaction using different types of substrates, and results are concluded in **Table 2.6**. Almost all the substrates were converted into a product within 0.5 to 4 h with 100% selectivity and almost 100% conversion. There was observed no effect of electron-withdrawing or electron releasing substituents on the reaction but there was effect of bulkiness observed. For *p*-methyl and *p*-methoxy substituted acetophenone, there was 90-100% conversion observed (**Entry 12, 13**). We examined the effect of the position of substituents on the phenyl ring of the acetophenone. The parasubstituted acetophenone gave more easily reaction in case of fluoro-, chloro- and bromo- substituents. As we proceed the reaction with

ortho- and meta- position substituted acetophenones, there was effect of position of the substituent perceived in case of bromo- and it might be because of the steric hindrance of the substituent group (Entry 7-9).[63] For o-,m-,p- fluoro- and chloro- substituents (Entry 2-6) there was no significant difference observed in conversion and selectivity. It estimated from the previous reports that might be bromo- on orthoposition hinders the reaction site and after increasing reaction time, the conversion found 86% which in the case of para-bromo was found 96%.[63] The effect of bulkiness was perceived when we move from fluoro to iodo substituted acetophenone. For 1-(4-iodophenyl)ethan-1one, steric hindrance caused a drastic decrease in conversion in 24h which is only 39% (Entry 10).[64] It may be due to the internal catalysis phenomena of porous material in which bulky substituent cannot pass through the pores of the catalyst.[65] The same phenomena examined in the case of benzophenone that there is only 80% conversion observed in 4h (Entry 11). Next, to explore the activity of the catalyst, the same reaction was performed with cyclic ketones such cyclopentanone, cyclohexanone and 2as methylcyclohexan-1-one and these all were converted 100% into products within 0.5 h with 100% selectivity (Entry 14-16). There was no effect observed of methyl substituent on cyclohexenone. With heterocyclic compounds such as 1-(tetrahydrothiophen-2-yl)ethan-1one, 100% conversion observed in 2h (Entry 18). When we performed reaction with (E)-4-phenyl but-3-en-2-one and 2,3-dihydro-1H-inden-1-one, 100% conversion observed with 100% selectivity (Entry 17, 19). We have performed reaction with amino- and hydroxy-substituted acetophenone but not considerable conversion observed.[63] All the conversion of substrate was analysed by GC-MS analysis and the general catalytic reaction is shown in **Scheme 2.2.** 

$$R_{1} = -H, -F, -CI, -Br, -Me, -OMe$$

$$R_{1} = -H$$

$$R_{2} = -H$$

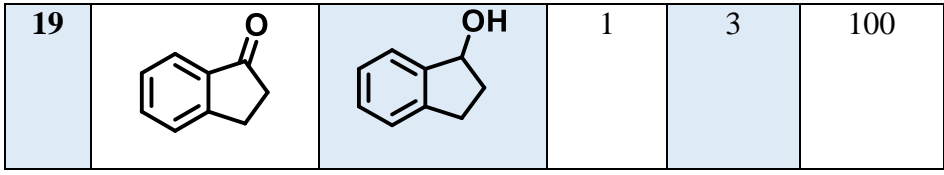
$$R_{2} = -Ph$$

**Scheme 2.2.** General catalytic transfer hydrogenation of substituted acetophenones and heterocyclic ketones.

**Table 2.6.** Substrate scope for reduction of ketones to corresponding alcohols

S.	Substrate	Product	NaBH <sub>4</sub>	Time	Conv.
No.			(eq.)	( <b>h</b> )	(%)
1		OH	0.5	0.75	100
2	o   F	OH F	1	1	100
3	O F	OH F	1	2	99
4	O F	OH F	1	2	100
5	o ci	OH CI	1	2	96
6	° Co	OH C	1	2	88

7	O Br	OH Br	1	3.5	86
8	o Br	OH Br	1	3	100
9	Br	OH Br	1	2	96
10		OH C	1	24	39
11		OH OH	1	4	80
12		<u> </u>	1	2	90
13	MeO	MeO	1	2	100
14		ОН	1	0.75	100
15	°=(	ОН	0.5	0.5	100
16		OH	0.5	0.5	100
17		OH OH	1	3	100
18	s ú	S OH	1	2	100



**Reaction conditions**: Substrate = 1 mmol, reducing agent (NaBH<sub>4</sub> = 0.5-1 mmol), catalyst (ZnO-Cu(OH)Cl/MCM-41) = 3 mg, water = 2 mL, temperature = 40 °C, time = 0.5-24 h.

Generally, the hydrogenation reactions involve harsh reaction conditions such as high temperature, molecular hydrogen as a hydrogen source, and use of expensive catalysts. Based on different catalysts and substrates, it is challenging to compare the reduction of ketones. However, to compare this work with some reported literature, we compile some of the recently reported works in the hydrogenation of ketones [Table 2.7].

**Table 2.7.** Comparison of ZnO-Cu(OH)Cl/MCM-41 and some previously reported work of hydrogenation

S.	Catalyst	Substrate	H-Source	Solvent	Time	Temp	Yield	Ref
No			/Additive		(h)	(°C)	(%)	
1	[FeHBr(	Acetophen	H <sub>2</sub> (5	EtOH	16	20	99	[66]
	CO)	one (0.416	bar)/					
	(PNP)]	mmol)	KO <sup>t</sup> Bu (5					
	complex		mol%)					
	(1							
	mol%)							
2	Rheniu	Acetophen	H <sub>2</sub> (50	Toluene	18	120	98	[67]
	m	one (0.25	bar)/	(2 mL)				
	complex	mmol)	tBuOK (1					
	(0.5		mol%)					
	mol%)							
3	Co/ZrLa	Acetophen	H <sub>2</sub> (2	H <sub>2</sub> O	10	40	100	[68]
	$_{0.2}O_{x}$ (50	one (0.83	MPa)					
	mg)	mmol)						
4	Pd- NPs	4-methoxy	H <sub>2</sub> (1	H <sub>2</sub> O	3	RT	99	[69]
	(4	acetophen	atm)					
	mol%)	one (0.05						
		mmol)						

5	Co-900	Acetophen	H <sub>2</sub> (2	H <sub>2</sub> O	12	RT	100	[70]
	catalyst	one (1	MPa)	(10 mL)				
	(20 mg)	mmol)						
6	Ir- Spiro	Acetophen	H <sub>2</sub> (50	EtOH	5	RT	100	[71]
U	PAP	one	atm)/	(2 mL)		KI	100	[/1]
	1 AI	one	tBuOK	(2 IIIL)				
			(0.02 M)					
7	DANE	Acatamban		шо	0.75	35	97	[72]
,	PANF-	Acetophen	NaBH <sub>4</sub>	H <sub>2</sub> O	0.73	33	91	[/2]
	QAS (10	one (1	(0.5					
0	mol%)	mmol)	mmol)	DOE	10	40	00	[72]
8	nBu <sub>4</sub> NC	Acetophen	NaBH <sub>4</sub>	DCE	13	40	90	[73]
	1 (7.5	one	(0.5					
	mol%)		mmol)/					
			NaOH					
			(30					
			mol%)					
9	Fluorous	Acetophen	BH <sub>3</sub> .THF	THF	1	RT	99	[74]
	oxazabo	one (0.25	(0.5					
	rolidine	mmol)	mmol)					
	(4.5							
	mol%)							
10	Fluorous	Ketone	BH <sub>3</sub> .THF	THF	1.5	RT	93	[74]
	diphenyl	(0.5 mmol)	(2 eq.)					
	prolinol							
	(0.05							
	mmol)							
11	ZnO-	Acetophen	NaBH <sub>4</sub>	H <sub>2</sub> O (2	0.75	40	100	Thi
	Cu(OH)	one (1	(0.5	mL)				s
	Cl/MC	mmol)	mmol)					wor
	M-41 (3							k
	mg)							

Based on our experimental result and available previous reports [75–77] the plausible mechanism of reduction of ketones catalyzed by ZnO-Cu(OH)Cl/MCM-41 nanoparticles with 2.46 wt% zinc and 6.39 wt% copper in aqueous medium using NaBH<sub>4</sub> (**Figure 2.9**) was proposed. Cao *et al.* and Lai *et al.* reported that the NaBH<sub>4</sub> reacts with water and produces NaBO<sub>2</sub> and hydride ion (**step 1**). [75,78] This hydride ion adsorbs on the surface of the catalyst and this hydride gave a very fast reduction of the ketone to alcohol (**step 2 and 3**).

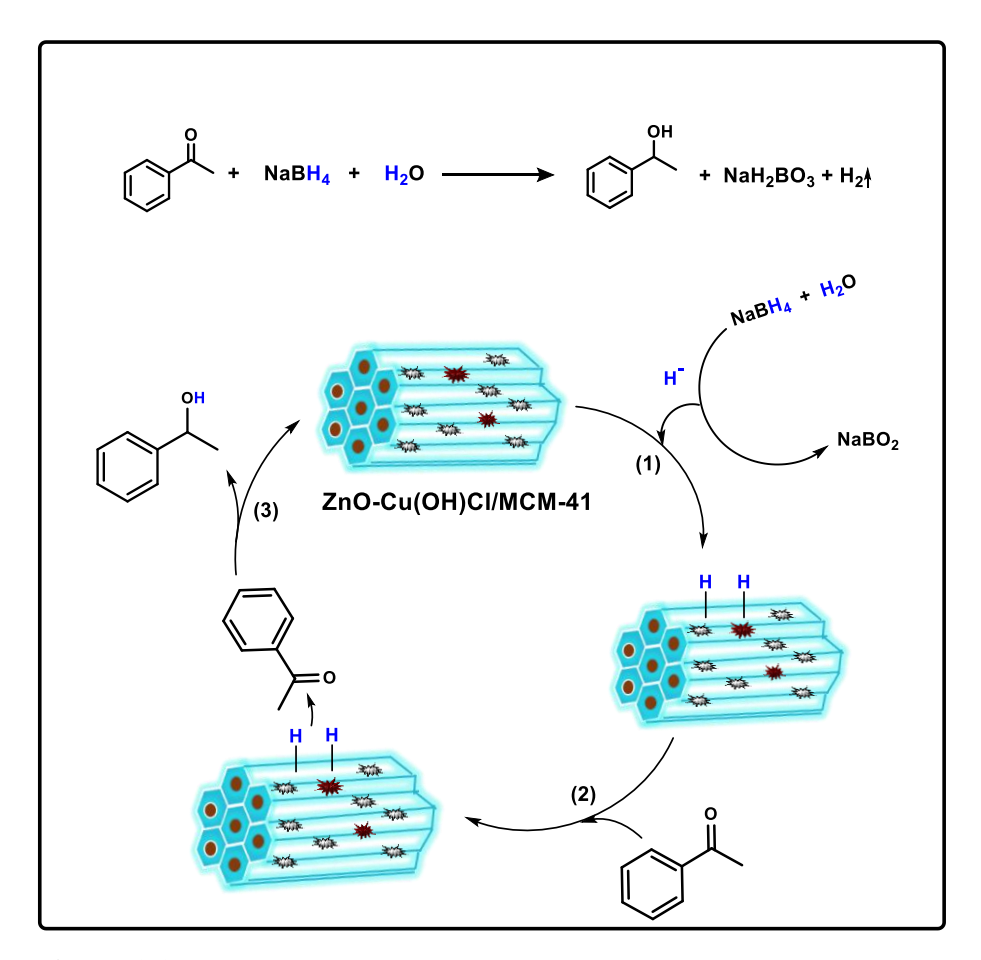


**Figure 2.9**. Plausible Mechanism of reduction of ketone using NaBH<sub>4</sub>, water and catalyst

# 2.3.3. Kinetic and recycle study

The reduction of acetophenone was observed 100% in 0.75 h using 3 mg catalyst with water. For the study, the kinetics of the reaction, periodically sample was taken by injection for GC analysis. The sample was taken on 15 min, 30 min, 45 min, and observed conversion were respectively 28, 46, 100%. The kinetic study of the model reaction shown in **Figure 2.10**.

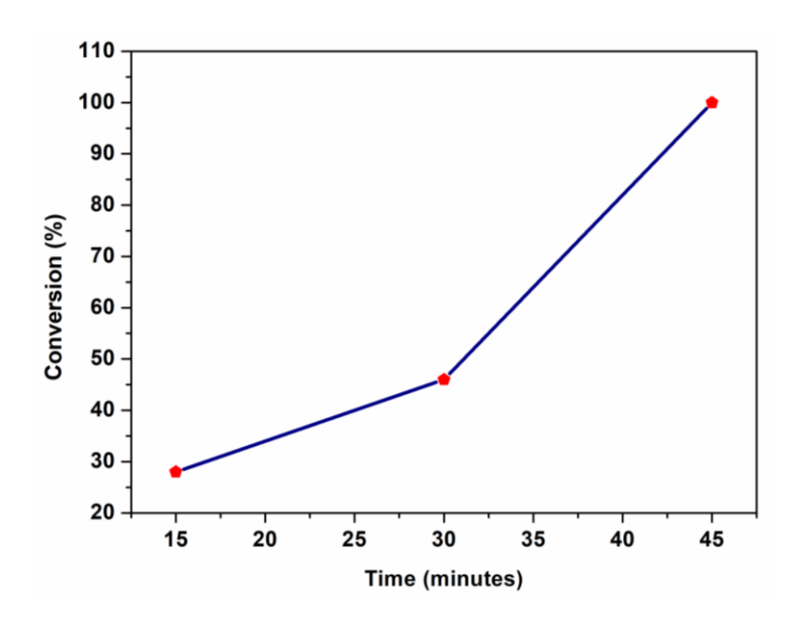


**Figure 2.10.** Kinetic study of the conversion of acetophenone to 1-Phenyl ethanol. **Reaction conditions**: Substrate = 1 mmol, reducing agent (NaBH<sub>4</sub>) = 0.5 mmol, catalyst (ZnO-Cu(OH)Cl/MCM-41) = 3 mg, water = 2 mL, = 40 °C, time = 15-60 min.

The leaching test performed to know the reusability of the catalyst throughout the catalytic reaction. For this test, after completion of reaction the catalyst was filtered and separated to perform ICP-AES analysis with the supernatant and this result indicate no considerable leaching of the catalyst (**Table 2.8**).

**Table 2.8.** ICP-AES data of catalyst ZnO-Cu(OH)Cl/MCM-41 after catalysis

Sample	ICP-AES (ppm)			
ZnO-Cu(OH)Cl/MCM-41	Cu	Zn	Si	
	0.059	0.635	4.43	

To know the reusability of the catalyst ZnO-Cu(OH)Cl/MCM-41 nanoparticles with 2.46 wt% zinc and 6.39 wt% copper, we have performed the recycle study for the reduction of the acetophenone to 1-Phenyl ethanol as shown in **Figure 2.11**. After completion of the reaction one time, the reaction mixture was centrifuged, and the catalyst was separated from the reaction mixture.[79] Then dried at

room temperature and again reuse this for the next cycle with the same reaction condition, and we observed almost 100% conversion up to four cycles. After four cycles, the conversion decreased to 89% which maybe because of the increase of carbon content, which was trapped inside the pores of MCM-41 from the substrate.[80] The coke deposition also confirmed by XPS analysis in which the carbon content increases when we compare both fresh and spent catalyst samples. Hence, our synthesized nanoparticle is recyclable catalyst.[81,82] There is reduction of copper observed after recycle by XPS analysis of spent but this reduction of Cu(ii) into Cu(0) catalyse the reduction reaction and this Cu(0) again oxidized to copper oxide in alkaline medium.[83,84]

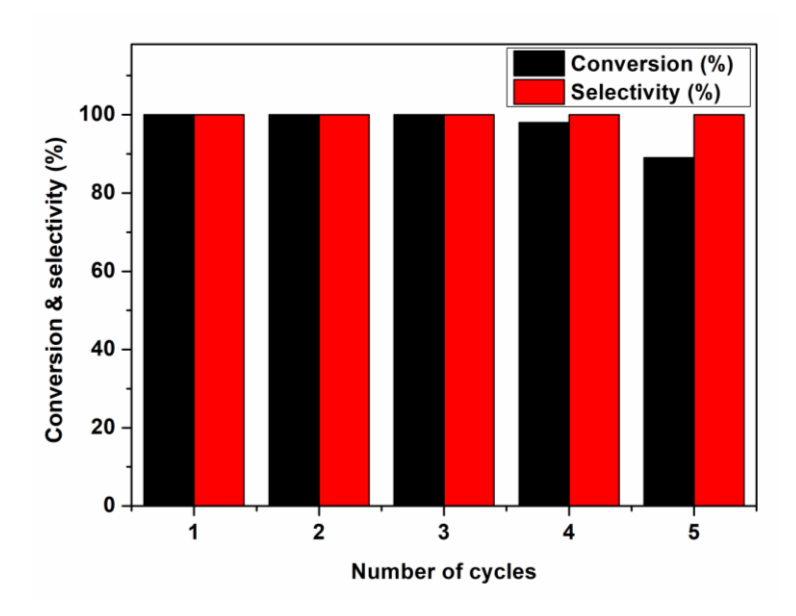


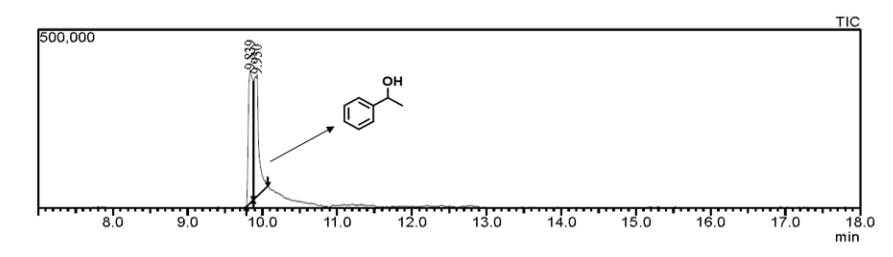
**Figure 2.11.** Recycle study of the catalyst for conversion of acetophenone to 1- Phenyl ethanol. **Reaction conditions**: Substrate = 1 mmol, reducing agent (NaBH<sub>4</sub>) = 0.5 mmol, catalyst (ZnO-Cu(OH)Cl/MCM-41) = 3 mg, water = 2 mL, = 40 °C, time = 60 min.

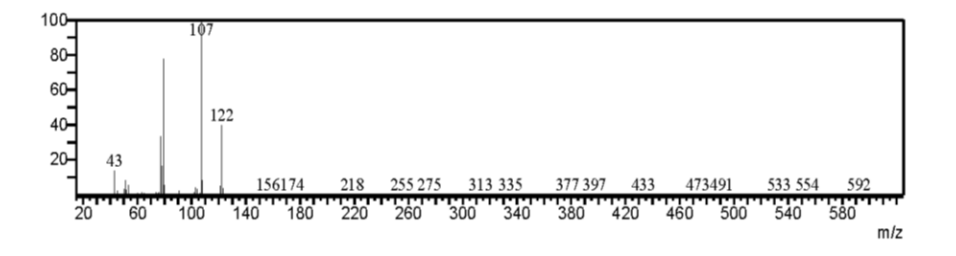
## 2.4. Conclusions

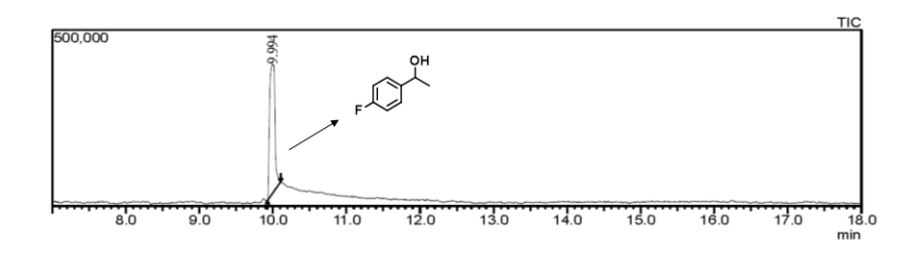
In conclusion, ZnO-Cu(OH)Cl/MCM-41 nanoparticles with 2.46 wt% zinc and 6.39 wt% copper is a heterogeneous catalyst with high surface area and stability for the reduction of ketones, and it's a very lesser amount (3 mg) is required for 100% conversion. The nanomaterial ZnO-Cu(OH)Cl/MCM-41 nanoparticles with 2.46 wt% zinc and 6.39

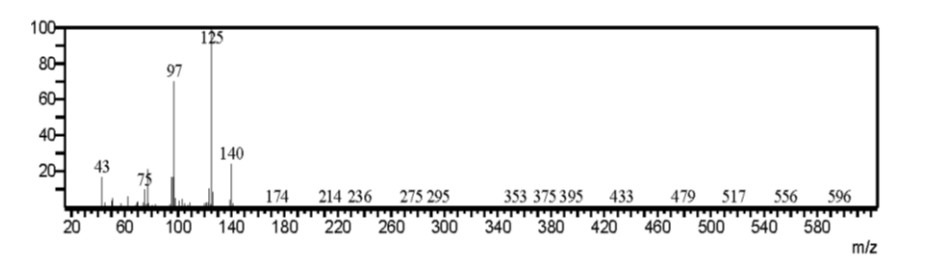
wt% copper was synthesized by wetness impregnation technique by using water as a solvent at room temperature. HR-TEM and BET studies proved the incorporation of zinc and copper species on the surface of MCM-41 and inside the pores of MCM-41, which leads to decrease in surface area of MCM-41 in metal nanoparticles ZnO-Cu(OH)Cl/MCM-41 nanoparticles with 2.46 wt% zinc and 6.39 wt% copper. This catalyst was used the first time for reduction of ketones by transfer hydrogenation using water as a solvent, provide the basis for developing the new potential supports.

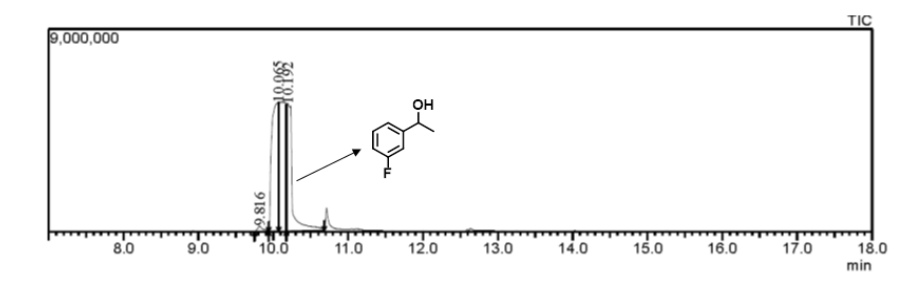
# 2.5. GC-MS spectra of analyzed data of conversion of ketones to corresponding alcohol of different type of substrate

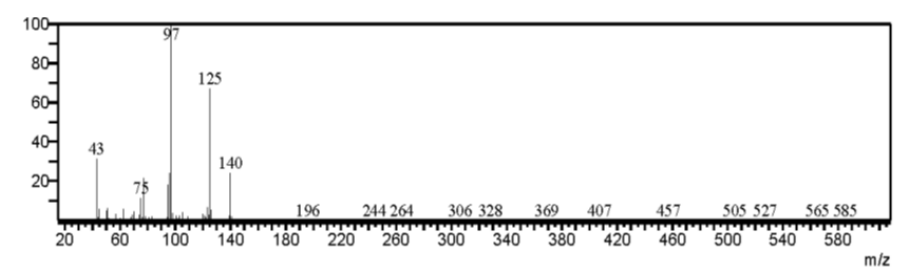


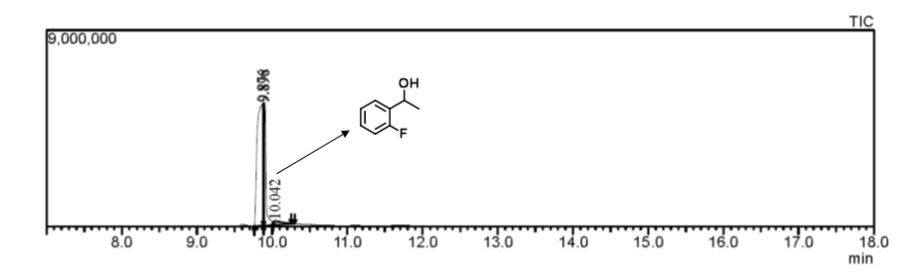


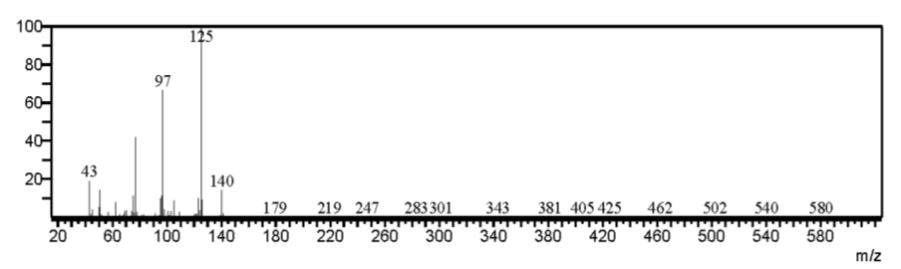


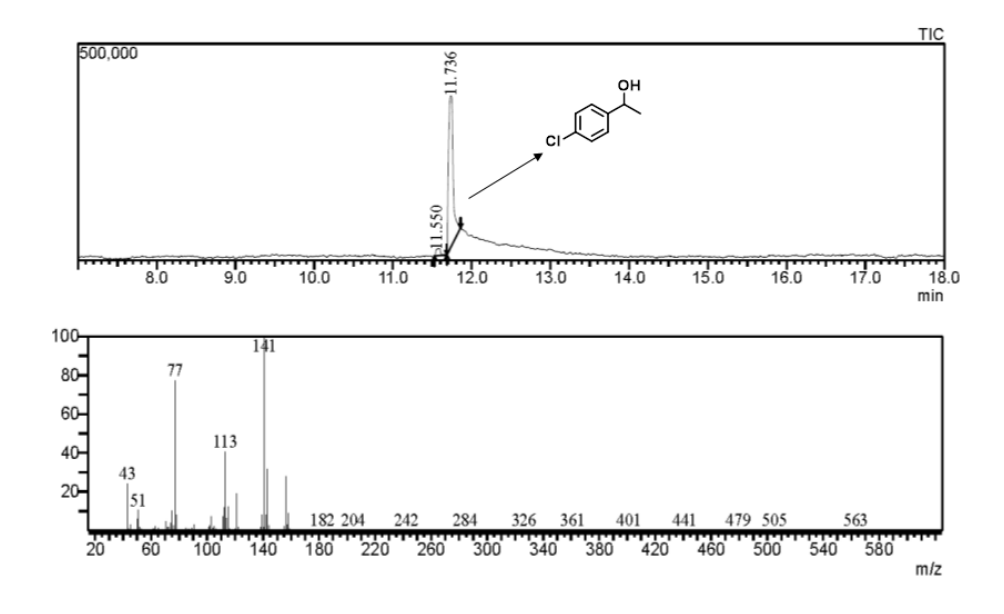


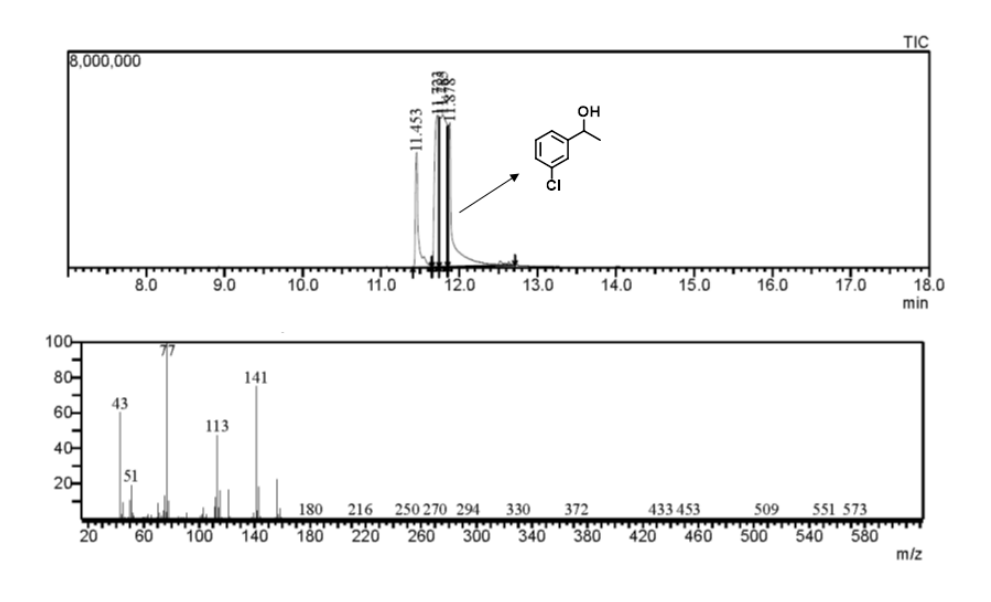


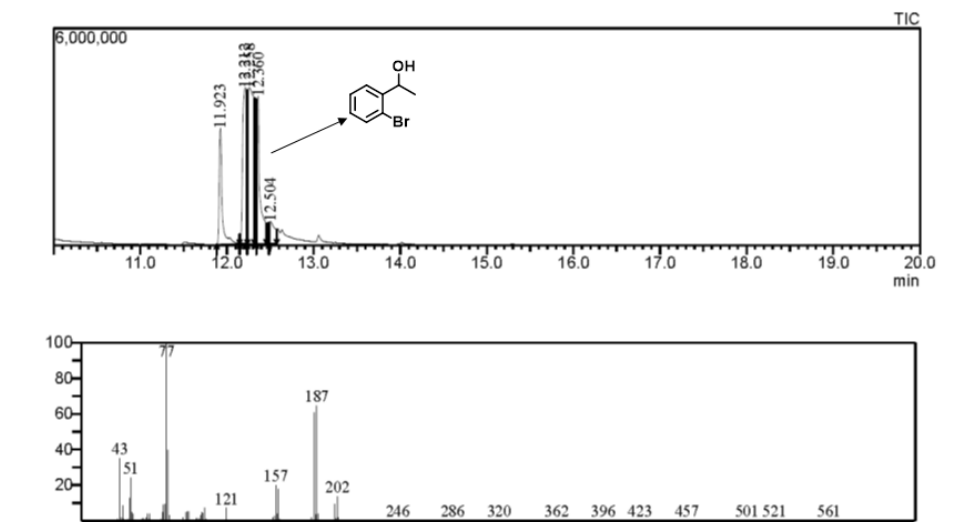


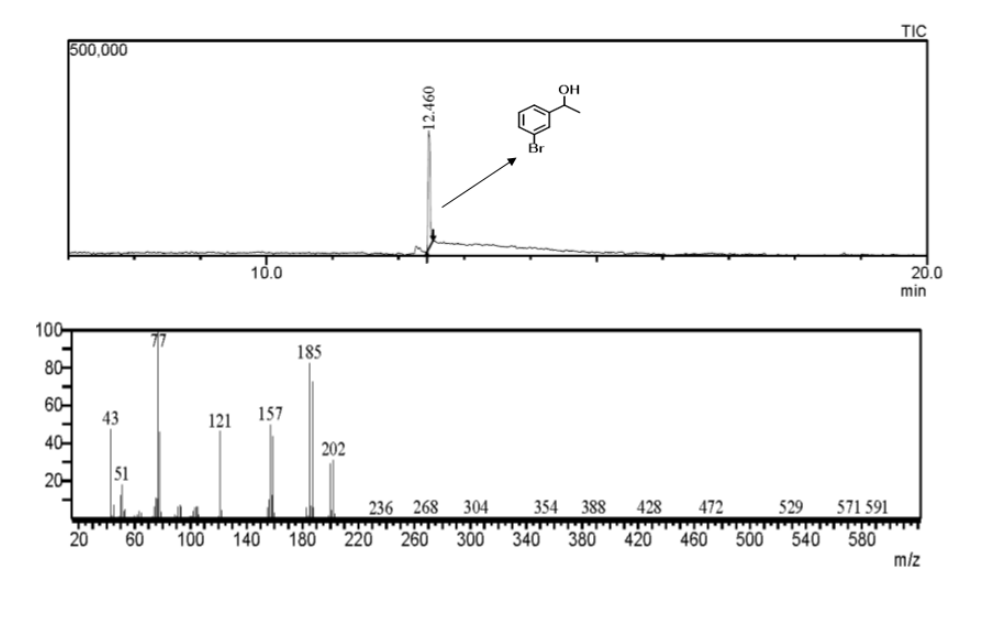


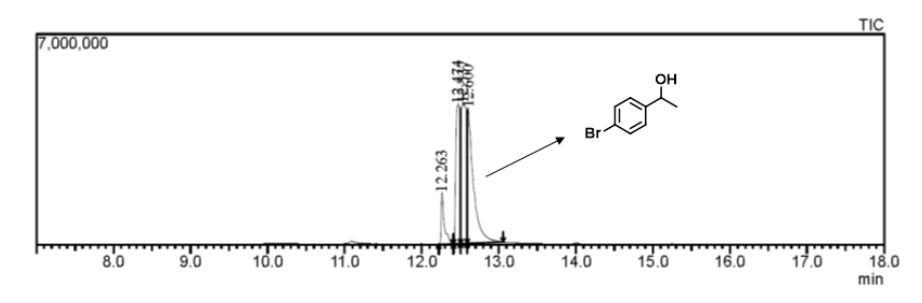


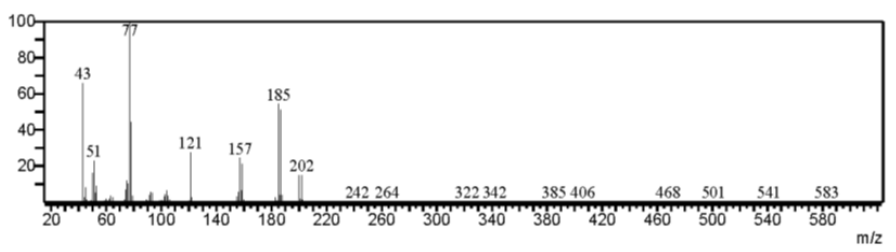


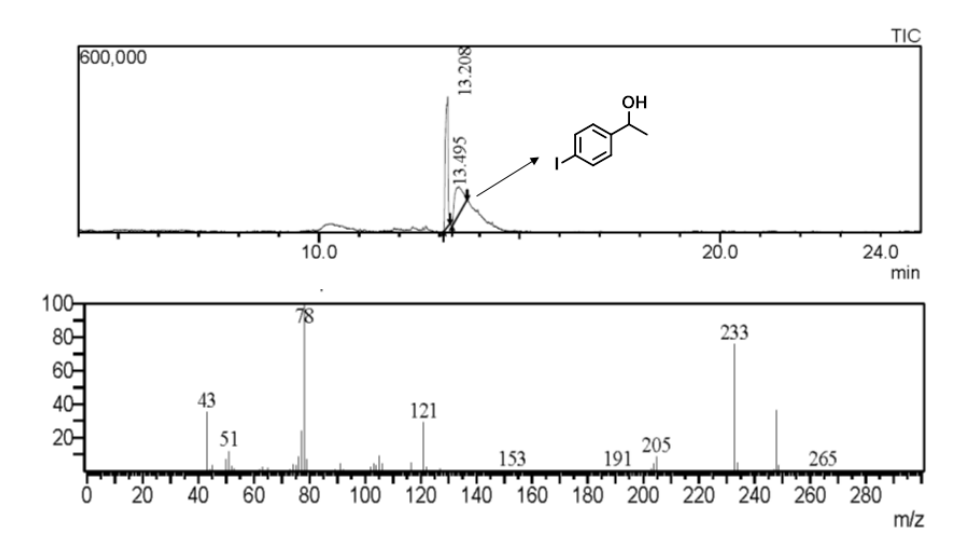


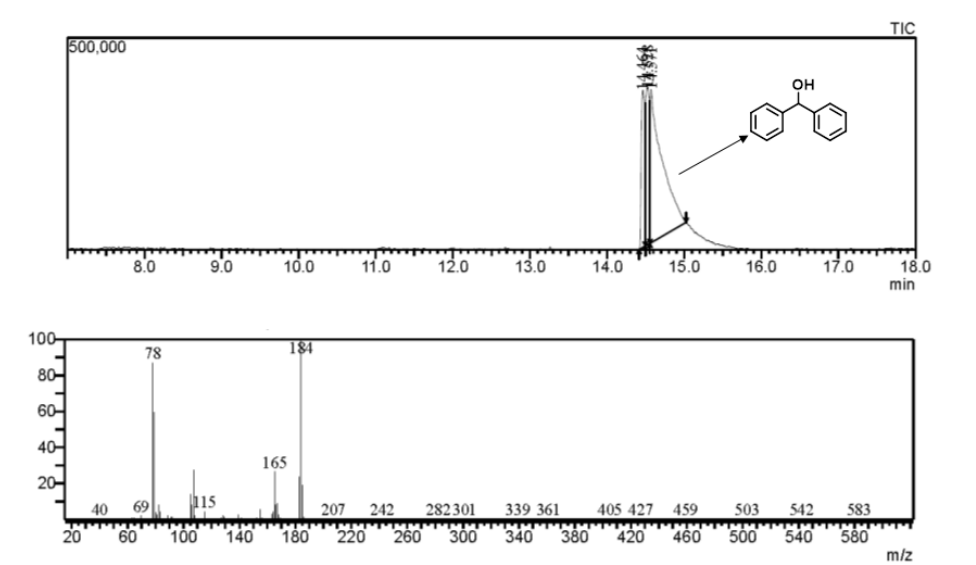


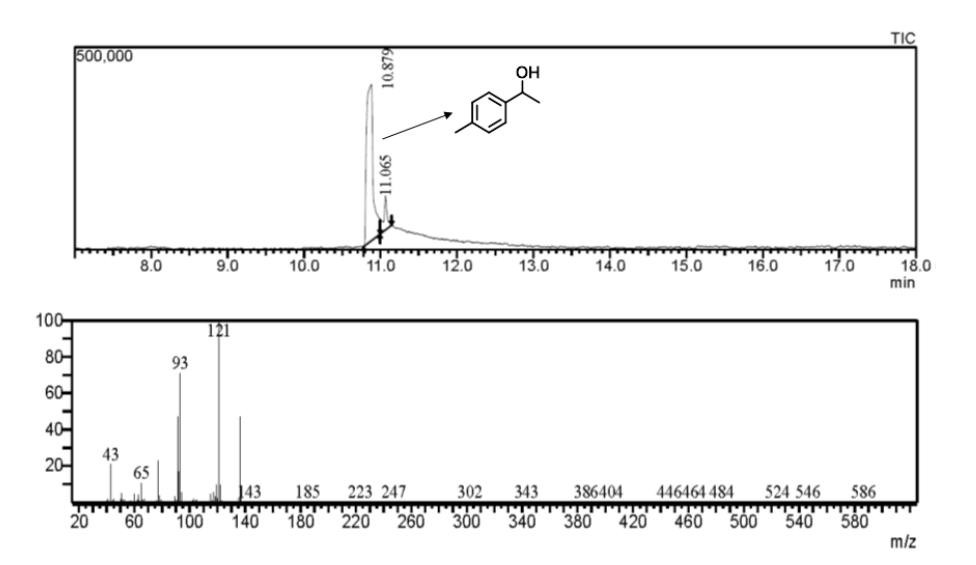


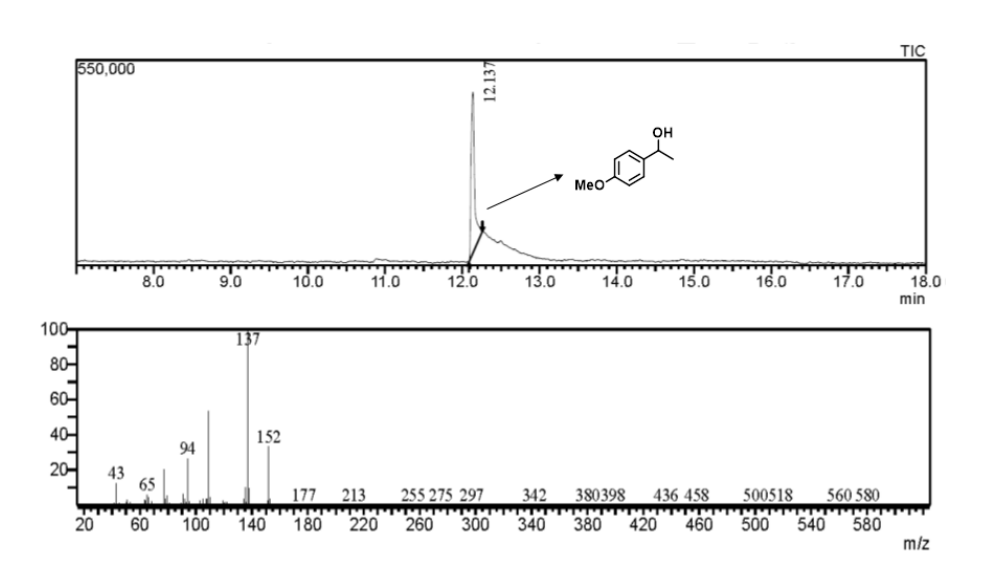


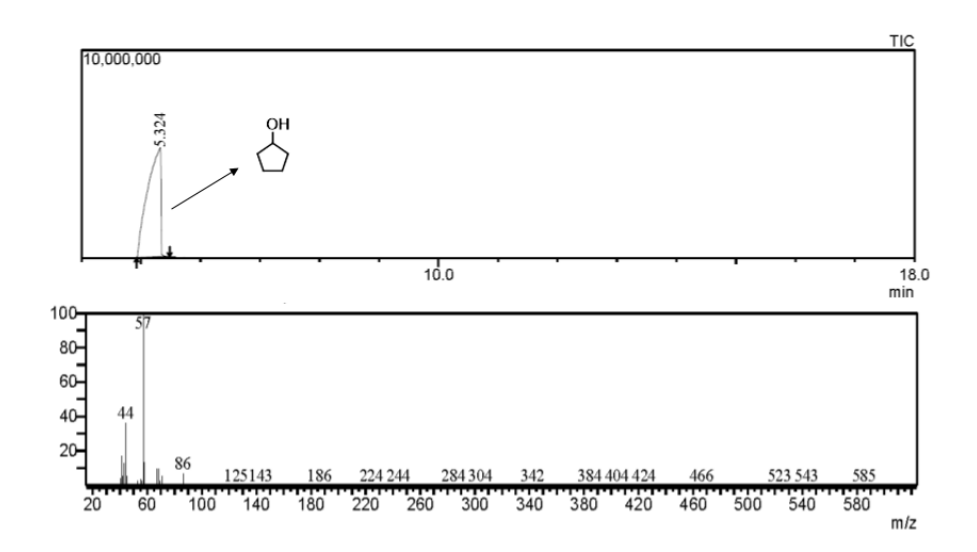


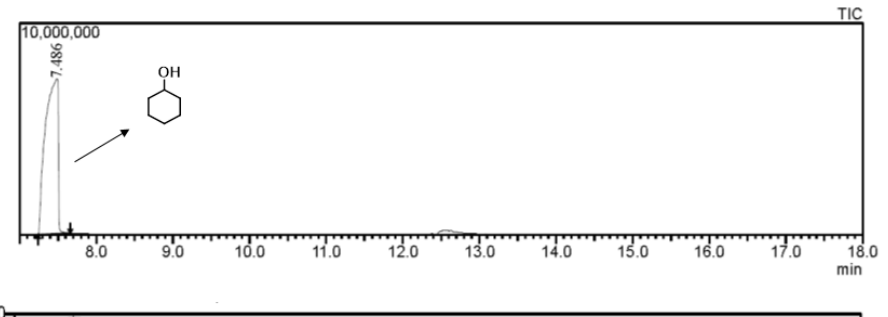


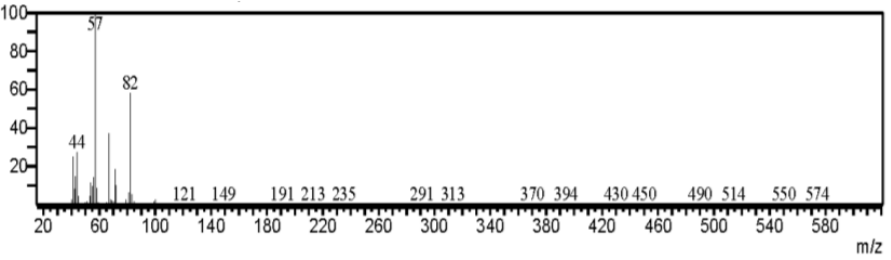


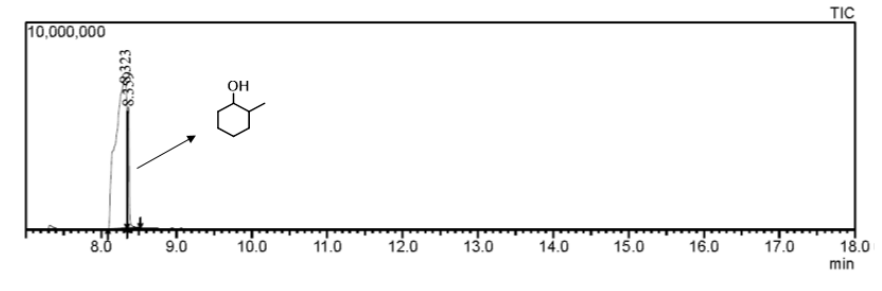


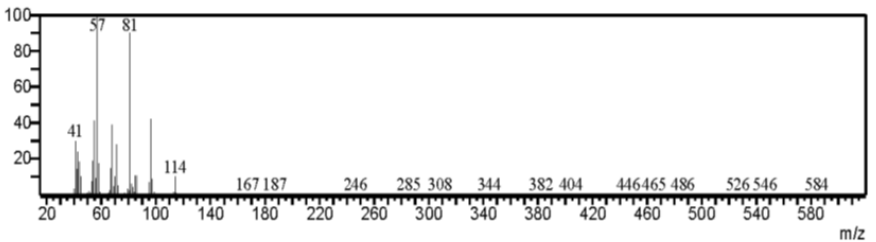


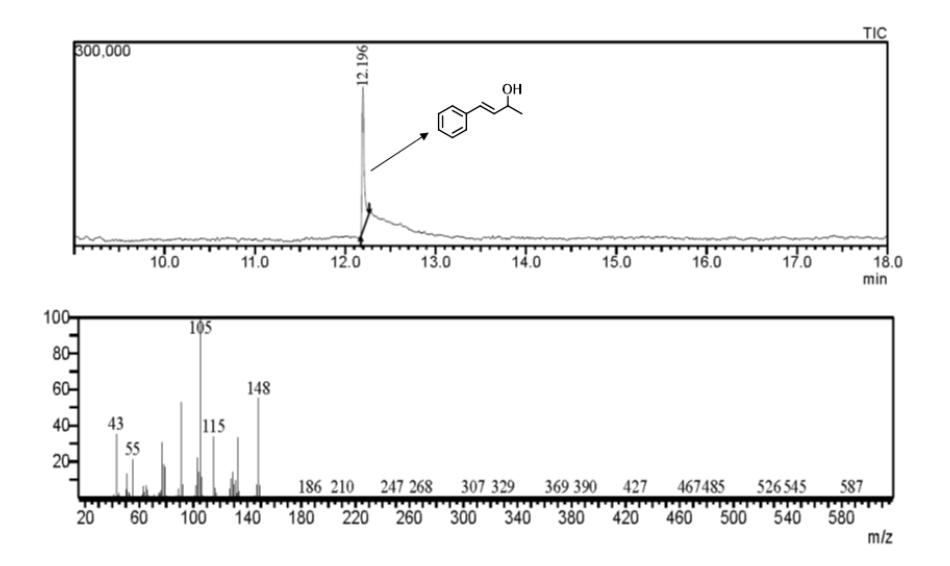


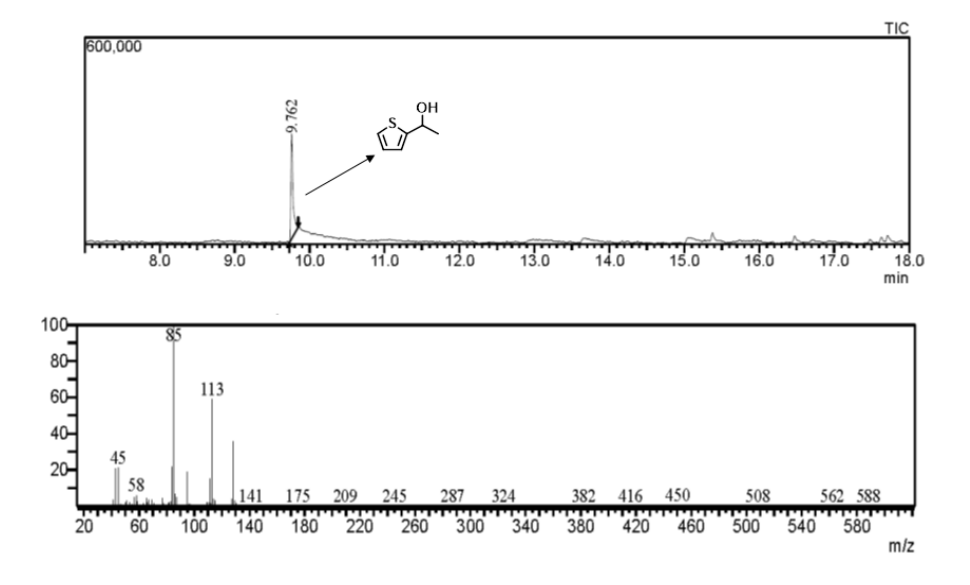


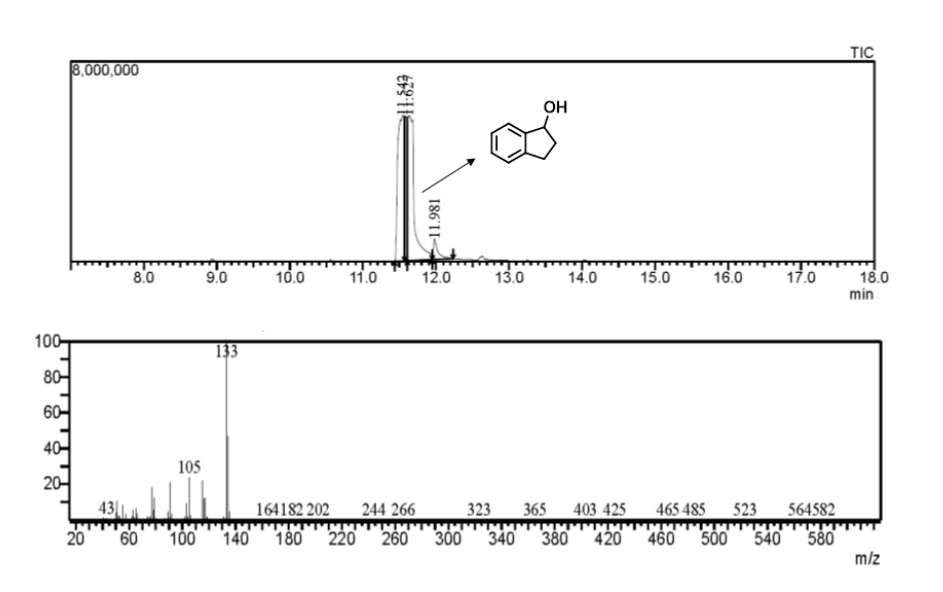












#### 2.6. References

- [1] T.S. Rodrigues, A.G.M. da Silva, P.H.C. Camargo, Nanocatalysis by noble metal nanoparticles: controlled synthesis for the optimization and understanding of activities, J. Mater. Chem. A. 7 (2019) 5857–5874. https://doi.org/10.1039/C9TA00074G.
- [2] C. Zhang, S. Li, T. Wang, G. Wu, X. Ma, J. Gong, Pt-based coreshell nanocatalysts with enhanced activity and stability for CO oxidation, Chem. Commun. 49 (2013) 10647–10649. https://doi.org/10.1039/C3CC45957H.
- [3] S. Chaturvedi, P.N. Dave, N.K. Shah, Applications of nanocatalyst in new era, J. Saudi Chem. Soc. 16 (2012) 307–325. https://doi.org/10.1016/j.jscs.2011.01.015.
- [4] Q. Chaudhry, L. Castle, Food applications of nanotechnologies: An overview of opportunities and challenges for developing countries, Trends Food Sci. Technol. 22 (2011) 595–603. https://doi.org/10.1016/j.tifs.2011.01.001.
- [5] R. Narayanan, M.A. El-Sayed, Catalysis with Transition Metal Nanoparticles in Colloidal Solution: Nanoparticle Shape Dependence and Stability, J. Phys. Chem. B. 109 (2005) 12663–12676. https://doi.org/10.1021/jp051066p.
- [6] A. Corma, Heterogeneous Catalysis: Understanding for Designing, and Designing for Applications, Angew. Chem. Int. Ed. 55 (2016) 6112–6113. https://doi.org/10.1002/anie.201601231.
- [7] K. Zhou, R. Wang, B. Xu, Y. Li, Synthesis, characterization and catalytic properties of CuO nanocrystals with various shapes, Nanotechnology.
   17 (2006) 3939–3943. https://doi.org/10.1088/0957-4484/17/15/055.
- [8] E. Geravand, Z. Shariatinia, F. Yaripour, S. Sahebdelfar, Copperbased nanocatalysts for 2-butanol dehydrogenation: Screening and optimization of preparation parameters by response surface methodology, Korean J. Chem. Eng. 32 (2015) 2418–2428. https://doi.org/10.1007/s11814-015-0087-x.
- [9] V. Hoseinpour, N. Ghaemi, Novel ZnO–MnO2–Cu2O triple nanocomposite: Facial synthesis, characterization, antibacterial activity and visible light photocatalytic performance for dyes degradation-A comparative study, Mater. Res. Express. 5 (2018) 085012. https://doi.org/10.1088/2053-1591/aad2c6.
- [10] B.L. Kniep, F. Girgsdies, T. Ressler, Effect of precipitate aging on the microstructural characteristics of Cu/ZnO catalysts for methanol steam reforming, J. Catal. 236 (2005) 34–44. https://doi.org/10.1016/j.jcat.2005.09.001.
- [11] P.H. Matter, D.J. Braden, U.S. Ozkan, Steam reforming of methanol to H2 over nonreduced Zr-containing CuO/ZnO catalysts, J. Catal. 223 (2004) 340–351. https://doi.org/10.1016/j.jcat.2004.01.031.
- [12] M. Behrens, S. Zander, P. Kurr, N. Jacobsen, J. Senker, G. Koch, T. Ressler, R.W. Fischer, R. Schlögl, Performance Improvement of Nanocatalysts by Promoter-Induced Defects in the Support

- Material: Methanol Synthesis over Cu/ZnO:Al, J. Am. Chem. Soc. 135 (2013) 6061–6068. https://doi.org/10.1021/ja310456f.
- [13] S. Zander, E.L. Kunkes, M.E. Schuster, J. Schumann, G. Weinberg, D. Teschner, N. Jacobsen, R. Schlögl, M. Behrens, The Role of the Oxide Component in the Development of Copper Composite Catalysts for Methanol Synthesis, Angew. Chem. Int. Ed. 52 (2013) 6536–6540. https://doi.org/10.1002/anie.201301419.
- [14] M.B. Fichtl, J. Schumann, I. Kasatkin, N. Jacobsen, M. Behrens, R. Schlögl, M. Muhler, O. Hinrichsen, Counting of Oxygen Defects versus Metal Surface Sites in Methanol Synthesis Catalysts by Different Probe Molecules, Angew. Chem. Int. Ed. 53 (2014) 7043–7047. https://doi.org/10.1002/anie.201400575.
- [15] J.P. Breen, J.R.H. Ross, Methanol reforming for fuel-cell applications: development of zirconia-containing Cu–Zn–Al catalysts, Catal. Today. 51 (1999) 521–533. https://doi.org/10.1016/S0920-5861(99)00038-3.
- [16] X. Chen, Y. Huang, X. Zhang, C. Li, J. Chen, K. Wang, Graphene supported ZnO/CuO flowers composites as anode materials for lithium ion batteries, Mater. Lett. 152 (2015) 181–184. https://doi.org/10.1016/j.matlet.2015.03.136.
- [17] R.K. Sharma, R. Gaur, M. Yadav, A. Goswami, R. Zbořil, M.B. Gawande, An efficient copper-based magnetic nanocatalyst for the fixation of carbon dioxide at atmospheric pressure, Sci. Rep. 8 (2018) 1–12. https://doi.org/10.1038/s41598-018-19551-3.
- [18] H.S. Saroyan, A. Arampatzidou, D. Voutsa, N.K. Lazaridis, E.A. Deliyanni, Activated carbon supported MnO2 for catalytic degradation of reactive black 5, Colloids Surf. Physicochem. Eng. Asp. 566 (2019) 166–175. https://doi.org/10.1016/j.colsurfa.2019.01.025.
- [19] Y. Li, L. Xiao, F. Liu, Y. Dou, S. Liu, Y. Fan, G. Cheng, W. Song, J. Zhou, Core-shell structure Ag@Pd nanoparticles supported on layered MnO2 substrate as toluene oxidation catalyst, J. Nanoparticle Res. 21 (2019) 28. https://doi.org/10.1007/s11051-019-4467-8.
- [20] X. Zou, Z. Rui, H. Ji, Core—Shell NiO@PdO Nanoparticles Supported on Alumina as an Advanced Catalyst for Methane Oxidation, ACS Catal. 7 (2017) 1615–1625. https://doi.org/10.1021/acscatal.6b03105.
- [21] M. Mirza-Aghayan, M. Kalantari, R. Boukherroub, Palladium oxide nanoparticles supported on graphene oxide: A convenient heterogeneous catalyst for reduction of various carbonyl compounds using triethylsilane, Appl. Organomet. Chem. 33 (2019) e4837. https://doi.org/10.1002/aoc.4837.
- [22] Y. Chen, X. Ji, B. Paul, S. Vadivel, Room temperature photocatalytic conversion of aldehydes to esters using gold supported cerium oxide nanoparticles under visible light irradiation, Mater. Lett. 237 (2019) 113–117. https://doi.org/10.1016/j.matlet.2018.11.070.

- [23] A. Glotov, N. Levshakov, A. Stavitskaya, M. Artemova, P. Gushchin, E. Ivanov, V. Vinokurov, Y. Lvov, Templated self-assembly of ordered mesoporous silica on clay nanotubes, Chem. Commun. 55 (2019) 5507–5510. https://doi.org/10.1039/C9CC01935A.
- [24] C.M. A. Parlett, K. Wilson, A. F. Lee, Hierarchical porous materials: catalytic applications, Chem. Soc. Rev. 42 (2013) 3876–3893. https://doi.org/10.1039/C2CS35378D.
- [25] Q. Wang, M. Zhu, B. Dai, J. Zhang, Zn supported on titania-doped mesoporous silicate MCM-41 as efficient catalysts for acetylene hydration, Catal. Sci. Technol. 9 (2019) 981–991. https://doi.org/10.1039/C8CY02246A.
- [26] M. Xia, M. Long, Y. Yang, C. Chen, W. Cai, B. Zhou, A highly active bimetallic oxides catalyst supported on Al-containing MCM-41 for Fenton oxidation of phenol solution, Appl. Catal. B Environ. 110 (2011) 118–125. https://doi.org/10.1016/j.apcatb.2011.08.033.
- [27] D. Rath, K.M. Parida, Copper and Nickel Modified MCM-41 An Efficient Catalyst for Hydrodehalogenation of Chlorobenzene at Room Temperature, Ind. Eng. Chem. Res. 50 (2011) 2839–2849. https://doi.org/10.1021/ie101314f.
- [28] J. Ding, M. Cui, T. Ma, R. Shao, W. Xu, P. Wang, Catalytic amination of glycerol with dimethylamine over different type ofheteropolyacid/Zr-MCM-41 catalysts, Mol. Catal. 457 (2018) 51–58. https://doi.org/10.1016/j.mcat.2018.07.017.
- [29] D. B. Nale, D. Rath, K. M. Parida, A. Gajengi, B. M. Bhanage, Amine modified mesoporous Al 2 O 3 @MCM-41: an efficient, synergetic and recyclable catalyst for the formylation of amines using carbon dioxide and DMAB under mild reaction conditions, Catal. Sci. Technol. 6 (2016) 4872–4881. https://doi.org/10.1039/C5CY02277K.
- [30] B. Dai, B. Wen, M. Zhu, L. Kang, F. Yu, Nickel catalysts supported on amino-functionalized MCM-41 for syngas methanation, RSC Adv. 6 (2016) 66957–66962. https://doi.org/10.1039/C6RA07451K.
- [31] F.J. Méndez, O.E. Franco-López, X. Bokhimi, D.A. Solís-Casados, L. Escobar-Alarcón, T.E. Klimova, Dibenzothiophene hydrodesulfurization with NiMo and CoMo catalysts supported on niobium-modified MCM-41, Appl. Catal. B Environ. 219 (2017) 479–491. https://doi.org/10.1016/j.apcatb.2017.07.079.
- [32] P.M. Carraro, B.S. Goldani, D. Alves, A.G. Sathicq, G.A. Eimer, G.P. Romanelli, R. Luque, Stability and Activity of Zn/MCM-41 Materials in Toluene Alkylation: Microwave Irradiation vs Continuous Flow, Catalysts. 9 (2019) 136. https://doi.org/10.3390/catal9020136.
- [33] V. Parvulescu, B.-L. Su, Iron, cobalt or nickel substituted MCM-41 molecular sieves for oxidation of hydrocarbons, Catal. Today. 69 (2001) 315–322. https://doi.org/10.1016/S0920-5861(01)00384-4.

- [34] A. Lewandowska, S. Monteverdi, M. Bettahar, M. Ziolek, MCM-41 mesoporous molecular sieves supported nickel—physicochemical properties and catalytic activity in hydrogenation of benzene, J. Mol. Catal. Chem. 188 (2002) 85–95. https://doi.org/10.1016/S1381-1169(02)00339-4.
- [35] R. Wojcieszak, S. Monteverdi, M. Mercy, I. Nowak, M. Ziolek, M.M. Bettahar, Nickel containing MCM-41 and AlMCM-41 mesoporous molecular sieves: Characteristics and activity in the hydrogenation of benzene, Appl. Catal. Gen. 268 (2004) 241–253. https://doi.org/10.1016/j.apcata.2004.03.047.
- [36] M. Vallet-Regi, A. Rámila, R.P. del Real, J. Pérez-Pariente, A New Property of MCM-41: Drug Delivery System, Chem. Mater. 13 (2001) 308–311. https://doi.org/10.1021/cm0011559.
- [37] A.F. Trindade, P.M.P. Gois, C.A.M. Afonso, Recyclable Stereoselective Catalysts, Chem. Rev. 109 (2009) 418–514. https://doi.org/10.1021/cr800200t.
- [38] M.M. Sheeba, S. Preethi, A. Nijamudheen, M.M. Tamizh, A. Datta, L. J. Farrugia, R. Karvembu, Half-sandwich Ru(η 6 -C 6 H 6) complexes with chiral aroylthioureas for enhanced asymmetric transfer hydrogenation of ketones experimental and theoretical studies, Catal. Sci. Technol. 5 (2015) 4790–4799. https://doi.org/10.1039/C5CY00774G.
- [39] D.G. Desai, S.S. Swami, R.S. Nandurdikar, SELECTIVE REDUCTION OF ALDEHYDES TO ALCOHOLS BY FeS-NH4Cl-CH3OH-H2O SYSTEM\*, Synth. Commun. 32 (2002) 931–933. https://doi.org/10.1081/SCC-120002707.
- [40] G.D. Yadav, R.K. Mewada, Selective hydrogenation of acetophenone to 1-phenyl ethanol over nanofibrous Ag-OMS-2 catalysts, Catal. Today. 198 (2012) 330–337. https://doi.org/10.1016/j.cattod.2012.06.028.
- [41] Y. Wang, P. Prinsen, K.S. Triantafyllidis, S.A. Karakoulia, A. Yepez, C. Len, R. Luque, Batch versus Continuous Flow Performance of Supported Mono- and Bimetallic Nickel Catalysts for Catalytic Transfer Hydrogenation of Furfural in Isopropanol, ChemCatChem. 10 (2018) 3459–3468. https://doi.org/10.1002/cctc.201800530.
- [42] Y. Wang, P. Prinsen, K.S. Triantafyllidis, S.A. Karakoulia, P.N. Trikalitis, A. Yepez, C. Len, R. Luque, Comparative Study of Supported Monometallic Catalysts in the Liquid-Phase Hydrogenation of Furfural: Batch Versus Continuous Flow, ACS Sustain. Chem. Eng. 6 (2018) 9831–9844. https://doi.org/10.1021/acssuschemeng.8b00984.
- [43] Q. Wang, M. Zhu, B. Dai, J. Zhang, Zn supported on titania-doped mesoporous silicate MCM-41 as efficient catalysts for acetylene hydration, Catal. Sci. Technol. 9 (2019) 981–991. https://doi.org/10.1039/C8CY02246A.
- [44] K.M.S. Khalil, Cerium modified MCM-41 nanocomposite materials via a nonhydrothermal direct method at room temperature, J. Colloid Interface Sci. 315 (2007) 562–568. https://doi.org/10.1016/j.jcis.2007.07.030.

- [45] A. Samavati, Z. Samavati, A.F. Ismail, M.H.D. Othman, M.A. Rahman, I.S. Amiri, Effect of organic ligand-decorated ZnO nanoparticles as a cathode buffer layer on electricity conversion efficiency of an inverted solar cell, RSC Adv. 8 (2018) 1418–1426. https://doi.org/10.1039/C7RA11902J.
- [46] F. Raji, M. Pakizeh, Study of Hg(II) species removal from aqueous solution using hybrid ZnCl2-MCM-41 adsorbent, Appl. Surf. Sci. 282 (2013) 415–424. https://doi.org/10.1016/j.apsusc.2013.05.145.
- [47] X. Diao, Y. Hu, Y. He, F. Quan, C. Wei, Preparation of 3,3,3-trifluoropropyl functionalized hydrophobic mesoporous silica and its outstanding adsorption properties for dibutyl phthalate, RSC Adv. 7 (2017) 8338–8346. https://doi.org/10.1039/C6RA27958A.
- [48] C. Huo, J. Ouyang, H. Yang, CuO nanoparticles encapsulated inside Al-MCM-41 mesoporous materials via direct synthetic route, Sci. Rep. 4 (2014) 3682. https://doi.org/10.1038/srep03682.
- [49] R. Muthusami, M. Moorthy, K. Irena, A. Govindaraj, C. Manickam, R. Rangappan, Designing a biomimetic catalyst for phenoxazinone synthase activity using a mesoporous Schiff base copper complex with a novel double-helix morphology, New J. Chem. 42 (2018) 18608–18620. https://doi.org/10.1039/C8NJ03638A.
- [50] M. do S.B. Fontes, D.M. de A. Melo, C. de C. Costa, R.M. Braga, M.A. de F. Melo, J.A.B.L.R. Alves, M. do S.B. Fontes, D.M. de A. Melo, C. de C. Costa, R.M. Braga, M.A. de F. Melo, J.A.B.L.R. Alves, http://www.scielo.br/scielo.php?script=sci\_abstract&pid=S1516-14392015000300608&lng=en&nrm=iso&tlng=es, Mater. Res. 18 (2015) 608–613. https://doi.org/10.1590/1516-1439.019015.
- [51] P.M. Carraro, B.S. Goldani, D. Alves, A.G. Sathicq, G.A. Eimer, G.P. Romanelli, R. Luque, Stability and Activity of Zn/MCM-41 Materials in Toluene Alkylation: Microwave Irradiation vs Continuous Flow, Catalysts. 9 (2019) 136. https://doi.org/10.3390/catal9020136.
- [52] Q. Wang, M. Zhu, C. Xu, H. Zhang, X. Wang, B. Dai, J. Zhang, Zn–Cu bimetallic catalysts supported on pure silica MCM-41 for acetylene hydration reaction, New J. Chem. 42 (2018) 6507–6514. https://doi.org/10.1039/C8NJ00707A.
- [53] C. Huo, J. Ouyang, H. Yang, CuO nanoparticles encapsulated inside Al-MCM-41 mesoporous materials via direct synthetic route, Sci. Rep. 4 (2014) 3682. https://doi.org/10.1038/srep03682.
- [54] A. Torabinejad, N. Nasirizadeh, M.E. Yazdanshenas, H.-A. Tayebi, Synthesis of conductive polymer-coated mesoporous MCM-41 for textile dye removal from aqueous media, J. Nanostructure Chem. 7 (2017) 217–229. https://doi.org/10.1007/s40097-017-0232-7.
- [55] J. Requies, M.B. Güemez, A. Iriondo, V.L. Barrio, J.F. Cambra, P.L. Arias, Bio n-Butanol Partial Oxidation to Butyraldehyde in Gas Phase on Supported Ru and Cu Catalysts, Catal. Lett. 142 (2012) 417–426. https://doi.org/10.1007/s10562-012-0793-5.

- [56] N. Cakiryilmaz, H. Arbag, N. Oktar, G. Dogu, T. Dogu, Catalytic performances of Ni and Cu impregnated MCM-41 and Zr-MCM-41 for hydrogen production through steam reforming of acetic acid, Catal. Today. 323 (2019) 191–199. https://doi.org/10.1016/j.cattod.2018.06.004.
- [57] N. Kamarulzaman, M.F. Kasim, N.F. Chayed, Elucidation of the highest valence band and lowest conduction band shifts using XPS for ZnO and Zn0.99Cu0.01O band gap changes, Results Phys. 6 (2016) 217–230. https://doi.org/10.1016/j.rinp.2016.04.001.
- [58] T. Imyen, N. Yigit, P. Dittanet, N. Barrabés, K. Föttinger, G. Rupprechter, P. Kongkachuichay, Characterization of Cu–Zn/Core–Shell Al-MCM-41 as a Catalyst for Reduction of NO: Effect of Zn Promoter, Ind. Eng. Chem. Res. 55 (2016) 13050–13061. https://doi.org/10.1021/acs.iecr.6b03990.
- [59] T. Ghosh, P. Chandra, A. Mohammad, S.M. Mobin, Benign approach for methyl-esterification of oxygenated organic compounds using TBHP as methylating and oxidizing agent, Appl. Catal. B Environ. 226 (2018) 278–288. https://doi.org/10.1016/j.apcatb.2017.12.056.
- [60] J. Singh Meena, M.-C. Chu, Y.-C. Chang, H.-C. You, R. Singh, P.-T. Liu, H.-P. D. Shieh, F.-C. Chang, F.-H. Ko, Effect of oxygen plasma on the surface states of ZnO films used to produce thin-film transistors on soft plastic sheets, J. Mater. Chem. C. 1 (2013) 6613–6622. https://doi.org/10.1039/C3TC31320D.
- [61] Y. Cheng, S. Lu, W. Xu, H. Wen, J. Wang, Fabrication of superhydrophobic Au–Zn alloy surface on a zinc substrate for roll-down, self-cleaning and anti-corrosion properties, J. Mater. Chem. A. 3 (2015) 16774–16784. https://doi.org/10.1039/C5TA03979G.
- [62] R. Watari, N. Matsumoto, S. Kuwata, Y. Kayaki, Distinct Promotive Effects of 1,8-Diazabicyclo[5.4.0]undec-7-ene (DBU) on Polymer Supports in Copper-Catalyzed Hydrogenation of C=O Bonds, ChemCatChem. 9 (2017) 4501–4507. https://doi.org/10.1002/cctc.201701316.
- [63] P. Soni, U.C. Banerjee, Enantioselective reduction of acetophenone and its derivatives with a new yeast isolate Candida tropicalis PBR-2 MTCC 5158, Biotechnol. J. 1 (2006) 80–85. https://doi.org/10.1002/biot.200500020.
- [64] X.-Q. Guo, Y.-N. Wang, D. Wang, L.-H. Cai, Z.-X. Chen, X.-F. Hou, Palladium, iridium and ruthenium complexes with acyclic imino-N-heterocyclic carbenes and their application in aquaphase Suzuki–Miyaura cross-coupling reaction and transfer hydrogenation, Dalton Trans. 41 (2012) 14557–14567. https://doi.org/10.1039/C2DT31989F.
- [65] T. Kiyonaga, M. Higuchi, T. Kajiwara, Y. Takashima, J. Duan, K. Nagashima, S. Kitagawa, Dependence of crystal size on the catalytic performance of a porous coordination polymer, Chem. Commun. 51 (2015) 2728–2730. https://doi.org/10.1039/C4CC07562E.

- [66] R. Huber, A. Passera, A. Mezzetti, Iron(II)-Catalyzed Hydrogenation of Acetophenone with a Chiral, Pyridine-Based PNP Pincer Ligand: Support for an Outer-Sphere Mechanism, Organometallics. 37 (2018) 396–405. https://doi.org/10.1021/acs.organomet.7b00816.
- [67] H. Li, D. Wei, A. Bruneau-Voisine, M. Ducamp, M. Henrion, T. Roisnel, V. Dorcet, C. Darcel, J.-F. Carpentier, J.-F. Soulé, J.-B. Sortais, Rhenium and Manganese Complexes Bearing Amino-Bis(phosphinite) Ligands: Synthesis, Characterization, and Catalytic Activity in Hydrogenation of Ketones, Organometallics.
   37 (2018) 1271–1279. https://doi.org/10.1021/acs.organomet.8b00020.
- [68] Y. Ma, G. Xu, H. Wang, Y. Wang, Y. Zhang, Y. Fu, Cobalt Nanocluster Supported on ZrREnOx for the Selective Hydrogenation of Biomass Derived Aromatic Aldehydes and Ketones in Water, ACS Catal. 8 (2018) 1268–1277. https://doi.org/10.1021/acscatal.7b03470.
- [69] Y. Liu, S. He, Z. Quan, H. Cai, Y. Zhao, B. Wang, Mild palladium-catalysed highly efficient hydrogenation of CN, C–NO2, and CO bonds using H2 of 1 atm in H2O, Green Chem. 21 (2019) 830–838. https://doi.org/10.1039/C8GC03285H.
- [70] W. Gong, Y. Lin, C. Chen, M. Al-Mamun, H.-S. Lu, G. Wang, H. Zhang, H. Zhao, Nitrogen-Doped Carbon Nanotube Confined Co–Nx Sites for Selective Hydrogenation of Biomass-Derived Compounds, Adv. Mater. 31 (2019) 1808341. https://doi.org/10.1002/adma.201808341.
- [71] J.-H. Xie, X.-Y. Liu, J.-B. Xie, L.-X. Wang, Q.-L. Zhou, An Additional Coordination Group Leads to Extremely Efficient Chiral Iridium Catalysts for Asymmetric Hydrogenation of Ketones, Angew. Chem. Int. Ed. 50 (2011) 7329–7332. https://doi.org/10.1002/anie.201102710.
- [72] J. Du, G. Xu, H. Lin, G. Wang, M. Tao, W. Zhang, Highly efficient reduction of carbonyls, azides, and benzyl halides by NaBH 4 in water catalyzed by PANF-immobilized quaternary ammonium salts, Green Chem. 18 (2016) 2726–2735. https://doi.org/10.1039/C5GC02621K.
- [73] X.-S. Ning, X.-J. Dong, Z.-F. Xiao, C.-Z. Yao, Y.-B. Kang, Ion-Pair-Catalyzed Sodium Borohydride Reduction in Aprotic Organic Solvents, Asian J. Org. Chem. 4 (2015) 333–336. https://doi.org/10.1002/ajoc.201402281.
- [74] Z. Dalicsek, F. Pollreisz, Á. Gömöry, T. Soós, Recoverable Fluorous CBS Methodology for Asymmetric Reduction of Ketones, Org. Lett. 7 (2005) 3243–3246. https://doi.org/10.1021/ol051024j.
- [75] Y.-Q. Cao, Z. Dai, B.-H. Chen, R. Liu, Sodium borohydride reduction of ketones, aldehydes and imines using PEG400 as catalyst without solvent, J. Chem. Technol. Biotechnol. 80 (2005) 834–836. https://doi.org/10.1002/jctb.1297.
- [76] M. Niakan, Z. Asadi, Selective Reduction of Nitroarenes Catalyzed by Sustainable and Reusable DNA-supported Nickel

- Nanoparticles in Water at Room Temperature, Catal. Lett. 149 (2019) 2234–2246. https://doi.org/10.1007/s10562-019-02741-7.
- [77] M. Karthik, P. Suresh, Greener Synthesis of Reduced Graphene Oxide-Nickel Nanocomposite: Rapid and Sustainable Catalyst for the Reduction of Nitroaromatics, ChemistrySelect. 2 (2017) 6916–6928. https://doi.org/10.1002/slct.201701314.
- [78] Q. Lai, D. Alligier, K.-F. Aguey-Zinsou, U.B. Demirci, Hydrogen generation from a sodium borohydride—nickel core@shell structure under hydrolytic conditions, Nanoscale Adv. 1 (2019) 2707–2717. https://doi.org/10.1039/C9NA00037B.
- [79] M. Shekouhy, A. Moaddeli, A. Khalafi-Nezhad, A novel one-pot three component approach to 6-substituted 2,4-diamino-1,3,5-triazines using nano-sized copper/zinc-modified MCM-41 (Cu/Zn-MCM-41) as a new heterogeneous mesoporous catalyst, J. Ind. Eng. Chem. 50 (2017) 41–49. https://doi.org/10.1016/j.jiec.2017.01.001.
- [80] I. Sádaba, M.L. Granados, A. Riisager, E. Taarning, Deactivation of solid catalysts in liquid media: the case of leaching of active sites in biomass conversion reactions, Green Chem. 17 (2015) 4133–4145. https://doi.org/10.1039/C5GC00804B.
- [81] S. Singh, A. Patel, Mono lacunary phosphotungstate anchored to MCM-41 as recyclable catalyst for biodiesel production via transesterification of waste cooking oil, Fuel. 159 (2015) 720–727. https://doi.org/10.1016/j.fuel.2015.07.004.
- [82] K. Mal, S. Chatterjee, A. Bhaumik, C. Mukhopadhyay, Mesoporous MCM-41 Silica Supported Pyridine Nanoparticle: A Highly Efficient, Recyclable Catalyst for Expeditious Synthesis of Quinoline Derivatives through Domino Approach, ChemistrySelect. 4 (2019) 1776–1784. https://doi.org/10.1002/slct.201803708.
- [83] A. Kumar Sasmal, S. Dutta, T. Pal, A ternary Cu 2 O–Cu–CuO nanocomposite: a catalyst with intriguing activity, Dalton Trans. 45 (2016) 3139–3150. https://doi.org/10.1039/C5DT03859F.
- [84] M. Basu, A.K. Sinha, M. Pradhan, S. Sarkar, Y. Negishi, T. Pal, Fabrication and Functionalization of CuO for Tuning Superhydrophobic Thin Film and Cotton Wool, J. Phys. Chem. C. 115 (2011) 20953–20963. https://doi.org/10.1021/jp206178x.

# **CHAPTER 3**

# Bimetallic CoNi Nanoflowers for Catalytic Transfer Hydrogenation of Terminal Alkynes

# 3.1. Inroduction

In the last few years, transition metal-based bimetallic nanomaterials have gained much attention owing to their extraordinary properties, variable oxidation states and coordination numbers.[1,2] Bimetallic nanomaterials as multifunctional materials have been developed for various applications such as in catalysis, [3,4] energy storage, [5] electrocatalysis,[6] sensors[7,8] biological application, environmental remediation etc.[9] Additionally, owing to their excellent redox activity, cost-effectiveness and natural abundance, environmental compatibility of 3d-transition metals favor them an economical, sustainable and convenient choice for catalytic applications.[10,11] Hence, the development of transition metal-based materials is in great demand. Due to the synergistic effect between existing metal components, the bimetallic nanomaterials have been proven multifunctional materials[12] and discovered to enhance the chemical, magnetic, electrical, and biological activities and reduce the process cost.[13,14] Also, the bimetallic nanoparticles show excellent efficiency and catalytic activity than their monometallic nanoparticles.[12,15] Owing to these benefits, bimetallic transition metal nanoparticles are explored as sustainable, recyclable catalysts for various organic transformations.[16] Moreover, the magnetic nanoparticles evolved as sustainable, stable, recyclable catalysts due to their easy separation from the reaction mixture using an external magnet. Hence, magnetic nanocatalyst is the best choice for catalytic conversion reactions.

The hydrogenation of C-C multiple bonds is one of the most important reactions in organic synthesis and pharmaceutical industries.

Also, the product of C-C hydrogenation, i.e., the alkane, is in high demand due to its use as raw materials in chemical industries and for the synthesis of various gasoline and oils.[17] However, using a catalyst, the complete hydrogenation of unsaturated C-C triple bond is still challenging.[18] Though the noble metal catalysts (Pd[19], Pt[20,21], Au[22], Pt/Nb<sub>2</sub>O<sub>5</sub>[23]) exhibited remarkable activity, the high cost and limited availability hinder their application in industries.[9,24]

Additionally, some other catalysts were reported, such as Ni[25,26], Cu[27,28], Co[29], Fe[30,31] as monometallic catalysts, whereas Au@Ni[32], Ni/Fe<sub>3</sub>O<sub>4</sub>[33], Pd/Ni[34], Al-rGO/Ni-Pd[35], Ni/Ru/Pt/Au[36] as a bimetallic catalyst. Raney nickel is widely used in industries and chemical laboratories for various hydrogenation reactions as an efficient catalyst that adsorbs hydrogen in its pores[37] but is pyrophoric, air sensitive and requires extra precautions and safety measures while transporting.[38] Also, the hydrogenation using organometallic complexes has some drawbacks of non-recyclability, hard synthetic process, and air sensitivity. In this context, nanoparticles have gained the great attention of the scientific community due to their high surface area, recyclability and easy synthetic process.[39] Hence, developing a better alternative is required, and for this purpose, first-row transition metal nanoparticles can be considered an alternative of noble metals.[40,41]

However, the hydrogenation using a various metal catalyst with hydrogen gas or reducing agents were widely reported. Hydrogen gas leads to selective hydrogenation of alkyne into alkene rather than alkane, which is an excellent finding in organic synthesis.[42] However, using hydrogen gas and its storage in chemical laboratories and industries is still challenging due to safety issues.[43] So, the use of reducing agents like formic acid, isopropyl alcohol, hydrazine hydrate, ammonia borane, NaBH<sub>4</sub>, glycerol etc., used to preferred and explored for industrial purposes due to economic reasons.[35] Hence, using bimetallic nanocatalyst with reducing agents for the hydrogenation of alkynes is the better choice. Among transition metal nanomaterials, the Ni-based

catalyst shown excellent catalytic activity for hydrogenation reactions owing to its low cost, redox properties and magnetic behavior, so the use of nickel metal with any other metal is the best choice.

Keeping these above points in mind, herein, we report a bimetallic catalyst of cobalt and nickel metal for hydrogenation of alkynes using hydrazine hydrate as a reducing agent. The synthesized nanocatalyst has flower-shaped morphology, and the same was utilized for catalytic hydrogenation of alkynes with 100% conversion and excellent selectivity with recyclability up to six cycles. The synthesized bimetallic CoNi nanoflower (containing 50 wt% Co, 50% wt% Ni) is an efficient, magnetically separable, cost-effective catalyst for hydrogenation of terminal alkynes (15 examples).

# 3.2. Experimental

#### 3.2.1. Materials

All starting materials used as purchased. Cobalt chloride hexahydrate (CoCl<sub>2</sub>.6H<sub>2</sub>O), Nickel Chloride (NiCl<sub>2</sub>.6H<sub>2</sub>O), and sodium hydroxide (NaOH) pellet were purchased from Merck, India. Ethylene Glycol, Hydrazine hydrate (N<sub>2</sub>H<sub>4</sub>. 2H<sub>2</sub>O) and alkynes were purchased from Sigma-Aldrich, and other solvents were used as received.

# 3.2.2. Catalyst Preparation

For synthesizing CoNi nanoflower, 2.38 gm Cobalt chloride hexahydrate (CoCl<sub>2</sub>.6H<sub>2</sub>O) and 2.38 gm Nickel Chloride (NiCl<sub>2</sub>.6H<sub>2</sub>O) were dissolved in ethylene glycol with mechanical stirring at 80 °C. After 10 min, add NaOH to maintain the pH at 10.5 and stir the reaction mixture for another 20 min. After 20 min, add 16 mL hydrazine hydrate to the above reaction mixture. After 1 hr, the black color precipitate was obtained with a clear solution. Furthermore, centrifuged the above reaction mixture containing precipitate, washed with ethanol and water three times, and dried overnight in a vacuum at 80 °C. The obtained black color particles are named CoNi nanoflower. The cobalt and nickel salts were used in 1:1 molar ratio.

$$2Ni^{2+} + N_2H_4 + 4OH^- \rightarrow 2Ni + N_2 + 4H_2O$$
  
 $2Co^{2+} + N_2H_4 + 4OH^- \rightarrow 2Co + N_2 + 4H_2O$ 

With a similar method, pure monometallic Co and Ni nanomaterials were also synthesized and used for the catalytic hydrogenation reaction.

# 3.2.3. General catalytic reaction

In a typical catalytic hydrogenation reaction, terminal alkyne substrate (0.5 mmol), CoNi catalyst (10 mg), Hydrazine hydrate 99% (2 mmol), Ethanol (2 mL) in a round bottom flask equipped with condenser at magnetic stirring bar. The reaction mixture reflux for the appropriate time (10-22 h) at 80 °C. After completion of the reaction, the reaction mixture was allowed to cool at room temperature and separated the catalyst with magnet, and the reaction mixture was diluted, filtered and given to record the Shimadzu GC-MS analysis for calculating conversion and selectivity.

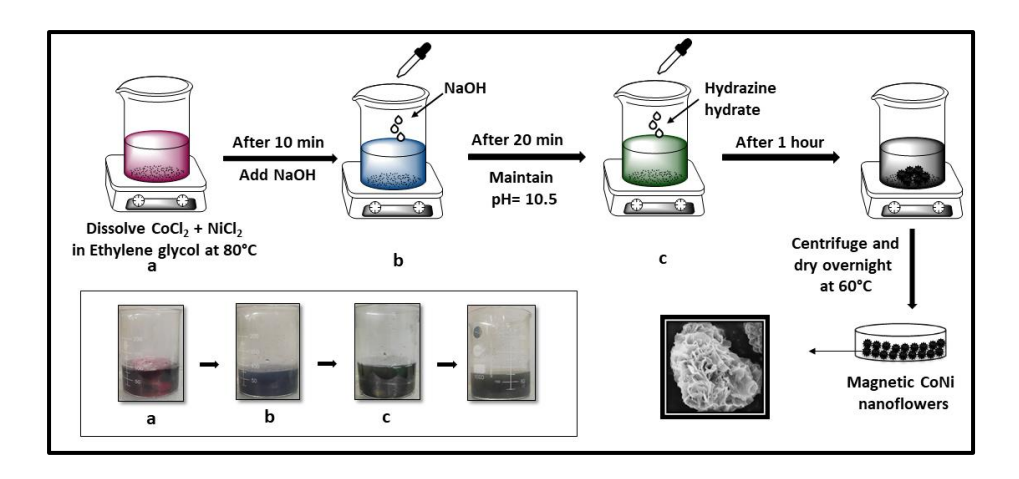
## 3.2.4. Physicochemical measurements

The details about the PXRD, FE-SEM, HR-TEM, BET characterization and utilized instruments have been discussed in chapter 2 in physicochemical measurements section. Thermogravimetric analysis was performed using METTLER TOLEDO (TGA/DSC 1) to evaluate the thermal stability of nanocatalyst. The X-ray Photoelectron Spectroscopy (XPS) analysis of fresh and spent catalysts was recorded using Scient Omicron Multiprobe MXPS spectrometer. Magnetic properties were analysed using Lake Shore VSM (Model 7410 series VSM) at room temperature. Identification of the products of catalytic reactions carried out using Shimadzu GC-MS, QP2010 mass spectrometer.

#### 3.3. Results and discussion

#### 3.3.1. Characterization of CoNi nanoflower

The synthetic procedure of bimetallic CoNi nanoflower is shown in **Scheme 3.1**. The bimetallic CoNi nanoflower was synthesized by modifying the reported liquid phase reduction method.[44,45]



**Scheme 3.1**. Schematic representation of the synthesis of bimetallic CoNi nanoflower.

The powder X-ray diffraction pattern shows three strong peaks at 44.4°, 51.6° and 76.3° as shown in **Figure 3.1A**. These peaks shifted slightly from both FCC Ni and FCC Cobalt reported nanoflower with JCPDS Card no. 04-085 and 15-0806, respectively, as shown in **Figure 3.1A**(inset).[46,47] The peaks exhibited in PXRD spectra were assigned for the plane (111), (200) and (220), respectively, of the FCC phase of CoNi nanoflower.[48] The crystallite size was calculated with the Debye-Scherrer equation was 41 nm.

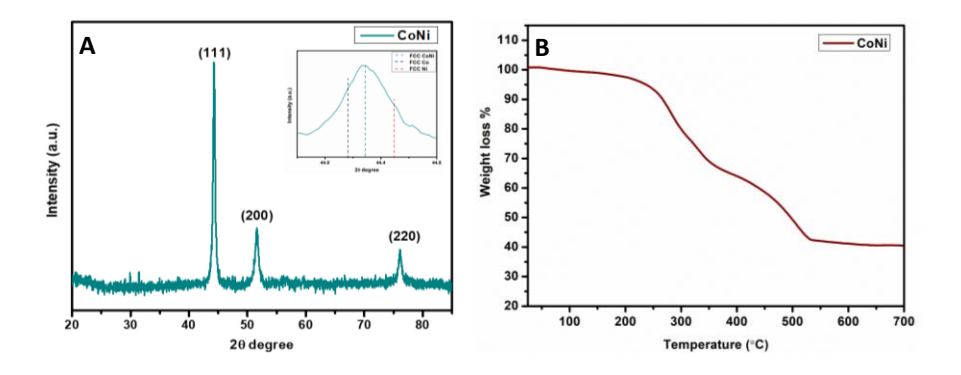


**Figure 3.1**. **(A)** XRD pattern (in the inset, the zoom view of PXRD for reference), **(B)** TGA curve of bimetallic CoNi nanoflower.

Furthermore, TGA was performed to analyze the thermal stability of the synthesized bimetallic CoNi nanoflower from room temperature to 700 °C, as shown in **Figure 3.1B**. It was observed that the nanoflower showed three major weight loss regions (i) Below 190 °C, (ii) up to 370 °C and above 370 °C. In this region, the observed

weight loss was 2.151 wt%, 31.594 wt% and 23.887 wt%, respectively. The first weight loss is attributed to the removal of adsorbed solvents and water molecules and the weight loss after 190 °C, might be the removal of trapped organic species inside the pores of nanoflower.[49] This result confirmed the thermal stability of bimetallic CoNi nanoflower at higher temperatures.

After performing TGA analysis, BET measurements of bimetallic CoNi nanoflower were performed to analyze the surface area and porosity at 77K and 1 bar pressure. The N<sub>2</sub> adsorption-desorption isotherms are shown in **Figure 3.2A**. The calculated specific surface area is 5.026 m<sup>2</sup>/g. The adsorption curve is depicted as a type IV curve confirming the presence of mesopores.[50–52] This mesopore formation confirmed with the pore size distribution curve shown in **Figure 3.2B**, which reveal the BJH pore size is 3.78 nm and pore volume is 0.045 cm<sup>3</sup>/g.

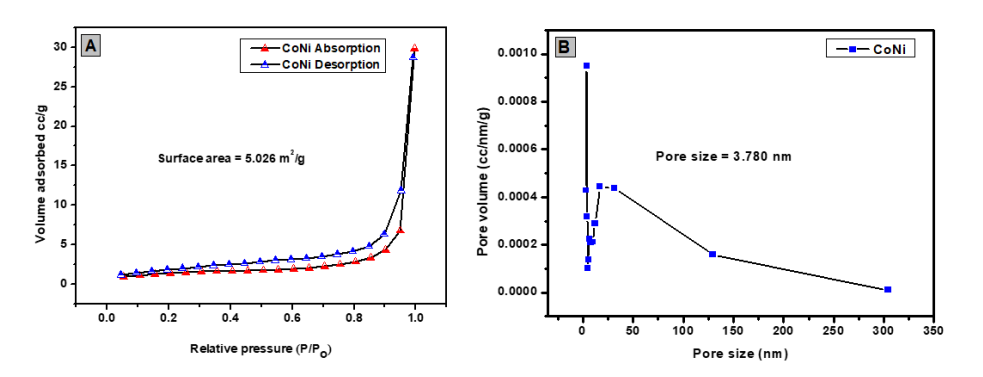


**Figure 3.2**. N<sub>2</sub> adsorption desorption study for (**A**) surface area and (**B**) pore size distribution.

The morphological study was performed using FE-SEM analysis of the synthesized nanoflower as shown in **Figure 3.3**. The FE-SEM images revealed the flower like shape of bimetallic CoNi nanoflower as shown in **Figure 3.3(A-C)**.[53–55] Furthermore, to confirm the presence of element and the approximate weight ratio of the CoNi nanoflower, the elemental analysis and mapping analysis were performed as shown in **Figure 3.3(D-F)**. The elemental analysis confirmed the presence of both Co and Ni element with approximate 1:1

weight% ratio. Hence, the synthesized nanoflower confirmed as nanoflower shaped with equal weight% ratio of Co and Ni element. Also, the average particle size was calculated which was found to be 44 nm.

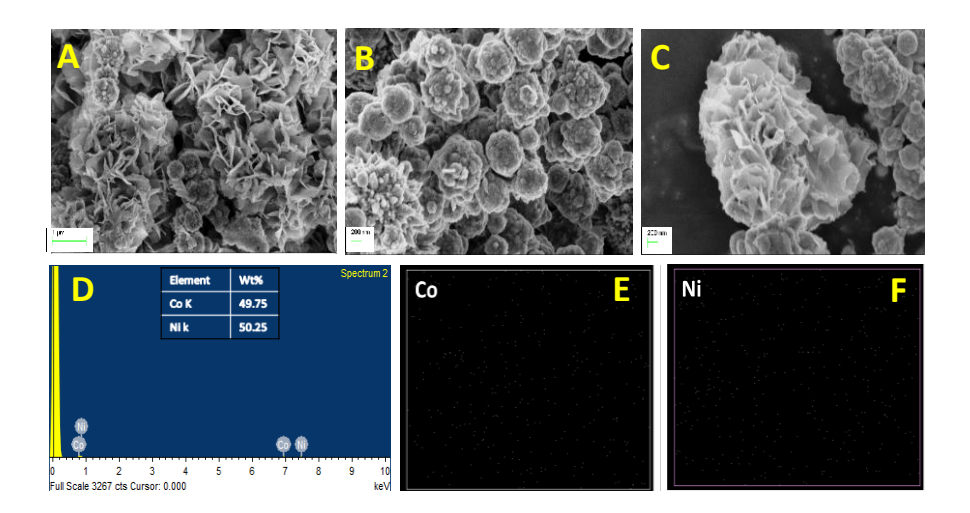


**Figure 3.3**. SEM images of bimetallic CoNi nanoflower at (**A**) 1μm (**B-C**) 200 nm, (**D**) EDAX pattern of bimetallic CoNi nanoflower, (**E-F**) elemental mapping of Co and Ni element.

Moreover, to investigate the other structural information of nanoflower, the HR-TEM analysis was performed, and the obtained images were in agreement of SEM images. The HR-TEM images confirmed the morphology of bimetallic CoNi nanomaterials as flower-shaped (**Figure 3.4(A-E**)).[56–58] The leaves of the nanoflower can be seen in the images. The selective area electron diffraction (SAED) pattern (**Figure 3.4F**) shows the bright spot with concentric rings reveals the high crystallinity of CoNi nanoflower.[59,60]

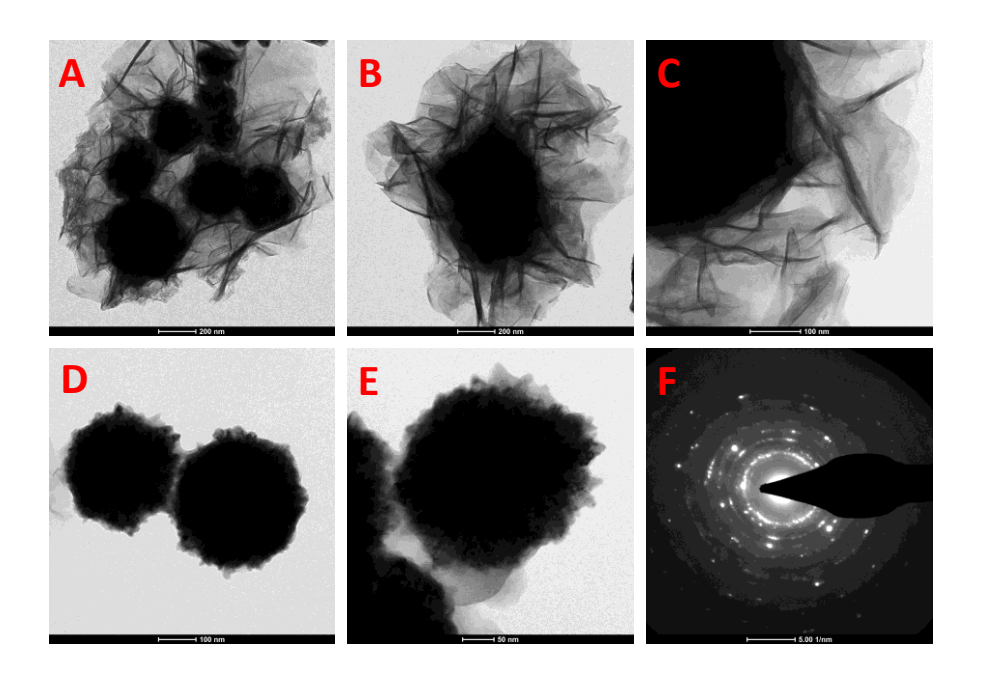


**Figure 3.4**. HR-TEM images of bimetallic CoNi nanoflower at (**A-B**) 200 nm, (**C-D**) 100 nm and (**E**) 50 nm and Selective area electron diffraction (SAED) pattern at 5.00 1/nm.

Additionally, to check the magnetic property of bimetallic CoNi nanoflower, vibrating sample magnetometer (VSM) studies were performed, and M-H loop was recorded at room temperature (**Figure 3.5**). The saturation magnetization ( $M_s$ ) was recorded to be 90.62 emu/g and retentivity ( $M_r$ ) 2.63 emu/g, and coercivity 61.61 Oe. The remanence ratio ( $M_r/M_s$ ) was calculated to be 0.029.

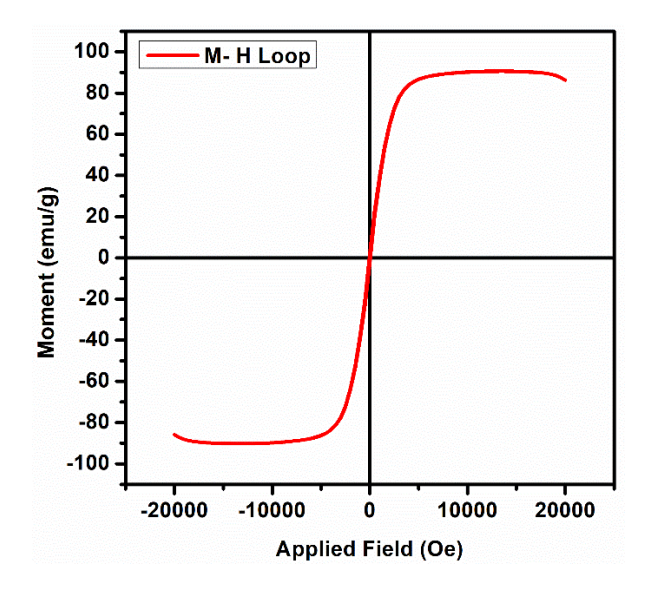


**Figure 3.5.** Hysteresis loop of bimetallic CoNi nanoflower at room temperature.

Furthermore, the chemical composition and oxidation state of the bimetallic CoNi nanoflower as analysed using XPS analysis as shown in Figure 3.6. The individual study of cobalt and nickel element was performed for bimetallic CoNi nanoflowers and the results shown in Figure 3.6(A-B). The presence of Co, Ni and O element in bimetallic CoNi nanoflower was confirmed in survey scan (**Figure 3.6C**).[50,61] The XPS spectra of Co element exhibited peaks at 778.1 eV, 792.6 eV, 780.86 eV and 796.5 eV. The peak at 778.1 and 792.6 eV for Co 2p<sub>3/2</sub> and Co 2p<sub>1/2</sub> respectively reveals the presence of metallic cobalt Co(0).[62,63] The peaks at 780.86 eV and its satellite at 785.9 eV reflect the presence of cobalt oxide (CoO).[61,64] Similarly, the XPS spectra of Ni element was performed which showed peaks at 852.7 eV and 870 eV of Ni 2p<sub>3/2</sub> and Ni 2p<sub>1/2</sub> respectively reflect the presence the metallic Ni(0).[65,66] The deconvoluted peak at 855.1 eV and satellite peak at 860.9 eV attributed the presence of NiO.[8,67,68] The peak 860.9 eV and 879.4 eV were ascribed to the satellite peak of Ni 2p<sub>3/2</sub> and Ni 2p<sub>1/2</sub> respectively.[65] The presence of Co(0)/Ni(0) is in good agreement of the PXRD data for bimetallic CoNi fcc nanoflower. The presence of CoO and NiO either due to surface oxidation of metallic Co and Ni in the exposure to air or due to incomplete reduction of Co and Ni elements.[61,62,65]

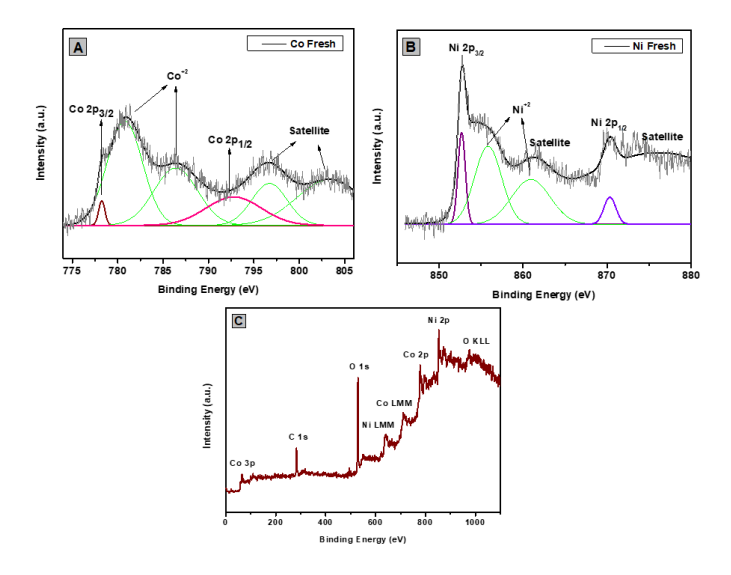


**Figure 3.6**. XPS analysis of CoNi nanoflower for (**A**) Co 2p, (**B**) Ni 2p, and (**C**) survey scan.

# 3.3.2. Catalytic results:

The hydrogenation of terminal alkyne into alkane by using bimetallic CoNi nanoflower and hydrazine hydrate as reducing agent with ethanol as solvent was performed. Phenylacytylene considered as model; substrate and all the optimization reactions were performed using this as shown in **Scheme 3.2**.

**Scheme 3.2**. General catalytic scheme of phenyl acetylene using bimetallic CoNi nanoflower.

A systematic investigation of hydrogenation reaction was performed using phenyl acetylene as a model substrate to select the best reaction condition by varying the solvent, reaction time, temperature, catalyst and reducing agent. Initially, the catalyst screening was performed, and CoCl<sub>2</sub>, NiCl<sub>2</sub>, CoNi, CuNi, Co and Ni nanocatalysts were used (Figure 3.7). When the hydrogenation reaction was performed with synthesized bimetallic CuNi catalyst, the conversion was 73% with 76% selectivity for the major product ethyl benzene. In contrast, when reaction performed with monometallic Co and Ni catalyst, the conversion was 63% and 53% respectively with 68% and 40% selectivity for ethyl benzene. When the same reaction was performed with bimetallic CoNi nanoflower, the conversion of phenyl acetylene into ethyl benzene is 100% with 100% selectivity. This data shows that the bimetallic CoNi nanoflower is excellent choice for the hydrogenation reaction of phenyl acetylene. Further, all reactions and optimization were carried out with bimetallic CoNi nanoflower. A reaction without catalyst was also performed and only 37% conversion observed with 41% selectivity for major product that shows the importance of synthesized bimetallic CoNi nanoflower.

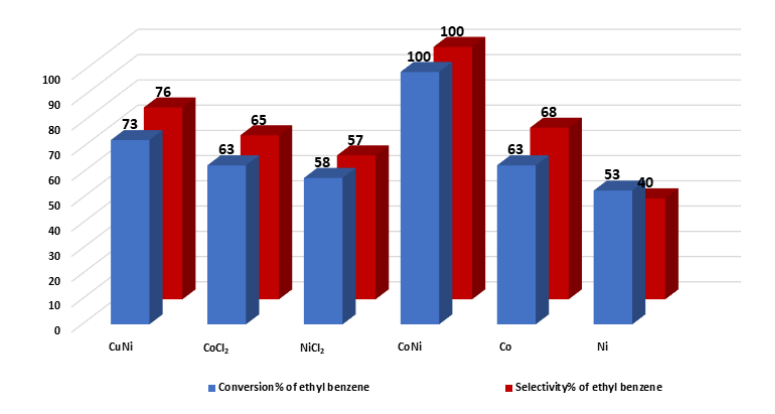


**Figure 3.7.** Effect of different catalyst on hydrogenation of phenyl acetylene into ethyl benzene. **Reaction conditions**: Substrate = 1 mmol, hydrazine hydrate = 2 mmol, solvent (EtOH) = 2 mL, catalyst = 10 mg, time = 10 h, temperature =  $80 \, ^{\circ}\text{C}$ .

Furthermore, the catalyst loading was investigated and the best results obtained with 10 mg of the catalyst with 100% conversion and 100% selectivity of phenyl acetylene into ethyl benzene (**Figure 3.8A**). It was observed that the conversion was dependent on the amount of catalyst used in the reaction. After optimizing catalyst amount, effect of the amount of reducing agent was tested using 0.5 to 2 mmol and the results show that 2 mmol of reducing agent hydrazine hydrate is sufficient for hydrogenation of 0.5 mmol of phenyl acetylene (Figure **3.8B**). Hence, further optimization was analysed using 2 mmol of hydrazine hydrate with 10 mg of the CoNi nanoflower as catalyst. Additionally, the substrate amount was also tested from 0.5 mmol to 1.5 mmol and the results show that as the amount of substrate increases, the conversion of phenyl acetylene was decreases. In all the results, selectivity for ethyl benzene was higher than styrene (Figure 3.8C). Since 0.5 mmol of phenyl acetylene was converted into product with 100% selectivity, so further all the reactions were performed using 0.5 mmol of phenyl acetylene with 10 mg of catalyst and 2 mmol of reducing agent. Furthermore, the screening of different solvents was performed and ethanol, methanol, acetonitrile, toluene, THF was used with above optimized reaction conditions (Figure 3.8D). It was observed that the conversion with polar protic solvents is higher in comparison to the non-polar solvents.[69] The neat reaction was also performed and the obtained conversion was 35% with 29% selectivity towards ethyl benzene. The highest conversion was observed with ethanol as a solvent, so further all reactions carried out with ethanol as solvent. Furthermore, the influence of temperature was investigated and the results depicted that the conversion of phenyl acetylene increases with increase in temperature as shown in **Figure 3.8E**. When reaction was performed at room temperature then only 53% conversion with 56% selectivity observed for ethyl benzene. Hence it was confirmed that for complete hydrogenation of phenyl acetylene 80°C temperature required.

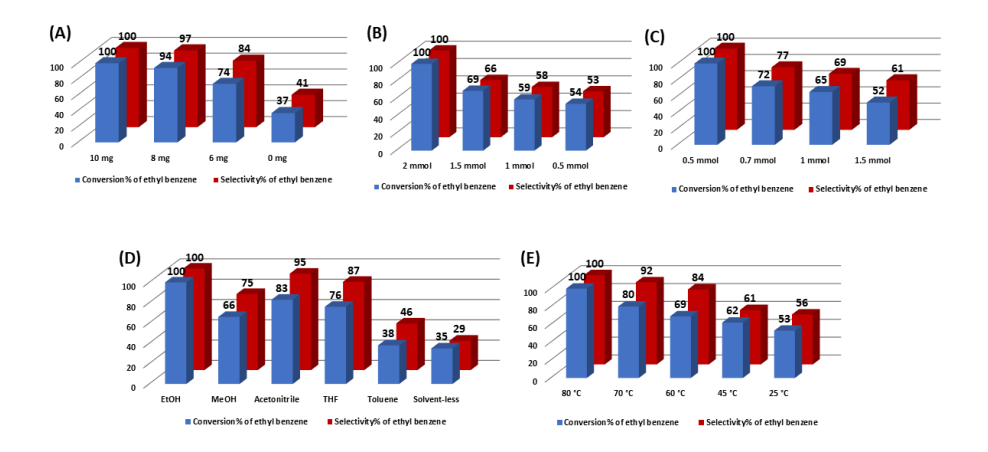


**Figure 3.8.** Effect of **(A)** catalyst amount **(B)** hydrazine hydrate amount **(C)** substrate amount **(D)** solvent and **(E)** temperature on hydrogenation of phenyl acetylene into ethyl benzene. **Reaction conditions**: Substrate = 0.5-1.5 mmol, catalyst = 0-10 mg, hydrazine hydrate = 0.5-2 mmol, solvent = 2 mL, time = 10 h, temperature = 25-80 °C.

Additionally, the effect of different reducing agent was performed and for that, formic acid and triethylamine additive was used instead of hydrazine hydrate and the results presented in **Table 3.1**. Interestingly, in case of formic and Et<sub>3</sub>N the conversion is selective towards styrene instead of ethyl benzene with 43% conversion. Hence, it was noted that the best optimized reaction condition for the hydrogenation of 0.5 mmol phenyl acetylene into ethyl benzene involves the use of 2 mmol hydrazine hydrate, 10 mg CoNi nanoflower and 2 mL ethanol required at 80 °C.

**Table 3.1.** Effect of reducing agent on hydrogenation of phenyl acetylene.

Endage	Reducing	Additive	Conversion	Selectiv	ity (%)
Entry	agent		(%)	a	b
1	N <sub>2</sub> H <sub>4</sub> .2H <sub>2</sub> O	-	100	100	-
2	НСООН	Et <sub>3</sub> N	43	-	100

**Reaction conditions**: Substrate = 0.5 mmol, hydrazine hydrate = 2 mmol, solvent (EtOH) = 2 mL, catalyst = 10 mg, time = 10 h, temperature = 80 °C.

After screening best reaction condition for the hydrogenation of phenyl acetylene, further the scope of reaction was performed using phenyl acetylene derivatives (**Table 3.2**). The reaction was affected by electron-rich and electron-deficient substituents. The electron-rich substituents (-Me, -OMe) and electron-deficient substituents (-F, -Br, -NH<sub>2</sub>) both shows the excellent conversion of 100% with 100% selectivity of corresponding alkane (Table 3.2, Entry 2-7). Although, the conversion of electron-withdrawing substituents took more time in comparison to that of electron-donating substituents, which revealed the electronic effect of alkynes on the catalytic activity.[28] Furthermore, hydrogenation of heterocyclic substrates was also investigated (Table 3.2, Entry 8-10) and it was observed that all substrate 100% converted into corresponding products with almost 100% selectivity. The hydrogenation of *ortho*- substituted alkyne (**Table 3.2, Entry 4 and 10**) took more time in comparison to para- substituted alkyne for complete conversion due to steric hindrance (Table 3.2, Entry 3 and 8) which indicate the effect of substituent position. The hydrogenation of 2ethynyl pyridine shows less selectivity i.e. 94% towards corresponding alkane in comparison to 4-ethynyl pyridine and 3-ethynyl pyridine i.e. 100%. Additionally, the hydrogenation of di-substituted alkyne took more time in comparison to mono-substituted aryl alkyne (Table 3.2, Entry 11) and the substrate showed 100% conversion and 100% selectivity. Moreover, some small alkynes were also analysed for hydrogenation reaction and all substrates were converted 100% into corresponding alkane and alkene with almost 100% selectivity (**Table**  **3.2, Entry 12-15**). The results showed that the CoNi nanoflower are efficient catalyst for hydrogenation of alkynes. All the conversion and selectivity was confirmed by GC-MS analysis (Section 3.5). The general catalytic reaction scheme is as shown in Scheme 3.3.

**Scheme 3.3**. General catalytic scheme of substituted phenyl acetylene and heterocyclic alkynes by using bimetallic CoNi nanoflower.

**Table 3.2**. Substrate scope of hydrogenation of alkynes into alkanes

,		Time	Conv.	Sel. (%)		
Entry	Substrate	( <b>h</b> )	(%)	a	b	
1		10	100	100	-	
2		12	100	100	-	
3	MeO	12	100	100	-	
4	OMe	17	100	100	-	
5	H <sub>2</sub> N	16	100	100	-	

6	Br	20	100	100	-
7	F	20	100	100	-
8		14	100	100	1
9		14	100	100	-
10	Z	14	100	92	8
11		22	100	100	-
12	OH	11	100	100	-
13	OH	10	100	100	-
14		11	100	46	54
15	S	8	100	100	1

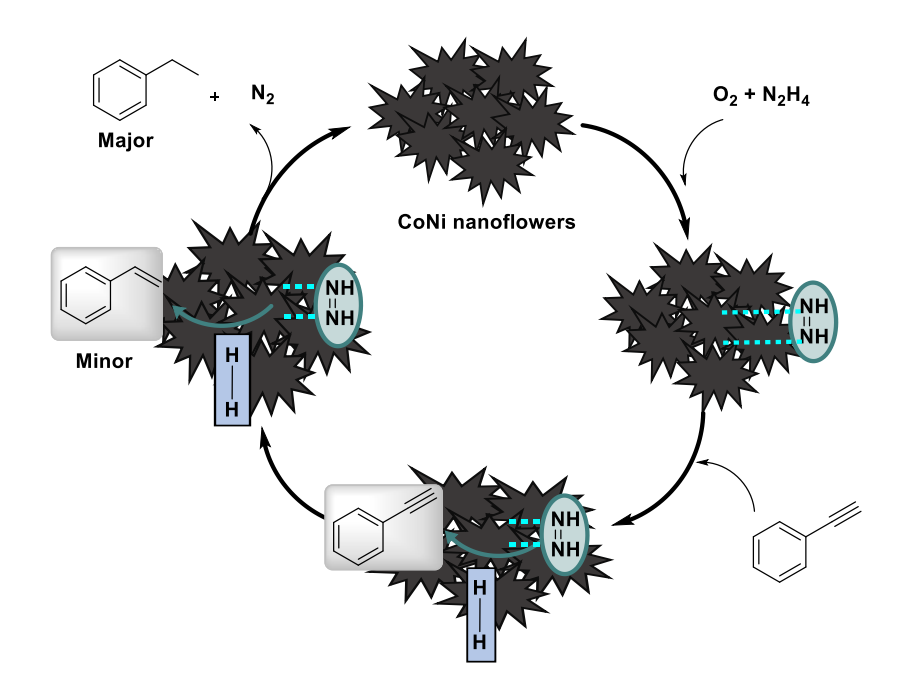
**Reaction Conditions**: Substrate = 0.5 mmol, catalyst = 10 mg, hydrazine hydrate = 2 mmol, solvent (EtOH) = 2 mL, temperature = 80 °C, time = 10-22 h. All conversion and selectivity confirmed by Shimadzu GC-MS analysis.

To compare this work with some reported literature, we compile some of the recently reported works where hydrazine hydrate and hydrogen gas was utilized for the hydrogenation of terminal alkynes to alkanes and the results exhibited that CoNi bimetallic catalyst showed promising catalytic activity without using harsh reaction conditions [**Table 3.3**].

**Table 3.3.** Comparison of hydrogenation of alkynes using bimetallic CoNi with some previously reported work.

S.	Catalyst	Substrate	H-Source	Time	Temp	Yield/	Ref.
No.			/Additives	(h)	(°C)	Sel (%)	
1	Au@Ni	Phenyl	H <sub>2</sub> gas (50	4	50	100/100	[70]
	core-shell	acetylene	psi)				
	NPs						
2	Pd/Ni-B	Phenyl	H <sub>2</sub> gas (20	0.083	RT	100/100	[34]
	catalyst	acetylene	bar)				
3	Pt@Cu-	Phenyl	H <sub>2</sub> gas (1	2	40	93/100	[20]
	MOC	acetylene	bar)			, , , , , ,	
		-					
4	N-assembly	Phenyl	H <sub>2</sub> gas (20	8	230	100/100	[71]
	carbons	acetylene	bar)				
	(NACs) 5						
	mg						
5	Rh <sub>4</sub> Co	Phenyl	N <sub>2</sub> H <sub>4</sub> .H <sub>2</sub> O	8	60	71	[73]
	nanocatalyst	acetylene	(4.7 mmol)				
6	Cu/Cu-BTC-	Phenyl	N <sub>2</sub> H <sub>4</sub> .H <sub>2</sub> O	6	80	97/94	[69]
· ·	MOF	acetylene	(2.4 mmol)		00	) // / <del>-</del>	[07]
7	Cu/D NPs	Phenyl	N <sub>2</sub> H <sub>4</sub> .H <sub>2</sub> O	24	60	39	[27]
	(20 mg)	acetylene	(0.1  mL) +				
		(1 mmol)	aq. NH <sub>3</sub>				
			(0.025 mL)				
8	MoO <sub>2</sub>	Phenyl	N <sub>2</sub> H <sub>4</sub> .H <sub>2</sub> O	0.5	30	0.2	[74]
	catalyst (20	acetylene	(1.5 mmol)				
	mg)	(0.5					
		mmol)					
9	Pd@Pt core-	Phenyl	N <sub>2</sub> H <sub>4</sub> ·H <sub>2</sub> O	30	60	85/94	[75]
	shell NPs	acetylene	(20 mL) +				
		(0.5	aqueous NH <sub>3</sub>				
		mmol)	(10 mL, 28–				
			30%)				
10	Bimetallic	Pheny	N <sub>2</sub> H <sub>4</sub> .H <sub>2</sub> O (2	10	80	100/100	This
	CoNi	acetylene	mmol)				work
	nanoflower						

Based on experimental results and previous reports, [69,76] the plausible mechanism was proposed for catalytic hydrogenation of alkynes using CoNi nanoflower and hydrazine hydrate as reducing agent with ethanol as solvent (Scheme 3.4). It was reported earlier that in presence of air or oxidizing agent, the hydrazine hydrate activated on the surface of the catalyst and converted into diimide and this diimide generate the hydrogen which react with phenyl acetylene. The presence of catalyst facilitates the reduction reaction of phenyl acetylene into styrene and later on ethyl benzene as shown in plausible mechanistic pathway. To confirm this mechanism, the same reaction was performed in presence of N<sub>2</sub> and Ar atmosphere in de-aerated flask and in both the cases the conversion of phenyl acetylene was very less and this result supported our proposed mechanism in which the presence of air plays an important role. The diimide formation was the key for the hydrogenation reaction which is produced by the synthesized CoNi nanoflower via dissolved oxygen present in the reaction mixture. Hence, the control experiment confirmed the insitu diimide formation which transfer hydrogen to phenyl acetylene followed by conversion of styrene and then ethyl benzene.



**Scheme 3.4**. Plausible mechanism of catalytic hydrogenation of alkynes into alkanes.

#### 3.3.3 Kinetic and recycle study

The kinetic study of hydrogenation reaction of phenyl acetylene into corresponding alkane and alkene was performed by taking samples periodically on 2, 4, 6, 8 and 10 hours from the reaction mixture and given for GC-MS analysis and the observed conversion was 56%, 61%, 64%, 70% and 100% respectively (**Figure 3.9A**). The selectivity of ethyl benzene increases with increase in time. Furthermore, to investigate the recyclability and reusability of the bimetallic CoNi catalyst, the recycle study was performed.[39] After completion of hydrogenation reaction of phenyl acetylene, the magnetic catalyst was separated by magnet and the reaction mixture was injected for GC-MS analysis. The separated catalyst was dried overnight at room temperature and reuse for next cycle and the same process repeated and the obtained conversion and selectivity was shown in **Figure 3.9B**. The magnetically separable catalyst shown excellent conversion and selectivity up to 6 cycles.

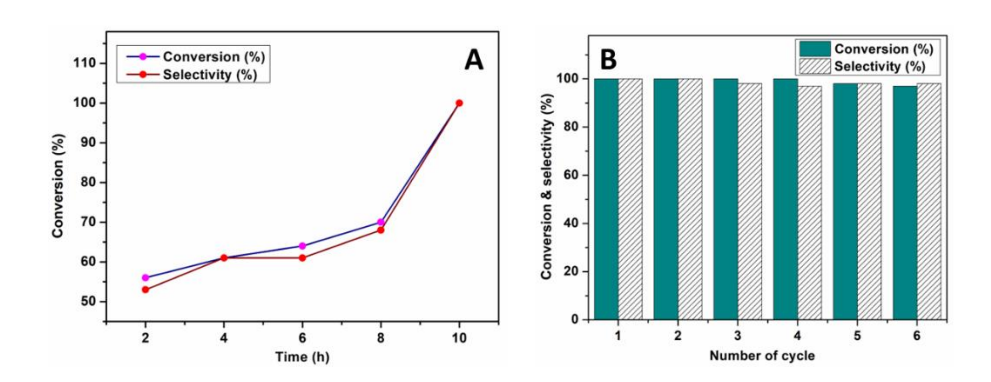


**Figure 3.9.** (**A**) Kinetic study of conversion of phenyl acetylene into ethyl benzene and (**B**) recycle study of the catalyst for hydrogenation reaction of phenyl acetylene. **Reaction conditions**: Substrate = 1 mmol, catalyst (CoNi nanoflower) = 10 mg, hydrazine hydrate = 2 mmol, solvent (EtOH) = 2 mL, temperature =  $80 \, ^{\circ}$ C, time = 2- $10 \, \text{h}$ .

Additionally, to check the stability of bimetallic CoNi nanoflower, the spent catalyst was analysed by XPS analysis as shown in **Figure 3.10**. In the XPS spectra of Co element, the peak ascribed at 780.58 eV and 796.2 eV of Co 2p<sub>3/2</sub> and Co 2p<sub>1/2</sub> respectively revealed the existence

of CoO.[77] The peaks at 783.8 eV and 801.9 eV were attributed for the satellite peaks of Co 2p<sub>3/2</sub> and Co 2p<sub>1/2</sub> respectively as shown in **Figure 3.10(A)**. Furthermore, the XPS spectra of Ni element was also analysed and the peaks exhibited at 855.2 eV and 872.8 eV for the presence of Nickel oxide (NiO).[67,78] The peaks at 860.8 eV and 878.8 eV were attributed as the satellite peaks of Ni 2p<sub>3/2</sub> and Ni 2p<sub>1/2</sub> respectively as shown in **Figure 3.10(B)**.[68] The oxidation of the metallic CoNi catalyst in spent, may be due to washing and drying process of the catalyst while using it for the recycle study.[65] In given survey scan **Figure 3.10(C)**, the presence of Co, Ni, C and O was confirmed. The increase in carbon amount is due to adsorption of substrate during the catalytic reaction.

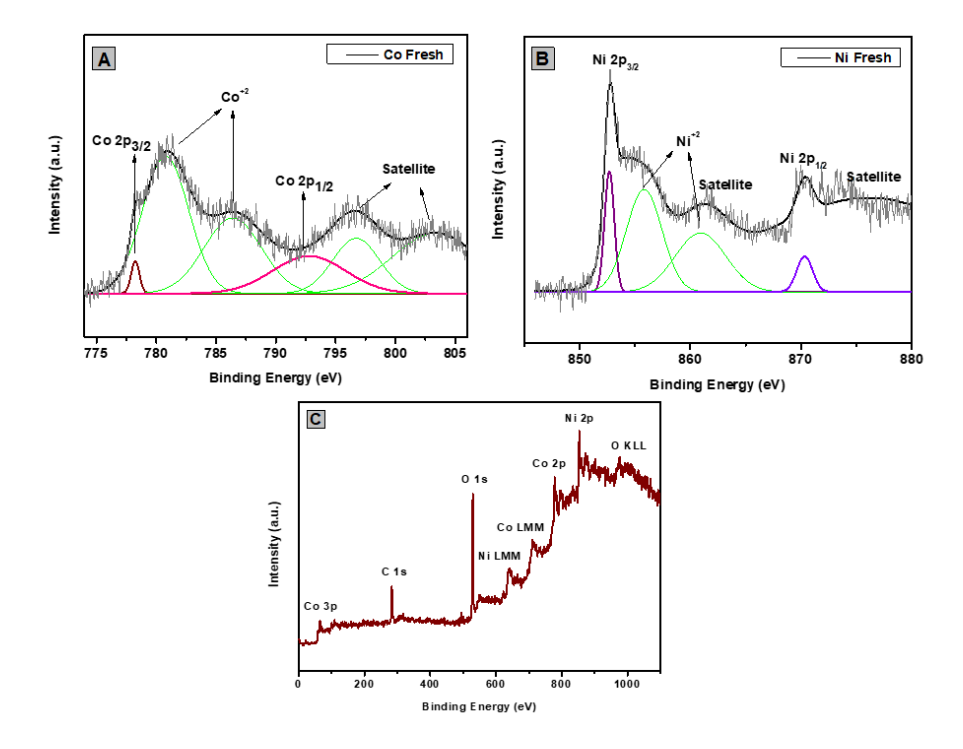


**Figure 3.10.** X-ray photoelectron spectroscopy analysis of (**A**) Co 2p, (**B**) Ni 2p and (**C**) survey scan of recovered CoNi nanoflowers.

Additionally, to check the sustainability of the catalyst after catalytic reaction we have performed the FE-SEM analysis of the recovered catalyst and the data shows that there were no significant changes observed in the morphology (**Figure 3.11**).

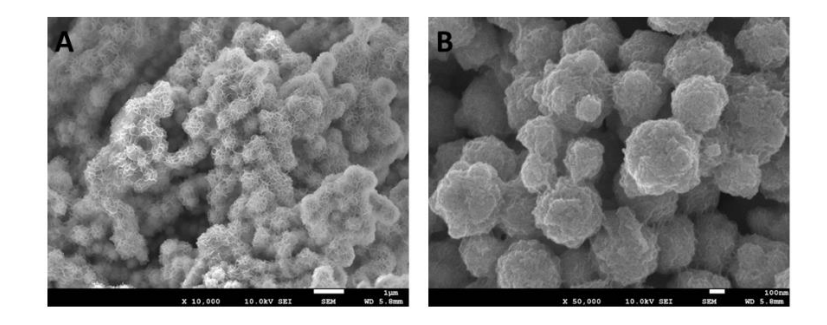


Figure 3.11. FE-SEM analysis of recycled CoNi nanoflower.

Additionally, the catalyst leaching was analysed using ICP-AES technique via hot filtration method.[39] For this, the reaction was carried out for 2 hours and then the catalyst was separated with magnet and the supernatant was filtered. The supernatant was proceed for further reaction for 10 hours and the sample was taken for GC-MS analysis. The GC-MS analysis data reveals that there was further conversion observed after removing the catalyst. The supernatant sample was also given for ICP-AES analysis to check the leaching of the catalyst and the data confirmed that there is no significant leaching was observed (**Table 3.4**).

**Table 3.4.** ICP-AES analysis of reaction mixture for leaching of CoNi nanoflower.

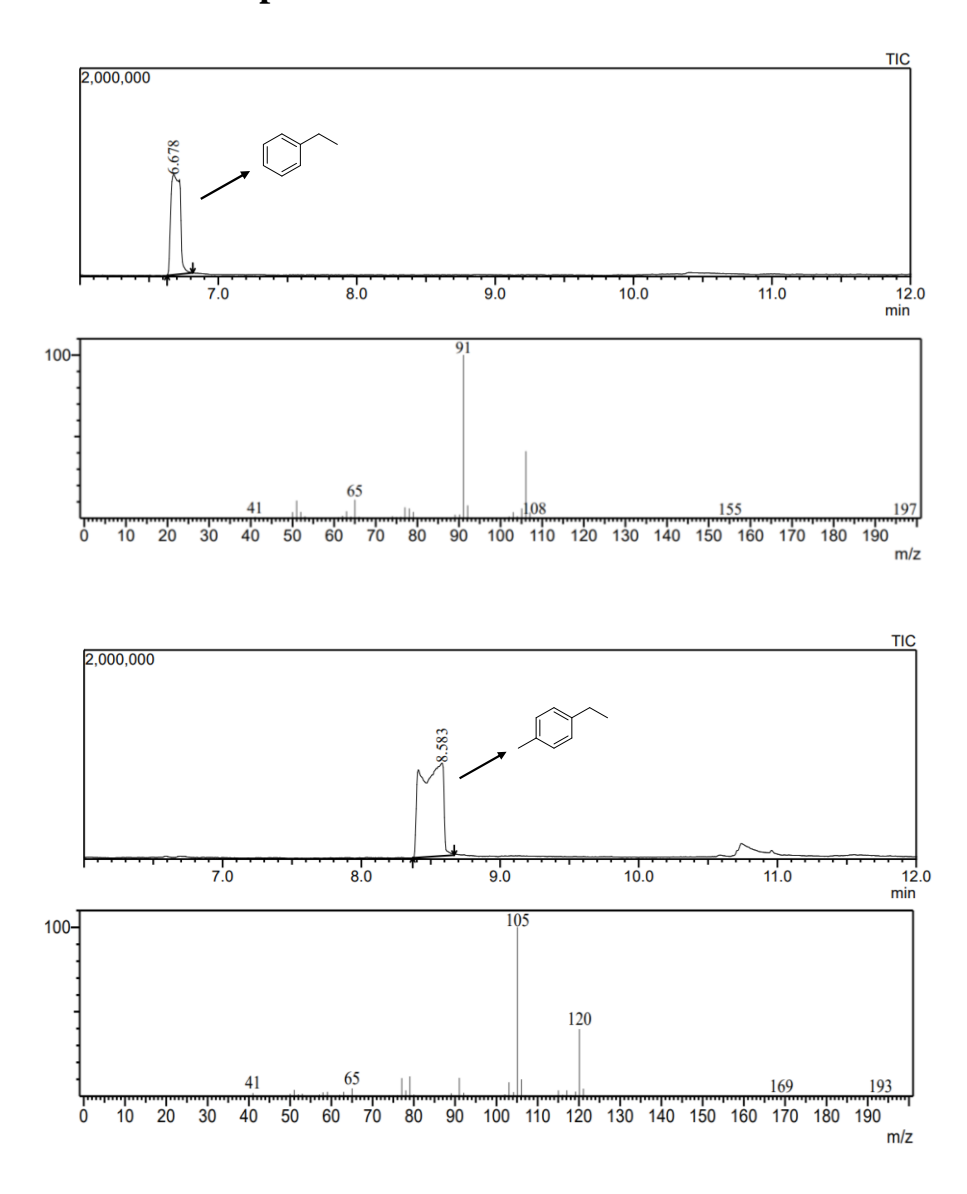
Sample	ICP-OES (mg/L)		
CoNi nanoflower	Со	Ni	
	0.027	0.012	

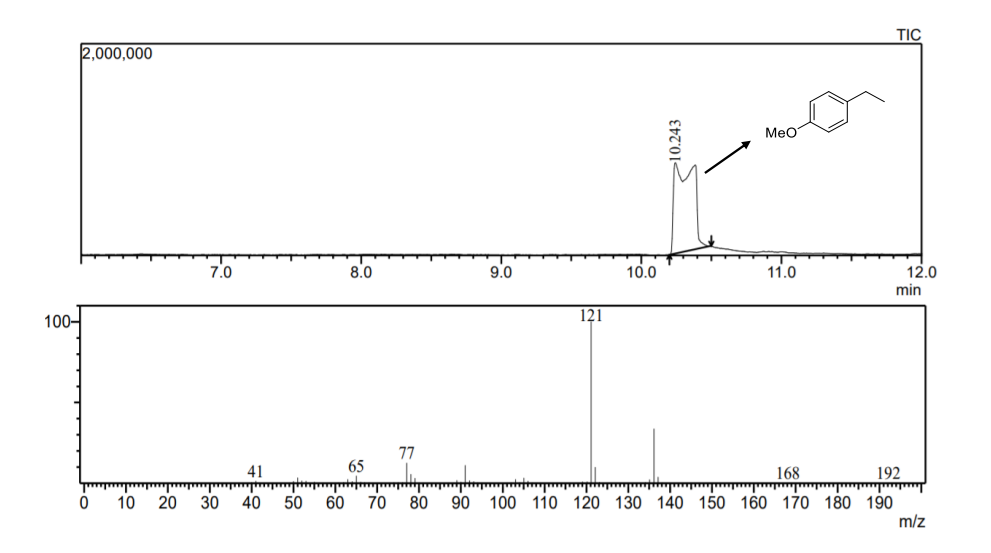
#### 3.4. Conclusions

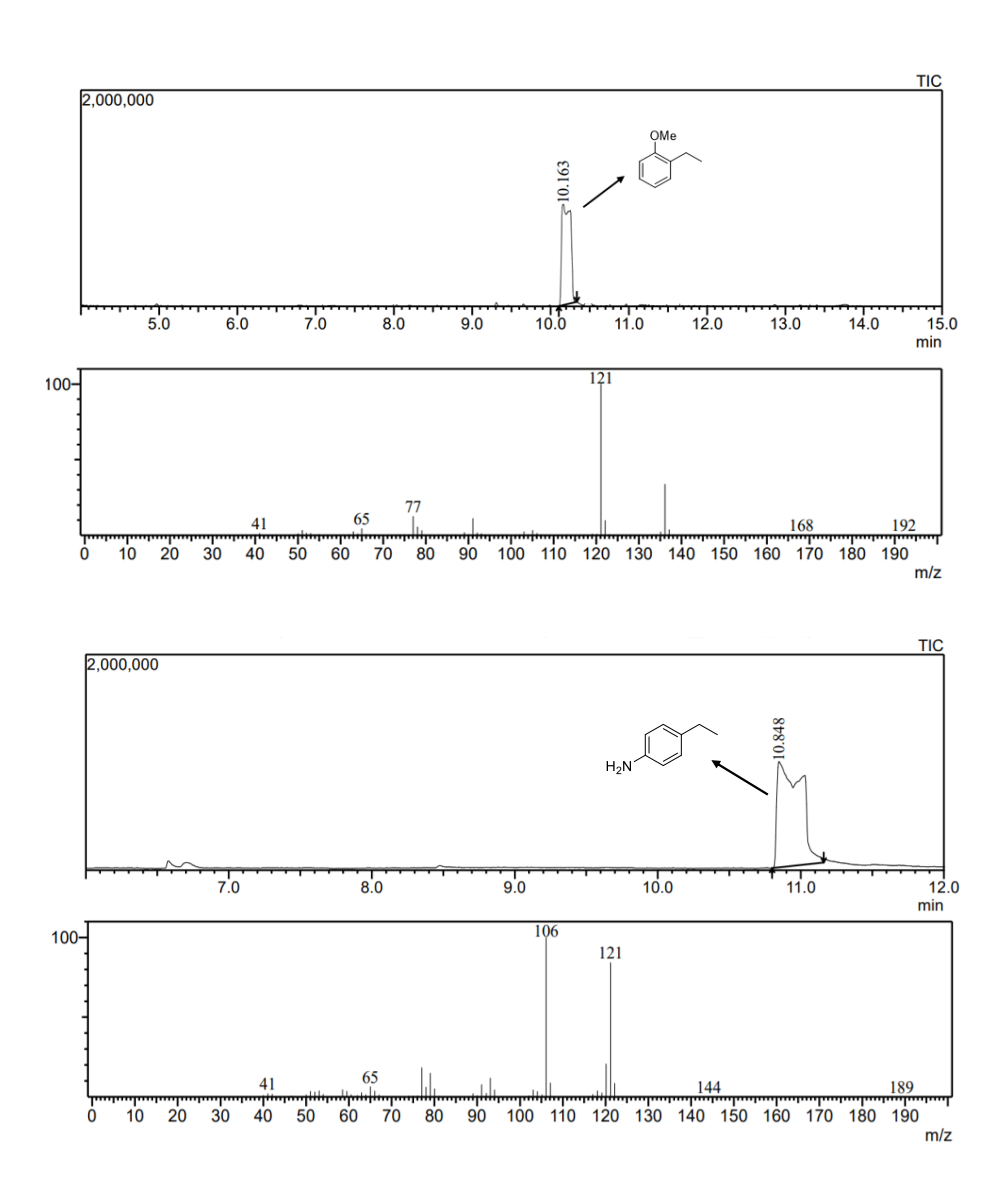
The bimetallic CoNi nanoflower prepared with facile liquid phase reduction method for catalytic hydrogenation of terminal alkynes. The preparation of CoNi nanoflowers was confirmed by X-ray diffraction technique. The flower shaped morphology was analysed by FE-SEM and TEM analysis. The synthesized nanoflowers showed excellent catalytic activity for transfer hydrogenation of alkyne (15 substrate) into alkane with 100% conversion and 100% selectivity with outstanding

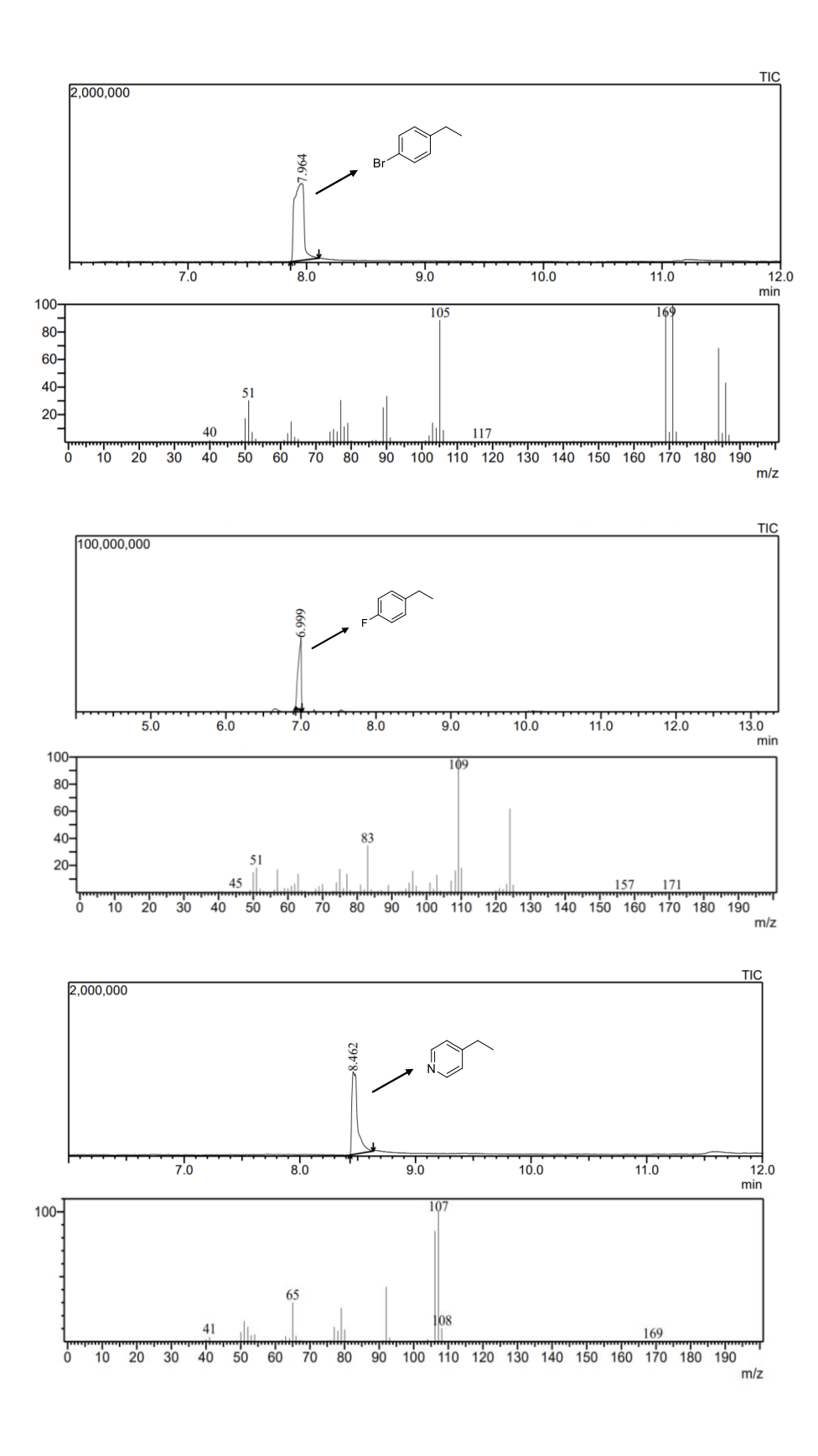
recyclability up to six cycles. Hence, the bimetallic CoNi nanoflower is easily synthesizable, cost-effective, magnetically separable, recyclable, and reusable material for catalysis.

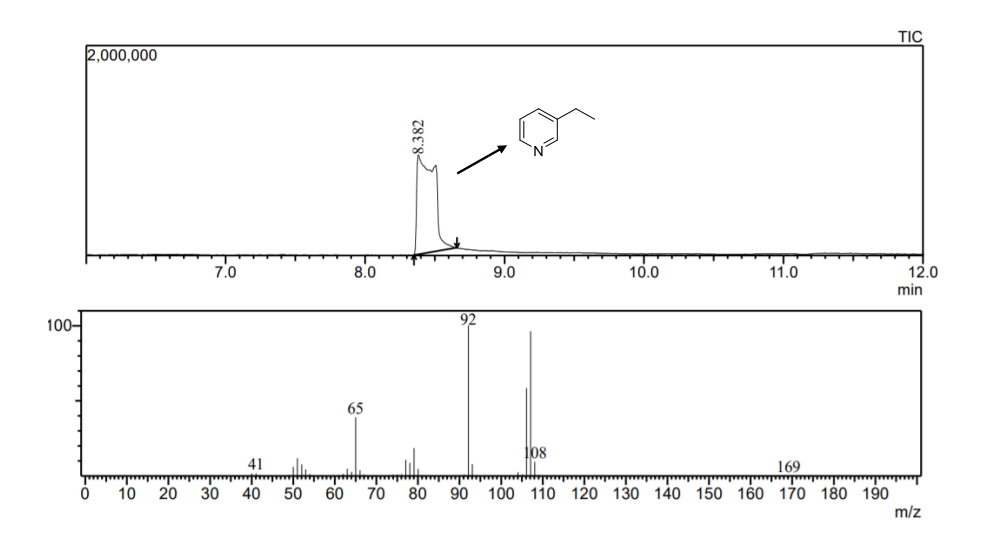
## **3.5.** GC-MS spectra of catalytic hydrogenation of all reactants and products

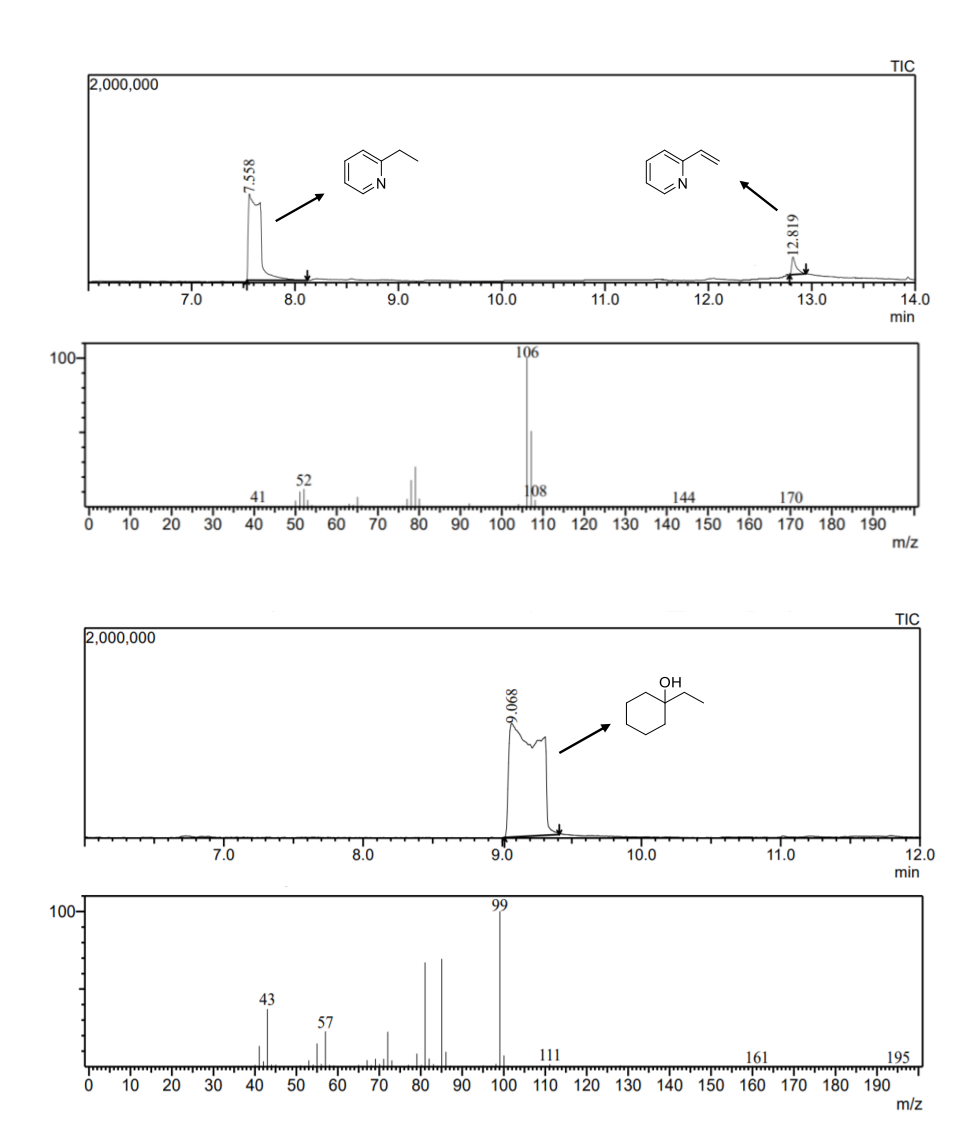


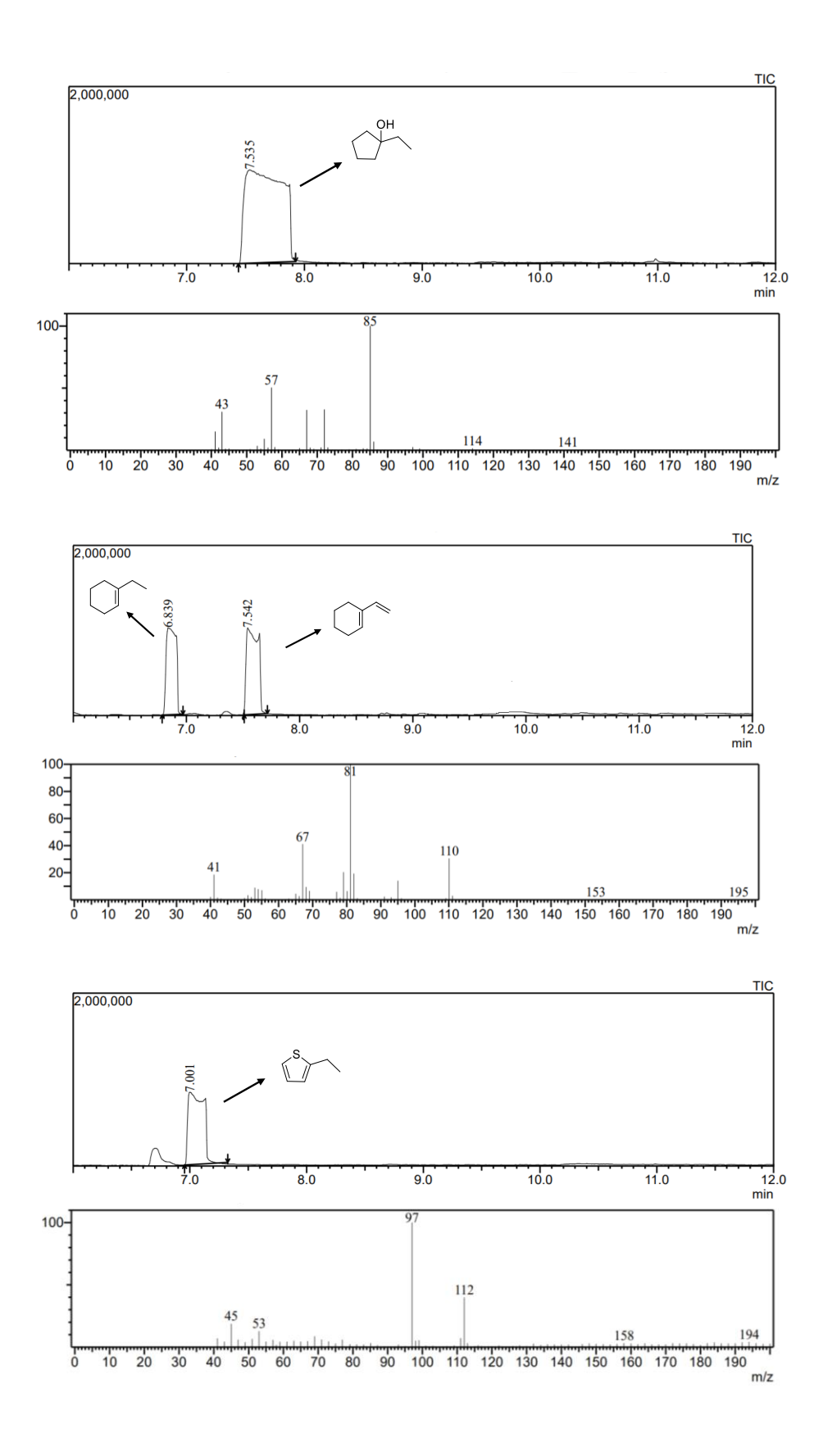












#### 3.6. References

- [1] S. Rana, J.P. Biswas, S. Paul, A. Paik, D. Maiti, Organic synthesis with the most abundant transition metal—iron: from rust to multitasking catalysts, Chem. Soc. Rev. 50 (2021) 243–472. https://doi.org/10.1039/D0CS00688B.
- [2] J.D. Hayler, D.K. Leahy, E.M. Simmons, A Pharmaceutical Industry Perspective on Sustainable Metal Catalysis, Organometallics. 38 (2019) 36–46. https://doi.org/10.1021/acs.organomet.8b00566.
- [3] P. Makkar, D. Gogoi, D. Roy, N.N. Ghosh, Dual-Purpose CuFe2O4-rGO-Based Nanocomposite for Asymmetric Flexible Supercapacitors and Catalytic Reduction of Nitroaromatic Derivatives, ACS Omega. 6 (2021) 28718–28728. https://doi.org/10.1021/acsomega.1c03377.
- [4] K. Sakthikumar, S. Rao Ede, S. Mishra, S. Kundu, Shape-selective synthesis of Sn(MoO 4 ) 2 nanomaterials for catalysis and supercapacitor applications, Dalton Trans. 45 (2016) 8897–8915. https://doi.org/10.1039/C6DT00208K.
- [5] N. Hussain, W. Yang, J. Dou, Y. Chen, Y. Qian, L. Xu, Ultrathin mesoporous F-doped  $\alpha$ -Ni(OH) 2 nanosheets as an efficient electrode material for water splitting and supercapacitors, J. Mater. Chem. A. 7 (2019) 9656–9664. https://doi.org/10.1039/C9TA01017C.
- [6] G. M. Tomboc, J. Kim, Y. Wang, Y. Son, J. Li, J. Young Kim, K. Lee, Hybrid layered double hydroxides as multifunctional nanomaterials for overall water splitting and supercapacitor applications, J. Mater. Chem. A. 9 (2021) 4528–4557. https://doi.org/10.1039/D0TA11606H.
- [7] S. Liu, K.S. Hui, K.N. Hui, Flower-like Copper Cobaltite Nanosheets on Graphite Paper as High-Performance Supercapacitor Electrodes and Enzymeless Glucose Sensors, ACS Appl. Mater. Interfaces. 8 (2016) 3258–3267. https://doi.org/10.1021/acsami.5b11001.
- [8] Z. Yao, G. Wang, Y. Shi, Y. Zhao, J. Jiang, Y. Zhang, H. Wang, One-step synthesis of nickel and cobalt phosphide nanomaterials via decomposition of hexamethylenetetramine-containing precursors, Dalton Trans. 44 (2015) 14122–14129. https://doi.org/10.1039/C5DT02319J.
- [9] M.B. Gawande, A. Goswami, F.-X. Felpin, T. Asefa, X. Huang, R. Silva, X. Zou, R. Zboril, R.S. Varma, Cu and Cu-Based Nanoparticles: Synthesis and Applications in Catalysis, Chem. Rev. 116 (2016) 3722–3811. https://doi.org/10.1021/acs.chemrev.5b00482.
- [10] I.-Y. Jeon, H.-J. Noh, J.-B. Baek, Nitrogen-Doped Carbon Nanomaterials: Synthesis, Characteristics and Applications, Chem. Asian J. 15 (2020) 2282–2293. https://doi.org/10.1002/asia.201901318.
- [11] J. Takaya, Catalysis using transition metal complexes featuring main group metal and metalloid compounds as supporting ligands,

- Chem. Sci. 12 (2021) 1964–1981. https://doi.org/10.1039/D0SC04238B.
- [12] H.-L. Jiang, Q. Xu, Recent progress in synergistic catalysis over heterometallic nanoparticles, J. Mater. Chem. 21 (2011) 13705–13725. https://doi.org/10.1039/C1JM12020D.
- [13] I. Mustieles Marin, J.M. Asensio, B. Chaudret, Bimetallic Nanoparticles Associating Noble Metals and First-Row Transition Metals in Catalysis, ACS Nano. 15 (2021) 3550–3556. https://doi.org/10.1021/acsnano.0c09744.
- [14] M. Zhou, C. Li, J. Fang, Noble-Metal Based Random Alloy and Intermetallic Nanocrystals: Syntheses and Applications, Chem. Rev. 121 (2021) 736–795. https://doi.org/10.1021/acs.chemrev.0c00436.
- [15] M. Liu, Z. Zhang, F. Okejiri, S. Yang, S. Zhou, S. Dai, Entropy-Maximized Synthesis of Multimetallic Nanoparticle Catalysts via a Ultrasonication-Assisted Wet Chemistry Method under Ambient Conditions, Adv. Mater. Interfaces. 6 (2019) 1900015. https://doi.org/10.1002/admi.201900015.
- [16] J. Govan, Y.K. Gun'ko, Recent Advances in the Application of Magnetic Nanoparticles as a Support for Homogeneous Catalysts, Nanomaterials. 4 (2014) 222–241. https://doi.org/10.3390/nano4020222.
- [17] D.C. Blakemore, L. Castro, I. Churcher, D.C. Rees, A.W. Thomas, D.M. Wilson, A. Wood, Organic synthesis provides opportunities to transform drug discovery, Nat. Chem. 10 (2018) 383–394. https://doi.org/10.1038/s41557-018-0021-z.
- [18] R. Nie, M. Miao, W. Du, J. Shi, Y. Liu, Z. Hou, Selective hydrogenation of CC bond over N-doped reduced graphene oxides supported Pd catalyst, Appl. Catal. B Environ. 180 (2016) 607–613. https://doi.org/10.1016/j.apcatb.2015.07.015.
- [19] X. Li, Y. Pan, H. Yi, J. Hu, D. Yang, F. Lv, W. Li, J. Zhou, X. Wu, A. Lei, L. Zhang, Mott–Schottky Effect Leads to Alkyne Semihydrogenation over Pd-Nanocube@N-Doped Carbon, ACS Catal. 9 (2019) 4632–4641. https://doi.org/10.1021/acscatal.9b01001.
- [20] S.-L. Hou, J. Dong, Z.-H. Zhu, L.-C. Geng, Y. Ma, B. Zhao, Size-Tunable Ultrafine Pt Nanoparticles in Soluble Metal—Organic Cages: Displaying Highly Stereoselective Hydrogenation of  $\alpha$ -Pinene, Chem. Mater. 32 (2020) 7063–7069. https://doi.org/10.1021/acs.chemmater.0c02845.
- [21] L. Xia, D. Li, J. Long, F. Huang, L. Yang, Y. Guo, Z. Jia, J. Xiao, H. Liu, N-doped graphene confined Pt nanoparticles for efficient semi-hydrogenation of phenylacetylene, Carbon. 145 (2019) 47–52. https://doi.org/10.1016/j.carbon.2019.01.014.
- [22] T. Mitsudome, M. Yamamoto, Z. Maeno, T. Mizugaki, K. Jitsukawa, K. Kaneda, One-step Synthesis of Core-Gold/Shell-Ceria Nanomaterial and Its Catalysis for Highly Selective Semihydrogenation of Alkynes, J. Am. Chem. Soc. 137 (2015) 13452–13455. https://doi.org/10.1021/jacs.5b07521.

- [23] K. Su, Y. Wang, C. Zhang, Z. Gao, J. Han, F. Wang, Tuning the Pt species on Nb2O5 by support-induced modification in the photocatalytic transfer hydrogenation of phenylacetylene, Appl. Catal. B Environ. 298 (2021) 120554. https://doi.org/10.1016/j.apcatb.2021.120554.
- [24] Y. Qin, J. Lu, Z. Zou, H. Hong, Y. Li, Y. Li, L. Chen, J. Hu, Y. Huang, Metal-free chemoselective hydrogenation of unsaturated carbon–carbon bonds via cathodic reduction, Org. Chem. Front. 7 (2020) 1817–1822. https://doi.org/10.1039/D0QO00547A.
- [25] J.-W. Yu, X.-Y. Wang, C.-Y. Yuan, W.-Z. Li, Y.-H. Wang, Y.-W. Zhang, Synthesis of ultrathin Ni nanosheets for semihydrogenation of phenylacetylene to styrene under mild conditions, Nanoscale. 10 (2018) 6936–6944. https://doi.org/10.1039/C8NR00532J.
- [26] A.M. López-Vinasco, L.M. Martínez-Prieto, J.M. Asensio, P. Lecante, B. Chaudret, J. Cámpora, P.W.N.M. van Leeuwen, Novel nickel nanoparticles stabilized by imidazolium-amidinate ligands for selective hydrogenation of alkynes, Catal. Sci. Technol. 10 (2020) 342–350. https://doi.org/10.1039/C9CY02172H.
- [27] A. Dhakshinamoorthy, S. Navalon, D. Sempere, M. Alvaro, H. Garcia, Reduction of alkenes catalyzed by copper nanoparticles supported on diamond nanoparticles, Chem. Commun. 49 (2013) 2359–2361. https://doi.org/10.1039/C3CC39011J.
- [28] X. Zhang, H. Lin, J. Zhang, Y. Qiu, Z. Zhang, Q. Xu, G. Meng, W. Yan, L. Gu, L. Zheng, D. Wang, Y. Li, Decreasing Coordinated N Atoms in Single-Atom Cu Catalyst to Achieve Selective Transfer Hydrogenation of Alkynes, Chem. Sci. (2021). https://doi.org/10.1039/D1SC04344G.
- [29] H. Alawisi, H.D. Arman, Z.J. Tonzetich, Catalytic Hydrogenation of Alkenes and Alkynes by a Cobalt Pincer Complex: Evidence of Roles for Both Co(I) and Co(II), Organometallics. 40 (2021) 1062–1070. https://doi.org/10.1021/acs.organomet.1c00053.
- [30] J. Mondal, K. Truc Nguyen, A. Jana, K. Kurniawan, P. Borah, Y. Zhao, A. Bhaumik, Efficient alkene hydrogenation over a magnetically recoverable and recyclable Fe 3 O 4 @GO nanocatalyst using hydrazine hydrate as the hydrogen source, Chem. Commun. 50 (2014) 12095–12097. https://doi.org/10.1039/C4CC04770B.
- [31] R.B.N. Baig, S. Verma, R.S. Varma, M.N. Nadagouda, Magnetic Fe@g-C3N4: A Photoactive Catalyst for the Hydrogenation of Alkenes and Alkynes, ACS Sustain. Chem. Eng. 4 (2016) 1661–1664. https://doi.org/10.1021/acssuschemeng.5b01610.
- [32] V.A. Bharathan, R. Jain, C.S. Gopinath, C.P. Vinod, Diverse reactivity trends of Ni surfaces in Au@Ni core—shell nanoparticles probed by near ambient pressure (NAP) XPS, Catal. Sci. Technol. 7 (2017) 4489–4498. https://doi.org/10.1039/C7CY01070B.
- [33] V. Polshettiwar, B. Baruwati, R.S. Varma, Nanoparticle-supported and magnetically recoverable nickel catalyst: a robust and economic hydrogenation and transfer hydrogenation protocol, Green Chem. 11 (2009) 127–131. https://doi.org/10.1039/B815058C.

- [34] A.V. Nikam, A.A. Kulkarni, B.L.V. Prasad, Microwave-Assisted Batch and Continuous Flow Synthesis of Palladium Supported on Magnetic Nickel Nanocrystals and Their Evaluation as Reusable Catalyst, Cryst. Growth Des. 17 (2017) 5163–5169. https://doi.org/10.1021/acs.cgd.7b00639.
- [35] Z. Dağalan, S. Behboudikhiavi, M. Turgut, M. Sevim, A. Emre Kasapoğlu, B. Nişancı, Ö. Metin, Nickel-palladium alloy nanoparticles supported on reduced graphene oxide decorated with metallic aluminum nanoparticles (Al-rGO/NiPd): a multifunctional catalyst for the transfer hydrogenation of nitroarenes and olefins using water as a hydrogen source, Inorg. Chem. Front. 8 (2021) 2200–2212. https://doi.org/10.1039/D0QI01363C.
- [36] Y. Ito, H. Ohta, Y.M. A. Yamada, T. Enoki, Y. Uozumi, Transfer hydrogenation of alkenes using Ni/Ru/Pt/Au heteroquatermetallic nanoparticle catalysts: sequential cooperation of multiple nanometal species, Chem. Commun. 50 (2014) 12123–12126. https://doi.org/10.1039/C4CC04559A.
- [37] D. Delgado, F. Bizzotto, A. Zana, M. Arenz, Accelerated Durability Test for High-Surface-Area Oxyhydroxide Nickel Supported on Raney Nickel as Catalyst for the Alkaline Oxygen Evolution Reaction, ChemPhysChem. 20 (2019) 3147–3153. https://doi.org/10.1002/cphc.201900195.
- [38] N. Mahata, A.F. Cunha, J.J.M. Órfão, J.L. Figueiredo, Highly selective hydrogenation of CC double bond in unsaturated carbonyl compounds over NiC catalyst, Chem. Eng. J. 188 (2012) 155–159. https://doi.org/10.1016/j.cej.2012.01.127.
- [39] N. Choudhary, T. Ghosh, S.M. Mobin, Ketone Hydrogenation by Using ZnO–Cu(OH)Cl/MCM-41 with a Splash of Water: An Environmentally Benign Approach, Chem. Asian J. 15 (2020) 1339–1348. https://doi.org/10.1002/asia.201901610.
- [40] G. Zhang, S.K. Hanson, Cobalt-catalyzed transfer hydrogenation of CO and CN bonds, Chem. Commun. 49 (2013) 10151–10153. https://doi.org/10.1039/C3CC45900D.
- [41] G. A. Filonenko, R. van Putten, E.J. M. Hensen, E. A. Pidko, Catalytic (de)hydrogenation promoted by non-precious metals Co, Fe and Mn: recent advances in an emerging field, Chem. Soc. Rev. 47 (2018) 1459–1483. https://doi.org/10.1039/C7CS00334J.
- [42] G.M. Richardson, I. Douair, S.A. Cameron, J. Bracegirdle, R.A. Keyzers, M.S. Hill, L. Maron, M.D. Anker, Hydroarylation of olefins catalysed by a dimeric ytterbium(II) alkyl, Nat. Commun. 12 (2021) 3147. https://doi.org/10.1038/s41467-021-23444-x.
- [43] D. Wang, D. Astruc, The Golden Age of Transfer Hydrogenation, Chem. Rev. 115 (2015) 6621–6686. https://doi.org/10.1021/acs.chemrev.5b00203.
- [44] N. Chen, J.-T. Jiang, C.-Y. Xu, S.-J. Yan, L. Zhen, Rational Construction of Uniform CoNi-Based Core-Shell Microspheres with Tunable Electromagnetic Wave Absorption Properties, Sci. Rep. 8 (2018) 3196. https://doi.org/10.1038/s41598-018-21047-z.

- [45] D. Wang, Y. Li, Bimetallic Nanocrystals: Liquid-Phase Synthesis and Catalytic Applications, Adv. Mater. 23 (2011) 1044–1060. https://doi.org/10.1002/adma.201003695.
- [46] M.Y. Rafique, L. Pan, W.S. Khan, M.Z. Iqbal, H. Qiu, M.H. Farooq, M. Ellahi, Z. Guo, Controlled synthesis, phase formation, growth mechanism, and magnetic properties of 3-D CoNi alloy microstructures composed of nanorods, CrystEngComm. 15 (2013) 5314–5325. https://doi.org/10.1039/C3CE40385H.
- [47] H.-B. Zhao, J.-B. Cheng, J.-Y. Zhu, Y.-Z. Wang, Ultralight CoNi/rGO aerogels toward excellent microwave absorption at ultrathin thickness, J. Mater. Chem. C. 7 (2019) 441–448. https://doi.org/10.1039/C8TC05239E.
- [48] B. Quan, X. Liang, G. Ji, Y. Zhang, G. Xu, Y. Du, Cross-Linking-Derived Synthesis of Porous CoxNiy/C Nanocomposites for Excellent Electromagnetic Behaviors, ACS Appl. Mater. Interfaces. 9 (2017) 38814–38823. https://doi.org/10.1021/acsami.7b13411.
- [49] Y. Ling, M. Zhang, J. Zheng, J. Xu, T. Hayat, N. S. Alharbi, Formation of uniform magnetic C@CoNi alloy hollow hybrid composites with excellent performance for catalysis and protein adsorption, Dalton Trans. 47 (2018) 7839–7847. https://doi.org/10.1039/C8DT01480A.
- [50] Z. Xia, L. Niu, Y. An, G. Bian, T. Li, G. Bai, Ni–Al/CoOxcatalyzed hydrodeoxygenation of 5-hydroxymethylfurfural into 2,5-dimethylfuran at low temperatures without external hydrogen, Green Chem. (2021). https://doi.org/10.1039/D1GC02758A.
- [51] M. A. Małecka, P. Woźniak, Hierarchical macroparticles of ceria with tube-like shape synthesis and properties, CrystEngComm. (2021). https://doi.org/10.1039/D1CE00755F.
- [52] N. Li, Z.-W. Zhang, J.-N. Zhang, Y. Ma, X.-Y. Chen, Y. Fan, Size modulation of MIL-125 nanocrystals to promote the catalytic performance towards oxidative desulfurization, Dalton Trans. 50 (2021) 6506–6511. https://doi.org/10.1039/D1DT00774B.
- [53] M.C. Arno, M. Inam, A.C. Weems, Z. Li, A.L.A. Binch, C.I. Platt, S.M. Richardson, J.A. Hoyland, A.P. Dove, R.K. O'Reilly, Exploiting the role of nanoparticle shape in enhancing hydrogel adhesive and mechanical properties, Nat. Commun. 11 (2020) 1420. https://doi.org/10.1038/s41467-020-15206-y.
- [54] Y. Yin, Y. Xiao, G. Lin, Q. Xiao, Z. Lin, Z. Cai, An enzyme—inorganic hybrid nanoflower based immobilized enzyme reactor with enhanced enzymatic activity, J. Mater. Chem. B. 3 (2015) 2295–2300. https://doi.org/10.1039/C4TB01697A.
- [55] L. Zhang, Y. Zhu, A review of controllable synthesis and enhancement of performances of bismuth tungstate visible-light-driven photocatalysts, Catal. Sci. Technol. 2 (2012) 694–706. https://doi.org/10.1039/C2CY00411A.
- [56] Y. Imura, R. Akiyama, S. Furukawa, R. Kan, C. Morita-Imura, T. Komatsu, T. Kawai, Au–Ag Nanoflower Catalysts with Clean Surfaces for Alcohol Oxidation, Chem. Asian J. 14 (2019) 547–552. https://doi.org/10.1002/asia.201801711.

- [57] A. Prabakaran, F. Dillon, J. Melbourne, L. Jones, R.J. Nicholls, P. Holdway, J. Britton, A.A. Koos, A. Crossley, P.D. Nellist, N. Grobert, WS2 2D nanosheets in 3D nanoflowers, Chem. Commun. 50 (2014) 12360–12362. https://doi.org/10.1039/C4CC04218B.
- [58] M. Fang, G. Dong, R. Wei, J.C. Ho, Hierarchical Nanostructures: Design for Sustainable Water Splitting, Adv. Energy Mater. 7 (2017) 1700559. https://doi.org/10.1002/aenm.201700559.
- [59] L. Zhou, W. Wang, H. Xu, S. Sun, M. Shang, Bi2O3 Hierarchical Nanostructures: Controllable Synthesis, Growth Mechanism, and their Application in Photocatalysis, Chem. Eur. J. 15 (2009) 1776–1782. https://doi.org/10.1002/chem.200801234.
- [60] L. Zhang, Z.-S. Wang, Enhancing the Performance of Dye-Sensitized Solar Cells with a Gold-Nanoflowers Box, Chem. Asian J. 11 (2016) 3283–3289. https://doi.org/10.1002/asia.201601228.
- [61] X. Zhang, F. Yan, S. Zhang, H. Yuan, C. Zhu, X. Zhang, Y. Chen, Hollow N-Doped Carbon Polyhedron Containing CoNi Alloy Nanoparticles Embedded within Few-Layer N-Doped Graphene as High-Performance Electromagnetic Wave Absorbing Material, ACS Appl. Mater. Interfaces. 10 (2018) 24920–24929. https://doi.org/10.1021/acsami.8b07107.
- [62] S. Khorsand, K. Raeissi, F. Ashrafizadeh, M.A. Arenas, Superhydrophobic nickel—cobalt alloy coating with micro-nano flower-like structure, Chem. Eng. J. 273 (2015) 638–646. https://doi.org/10.1016/j.cej.2015.03.076.
- [63] Y. Feng, X.-Y. Yu, U. Paik, Nickel cobalt phosphides quasi-hollow nanocubes as an efficient electrocatalyst for hydrogen evolution in alkaline solution, Chem. Commun. 52 (2016) 1633–1636. https://doi.org/10.1039/C5CC08991C.
- [64] Y. Hou, Z. Wen, S. Cui, S. Ci, S. Mao, J. Chen, An Advanced Nitrogen-Doped Graphene/Cobalt-Embedded Porous Carbon Polyhedron Hybrid for Efficient Catalysis of Oxygen Reduction and Water Splitting, Adv. Funct. Mater. 25 (2015) 872–882. https://doi.org/10.1002/adfm.201403657.
- [65] F. Chen, J. Ding, K. Guo, L. Yang, Z. Zhang, Q. Yang, Y. Yang, Z. Bao, Y. He, Q. Ren, CoNi Alloy Nanoparticles Embedded in Metal–Organic Framework-Derived Carbon for the Highly Efficient Separation of Xenon and Krypton via a Charge-Transfer Effect, Angew. Chem. Int. Ed. 60 (2021) 2431–2438. https://doi.org/10.1002/anie.202011778.
- [66] M.C. Biesinger, B.P. Payne, A.P. Grosvenor, L.W.M. Lau, A.R. Gerson, R.St.C. Smart, Resolving surface chemical states in XPS analysis of first row transition metals, oxides and hydroxides: Cr, Mn, Fe, Co and Ni, Appl. Surf. Sci. 257 (2011) 2717–2730. https://doi.org/10.1016/j.apsusc.2010.10.051.
- [67] H. Zhang, Y. Lu, C.-D. Gu, X.-L. Wang, J.-P. Tu, Ionothermal synthesis and lithium storage performance of core/shell structured amorphous@crystalline Ni–P nanoparticles, CrystEngComm. 14 (2012) 7942–7950. https://doi.org/10.1039/C2CE25939G.

- [68] X. Feng, Y. Huang, C. Li, X. Chen, S. Zhou, X. Gao, C. Chen, Controllable synthesis of porous NiCo2O4/NiO/Co3O4 nanoflowers for asymmetric all-solid-state supercapacitors, Chem. Eng. J. 368 (2019) 51–60. https://doi.org/10.1016/j.cej.2019.02.191.
- [69] A.K. Kar, R. Srivastava, An efficient and sustainable catalytic reduction of carbon–carbon multiple bonds, aldehydes, and ketones using a Cu nanoparticle decorated metal organic framework, New J. Chem. 42 (2018) 9557–9567. https://doi.org/10.1039/C8NJ01704B.
- [70] A.B. Vysakh, A. Lazar, V. Yadukiran, A.P. Singh, C.P. Vinod, Phenylacetylene hydrogenation on Au@Ni bimetallic core–shell nanoparticles synthesized under mild conditions, Catal. Sci. Technol. 6 (2016) 708–712. https://doi.org/10.1039/C5CY02005K.
- [71] Z. Luo, R. Nie, V.T. Nguyen, A. Biswas, R.K. Behera, X. Wu, T. Kobayashi, A. Sadow, B. Wang, W. Huang, L. Qi, Transition metal-like carbocatalyst, Nat. Commun. 11 (2020) 4091. https://doi.org/10.1038/s41467-020-17909-8.
- [72] A.A. Kassie, C.R. Wade, Catalytic Activity of a Zr MOF Containing POCOP-Pd Pincer Complexes, Organometallics. 39 (2020)
   https://doi.org/10.1021/acs.organomet.0c00164.
- [73] J. Lin, J. Chen, W. Su, Rhodium-Cobalt Bimetallic Nanoparticles: A Catalyst for Selective Hydrogenation of Unsaturated Carbon-Carbon Bonds with Hydrous Hydrazine, Adv. Synth. Catal. 355 (2013) 41–46. https://doi.org/10.1002/adsc.201200576.
- [74] C. Zhang, J. Lu, M. Li, Y. Wang, Z. Zhang, H. Chen, F. Wang, Transfer hydrogenation of nitroarenes with hydrazine at near-room temperature catalysed by a MoO2 catalyst, Green Chem. 18 (2016) 2435–2442. https://doi.org/10.1039/C5GC02460A.
- [75] K.J. Datta, K.K.R. Datta, M.B. Gawande, V. Ranc, K. Čépe, V. Malgras, Y. Yamauchi, R.S. Varma, R. Zboril, Pd@Pt Core-Shell Nanoparticles with Branched Dandelion-like Morphology as Highly Efficient Catalysts for Olefin Reduction, Chem. Eur. J. 22 (2016) 1577–1581. https://doi.org/10.1002/chem.201503441.
- [76] A. Dhakshinamoorthy, S. Navalon, D. Sempere, M. Alvaro, H. Garcia, Reduction of alkenes catalyzed by copper nanoparticles supported on diamond nanoparticles, Chem. Commun. 49 (2013) 2359–2361. https://doi.org/10.1039/C3CC39011J.
- [77] H. Yang, J. Ouyang, A. Tang, Single Step Synthesis of High-Purity CoO Nanocrystals, J. Phys. Chem. B. 111 (2007) 8006–8013. https://doi.org/10.1021/jp070711k.
- [78] J. Yan, Y. Huang, Y. Yan, L. Ding, P. Liu, High-Performance Electromagnetic Wave Absorbers Based on Two Kinds of Nickel-Based MOF-Derived Ni@C Microspheres, ACS Appl. Mater. Interfaces. 11 (2019) 40781–40792. https://doi.org/10.1021/acsami.9b12850.

#### **CHAPTER 4**

# Conversion of Biomass-Derived Aldehydes using Environmentally Benign CuNi nanocatalyst

#### 4.1. Introduction

Biomass is derived from plant or animal-based material that can directly be used as fuel to produce heat via combustion or electricity.[1] To satisfy the energy demand, the development of sustainable renewable energy sources is need of an hour due to the depletion of fossil fuels.[2] Also, the use of non-renewable fossil fuels increases greenhouse gas emissions and leads to climate change. However, more than 80% of energy demand is mainly fulfilled from non-renewable fossil fuels. For this purpose, biomassderived materials can be used as an alternative to non-renewable fossil fuels. Plants and crops capture around 1% solar energy in the form of complex molecules via photosynthesis, such as lignin, cellulose, hemicellulose and carbohydrates.[3,4] Furfural is a lignocellulosic biomass-derived platform molecule that can be converted into value-added chemicals for energy usage or biofuel precursors.[5,6] Since furfuryl alcohol is an essential intermediate of the drug, resin and adhesive synthesis, the selective conversion of furfural to furfuryl alcohol is an important step in industrial applications.[7–9] The presence of C=C bond and C=O bond in the furan ring decrease the selectivity of hydrogenation of only C=O bond. The side products from hydrogenolysis of C-O/C=C bonds were obtained; hence, the selective hydrogenation of furan-based compounds like furfural and 5-(hydroxymethyl) furfural (HMF) has great importance. The furfuryl alcohol, further via hydrolysis, can be converted into levulinic acid and later reduced into γ-valerolactone (GVL), which is considered a valuable platform molecule for the production of biofuels.[10] Hence, the selective conversion of furfural

into furfuryl alcohol is an important pathway for the production of biofuels. Although, selective hydrogenation have been reported by using various homogeneous and heterogeneous catalysts such as Pt[11,12] Pd[12,13], Ru[14,15], Rh[16], Ir[17] based noble metal catalysts.

However, some major drawbacks of homogeneous catalysis such as over hydrogenation, unselective C–C cleavage, and use of flammable H<sub>2</sub> with high pressure and temperature are entailed, which may result in the decrease of selectivity toward targeted products as well as increased production cost, moisture sensitivity and non-recyclability.[18,19] In this context, the use of nanoparticles as heterogeneous catalysts is the best choice which is generally recyclable and reusable. Also, the process cost decreases when non-noble metal catalysts are used. Also, the size and shape tuning of the nanoparticles can increase the activity, selectivity, and stability.[20,21]

Moreover, several reports use monometallic and bimetallic nanocatalysts like Pt, Cu-Co[22], Cu/Cu<sub>2</sub>O-MC[23], nanoporous carbon[24], Cu-Fe[25], Ni-Fe[26] and Cu-, Ni-based catalysts for selective hydrogenation of furfural.[27] Additionally, supported CuNi metal oxides and alloys were reported for hydrogenation of furfural into tetrahydrofurfuryl alcohol (THFA), 2-methyl furan and furfuryl alcohol (FOL).[28–30] These reports indicate that for hydrogenation of furfural, the Cu and Ni metal show excellent activities, but the selectivity towards furfuryl alcohol is the primary concern with lower reaction temperature. However, it was reported that Ni-based catalyst showed greater activity for hydrogenation reactions.[31] Keeping this in mind, we synthesized CuNi bimetallic nanoparticles for the selective hydrogenation of furfural into furfuryl alcohol.

The hydrogenation of furfural is mainly reported with the use of highly flammable hydrogen gas at high temperatures. For a safer approach, the utilization of hydrogen gas as a hydrogenation source is avoided. In this concern, the use of alcohols for transfer hydrogenation is clean, cheap, environmentally benign and sustainable as removal of these alcohols is easy after reaction completion.[32] Moreover, the reported work of hydrogenation of furfural with alcohol like 2-propanol and 2-butyl alcohol performed at very high temperature like 180-230 °C with more reaction time.[33–36] Therefore, we utilized less amount of base for activation of the same to decrease the reaction time and increase the selectivity with lower temperature.

Herein, we report bimetallic, recyclable, magnetically separable CuNi-12 nanocatalyst (1:2 molar ratio of Cu: Ni) for the selective hydrogenation of furfural into furfuryl alcohol with the use of potassium hydroxide as base and 2-propanol as a hydrogen source. The synthesized nanocatalyst is a highly efficient catalyst for the hydrogenation of aldehydes and ketones with almost 100% conversion and 100% selectivity toward the corresponding alcohol product. The synergistic effect between the existing metal was also observed in the case of monometallic Cu and monometallic Ni. It was reported that the heterometallic nanocatalysts show greater efficiency and catalytic activity than their monometallic nanocatalysts.[22,37] The observed conversion of furfural into furfuryl alcohol is higher in the case of bimetallic CuNi nanocatalyst than monometallic Cu and Ni. The results are promising and provide an environmentally benign, sustainable and cost-effective pathway for the hydrogenation of biomass-derived aldehydes.

#### 4.2. Experimental

#### 4.2.1. Materials

Cetyl trimethyl ammonium bromide (CTAB) ≥99% pure, copper chloride (CuCl<sub>2</sub>) anhydrous ≥99.99% pure, and nickel chloride hexahydrate (NiCl<sub>2</sub>.6H<sub>2</sub>O) ≥99.9% pure were purchased from Merck, India. Hydrazine hydrate (N<sub>2</sub>H<sub>4</sub>.H<sub>2</sub>O) 80% in water, sodium hydroxide pellets (NaOH) 98% pure, KOH 100% pure, and aldehyde compounds ≥98-100% pure were purchased from Sigma-Aldrich. All solvents were used as received.

#### 4.2.2. Catalyst preparation

For synthesizing CuNi-12 nanocatalyst, the copper chloride and nickel chloride was used as precursor metal salts in deionized water at room temperature, as shown in Scheme 4.1. Initially, 72 mg of CTAB was dissolved into 100 mL of deionized water, and then 0.49 g copper chloride and 1.51 g nickel chloride were added to the above mixture of CTAB in round bottom flask stirred the mixture for 1 hour. The CTAB is used as surfacant and capping agent which control the shape of the nanoparticles by reducing the surface tension. After the formation of the homogeneous mixture, 10 mL of hydrazine hydrate was added and the reaction mixture was stirred for 1 hour. Further, the required amount of NaOH solution was added to maintain the pH at 12 as well to ensure the formation and stir the mixture for the next 1 hour. Here, the addition of NaOH is required as there is no nanoparticles formed with the only use of hydrazine hydrate. So, the NaOH plays an important role to maintain the pH as well as to accelarete the reaction. Additionally, the reaction between hydrazine hydrate, metal ions and NaOH provide inert atmosphere to the reaction by releasing nitrogen gas as shown below:[38]

$$Ni^{2+} + Cu^{2+} + N_2H_2 + OH^-$$
 Ni + Cu + N<sub>2</sub> + H<sub>2</sub>O

The black color magnetic precipitate was obtained collected on the magnetic bar. Further, the reaction mixture was washed with acetone, vacuum filtered, and dried overnight at room temperature. Based on the used ratio of copper and nickel metals, the nanoparticles were named CuNi-11, CuNi-12 and CuNi-21 with 1:1, 1:2 and 2:1 molar ratios.

#### 4.2.3. General catalytic procedure

In a general hydrogenation reaction, aldehydes, and ketones (1 mmol), CuNi-12 catalyst (8 mg), Base KOH (16 mg) and isopropyl alcohol (4 mL) in a glass reaction tube of 15 mL with stop cock were used at magnetic stirring bar and stirred for the appropriate time at 75 °C. After completion of the reaction, it was allowed to cool at room temperature, and the catalyst was separated using an external magnet. The separated

catalyst was used for the next cycle, and the reaction mixture was diluted and given for Shimadzu GC-MS analysis to analyze the product conversion and selectivity.

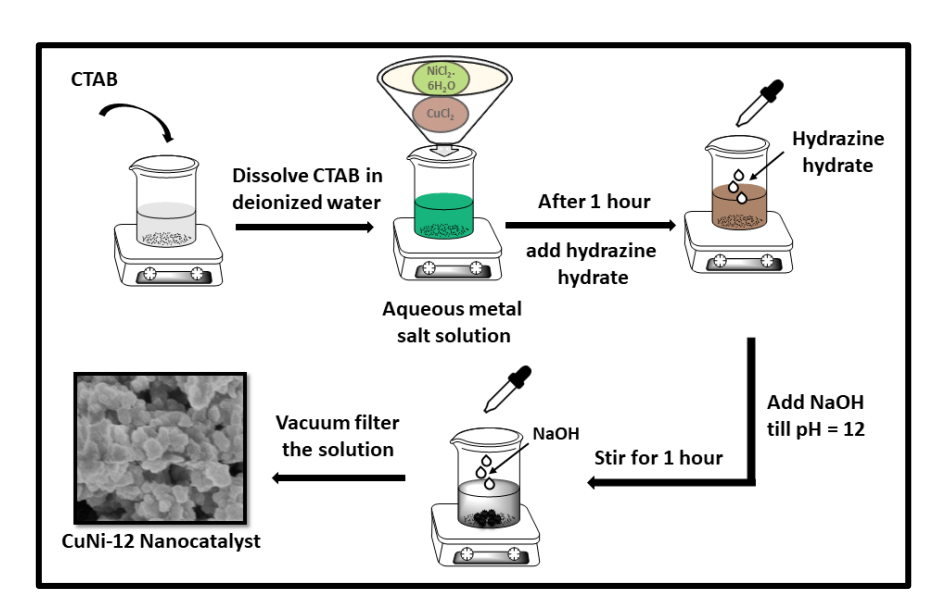
#### 4.2.4. Physicochemical measurements

The details about the PXRD, FE-SEM, HR-TEM, BET characterization and utilized instruments have been discussed in Chapter 2 in physicochemical measurements section. The details about TGA, XPS and VSM analysis were discussed already in Chapter 3 in physicochemical measurements section. The catalyst leaching was performed using ICP-Atomic Emission Spectroscopy (Model: ARCOS, Simultaneous ICP Spectrometer). Identification of the products of catalytic reactions carried out using Shimadzu GC-MS, QP2010 mass spectrometer.

#### 4.3. Results and discussion

#### 4.3.1 Characterization of CuNi-12 nanocatalyst

The bimetallic CuNi-12 nanocatalysts were synthesized at room temperature via a simple liquid-phase reduction method with modification of our work [38] as shown in **Scheme 4.1.** 



**Scheme 4.1.** Schematic representation of the synthesis of CuNi-12 nanocatalyst.

The synthesized nanocatalyst was characterized via various characterization techniques. Initially, the X-ray diffraction pattern of CuNi-12 nanocatalyst was recorded, as shown in **Figure 4.1A**. In the PXRD spectra, the obtained diffraction peaks at 32.20, 38.15, 61.23 for (100), (101), and (111) planes correspond to the presence of  $\beta$ -Ni(OH)<sub>2</sub> (JCPDS 14-0117). The peaks at 35.16 and 65.56 indicate the presence of CuO for ( $\overline{11}$ 1) and (022), respectively, as confirmed by JCPDS 80-1916. Additionally, the peaks at 43.95, 51.18, and 75.78 reveal the formation of metallic Cu FCC (JCPDS 04-0836) for (111), (200), and (220) planes, respectively. The average crystallite size was calculated by the Debye Scherrer equation was obtained to be 3 nm. The PXRD analysis data of other composition i.e. CuNi-11, CuNi-21, monometallic Cu and Ni was discussed earlier in our reported work.[38]

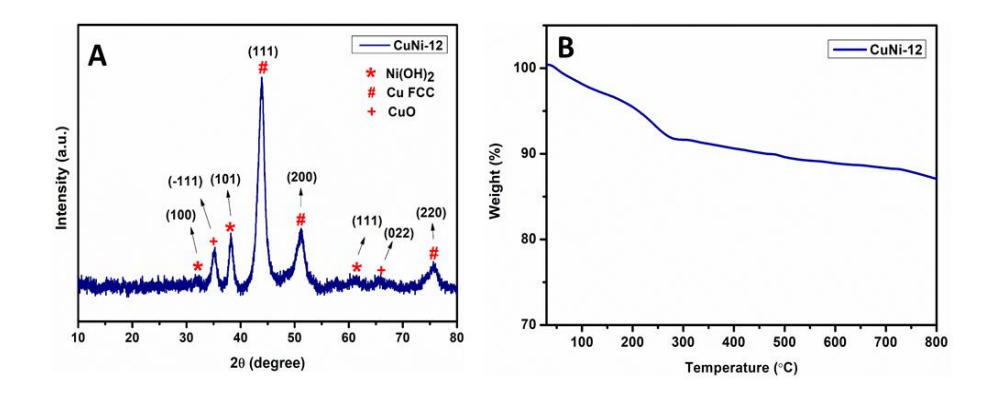


**Figure 4.1. (A)** PXRD and **(B)** thermogravimetric analysis of bimetallic CuNi-12 nanocatalyst.

The thermal decomposition of synthesized CuNi-12 nanocatalyst was analyzed by using thermogravimetric analysis from 30 °C to 800 °C temperature under nitrogen atmosphere, as shown in **Figure 4.1B**. In the TGA curve, two major weight loss was observed, i.e., below 280 °C and above 280 °C. In the first region, the total weight loss of 8.27 wt% was observed due to the removal of adsorbed CTAB and water molecules, and in the second region, the total weight loss of 4.62 wt% was observed, which was maybe owing to the decomposition of surfactant layer of CTAB from the surface of CuNi-12 nanocatalyst, and further complete oxidation of CTAB capping occurred.[39,40] The

observed results confirmed that the synthesized nanocatalyst is thermally stable up to 700 °C temperature.

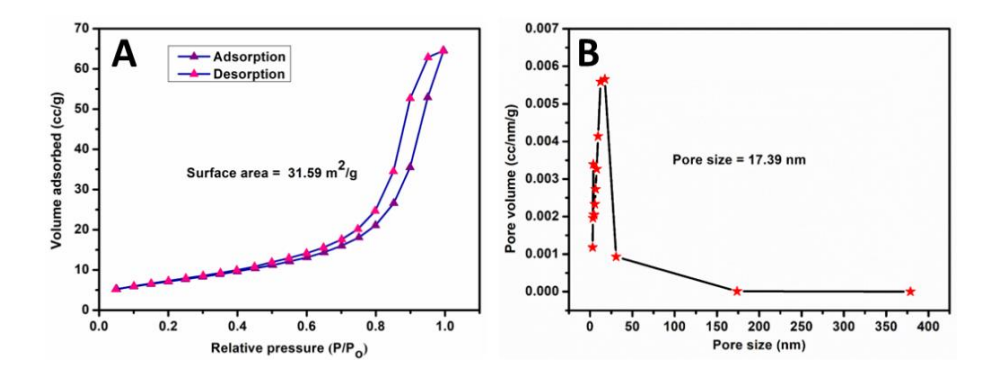


**Figure 4.2.** N<sub>2</sub> adsorption-desorption study for (**A**) surface area and (**B**) Pore size distribution of bimetallic CuNi-12 nanocatalyst.

Moreover, the surface area is essential to improving the catalytic activity by providing more active sites on the surface.[41] For this purpose, BET measurements were carried out to calculate the surface area, pore size and pore volume at 77K at 1 bar pressure, as shown in **Figure 4.2. Figure 4.2A** indicates the N<sub>2</sub> adsorption-desorption isotherm of the bimetallic CuNi-12 nanocatalyst, which exhibits the presence of mesopores with the presence type IV isotherm with H3 hysteresis loop[42] (**Figure 4.2A**) and the obtained specific surface area was 31.59 m<sup>2</sup>/g. Moreover, the calculated BJH pore size and pore volume were 17.39 nm and 0.10 cm<sup>3</sup>/g. This result further confirmed the presence of mesopores in the synthesized CuNi-12 nanocatalyst.[8,43]

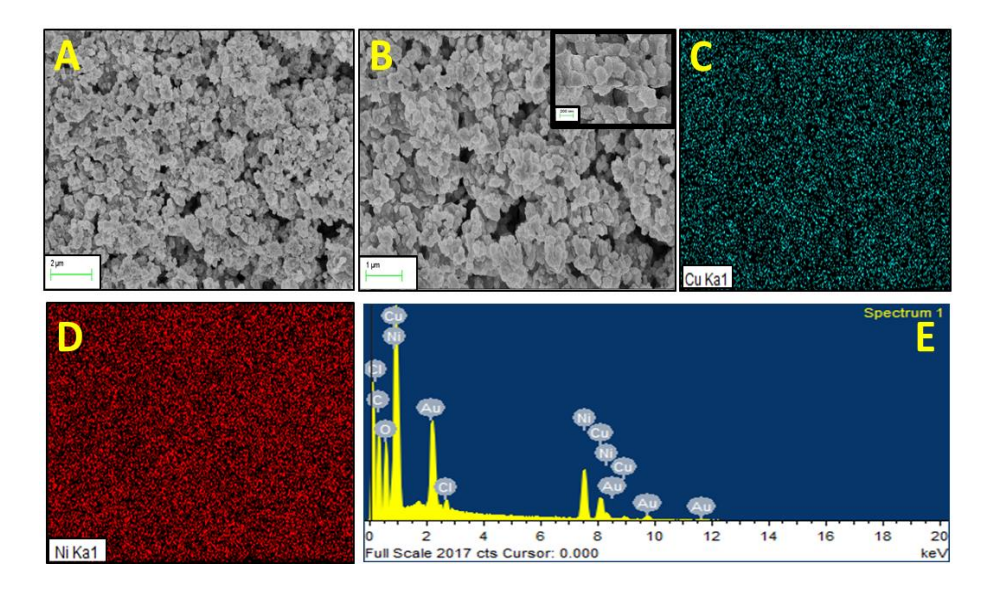


**Figure 4.3.** FE-SEM images at (**A**) 2 μm (**B**) 1 μm (zoom view in inset), mapping of (**C**) copper, (**D**) nickel, and (**E**) Elemental analysis of bimetallic CuNi-12 nanocatalyst.

Additionally, the morphology of the nanocatalyst is a crucial parameter for the catalytic properties. Hence, the morphological studies were performed using FE-SEM analysis, as shown in **Figure 4.3(A-B)**. The revealed surface morphology of the synthesized CuNi-12 nanocatalyst was a flakes-like structure (magnified image shown in the inset of **Figure 4.3B**).[44,45] Further, elemental analysis (EDX) and mapping were performed, and the results confirmed the presence of both Cu and Ni elements in an approximate 1:2 weight% ratio, as shown in **Figure 4.3(C-E)**. The average measured particle size was found to be 69 nm.

Furthermore, to get more structural data, HR-TEM analysis was performed, and the obtained data was in accordance with the FE-SEM imaging data (**Figure 4.4(A-C**)). The morphology of synthesized CuNi-12 nanocatalyst was flakes shaped structure.[46,47] The lattice fringes of the CuNi-12 bimetallic nanoparticles indicate that synthesized nanoparticles are crystalline in nature. Moreover, the selective area electron diffraction (SAED) pattern revealed the bright concentric rings of the CuNi-12 nanocatalyst, which is in good agreement with the HR-

TEM images that further confirm the crystalline nature of the bimetallic CuNi-12 nanocatalyst.[48]

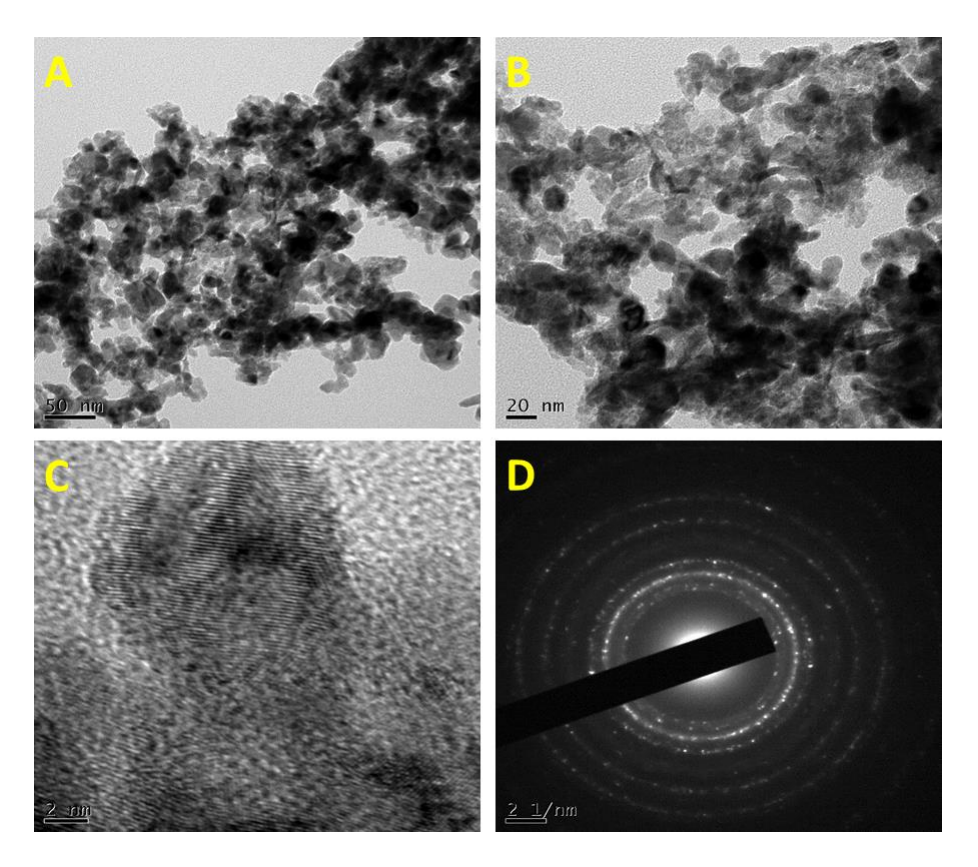


**Figure 4.4.** HR-TEM images of bimetallic CuNi-12 nanocatalyst at **(A)** 50 nm, **(B)** 20 nm, **(C)** 2 nm and **(D)** Selective area electron diffraction (SAED) pattern at 2 1/nm.

The magnetic nanocatalyst has the advantage of easily recyclability after completing the reaction using an external magnet, and in this regard, the magnetic properties of bimetallic CuNi-12 were explored using a vibrating sample magnetometer (VSM) study at room temperature (**Figure 4.5**). The values of saturation magnetization (Ms) = 16.277 emu/g, remanence (Mr) = 3.834 emu/g and remanence to saturation ratio (Mr/Ms) = 0.235 and coercivity (Hc) = 128.667 Oe were calculated from the obtained M-H loop curve. The bimetallic CuNi-12 nanocatalyst is ferromagnetic in nature.

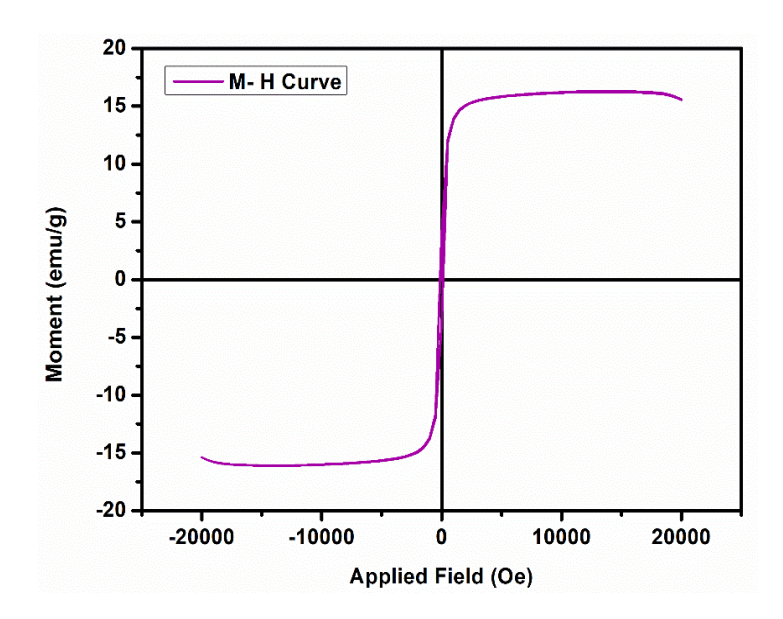


**Figure 4.5**. Hysteresis loop for magnetic properties of bimetallic CuNi-12 nanocatalyst at room temperature.

The chemical composition of the nanocatalyst is a significant factor in any catalytic process, and to analyze the same, X-ray photoelectron spectroscopy (XPS) analysis was performed. The XPS spectra of Cu 2p, Ni 2p and O 1s element were recorded as shown in Figure 4.6(A-C). The Cu 2p demonstrated two broad peaks of Cu 2p<sub>3/2</sub> at 932.62 eV and Cu 2p<sub>1/2</sub> for 952.91 eV, respectively owing to the presence of metallic Cu(0).[49] Also, the deconvoluted peak of Cu 2p<sub>3/2</sub> at 933.76 eV confirmed the presence of CuO.[50] Further, the XPS spectra of Ni 2p showed two peaks and their satellite peaks. The XPS spectra indicate two peaks at 856.23 eV and its satellite peak at 861.05 eV of Ni 2p<sub>3/2</sub> and 873.69 eV and its satellite peak at 879.89 eV of Ni  $2p_{1/2}$  for the presence of Ni<sup>+2</sup>.[51,52] The spin-orbit separation of 17.6 eV was calculated which confirms the presence of Ni(OH)<sub>2</sub>.[53,54] Also, the deconvoluted O 1s spectra peaks at 530.1 eV and 531.7 eV confirmed the presence of metallic oxide and hydroxide in synthesized CuNi-12 bimetallic nanocatalyst as shown in Figure 4.6C.[55] This data confirms the formation of copper oxide and nickel hydroxide in bimetallic CuNi-12 nanocatalyst. Additionally, to confirm the presence of all the elements, survey scan of fresh CuNi-12 catalyst was performed which indicate the presence of all elements Cu, Ni and O (**Figure 4.6D**).

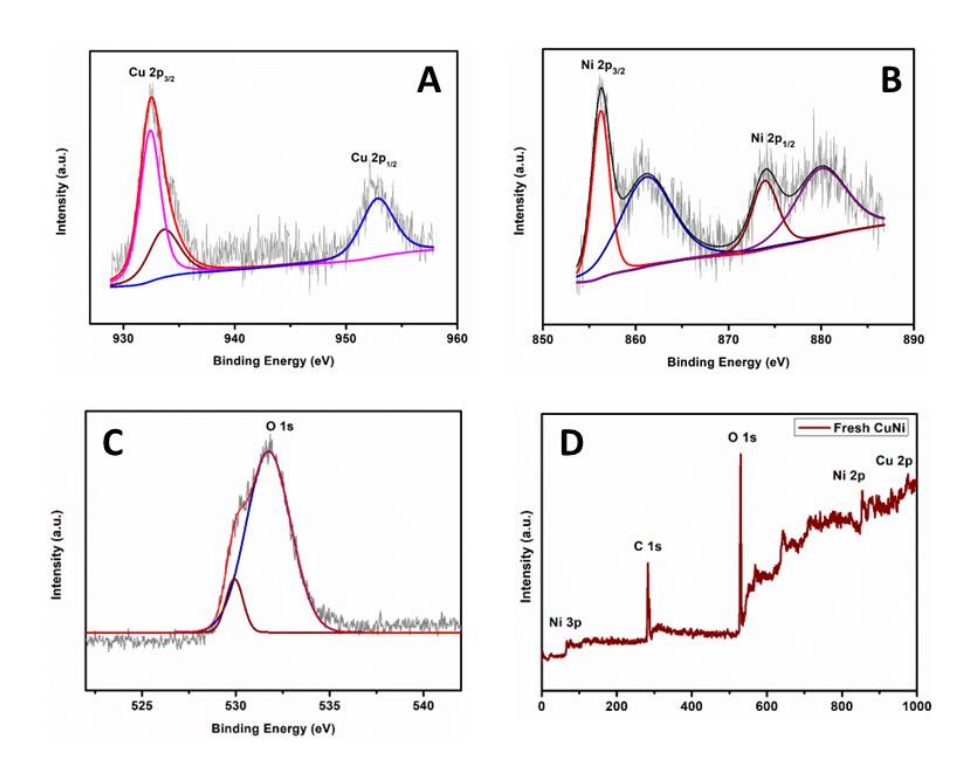


**Figure 4.6.** XPS analysis of fresh bimetallic CuNi-12 nanocatalysts (**A**) Cu 2p, (**B**) Ni 2p, (**C**) O 1s and (**D**) survey scan.

#### 4.3.2. Catalytic results

The synthesized bimetallic CuNi-12 nanocatalyst was utilized for catalytic conversion of biomass-derived aldehydes and ketones into corresponding alcohols using isopropyl alcohol and base.

Initially, the systematic investigation of the hydrogenation reaction of biomass was performed, using furfural as a model substrate to optimize the best suitable reaction condition. For this purpose, the effect of catalyst amount, the base amount, hydrogen source at various temperatures, bases and catalyst amount. Firstly, catalyst screening was performed using various catalysts. We have synthesized three metal ratios of Cu: Ni and named them CuNi-12, CuNi-11, and CuNi-21 on their molar ratios and the results in **Figure 4.7.** In all the combinations, CuNi-12 shows greater catalytic efficiency with 100% conversion and 100% selectivity of furfural to furfuryl alcohol. Bimetallic catalyst CuNi-12 contain 1:2 ratio of Cu: Ni which indicate that the catalyst containing more nickel amount shows greater activity whereas copper shows high redox properties which converted into zero oxidation state

insitu by adsorbing the hydride ion and promotes the hydrogenation reaction. To confirm this possibility, we have additionally performed the reaction with monometallic Cu and Ni catalysts, and in both cases, the conversion is less, which is 14% and 22%. This result confirms the synergistic effect of Cu and Ni in synthesized bimetallic CuNi-12 nanocatalyst to convert the furfural into furfuryl alcohol with 100% conversion and 100% selectivity. Hence, all the reactions were carried out using a CuNi-12 catalyst.

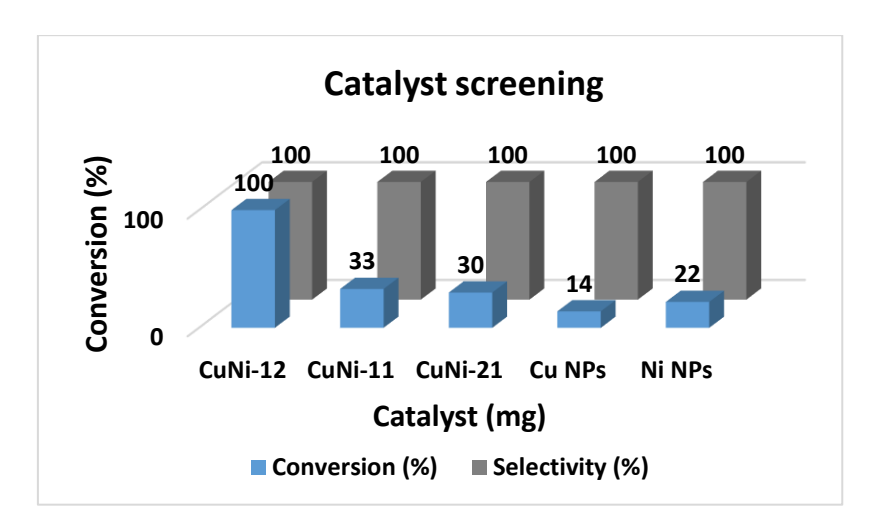


**Figure 4.7.** Screening of catalyst on the hydrogenation of furfural into furfuryl alcohol. **Reaction condition:** Substrate (furfural) = 1 mmol, catalyst = 10 mg, base (KOH) = 16 mg, temperature =  $75 \, ^{\circ}\text{C}$ .

Furthermore, the effect of catalyst was analyzed using 4, 6, 8, and 10 mg CuNi-12 bimetallic nanocatalyst with 1 mmol furfural, 16 mg base at 75 °C temperature, as shown in **Figure 4.8A**. As the catalyst amount was increased, the conversion was increased. When 4 mg and 6 mg of nanocatalyst were used for the reaction, 72% and 95% conversion was observed into furfuryl alcohol. The 100% conversion was observed in the case of 8 mg and 10 mg of bimetallic CuNi-12 nanocatalyst. Hence, all the reactions were carried out using 8 mg of the bimetallic CuNi-12 nanocatalyst. Additionally, the reaction was performed without catalyst and only 37% conversion was observed which indicate the importance of our catalyst for the hydrogenation reaction.

Additionally, the effect of the hydrogen source was analyzed using 2-propanol (isopropanol), 1-propanol, t-butanol, 1-butanol, MeOH, EtOH and water using a bimetallic CuNi-12 nanocatalyst and KOH as a base at 75 °C temperature. The reaction with 1-propanol, 1-butanol, t-butanol, MeOH, EtOH and water shows poor conversion, which is 36%, 14%, 13%, 31%, 24% and 9%, respectively, for the hydrogenation of furfural, as shown in **Figure 4.8B**.[56] In contrast, 2-propanol is found to be optimum hydrogen source with 100% conversion and 100% selectivity towards alcohol product. Therefore, all the reactions were performed using 2-propanol as a hydrogen source and solvent.

After finalizing 2-propanol as a hydrogen source, the base optimization was analyzed by varying several bases such as KOH, NaOH and K<sub>2</sub>CO<sub>3</sub> under the same reaction conditions (**Figure 4.8C**). In the case of NaOH, 87% conversion was obtained, with is quite good, whereas, in the case of K<sub>2</sub>CO<sub>3</sub>, only 13% conversion was obtained. In the case of strong base KOH, 100% conversion and 100% selectivity were observed. Since KOH showed more excellent conversion and selectivity and further all the reactions were performed using a KOH base.

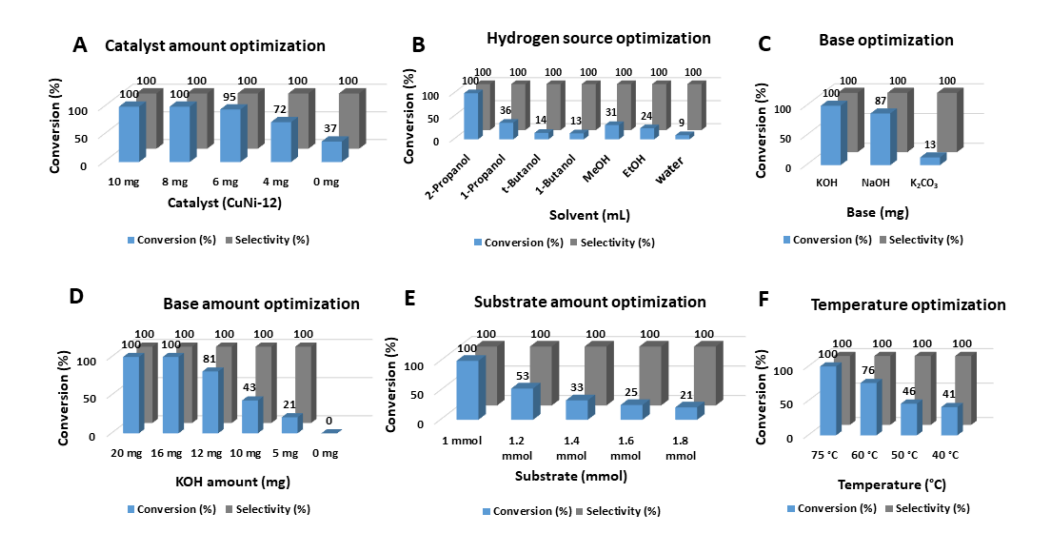


Figure 4.8. Effect of catalyst amount loading, hydrogen source with different base and base amount on conversion of furfural to furfuryl

alcohol. **Reaction conditions:** Substrate (furfural) = 1-1.8 mmol, catalyst = 0-10 mg, base (KOH) = 0-20 mg, temperature = 40-75 °C.

Since the above results indicate that KOH is the best suitable base for the hydrogenation reaction, the optimization of the KOH amount was analyzed with 10 mg of CuNi-12 catalyst and 4 mL 2-propanol as the hydrogen source and solvent (**Figure 4.8D**). When 5 mg of the base was used, only 21% conversion was observed whereas in the absence of base, no conversion was observed indicating that the base is required to hydrogenate furfural into furfuryl alcohol. When the base amount was increased to 20 mg, the conversion increased from 21% to 100%. When 16 mg of the base was utilized with the same reaction condition, 100% conversion was observed; hence, all the reactions were further performed using 16 mg KOH.

Furthermore, the effect of reaction temperature was analyzed, and the same reaction was carried out at various reaction temperatures such as 40 °C, 50 °C, 60 °C and 75 °C, as shown in **Figure 4.8E.** In the case of 40 °C, the conversion is relatively low in the case of 50 °C and 60 °C. Maximum 100% conversion and selectivity were observed at 75 °C; hence, all the reactions were carried out at this temperature.

After finalizing all the optimized reaction conditions, the effect of substrate amount was tested using 1 to 1.8 mmol of furfural with the above-optimized reaction conditions. The results reveal that as the amount of substrate increased, the furfural conversion decreased from 100% to 21% of furfuryl alcohol, as shown in **Figure 4.8F**. Hence, all the reactions were carried out with 1 mmol of substrate with 8 mg of bimetallic CuNi-12 nanocatalyst, 4 mL of 2-propanol and 16 mg of KOH at 75 °C.

After analyzing the best suitable reaction conditions, the substrate scope was analyzed using various substituted aldehydes and ketones (**Table 4.1**, **Entry 1-20**). All aldehydes (**Table 4.1**, **Entry 1-16**) were converted into corresponding products with 100% selectivity, whereas the ketone (**Table 4.1**, **Entry 17-20**) conversion took more time. First, the biomass-

derived aldehyde, i.e., HMF and cinnamaldehyde was utilized for hydrogenation. HMF was successfully converted into corresponding alcohol product with 100% conversion and 100% selectivity (**Table 4.1**, Entry 2). Although, 90% conversion of cinnamaldehyde into cinnamyl alcohol was obtained with 100% selectivity indicating the bulkiness affects the substrate's conversion (Table 4.1, Entry 3). However, when benzaldehyde was used as a substrate, the benzyl alcohol was observed within 3 hours with 100% conversion and 100% selectivity (**Table 4.1**, Entry 4). To extend this study, various electron-deficient and electronrich substituted aldehydes were utilized. Electron withdrawing groups like –CN, -Cl, -Br substituted aldehydes were primarily used for the hydrogenation reaction (**Table 4.1**, **Entry 5-10**). Almost all aldehydes were converted into corresponding alcohols, but the effect of substitution position on the ring was examined. The para-substituted aldehydes show conversion in less time, whereas ortho-, metasubstituted aldehydes took more time in case of all substituted aldehydes, which may be because the reaction site hinders the hydride attack.[40] The bromo- substituted aldehyde took more time than that of -chloro substituted aldehyde, which might be due to steric hindrance of the bulkiness of bromo- group. Although, there was not much difference was observed in reaction time in the case of all the halogen-substituted aldehydes. Also, there was no dehalogenation observed of halogenated aldehydes. Further, electron-rich substituted aldehyde was analyzed by taking meta-methyl benzaldehyde, and it was converted into corresponding alcohol within 6 hours with 96% conversion and 100% selectivity (Table 4.1, Entry 11). This data indicates that the effect of electron-deficient and electron-rich substituents on the aldehyde ring was perceived. Further, a bulky substrate 1-Naphthalene carboxaldehyde was utilized for hydrogenation reaction, and after 7 hours, 96% conversion was obtained, indicating the effect of bulkiness (Table 4.1, Entry 12). Furthermore, the same reaction was performed using cyclic aldehydes such as 1-Cyclohexene-1-carboxaldehyde, which shows 100% conversion with 100% selectivity (Table 4.1, Entry 13). Moreover, some heterocyclic aldehydes were also analyzed, such as 3pyridinecarboxaldehyde, 4-pyridinecarboxaldehyde and 2-imidazole carboxyldehyde at same reaction condition for appropriate time and 100% conversion with 100% selective alcohol was obtained (**Table 4.1**, **Entry 14-16**). After analyzing the activity of catalyst towards aldehydes, ketones were also explored using 2-methyl cyclopentanone, 4-chloroacetophenone, 4-methyl acetophenone and 4-methoxyacetophenone (**Table 4.1**, **Entry 17-20**). The hydrogenation of ketones was converted into product and took more time than aldehydes. All conversion and selectivity were confirmed with Shimadzu GC-MS analysis (**Section 4.5**). The general catalytic reaction is shown in **Scheme 4.2**.

R = H, -CH<sub>2</sub>OH

$$R = H, -CH2OH$$

$$R = -CN, -CI, -Br, -Me,$$

$$CuNi-12 \\
KOH, 2-Propanol, 75 °C$$

$$R = -CN, -CI, -Br, -Me,$$

**Scheme 4.2.** General catalytic conversion of biomass-derived aldehydes and ketones using CuNi-12 bimetallic nanocatalyst.

**Table 4.1.** Substrate scope of hydrogenation of aldehydes and ketones into alcohols

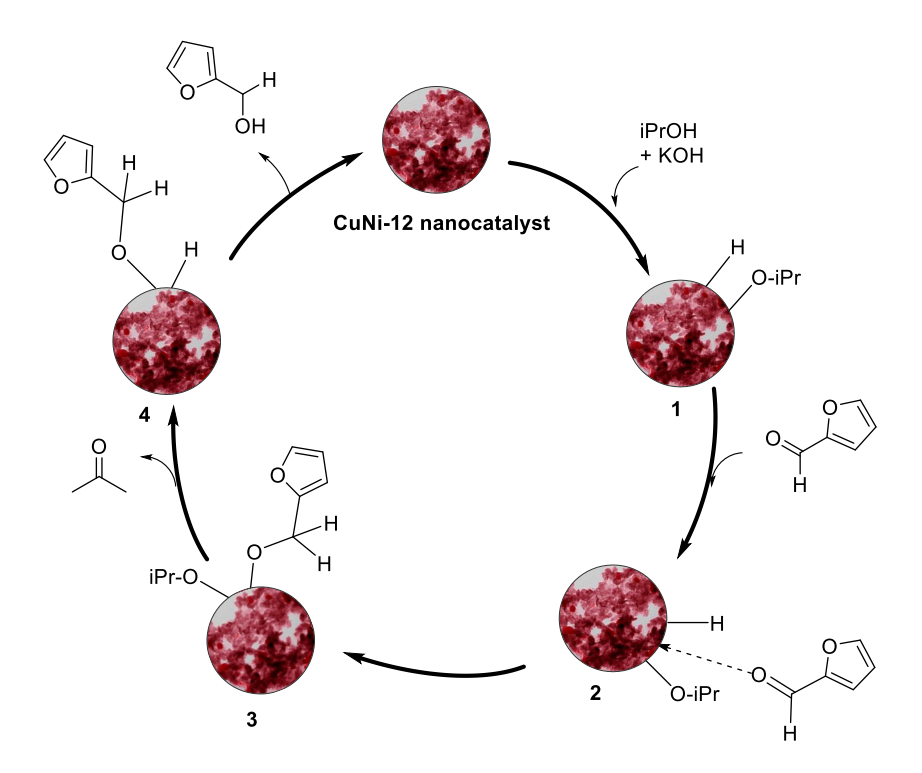
Entry	Substrate	Product	Time	Conv
			( <b>h</b> )	(%)
1	° °	OOH	1	100
2	но	НОООН	5	100
3	0	ОН	8	90
4	0	ОН	3	100

5	0	ОН	3	97
	CN	CN		
6	NC	NC	3	98
7	0	OH	3.5	100
8	O C	СІ	4	100
9	Br	OH Br	3.5	100
10	Br	Вг	4	100
11		ОН	6	96
12		НО	7	96
13	0	ОН	2.5	100
14	O	OH	6	100
15	O	OH	5	100
16	ZZZZ	HN OH	3	100
17	Ç	ОН	3	100

18	CI	OH	12	75
19		TO	15	95
20	MeO	OH MeO	12	89

**Reaction conditions:** Substrate = 1 mmol, catalyst (CuNi-12) = 8 mg, base (KOH) = 16 mg, time = 1-15 h, 2-propanol = 4 mL, temperature = 75 °C.

Based on previous reports and literature [56–58], the plausible mechanism was proposed for the transfer hydrogenation of furfural using CuNi-12 catalyst, as shown in Scheme 4.3. Primarily, the base additive promotes the oxidative addition of 2-propanol and CuNi-12 catalyst and produces an intermediate 1. The addition of base is important to promote the reaction faster as base abstract proton from the 2-propanol and produce hydride ion for hydrogenation reaction. Further, the aldehyde or ketone substrates adsorb on the surface of the CuNi-12 bimetallic catalyst with the coordination of the carbonyl group of the substrate with the catalyst surface to form intermediate 2. After that, an active H\* specie attack on the carbonyl group of the substrate produces 3. Additionally, the release of acetone molecule occurred, and then 4 generated where the C-OH bond formed. The acetone was produced due to the removal of two hydrogen atoms from 2-propanol. After that, the alcohol product was released, and the catalyst surface became free for further reaction.



**Scheme 4.3.** A plausible mechanism of hydrogenation of furfural into furfuryl alcohol.

Moreover, we have tried to summarize the work with some earlier reported hydrogenation reactions using various Cu and Ni-based catalysts (Table 4.2). As mentioned, bimetallic Cu-based NPs as catalyst was utilized highly flammable hydrogen gas at high temperature at 150-170 °C with moderate to excellent selectivity[22,59] whereas photocatalytic conversion was performed using base, hydrogen gas with 2-propanol which showed approx. 98% conversion with 93% selectivity.[23] Additionally, nickel based catalyst was also utilized as catalyst at 100-250 °C with H<sub>2</sub> gas and 2-propanol with excellent catalytic activity but high reaction time.[10,60,61] Based on these reports, as synthesized bimetallic CuNi-12 nanocatalyst showed greater efficiency with gas free approach at minimal temperature and less reaction time for the catalytic transfer hydrogen of biomass derived aldehydes i.e. furfural in terms of selectivity, reaction time and temperature. Hence, the present work involves sustainable and simple method for the conversion of furfurals with 100% conversion and 100% selectivity at 75°C temperature in 1 hour. Also, the synthesized CuNi12 catalyst provide large substrate scope of aldehydes and ketones which make the reaction simple, promising, efficient and economical for the transfer hydrogenation.

**Table 4.2.** Comparison of present work with some previously reported work.

S. No.	Catalyst	Substrate	H-Source /Additives	Time (h)	Temp (°C)	Conv. (%)	Sel. (%)	Ref.
1	Cu-Co Bimetalli c NPs (20 mg)	Furfural (1 mmol)	H <sub>2</sub> gas (0.5 MPa) + 10 mL H <sub>2</sub> O	3	150	100	100	[22]
2	CuFe@C -500	Furfural (1 mmol)	H <sub>2</sub> gas (0.5 MPa) + 10 mL H <sub>2</sub> O	3	150	84.2	67. 8	[22]
3	CuNi@C -500	Furfural (1 mmol)	H <sub>2</sub> gas (0.5 MPa) + 10 mL H <sub>2</sub> O	3	150	100	30. 8	[22]
4	Fe(NiFe) O <sub>4</sub> -SiO <sub>2</sub> (0.51 wt%)	Furfural	H <sub>2</sub> gas (20 bar)	4	250	94	100	[61]
5	Cu/Cu <sub>2</sub> O -MC (10 mg)	Furfural (0.05 mmol)	H <sub>2</sub> gas (1 bar) + 2- propanol (4 mL) + K <sub>2</sub> CO <sub>3</sub> (1.44)	16	LED,	97.8	92. 5	[23]
6	NP-Cu catalyst	Furfural (0.62 g)	H <sub>2</sub> gas (2 MPa) + 2-	3	170	100	100	[59]

	(Cu/C- 400)		propanol (15.4 g)					
	400)		(13.4 g)					
7	Ni@N/C -g-800 catalyst	Furfural (0.5 mmol)	H <sub>2</sub> gas (200 psi) + H <sub>2</sub> O + 2- propanol (34+01 mL)	6	100	99	98	[10]
8	Co/ZrLa 0.2O <sub>x</sub> catalyst	Furfural (0.5 mmol)	H <sub>2</sub> gas (2 MPa) + H <sub>2</sub> O (10 mL)	10	40	99	99	[62]
9	NiO NPs	HMF (2 mmol)	2-propanol (10 mL)	4	180	99	93	[60]
10	Ni- SAs/NC	Furfural (1 mmol)	2-propanol (8 mL) + N <sub>2</sub> (2 MPa)	3	130	95.6	96. 8	[63]
11	GO-Se- Pd	Benzaldeh yde (1 mmol)	KOH (0.2 mmol) + 2-propanol (5 mL)	3	80	97	100	[57]
12	CuNi-12	Furfural (1 mmol)	KOH (16 mg) + 2- propanol (4 mL)	1	75	100	100	This work

### 4.3.3 Kinetic and recycle study

Furthermore, the final optimized reaction conditions for hydrogenation of furfural (1 mmol) were analyzed with the use of base KOH (16 mg), CuNi-12 bimetallic catalyst (8 mg) with 2-propanol (4 mL) in 1 hour

reaction time. To study the kinetics of hydrogenation reaction of furfural, the sample was taken periodically by using injection and given the samples for GC-MS analysis. The sample was taken at 15, 30, 45 and 60 min, and the obtained conversion was 23, 55, 78 and 100% respectively, as shown in **Figure 4.9(A)**.

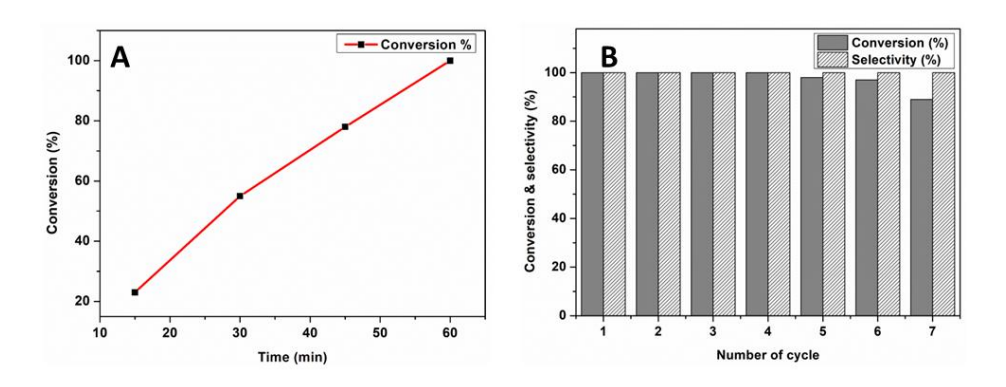


**Figure 4.9.** (**A**) Kinetic study and (**B**) Recycle study of bimetallic CuNi-12 nanocatalyst for conversion of furfural. **Reaction conditions**: Substrate (furfural) = 1 mmol, catalyst (CuNi-12) = 8 mg, base (KOH) = 16 mg, 2-propanol = 4 mL, temperature = 75 °C, time = 1 h.

After that, to check the reusability and recyclability of synthesized CuNi-12 nanocatalyst, the recycle study was performed for the hydrogenation of furfural to furfuryl alcohol, as shown in **Figure 4.9B**. After the first run, the catalyst was separated with a magnet, and the reaction mixture was given for GC-MS analysis to check the conversion and selectivity. Further, the catalyst was washed with water and then dried at room temperature. After drying the catalyst, the spent catalyst was reused for the next cycle with the appropriate reaction condition. Till six cycles, the conversion was almost 100% with 100% selectivity. In the seventh cycle, the conversion decreases to 89%, but the selectivity remains the same, i.e., 100%. The decrease in conversion with the cycles may be due to increased carbon content or coke deposition at the catalyst's surface and pores, reducing the active sites and deactivating the catalysts. [64,65]

Moreover, to check the stability of the bimetallic CuNi-12 nanocatalyst, the spent CuNi-12 nanocatalyst was analyzed using XPS

analysis (**Figure 4.10**). The XPS spectra of the Cu element show two peaks at 932.58 eV and 952.5 eV for Cu  $2p_{3/2}$  and Cu  $2p_{1/2}$  in the presence of metallic copper (0).[50,66] The XPS spectra of the Ni element show the peaks at 852.76 eV and 870.13 eV for Ni  $2p_{3/2}$  and Ni  $2p_{1/2}$ , respectively, confirming the presence of metallic nickel(0).[67,68] The catalyst is in Cu(0)/Ni(0), which is in its active form. This change in oxidation state of copper from CuO to Cu(0) was attributed to reaction of hydride ion during the course of reaction.[69]

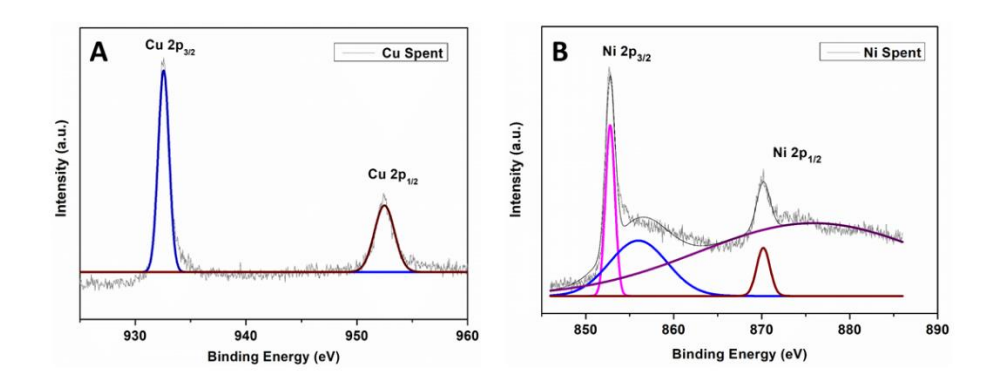


**Figure 4.10.** XPS spectra of (**A**) Cu 2p element (**B**) Ni 2p element of spent CuNi-12 nanocatalyst.

Additionally, to check the leaching of the catalyst, inductive coupled plasma atomic emission (ICP-AES) analysis was performed (**Table 4.3**). The catalyst was filtered, and the supernatant was given for ICP-AES analysis, and the obtained data confirmed no significant leaching was observed.

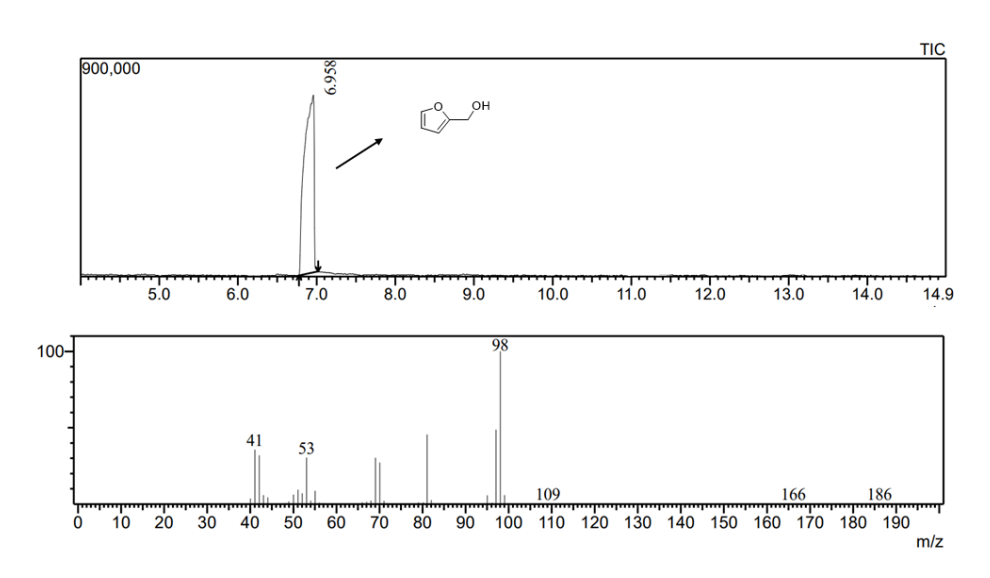
**Table 4.3.** ICP-AES analysis data of CuNi-12 nanocatalyst for hydrogenation reaction

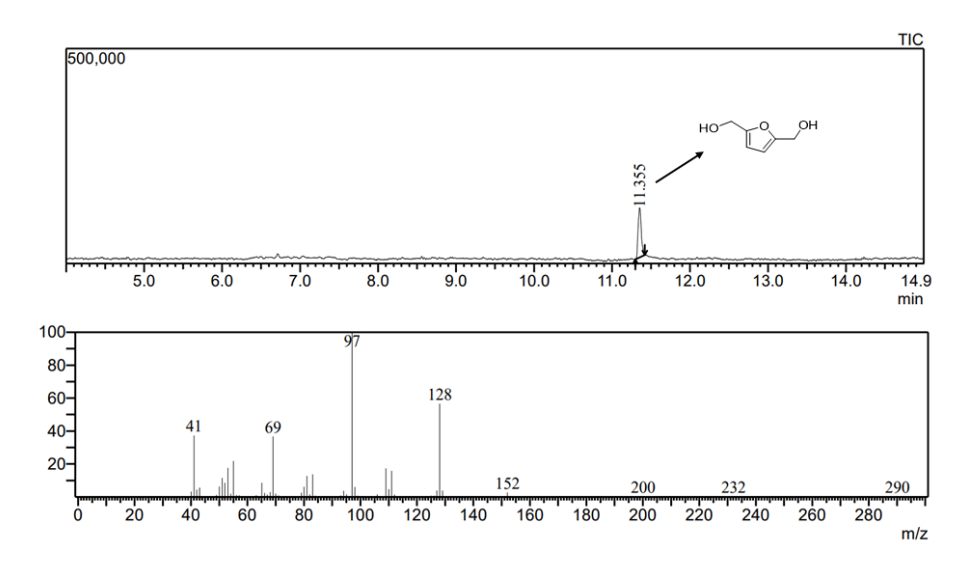
Sample	ICP-AES (ppm)	
CuNi-12 nanocatalyst	Cu	Ni
	0.101	0.633

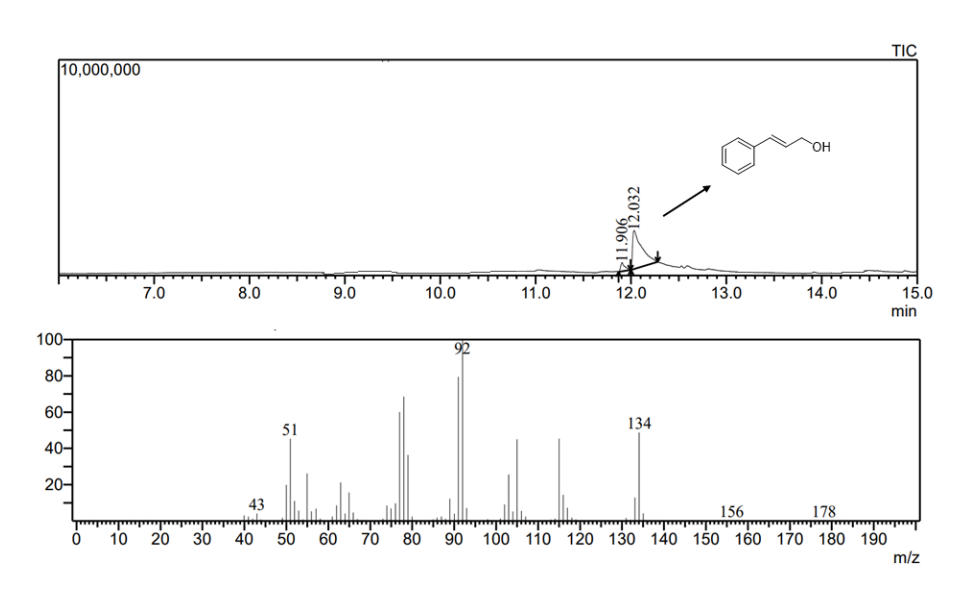
### 4.4. Conclusions

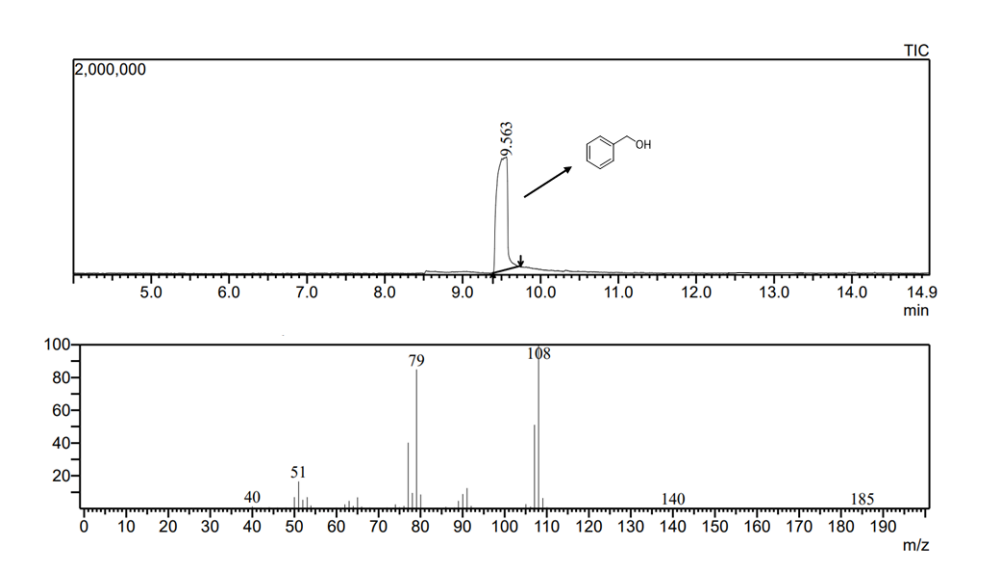
The magnetically separable CuNi-12 nanocatalyst was synthesized with 1:2 molar ratio with a simple method at room temperature and utilized for catalytic conversion of biomass-derived aldehydes into alcohols with 100% conversion and 100% selectivity. CuNi-12 nanocatalyst has high surface area of 31.592 m²/g and showed flakes-like morphology analyzed by BET and HR-TEM analysis respectively. The catalyst exhibited high efficiency for conversion of aldehydes and ketones by using base and 2-propanol. The synthesized CuNi-12 catalyst is efficient, highly active, cost-effective, magnetically separable and recyclable for up to seven cycles. This approach of catalytic conversion of biomass-derived aldehydes is sustainable and can be implemented for chemical industries.

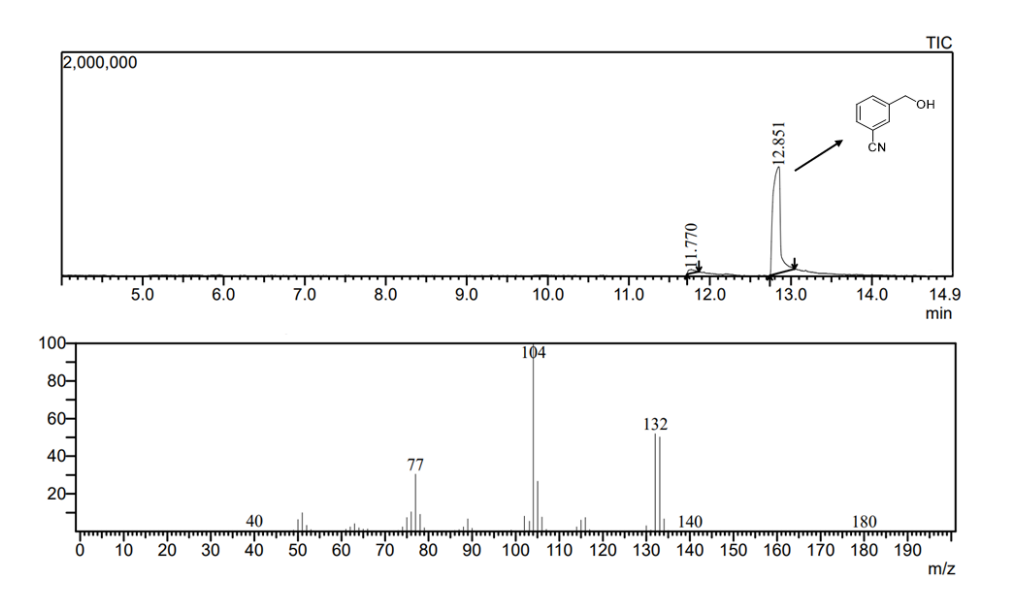
# 4.5. GC-MS spectra of catalytic hydrogenation of all reactants and products

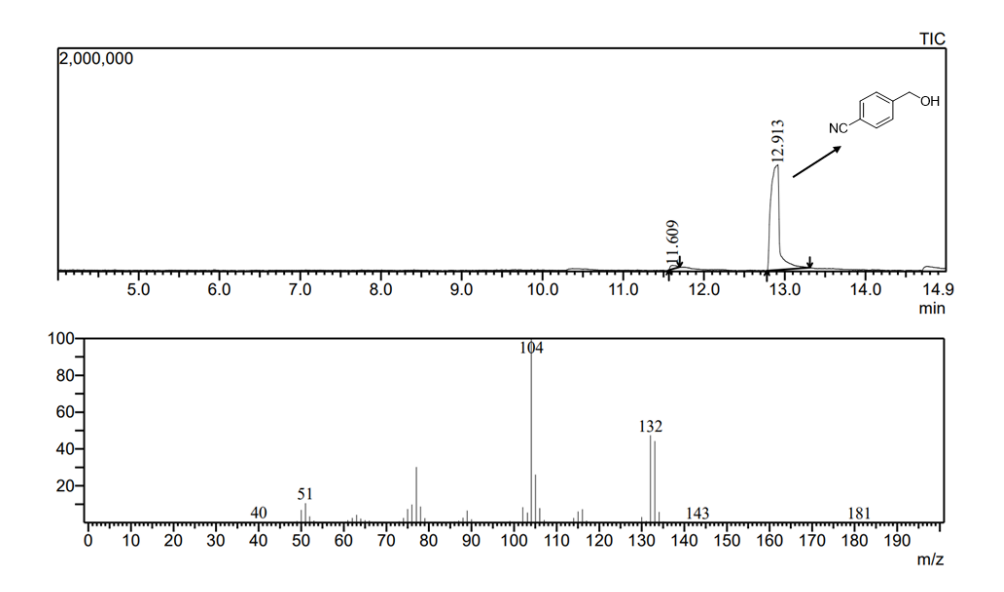


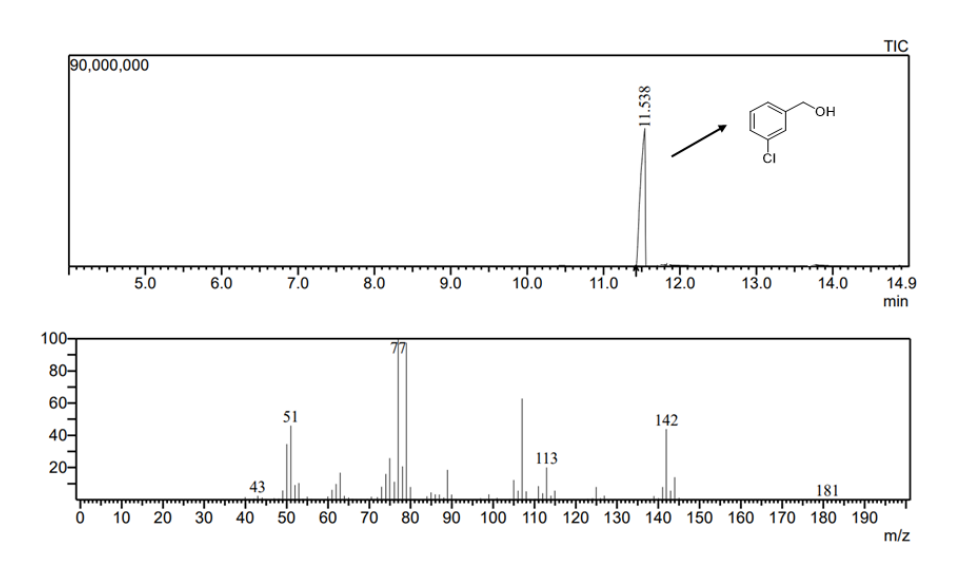


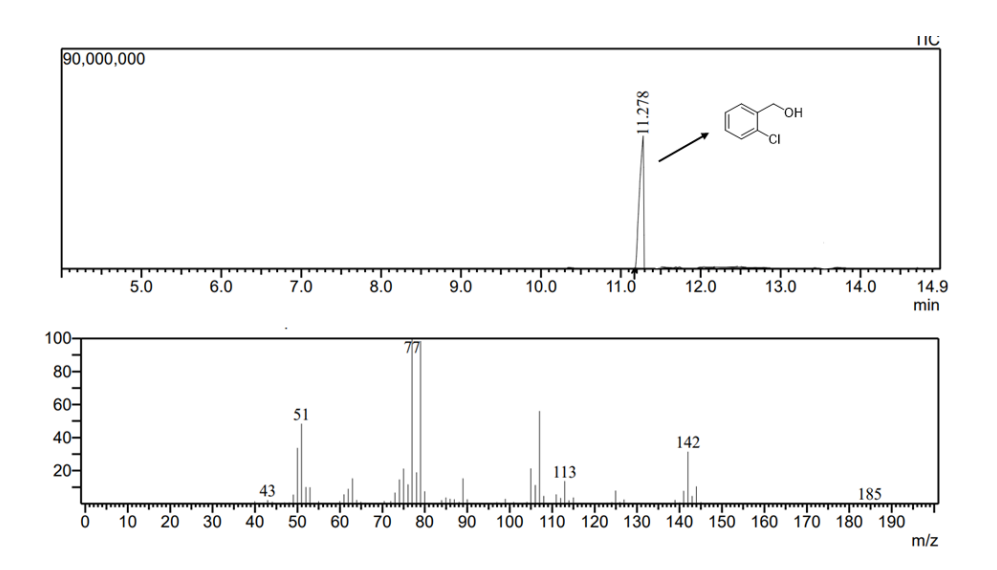


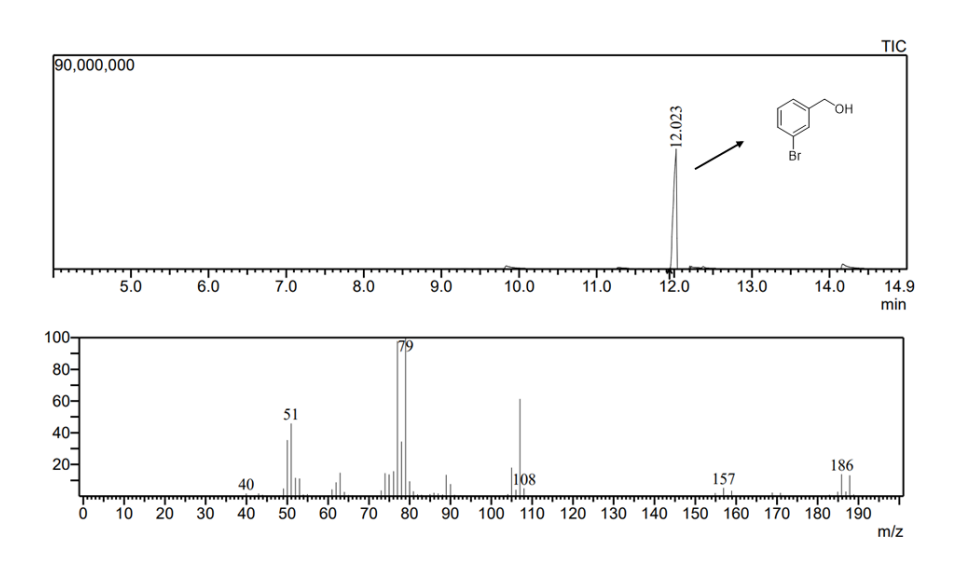


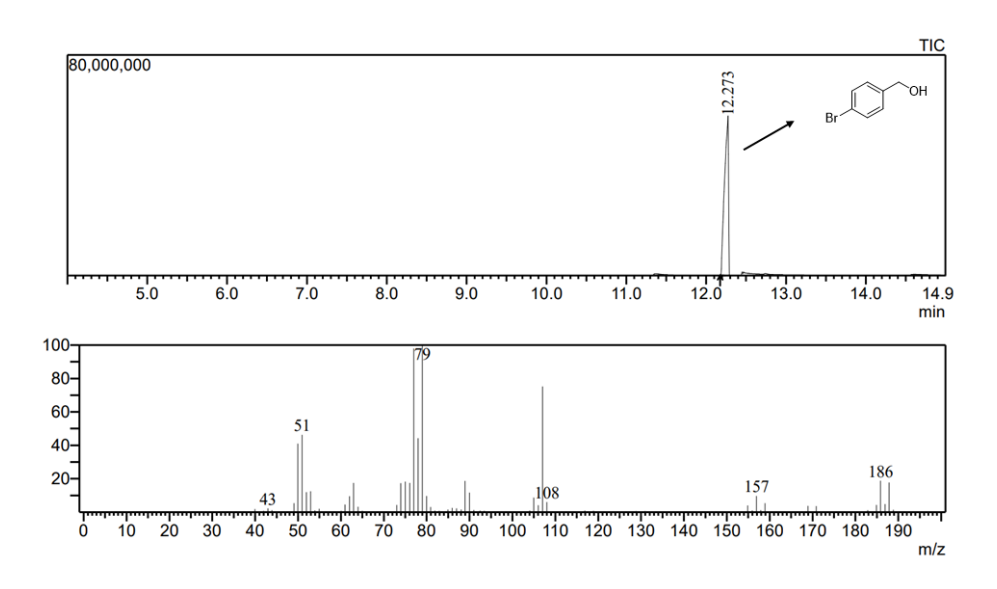


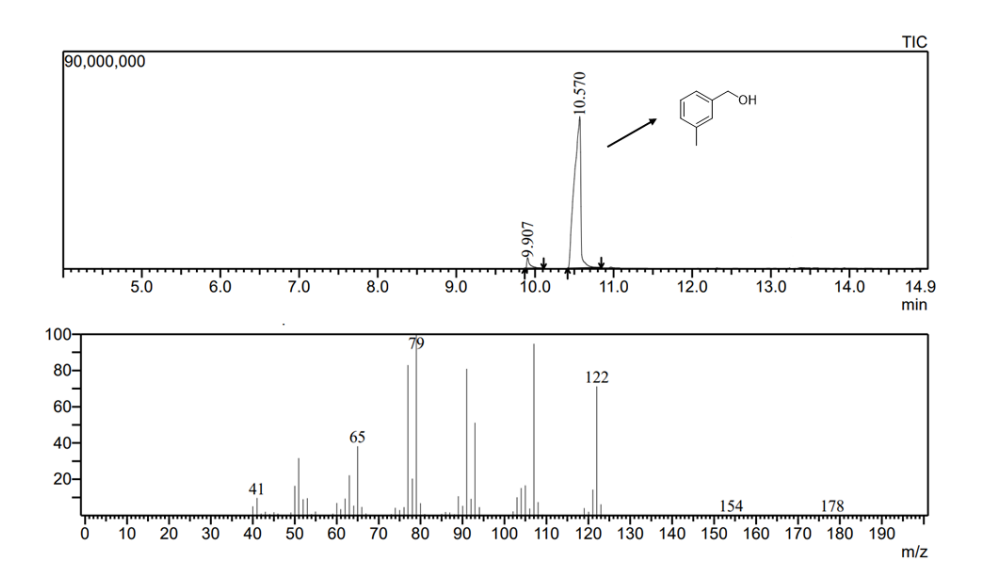


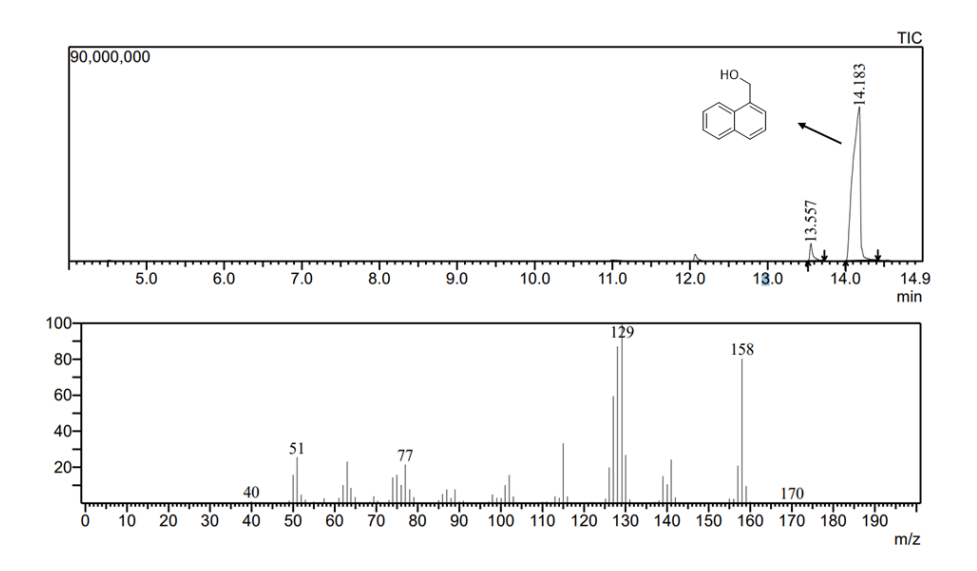


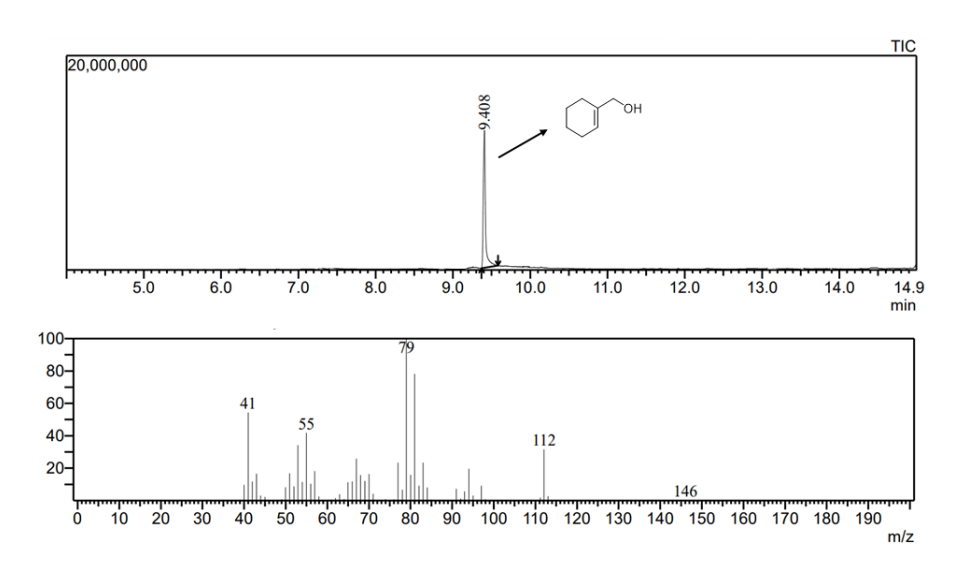


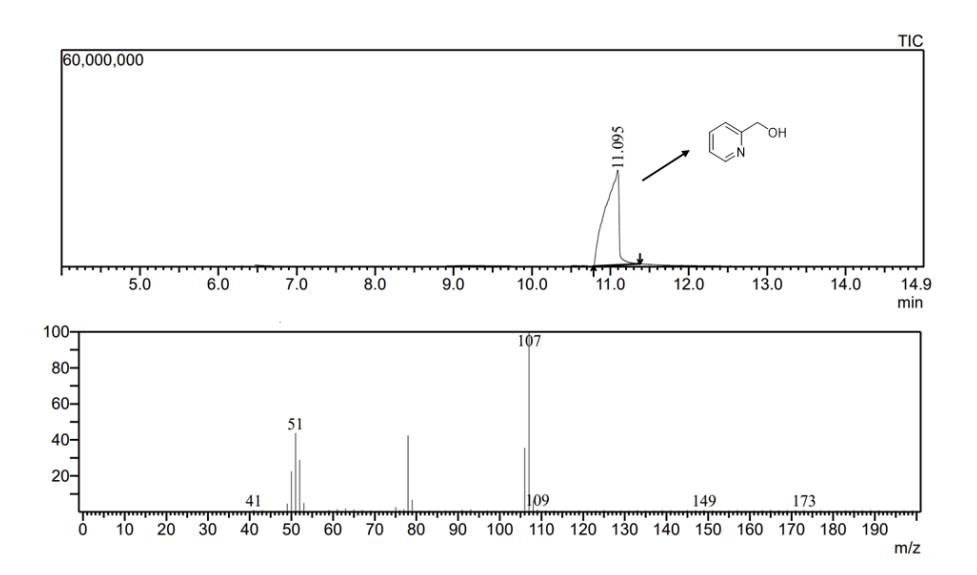


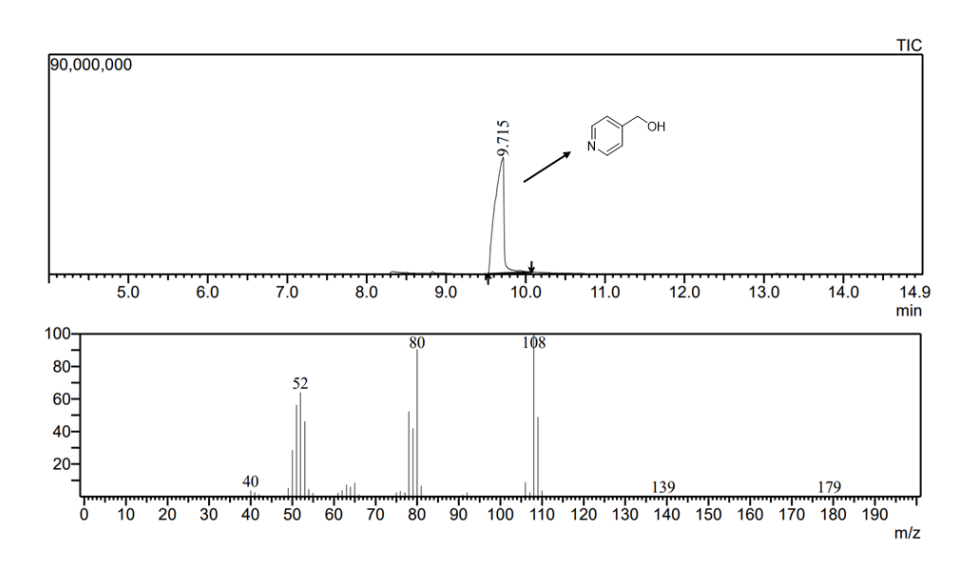


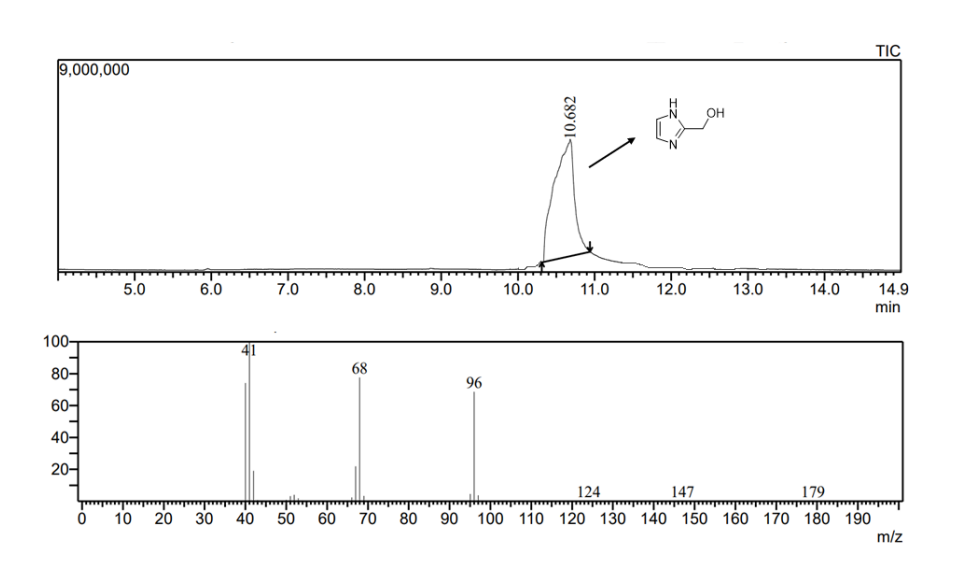


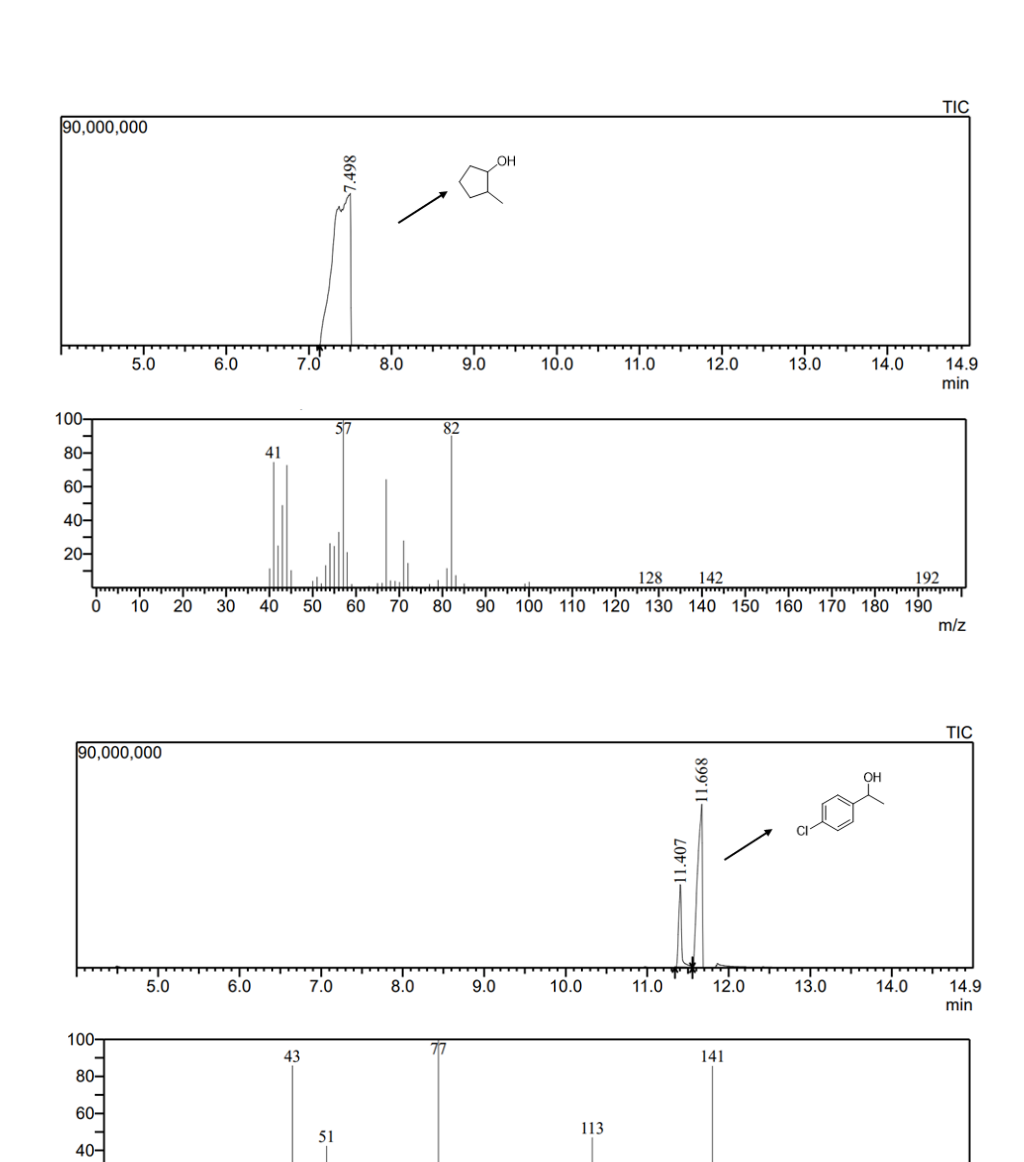


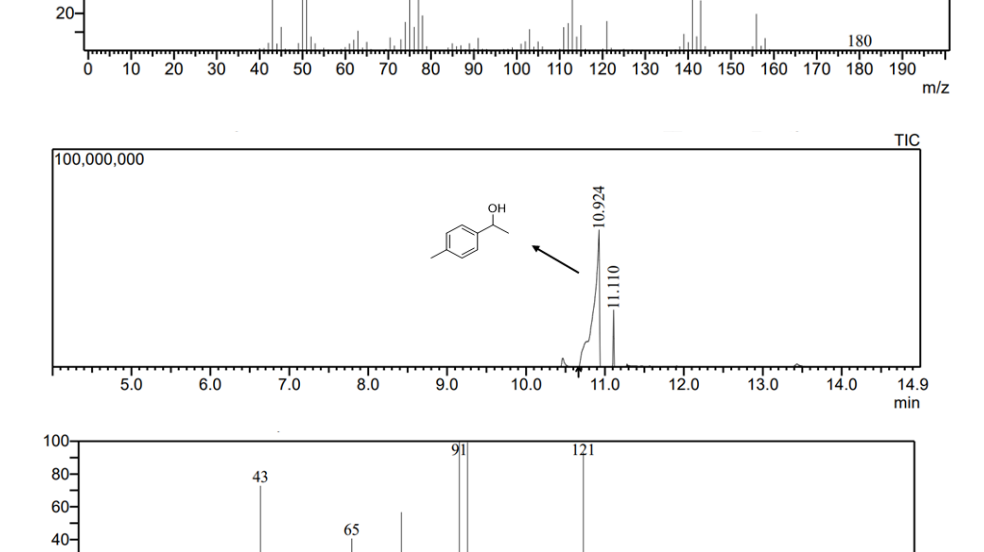






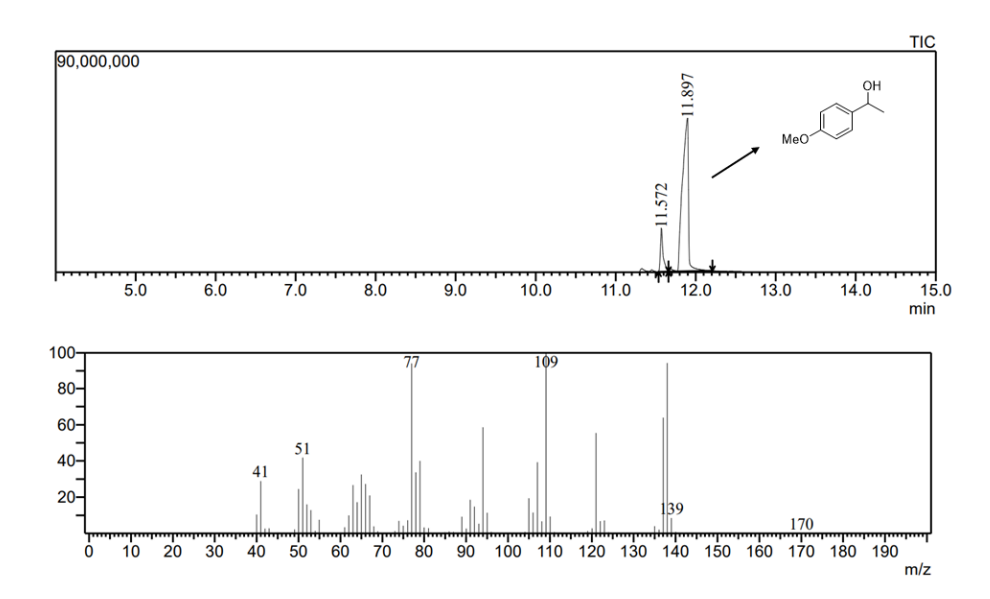






80 90 100 110 120 130 140 150 160 170 180 190

20-



#### 4.6. References

- [1] H. Xu, Z. Wang, J. Huang, Y. Jiang, Thermal Catalytic Conversion of Biomass-Derived Glucose to Fine Chemicals, Energy Fuels. 35 (2021) 8602–8616. https://doi.org/10.1021/acs.energyfuels.1c00715.
- [2] F. El Ouahabi, W. Smit, C. Angelici, M. Polyakov, U. Rodemerck, C. Fischer, V.N. Kalevaru, S. Wohlrab, S. Tin, G.P.M. van Klink, J.C. van der Waal, F. Orange, J.G. de Vries, Conversion of Biomass-Derived Methyl Levulinate to Methyl Vinyl Ketone, ACS Sustain. Chem. Eng. (2022). https://doi.org/10.1021/acssuschemeng.1c05694.
- [3] A. Corma, S. Iborra, A. Velty, Chemical Routes for the Transformation of Biomass into Chemicals, Chem. Rev. 107 (2007) 2411–2502. https://doi.org/10.1021/cr050989d.
- [4] J.B. Binder, R.T. Raines, Simple Chemical Transformation of Lignocellulosic Biomass into Furans for Fuels and Chemicals, J. Am. Chem. Soc. 131 (2009) 1979–1985. https://doi.org/10.1021/ja808537j.
- [5] X. Li, P. Jia, T. Wang, Furfural: A Promising Platform Compound for Sustainable Production of C4 and C5 Chemicals, ACS Catal. 6 (2016) 7621–7640. https://doi.org/10.1021/acscatal.6b01838.
- [6] A. Augustin, C. Chuaicham, M. Shanmugam, B. Vellaichamy, S. Rajendran, T.K. A. Hoang, K. Sasaki, K. Sekar, Recent development of organic–inorganic hybrid photocatalysts for biomass conversion into hydrogen production, Nanoscale Adv. 4 (2022) 2561–2582. https://doi.org/10.1039/D2NA00119E.
- [7] V. Vorotnikov, G. Mpourmpakis, D.G. Vlachos, DFT Study of Furfural Conversion to Furan, Furfuryl Alcohol, and 2-Methylfuran on Pd(111), ACS Catal. 2 (2012) 2496–2504. https://doi.org/10.1021/cs300395a.
- [8] Z. Xia, L. Niu, Y. An, G. Bian, T. Li, G. Bai, Ni–Al/CoOxcatalyzed hydrodeoxygenation of 5-hydroxymethylfurfural into 2,5-dimethylfuran at low temperatures without external hydrogen, Green Chem. (2021). https://doi.org/10.1039/D1GC02758A.
- [9] B. Liu, Z. Zhang, One-Pot Conversion of Carbohydrates into Furan Derivatives via Furfural and 5-Hydroxylmethylfurfural as Intermediates, ChemSusChem. 9 (2016) 2015–2036. https://doi.org/10.1002/cssc.201600507.
- [10] S. Nandi, A. Saha, P. Patel, N.H. Khan, R.I. Kureshy, A.B. Panda, Hydrogenation of Furfural with Nickel Nanoparticles Stabilized on Nitrogen-Rich Carbon Core—Shell and Its Transformations for the Synthesis of γ-Valerolactone in Aqueous Conditions, ACS Appl. Mater. Interfaces. 10 (2018) 24480–24490. https://doi.org/10.1021/acsami.8b04239.
- [11] M.J. Taylor, L.J. Durndell, M.A. Isaacs, C.M.A. Parlett, K. Wilson, A.F. Lee, G. Kyriakou, Highly selective hydrogenation of furfural over supported Pt nanoparticles under mild conditions, Appl. Catal. B Environ. 180 (2016) 580–585. https://doi.org/10.1016/j.apcatb.2015.07.006.

- [12] P.S. Moyo, L.C. Matsinha, B.C.E. Makhubela, Pd(II) and Pt(II) catalysed selective synthesis of furfuryl alcohol: Solvent effects and insights into the mechanism, J. Organomet. Chem. 922 (2020) 121362. https://doi.org/10.1016/j.jorganchem.2020.121362.
- [13] M. Lesiak, M. Binczarski, S. Karski, W. Maniukiewicz, J. Rogowski, E. Szubiakiewicz, J. Berlowska, P. Dziugan, I. Witońska, Hydrogenation of furfural over Pd–Cu/Al2O3 catalysts. The role of interaction between palladium and copper on determining catalytic properties, J. Mol. Catal. Chem. 395 (2014) 337–348. https://doi.org/10.1016/j.molcata.2014.08.041.
- [14] A.S. Gowda, S. Parkin, F.T. Ladipo, Hydrogenation and hydrogenolysis of furfural and furfuryl alcohol catalyzed by ruthenium(II) bis(diimine) complexes, Appl. Organomet. Chem. 26 (2012) 86–93. https://doi.org/10.1002/aoc.2819.
- [15] G. Valdebenito, S. Parra-Melipán, V. López, B. Aranda, E. García, A. Vega, C. Negrete-Vergara, S.A. Moya, P. Aguirre, Selective hydrogenation of furfural to furfuryl alcohol catalysed by ruthenium complexes containing phosphorus-nitrogen ligands, Appl. Organomet. Chem. 35 (2021) e6382. https://doi.org/10.1002/aoc.6382.
- [16] X. Qi, R. Zhou, H.-J. Ai, X.-F. Wu, HMF and furfural: Promising platform molecules in rhodium-catalyzed carbonylation reactions for the synthesis of furfuryl esters and tertiary amides, J. Catal. 381 (2020) 215–221. https://doi.org/10.1016/j.jcat.2019.11.008.
- [17] N. K. Oklu, B.C. E. Makhubela, Chemoselective and efficient catalytic hydrogenation of furfural by iridium and ruthenium half-sandwich complexes, New J. Chem. 44 (2020) 9382–9390. https://doi.org/10.1039/D0NJ01811B.
- [18] L. Bui, H. Luo, W.R. Gunther, Y. Román-Leshkov, Domino Reaction Catalyzed by Zeolites with Brønsted and Lewis Acid Sites for the Production of γ-Valerolactone from Furfural, Angew. Chem. Int. Ed. 52 (2013) 8022–8025. https://doi.org/10.1002/anie.201302575.
- [19] D.J. Cole-Hamilton, Homogeneous Catalysis--New Approaches to Catalyst Separation, Recovery, and Recycling, Science. (2003). https://doi.org/10.1126/science.1081881.
- [20] M.C. Arno, M. Inam, A.C. Weems, Z. Li, A.L.A. Binch, C.I. Platt, S.M. Richardson, J.A. Hoyland, A.P. Dove, R.K. O'Reilly, Exploiting the role of nanoparticle shape in enhancing hydrogel adhesive and mechanical properties, Nat. Commun. 11 (2020) 1420. https://doi.org/10.1038/s41467-020-15206-y.
- [21] J. Mondal, K. Truc Nguyen, A. Jana, K. Kurniawan, P. Borah, Y. Zhao, A. Bhaumik, Efficient alkene hydrogenation over a magnetically recoverable and recyclable Fe 3 O 4 @GO nanocatalyst using hydrazine hydrate as the hydrogen source, Chem. Commun. 50 (2014) 12095–12097. https://doi.org/10.1039/C4CC04770B.
- [22] W. Gong, C. Chen, H. Zhang, G. Wang, H. Zhao, In Situ Synthesis of Highly Dispersed Cu–Co Bimetallic Nanoparticles for Tandem Hydrogenation/Rearrangement of Bioderived Furfural in

- Aqueous-Phase, ACS Sustain. Chem. Eng. 6 (2018) 14919–14925. https://doi.org/10.1021/acssuschemeng.8b03418.
- [23] M. Zhang, Z. Li, Cu/Cu2O-MC (MC = Mesoporous Carbon) for Highly Efficient Hydrogenation of Furfural to Furfuryl Alcohol under Visible Light, ACS Sustain. Chem. Eng. 7 (2019) 11485—11492. https://doi.org/10.1021/acssuschemeng.9b01305.
- [24] Z. Yang, X. Chou, H. Kan, Z. Xiao, Y. Ding, Nanoporous Copper Catalysts for the Fluidized Electrocatalytic Hydrogenation of Furfural to Furfuryl Alcohol, ACS Sustain. Chem. Eng. 10 (2022) 7418–7425. https://doi.org/10.1021/acssuschemeng.2c02360.
- [25] M. Manikandan, A.K. Venugopal, A.S. Nagpure, S. Chilukuri, T. Raja, Promotional effect of Fe on the performance of supported Cu catalyst for ambient pressure hydrogenation of furfural, RSC Adv. 6 (2016) 3888–3898. https://doi.org/10.1039/C5RA24742J.
- [26] S. Sitthisa, W. An, D.E. Resasco, Selective conversion of furfural to methylfuran over silica-supported NiFe bimetallic catalysts, J. Catal. 284 (2011) 90–101. https://doi.org/10.1016/j.jcat.2011.09.005.
- [27] C. Xu, E. Paone, D. Rodríguez-Padrón, R. Luque, F. Mauriello, Recent catalytic routes for the preparation and the upgrading of biomass derived furfural and 5-hydroxymethylfurfural, Chem. Soc. Rev. 49 (2020) 4273–4306. https://doi.org/10.1039/D0CS00041H.
- [28] J. Wu, G. Gao, J. Li, P. Sun, X. Long, F. Li, Efficient and versatile CuNi alloy nanocatalysts for the highly selective hydrogenation of furfural, Appl. Catal. B Environ. 203 (2017) 227–236. https://doi.org/10.1016/j.apcatb.2016.10.038.
- [29] L. Luo, F. Yuan, F. Zaera, Y. Zhu, Catalytic hydrogenation of furfural to furfuryl alcohol on hydrotalcite-derived CuxNi3-xAlOy mixed-metal oxides, J. Catal. 404 (2021) 420–429. https://doi.org/10.1016/j.jcat.2021.10.009.
- [30] B. Seemala, C.M. Cai, R. Kumar, C.E. Wyman, P. Christopher, Effects of Cu–Ni Bimetallic Catalyst Composition and Support on Activity, Selectivity, and Stability for Furfural Conversion to 2-Methyfuran, ACS Sustain. Chem. Eng. 6 (2018) 2152–2161. https://doi.org/10.1021/acssuschemeng.7b03572.
- [31] Z. An, J. Li, Recent advances in the catalytic transfer hydrogenation of furfural to furfuryl alcohol over heterogeneous catalysts, Green Chem. 24 (2022) 1780–1808. https://doi.org/10.1039/D1GC04440K.
- [32] F. Alonso, P. Riente, M. Yus, Nickel Nanoparticles in Hydrogen Transfer Reactions, Acc. Chem. Res. 44 (2011) 379–391. https://doi.org/10.1021/ar1001582.
- [33] M.J. Gilkey, P. Panagiotopoulou, A.V. Mironenko, G.R. Jenness, D.G. Vlachos, B. Xu, Mechanistic Insights into Metal Lewis Acid-Mediated Catalytic Transfer Hydrogenation of Furfural to 2-Methylfuran, ACS Catal. 5 (2015) 3988–3994. https://doi.org/10.1021/acscatal.5b00586.
- [34] B. Wang, C. Li, B. He, J. Qi, C. Liang, Highly stable and selective Ru/NiFe2O4 catalysts for transfer hydrogenation of biomass-

- derived furfural to 2-methylfuran, J. Energy Chem. 26 (2017) 799–807. https://doi.org/10.1016/j.jechem.2017.04.008.
- [35] X. Chang, A.-F. Liu, B. Cai, J.-Y. Luo, H. Pan, Y.-B. Huang, Catalytic Transfer Hydrogenation of Furfural to 2-Methylfuran and 2-Methyltetrahydrofuran over Bimetallic Copper—Palladium Catalysts, ChemSusChem. 9 (2016) 3330—3337. https://doi.org/10.1002/cssc.201601122.
- [36] Z. Zhang, Z. Pei, H. Chen, K. Chen, Z. Hou, X. Lu, P. Ouyang, J. Fu, Catalytic in-Situ Hydrogenation of Furfural over Bimetallic Cu–Ni Alloy Catalysts in Isopropanol, Ind. Eng. Chem. Res. 57 (2018) 4225–4230. https://doi.org/10.1021/acs.iecr.8b00366.
- [37] H.-L. Jiang, Q. Xu, Recent progress in synergistic catalysis over heterometallic nanoparticles, J. Mater. Chem. 21 (2011) 13705–13725. https://doi.org/10.1039/C1JM12020D.
- [38] N. Choudhary, M. Abdelgaid, G. Mpourmpakis, S.M. Mobin, CuNi bimetallic nanocatalyst enables sustainable direct carboxylation reactions, Mol. Catal. 530 (2022) 112620. https://doi.org/10.1016/j.mcat.2022.112620.
- [39] P.H.K. Charan, G. Ranga Rao, Synthesis of CuNi and CuNi/SBA-15 by aqueous method at room temperature and their catalytic activity, Microporous Mesoporous Mater. 200 (2014) 101–109. https://doi.org/10.1016/j.micromeso.2014.08.029.
- [40] N. Choudhary, T. Ghosh, S.M. Mobin, Ketone Hydrogenation by Using ZnO–Cu(OH)Cl/MCM-41 with a Splash of Water: An Environmentally Benign Approach, Chem. Asian J. 15 (2020) 1339–1348. https://doi.org/10.1002/asia.201901610.
- [41] Y.-J. Liu, W.-T. Cao, M.-G. Ma, P. Wan, Ultrasensitive Wearable Soft Strain Sensors of Conductive, Self-healing, and Elastic Hydrogels with Synergistic "Soft and Hard" Hybrid Networks, ACS Appl. Mater. Interfaces. 9 (2017) 25559–25570. https://doi.org/10.1021/acsami.7b07639.
- [42] M. A. Małecka, P. Woźniak, Hierarchical macroparticles of ceria with tube-like shape synthesis and properties, CrystEngComm. 23 (2021) 6743–6754. https://doi.org/10.1039/D1CE00755F.
- [43] Z.A. ALOthman, A Review: Fundamental Aspects of Silicate Mesoporous Materials, Materials. 5 (2012) 2874–2902. https://doi.org/10.3390/ma5122874.
- [44] S.M. Salili, A. Ataie, M.R. Barati, Z. Sadighi, Characterization of mechano-thermally synthesized Curie temperature-adjusted La0.8Sr0.2MnO3 nanoparticles coated with (3-aminopropyl) triethoxysilane, Mater. Charact. 106 (2015) 78–85. https://doi.org/10.1016/j.matchar.2015.05.025.
- [45] S. Cabanas-Polo, Z. Gonzalez, A.J. Sanchez-Herencia, B. Ferrari, Influence of ultrasound on the instantaneous synthesis of tridimensional α-Ni(OH)2 nanostructures and derived NiO nanoparticles, CrystEngComm. 17 (2015) 6193–6206. https://doi.org/10.1039/C5CE00876J.
- [46] P.R. Solanki, M.K. Patel, M.A. Ali, B.D. Malhotra, A chitosan modified nickel oxide platform for biosensing applications, J.

- Mater. Chem. B. 3 (2015) 6698–6708. https://doi.org/10.1039/C5TB00494B.
- [47] G. Jeevanandham, R. Jerome, N. Murugan, M. Preethika, K. Vediappan, A.K. Sundramoorthy, Nickel oxide decorated MoS2 nanosheet-based non-enzymatic sensor for the selective detection of glucose, RSC Adv. 10 (2020) 643–654. https://doi.org/10.1039/C9RA09318D.
- [48] L. Zhou, W. Wang, H. Xu, S. Sun, M. Shang, Bi2O3 Hierarchical Nanostructures: Controllable Synthesis, Growth Mechanism, and their Application in Photocatalysis, Chem. Eur. J. 15 (2009) 1776–1782. https://doi.org/10.1002/chem.200801234.
- [49] S. Karthikeyan, C. Chuaicham, R.R. Pawar, K. Sasaki, W. Li, A.F. Lee, K. Wilson, Template free mild hydrothermal synthesis of core–shell Cu2O(Cu)@CuO visible light photocatalysts for Nacetyl-para-aminophenol degradation, J. Mater. Chem. A. 7 (2019) 20767–20777. https://doi.org/10.1039/C9TA07009E.
- [50] Y. Yu, R. Jin, J. Easa, W. Lu, M. Yang, X. Liu, Y. Xing, Z. Shi, Highly active and stable copper catalysts derived from copper silicate double-shell nanofibers with strong metal–support interactions for the RWGS reaction, Chem. Commun. 55 (2019) 4178–4181. https://doi.org/10.1039/C9CC00297A.
- [51] S.-Q. Liu, H.-R. Wen, Ying-Guo, Y.-W. Zhu, X.-Z. Fu, R. Sun, C.-P. Wong, Amorphous Ni(OH)2 encounter with crystalline CuS in hollow spheres: A mesoporous nano-shelled heterostructure for hydrogen evolution electrocatalysis, Nano Energy. 44 (2018) 7–14. https://doi.org/10.1016/j.nanoen.2017.11.063.
- [52] M. Chhetri, S. Sultan, C.N.R. Rao, Electrocatalytic hydrogen evolution reaction activity comparable to platinum exhibited by the Ni/Ni(OH)2/graphite electrode, Proc. Natl. Acad. Sci. 114 (2017) 8986–8990. https://doi.org/10.1073/pnas.1710443114.
- [53] S. Anantharaj, P. E. Karthik, S. Kundu, Petal-like hierarchical array of ultrathin Ni(OH) 2 nanosheets decorated with Ni(OH) 2 nanoburls: a highly efficient OER electrocatalyst, Catal. Sci. Technol. 7 (2017) 882–893. https://doi.org/10.1039/C6CY02282K.
- [54] N. Weidler, J. Schuch, F. Knaus, P. Stenner, S. Hoch, A. Maljusch, R. Schäfer, B. Kaiser, W. Jaegermann, X-ray Photoelectron Spectroscopic Investigation of Plasma-Enhanced Chemical Vapor Deposited NiOx, NiOx(OH)y, and CoNiOx(OH)y: Influence of the Chemical Composition on the Catalytic Activity for the Oxygen Evolution Reaction, J. Phys. Chem. C. 121 (2017) 6455–6463. https://doi.org/10.1021/acs.jpcc.6b12652.
- [55] S. Karthikeyan, K. Ahmed, A. Osatiashtiani, A.F. Lee, K. Wilson, K. Sasaki, B. Coulson, W. Swansborough-Aston, R.E. Douthwaite, W. Li, Pompon Dahlia-like Cu2O/rGO Nanostructures for Visible Light Photocatalytic H2 Production and 4-Chlorophenol Degradation, ChemCatChem. 12 (2020) 1699–1709. https://doi.org/10.1002/cctc.201902048.
- [56] J. Yang, M. Yuan, D. Xu, H. Zhao, Y. Zhu, M. Fan, F. Zhang, Z. Dong, Highly dispersed ultrafine palladium nanoparticles

- encapsulated in a triazinyl functionalized porous organic polymer as a highly efficient catalyst for transfer hydrogenation of aldehydes, J. Mater. Chem. A. 6 (2018) 18242–18251. https://doi.org/10.1039/C8TA07502F.
- [57] R. Bhaskar, H. Joshi, A.K. Sharma, A.K. Singh, Reusable Catalyst for Transfer Hydrogenation of Aldehydes and Ketones Designed by Anchoring Palladium as Nanoparticles on Graphene Oxide Functionalized with Selenated Amine, ACS Appl. Mater. Interfaces. 9 (2017) 2223–2231. https://doi.org/10.1021/acsami.6b10457.
- [58] A. Balouch, A. Ali Umar, A.A. Shah, M. Mat Salleh, M. Oyama, Efficient Heterogeneous Catalytic Hydrogenation of Acetone to Isopropanol on Semihollow and Porous Palladium Nanocatalyst, ACS Appl. Mater. Interfaces. 5 (2013) 9843–9849. https://doi.org/10.1021/am403087m.
- [59] C. Wang, Y. Liu, Z. Cui, X. Yu, X. Zhang, Y. Li, Q. Zhang, L. Chen, L. Ma, In Situ Synthesis of Cu Nanoparticles on Carbon for Highly Selective Hydrogenation of Furfural to Furfuryl Alcohol by Using Pomelo Peel as the Carbon Source, ACS Sustain. Chem. Eng. 8 (2020) 12944–12955. https://doi.org/10.1021/acssuschemeng.0c03505.
- [60] J. He, L. Schill, S. Yang, A. Riisager, Catalytic Transfer Hydrogenation of Bio-Based Furfural with NiO Nanoparticles, ACS Sustain. Chem. Eng. 6 (2018) 17220–17229. https://doi.org/10.1021/acssuschemeng.8b04579.
- [61] A. Halilu, T.H. Ali, A.Y. Atta, P. Sudarsanam, S.K. Bhargava, S.B. Abd Hamid, Highly Selective Hydrogenation of Biomass-Derived Furfural into Furfuryl Alcohol Using a Novel Magnetic Nanoparticles Catalyst, Energy Fuels. 30 (2016) 2216–2226. https://doi.org/10.1021/acs.energyfuels.5b02826.
- [62] Y. Ma, G. Xu, H. Wang, Y. Wang, Y. Zhang, Y. Fu, Cobalt Nanocluster Supported on ZrREnOx for the Selective Hydrogenation of Biomass Derived Aromatic Aldehydes and Ketones in Water, ACS Catal. 8 (2018) 1268–1277. https://doi.org/10.1021/acscatal.7b03470.
- [63] Y. Fan, C. Zhuang, S. Li, Y. Wang, X. Zou, X. Liu, W. Huang, G. Zhu, Efficient single-atom Ni for catalytic transfer hydrogenation of furfural to furfuryl alcohol, J. Mater. Chem. A. 9 (2021) 1110–1118. https://doi.org/10.1039/D0TA10838C.
- [64] C. Montero, A. Remiro, B. Valle, L. Oar-Arteta, J. Bilbao, A.G. Gayubo, Origin and Nature of Coke in Ethanol Steam Reforming and Its Role in Deactivation of Ni/La2O3–αAl2O3 Catalyst, Ind. Eng. Chem. Res. 58 (2019) 14736–14751. https://doi.org/10.1021/acs.iecr.9b02880.
- [65] W.J. Kim, E.W. Shin, J.H. Kang, S.H. Moon, Performance of Simodified Pd catalyst in acetylene hydrogenation: catalyst deactivation behavior, Appl. Catal. Gen. 251 (2003) 305–313. https://doi.org/10.1016/S0926-860X(03)00367-3.
- [66] M. Li, F. Cárdenas-Lizana, M.A. Keane, Combined catalytic action of supported Cu and Au in imine production from coupled

- benzyl alcohol and nitrobenzene reactions, Appl. Catal. Gen. 557 (2018) 145–153. https://doi.org/10.1016/j.apcata.2018.03.024.
- [67] E.L. Ratcliff, J. Meyer, K.X. Steirer, A. Garcia, J.J. Berry, D.S. Ginley, D.C. Olson, A. Kahn, N.R. Armstrong, Evidence for near-Surface NiOOH Species in Solution-Processed NiOx Selective Interlayer Materials: Impact on Energetics and the Performance of Polymer Bulk Heterojunction Photovoltaics, Chem. Mater. 23 (2011) 4988–5000. https://doi.org/10.1021/cm202296p.
- [68] O.U. Valdés-Martínez, C.E. Santolalla-Vargas, V. Santes, J.A. de los Reyes, B. Pawelec, J.L.G. Fierro, Influence of calcination on metallic dispersion and support interactions for NiRu/TiO2 catalyst in the hydrodeoxygenation of phenol, Catal. Today. 329 (2019) 149–155. https://doi.org/10.1016/j.cattod.2018.11.007.
- [69] J.Y. Kim, J.A. Rodriguez, J.C. Hanson, A.I. Frenkel, P.L. Lee, Reduction of CuO and Cu2O with H2: H Embedding and Kinetic Effects in the Formation of Suboxides, J. Am. Chem. Soc. 125 (2003) 10684–10692. https://doi.org/10.1021/ja0301673.

# **CHAPTER 5**

# CuNi Bimetallic Nanocatalyst Enables Sustainable Direct Carboxylation Reactions

#### 5.1. Introduction

Heterogeneous catalysis has attracted tremendous attention in modern industry as it plays a vital role in the production of chemicals and pharmaceuticals. Heterogeneous catalysts offer many advantages over homogeneous catalysts including the high catalytic stability under reaction conditions and recyclability through the facile separation of the liquid or gaseous products from the solid catalyst. Among the different fields of heterogeneous catalysis, catalysis by transition metal nanoparticles is one of the most important, owing to their inherent properties that include variation of metal oxidation state, high surface energy which increases the activity of surface atoms, high surface-tovolume ratio, environmental abundance, and cost-effectiveness. [1,2] Hence, the use of transition metal nanoparticles as heterogeneous catalysts is an attractive alternative to homogeneous metal complexes.[3] Additionally, bimetallic nanoparticles have drawn a greater interest than monometallic nanoparticles due to the synergistic effects between individual metals present in the bimetallic system[4–6], leading to higher chemical activity and enhanced chemical, biological, and magnetic properties.[7,8] Specifically, magnetic bimetallic nanocatalysts show promise in heterogeneous catalysis owing to their ease of separation directly from the reaction mixture using an external magnet.[9]

The transformation of C-C and C-H bonds has a major impact on the field of organic synthesis and pharmaceutical industry for the production of natural products and various crucial intermediates.[10] Specifically, aromatic carboxylic acids have found tremendous applications in the pharmaceutical and chemical industry.[11,12] For example, benzoic acid and its derivatives are commonly used as antimicrobial preservatives, flavouring agents, and food additives. Owing to their application, significant research efforts have been devoted to developing new synthetic protocols to produce these value-added synthons. One of the most promising approaches is the direct carboxylation of aromatic compounds to their corresponding aromatic acid analogues. However, the direct functionalization of aromatic non-activated C-H bonds remains a daunting task in synthetic and organometallic chemistry due to the high chemical stability and inert nature of the arenes C-H bonds.[13]

However, the carboxylation of arenes proceeds via four major pathways: (i) base-mediated (i.e. Kolbe-Schmitt reaction type)[14] (ii) Lewis-acid-mediated (i.e. Friedel-Crafts reaction type) (iii) transitionmetal catalyzed, and (iv) enzymatic carboxylation.[15] The basemediated carboxylation involves the use of a base to avoid the formation of undesired H<sub>2</sub>O, however, high pressure of CO<sub>2</sub> is still required. The carboxylation via Lewis-acid mediated pathway involves the use of AlCl<sub>3</sub>/Al with CO<sub>2</sub> gas which occurs on the most nucleophilic site of arenes.[16] Additionally, several studies have reported the C-H carboxylation of aromatic activation and compounds using monometallic catalysts, including Pd[17], Cu[18], Ni[19], Ir[20], Rh[21] which either involve the use of highly toxic CO or chemically stable CO<sub>2</sub> gases with oxidizing agents. Besides, some studies used N,N'-dicyclohexylcarbodiimide (DCC) as an additive with formic acid for the carboxylation reaction which required a catalytic amount of DCC and pre-activated substrate such as aryl halide instead of benzene, in addition to high reaction temperature.[22] Although, due to the low electrophilicity and high stability of CO2 and high toxicity of CO gases[23] developing alternative carboxylation protocols with reactive and eco-friendly carboxylating agents is highly desirable. Also, the existing procedure involves the use of non-recyclable, precious metal

complexes as catalysts with high loadings, oxidants, or activators along with the high reaction temperature and time. Henceforth, the development of a recyclable, cost-effective heterogeneous catalyst for the carboxylation of arene via an activator-free, gas-free, and additive-free approach needs to be explored.

In this context, formic acid is a suitable carbonyl source, owed to its non-toxicity, accessible synthetic approaches, and cost-effectiveness due to its availability as a by-product from the industrial sector.[24,25] Also, formic acid can be used as an alternative to CO and CO<sub>2</sub> gases for the carboxylation of arenes.[22,26] Moreover, several computational studies have been reported so far to elucidate the catalytic activation and decomposition strategies of formic acid on monometallic transition metal surfaces, such as Pt,[27] Cu,[28,29] Ni,[30,31] Au[32,33] and Pd[31] and bimetallic transition surfaces such as PtPd[34] and PdCu.[35,36] These studies pave the path for utilization of formic acid on copper and nickel metal surfaces for carboxylation reactions due to low cost and high abundance[37,38] over expensive metals like Pd, Pt, Ru, Rh noble metals as for industrial process, the cost-effectiveness is an important factor.

Keeping this in mind, we have explored and synthesized CuNi bimetallic nanocatalyst for the conversion of benzene with the use of formic acid in solvent-free condition for sustainable and environmentally benign approach.[24,39,40] Herein, we explored catalytic experiments in conjunction with DFT calculations to report an easily synthesizable, magnetically recoverable CuNi-11 bimetallic nanocatalyst for the catalytic conversion of arenes utilizing formic acid, with an activator-free, gas-free and solvent-free approach.

# 5.2. Experimental

#### 5.2.1. Materials

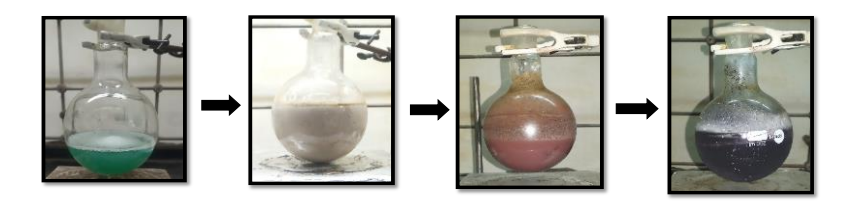
Cetyl trimethyl ammonium bromide (CTAB) ≥99% pure, copper chloride (CuCl<sub>2</sub>) anhydrous ≥99.99% pure, and nickel chloride hexahydrate (NiCl<sub>2</sub>.6H<sub>2</sub>O) ≥99.9% pure were purchased from Merck, India. Hydrazine hydrate (N<sub>2</sub>H<sub>4</sub>.H<sub>2</sub>O) 80% in water, sodium hydroxide pellets (NaOH) 98% pure, aryl compounds ≥98-100% pure, and formic acid 98% were purchased from Sigma-Aldrich. All solvents were used as received.

# 5.2.2. Catalyst preparation

Three nanocatalyst with Cu:Ni molar ratios of 1:1 (CuNi-11), 1:2 (CuNi-12), and 2:1 (CuNi-21) were synthesized.<sup>1,2</sup> The synthesis procedure of CuNi-11 is illustrated in **Scheme 5.1**. First, 292 mg CTAB were added into 100 mL deionized water in a 1000 mL round bottom flask. The solution was stirred at room temperature for 10 minutes. 2.7 g CuCl<sub>2</sub> and 5.3 g NiCl<sub>2</sub>.6H<sub>2</sub>O were added to the mixture, forming a green solution. After 1 hour, 20 mL of N<sub>2</sub>H<sub>4</sub>.H<sub>2</sub>O were added, changing solution colour to coffee brown. We note that N<sub>2</sub>H<sub>4</sub>.H<sub>2</sub>O acts as a reducing agent and provides N<sub>2</sub> inert atmosphere to the reaction as follows:

$$Ni^{2+} + Cu^{2+} + N_2H_2 + OH^-$$
 Ni + Cu + N<sub>2</sub> + H<sub>2</sub>O

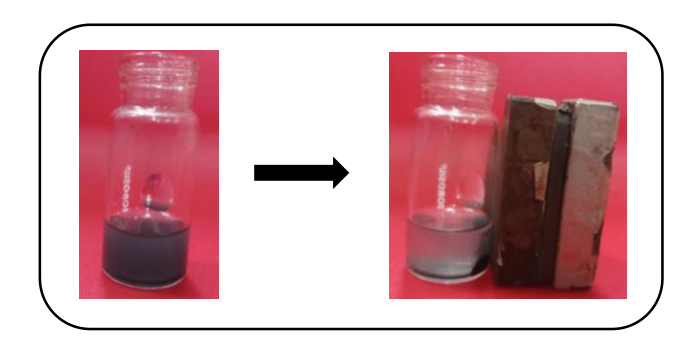
After 1 hour, the required amount of NaOH solution was added into the above mixture till pH approximate 11-12 with an ice bath producing a black solution. After stirring the solution for 6 hours, excess acetone was added into the reaction mixture to remove the excess CTAB. After vacuum filtering the black magnetic precipitate, CuNi nanocatalyst with a 1:1 molar ratio was obtained which named as CuNi-11.



Following the same methodology, and utilization of CuCl<sub>2</sub> and NiCl<sub>2</sub>.6H<sub>2</sub>O as metal chlorides, monometallic Cu and Ni nanocatalysts were synthesized.

#### 5.2.3. General catalytic carboxylation reaction

"The carboxylation reaction was performed in 15 mL sealed glass vial with a cap equipped with a magnetic stirrer bar. In the glass vial, aryl substrate (1 mmol), formic acid (12-15 mmol), and catalyst (15 mg or 0.0096 mol%) were stirred for required time at 55 °C. After completion of the reaction, the reaction mixture was cooled at room temperature. After that, the catalyst was removed with an external magnet and the reaction mixture was diluted with ethyl acetate and dried over vacuum and given for GC-MS analysis with HPLC methanol for recording conversion and selectivity. The recovered catalyst is washed with ethanol and water several times and dried at room temperature overnight. After each run, the catalyst was recovered and washed with the same procedure."



#### 5.2.4. Physicochemical measurements

The details about the PXRD, TGA, FE-SEM, HR-TEM, BET characterization and utilized instruments have been discussed in chapter 2 in physicochemical measurements section. However, the EDAX

elemental analysis and mapping was done by using Zeiss-Gemini Field-Emission Scanning Electron Microscope. FT-IR analysis was performed using PerkinElmer Spectrum at 400 to 4000 cm<sup>-1</sup>. The details about XPS and VSM analysis were discussed already in Chapter 3 in physicochemical measurements section. The leaching of the catalysts was analysed by using Inductively Coupled Plasma (ICP-OES) instrument with Model number: Nexion 2000B ICP-MS (Perkin Elmer). Identification of the products of catalytic reactions was carried out using Shimadzu GC-MS, QP2010 Mass Spectrometer and RTX-5 tubular diphenyl dimethyl polysiloxane capillary column, 30 m long, 0.25 mm diameter, and df value of 1.0 μm. The formation of substituted benzoic acids was confirmed by <sup>1</sup>H and <sup>13</sup>C NMR analysis using NMR Spectrometer, Model AVANCE III 400 MHz.

#### **5.2.5.** Computational Methods

Electronic structure calculations were performed at the Density Functional Theory (DFT) level using the CP2K package.[43] The Perdew-Burke-Ernzerh of exchange-correlation functional [44] was used in conjunction with Grimme's D3 method to account for adsorbatesurface dispersion interactions.[45] The core electrons of the atoms were treated using Goedecker, Teter, and Hutter pseudopotentials.<sup>6-8</sup> The electronic wavefunctions of Cu and Ni atoms were described using the double-ζ valence polarized basis sets, whereas triple-ζ valence polarized basis sets were used for C, O, and H with a kinetic cutoff of 600 Ry. [49] All structures relaxed using were Broyden-Fletcher-Goldfarb-Shanno minimization algorithm until forces between the atoms were less than  $4.0 \times 10^{-4}$  Hartree Bohr<sup>-1</sup>, with SCF threshold of 10<sup>-6</sup> Hartree. The minimum energy pathway for benzene carboxylation was investigated using climbing image nudged elastic band (CI-NEB) calculations.[50] Potential transition states were further tuned with the dimer method and verified with vibrational frequency analysis to have a single imaginary frequency along the reaction coordinate.

The crystalline structure of the most thermodynamically stable form of bimetallic CuNi-11 (i.e. face-centered cubic, FCC) was constructed by replacing 2 Ni atoms in an FCC Ni<sub>4</sub> conventional cell with 2 Cu atoms. The calculated lattice constants for the chemically ordered 1:1 Ni-Cu binary system are a = 3.49 Å, b = c = 3.61 Å, consistent with previous theoretical calculations. 11-13 The most stable (111) surface of CuNi was modelled by a periodic three-layered slab with a vacuum region in excess of 20 Å to avoid periodic interaction between slabs in the surface normal direction. The three-layered slab is testified and benchmarked in previous literature to be a reasonable model for adsorption and reaction mechanism studies through comparison with experiments and results of four- and five-layered models. 11,13-15 To reduce the computational load, the top two layers and the adsorbates were allowed to relax during geometry optimization and transition state search, whereas the bottom layer was fixed at its equilibrium bulk phase position.[51] Adsorption energies of the adsorbates on the surface were calculated based on the following equation:

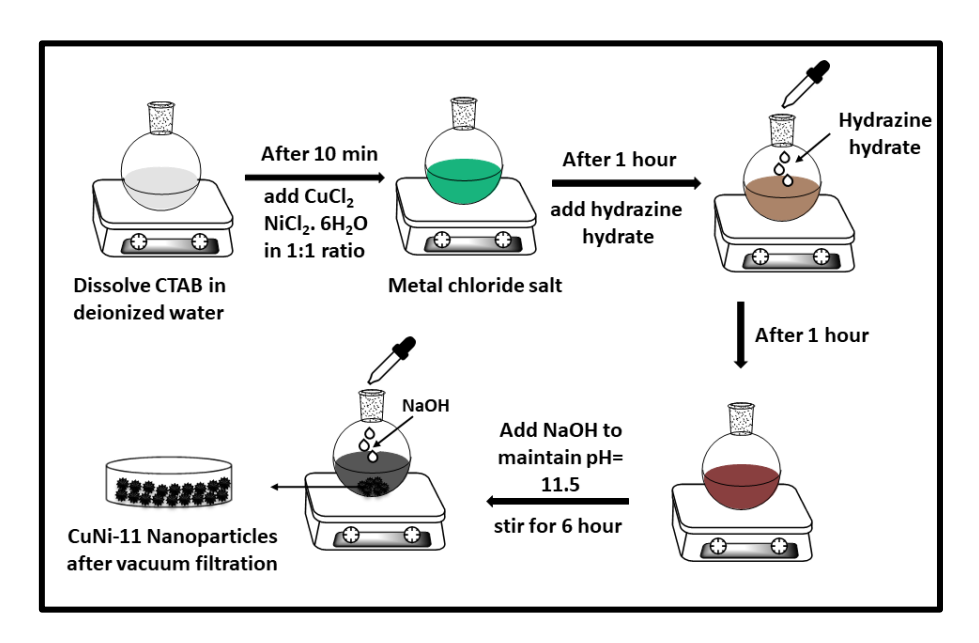
$$E_{ads} = E_{adsorbate/surface} - E_{clean surface} - E_{adsorbate}$$

where  $E_{adsorbates/surface}$  is the total energy of adsorbates on the surface,  $E_{clean\,surface}$  is the total energy of bare (111) CuNi surface, and  $E_{adsorbate}$  is the total energy of isolated adsorbate in the gas phase which was calculated by placing the isolated adsorbates in a cubic box of  $15\text{Å} \times 15\text{Å} \times 15\text{Å}$ . To evaluate solvent effects, single point energy calculations including solvation were further performed on the fully optimized gas phase structures. Solvent effects were considered through the self-consistent continuum solvation model by Andreussi  $et\,al.$  using formic acid as the solvent.[56]

#### 5.3. Results and discussion

# 5.3.1. Characterization of bimetallic CuNi-11 nanocatalysts

The synthesis of all CuNi nanocatalysts was performed by varying the Cu:Ni molar ratios such as CuNi-11(1:1), CuNi-12(1:2), CuNi-21(2:1), and monometallic Cu and Ni were also considered (**Scheme 5.1**).



**Scheme 5.1.** Schematic representation of the synthesis of CuNi-11 nanocatalyst.

All the synthesized nanocatalysts including CuNi-11, CuNi-12, CuNi-21, monometallic Cu, and monometallic Ni were synthesized and characterized by PXRD analysis (**Figure 5.1**).

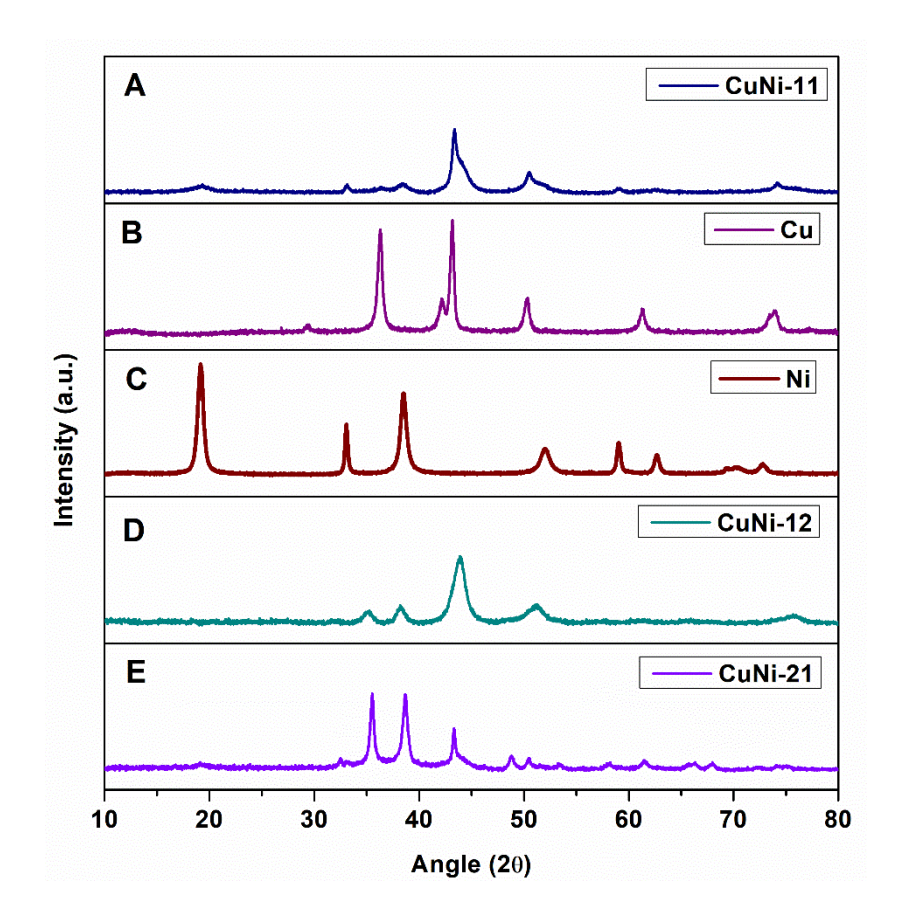


**Figure 5.1.** PXRD analysis of all synthesized nanocatalysts (i) CuNi-11, (ii) Cu, (iii) Ni, (iv) CuNi-12, (v) CuNi-21.

The PXRD analysis of CuNi-11 showed diffraction peaks at  $19.05^{\circ}$ ,  $33.22^{\circ}$ ,  $38.34^{\circ}$ ,  $58.94^{\circ}$ , and  $62.54^{\circ}$  corresponding to (001), (100), (101), (110), and (111) planes, respectively, which imply the presence of  $\beta$ -Ni(OH)<sub>2</sub> (JCPDS #14-0117) as shown in **Figure 5.2A**.[57,58] The diffraction peaks at  $43.41^{\circ}$ ,  $50.49^{\circ}$ , and  $74.16^{\circ}$  corresponded to (111), (200), and (220) planes, respectively, which are attributed to Cu (JCPDS#04-0836). [59,60] The PXRD peaks of CuNi-11 nanoparticles was compared with monometallic Cu and Ni nanoparticles (**Figure 5.1**), the shift in PXRD peaks suggested that the synthesized CuNi-11 nanoparticles is an alloy. The average crystallite size calculated by the Debye Scherrer equation was found to be 5 nm.

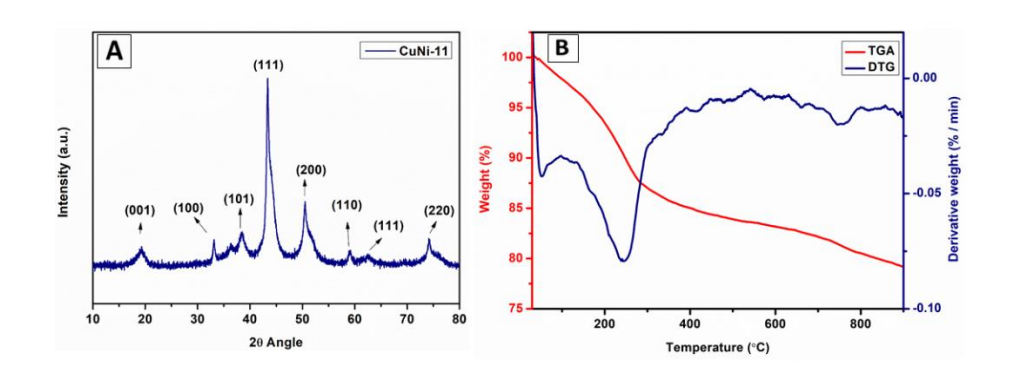


**Figure 5.2.** (**A**) PXRD spectra and (**B**) thermogravimetric analysis of CuNi-11 nanocatalyst.

Thermogravimetric analysis (TGA) was performed to check the thermal stability (**Figure 5.2B**) under N<sub>2</sub> atmosphere from 30 °C to 800 °C. There were two major weight losses observed in the region of (i) up to 250 °C and (ii) above 250 °C. The weight loss in these regions was observed at 8.29 wt% and 4.64 wt%, respectively. The first weight loss is due to the partial removal of adsorbed CTAB and water molecules[41,64] or decomposition of CTAB which was attached to the surface of CuNi-11. The second weight loss was attributed to the complete oxidation of CTAB layer capping. These results indicate the high thermal stability of the synthesized bimetallic CuNi-11 nanocatalyst up to high temperatures. For better clarification of weight loss with increasing the temperature, the differential derivative thermogravimetric analysis (DTG) was also added in **Figure 5.2B**.

Furthermore, the FT-IR spectrum of bimetallic CuNi-11 nanocatalyst was performed (**Figure 5.3**) and the absorption peaks at 3406 cm<sup>-1</sup> indicate the presence of CTAB for OH vibration of hydroxyl group.[61,62] The peaks at 2918, 1716, 1257 cm<sup>-1</sup> attributed to C-H stretching bands of CTAB surfactant.[63] The absorption peaks at 1636, 1496 cm<sup>-1</sup> attributed to asymmetric and symmetric stretching vibrations of N<sup>+</sup>—CH<sub>3</sub> and 760 cm<sup>-1</sup> assigned for Br<sup>-</sup> of CTAB.[9] The absorption peak at 455 cm<sup>-1</sup> was may be because of stretching vibration of metalmetal i.e. Cu-Ni band.[63] This data revealed the capping of CTAB on bimetallic CuNi-11 nanocatalyst.

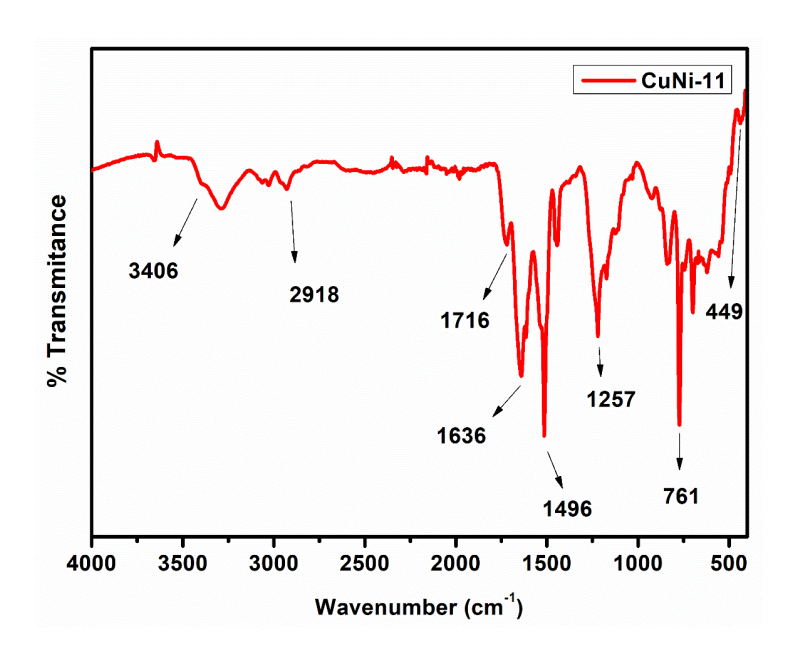


**Figure 5.3.** FT-IR spectrum of bimetallic CuNi-11 nanocatalyst.

High surface area plays a key role to enhance the catalytic performance. Thus, to quantify the surface area of the synthesized bimetallic catalysts, the N<sub>2</sub> adsorption-desorption studies were performed by employing Brunauer-Emmett-Teller (BET) surface area analyzer at 77 K and 1 bar. The calculated specific surface area, pore size, and pore volume were found to be 58.993 m<sup>2</sup>/g, 7.76 nm, and 0.136 cm<sup>3</sup>/g, respectively (**Figure 5.4**). The N<sub>2</sub> adsorption curve exhibited type IV isotherm with H3 hysteresis loop, indicating the presence of mesopores. [65,66] Moreover, CO<sub>2</sub> adsorption-desorption studies performed at 298 K and 1 bar revealed maximum CO<sub>2</sub> uptake of 95.546 m<sup>2</sup>/g. The results demonstrate that the CuNi-11 nanocatalyst is more selective towards CO<sub>2</sub> over N<sub>2</sub>, showing a potential for application of CuNi-11 nanocatalyst in CO<sub>2</sub> capture technologies. [67,68]

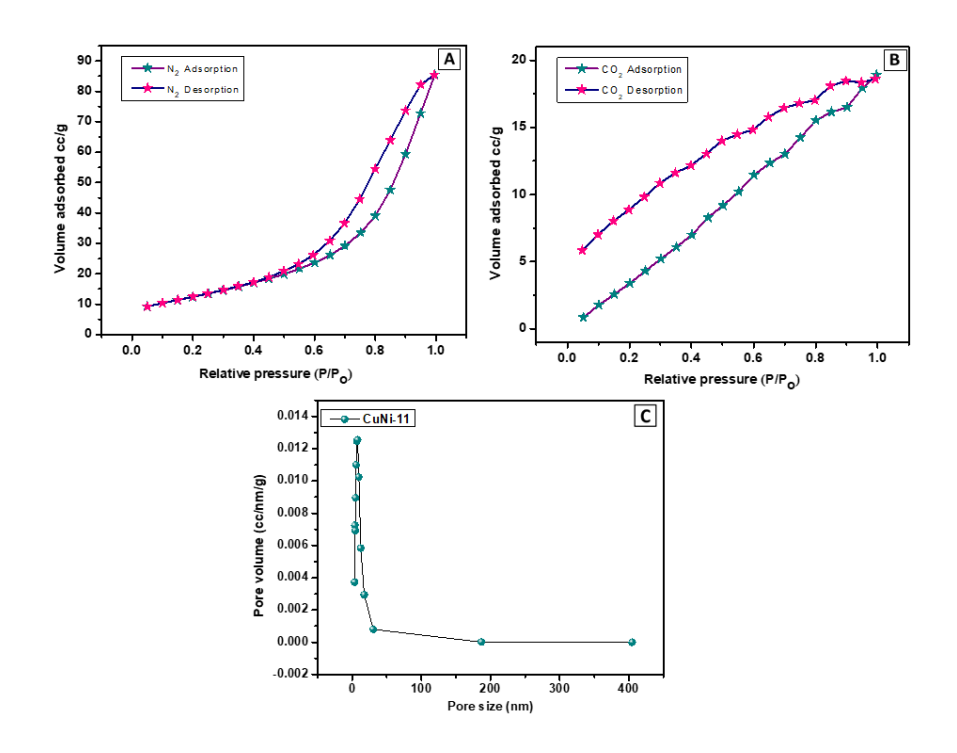


**Figure 5.4.** (**A**) N<sub>2</sub> adsorption-desorption (**B**) CO<sub>2</sub> adsorption-desorption (**C**) BJH pore-size distribution isotherm of CuNi-11 nanocatalyst.

Surface morphology plays an important role in the catalytic activity and selectivity[69,70] and for that, the surface morphological studies were performed using FE-SEM analysis of the CuNi-11 nanocatalyst. The overall morphology revealed nanoflakes type structures which were arranged in nanoflower-like shapes (**Figure 5.5(A-B)).** [71,72] Furthermore, the elemental analysis and mapping of CuNi-11 nanocatalyst confirmed the presence of Cu and Ni elements with a 1:1 wt% ratio (**Figure 5.5(C-E)**). Furthermore, the detailed morphology of the synthesized bimetallic CuNi-11 nanocatalyst was analyzed using HR-TEM (**Figure 5.6(A-C)**). The observed images were in accordance with FE-SEM imaging of nanoflakes-like structures. Additionally, the d-spacing was calculated from TEM images to be 0.27, 0.18, and 0.15 nm for (100), (110) planes of  $\beta$ -Ni(OH)<sub>2</sub>, and (200) plane of copper metal nanocatalysts (**Figure 5.6C**).[73] The d–spacing of the planes matched well with PXRD data peaks (**Figure 5.2A**). Further, the

SAED pattern showed the concentric rings which confirmed the crystalline nature of CuNi-11 nanocatalyst (**Figure 5.5D**).

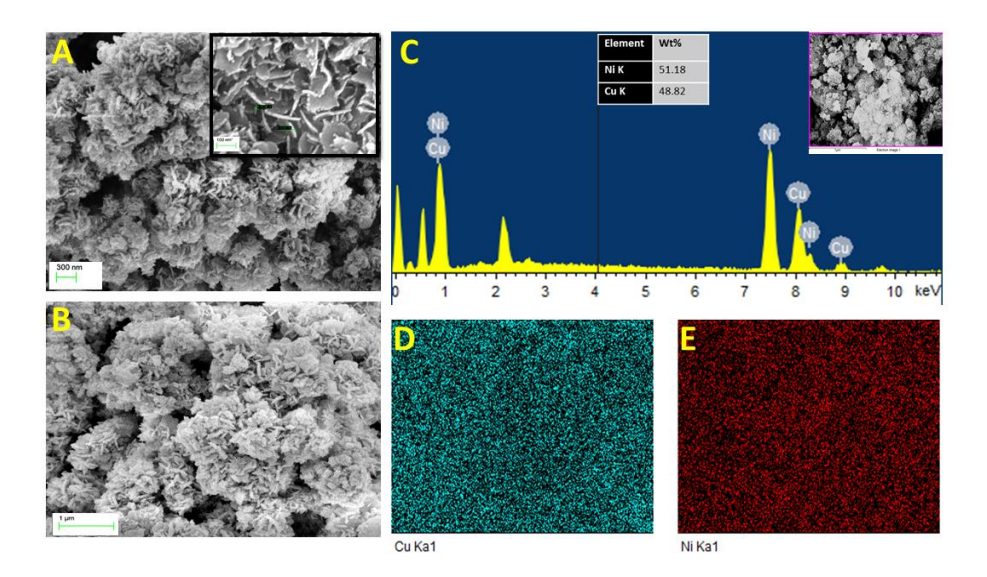


**Figure 5.5.** SEM images of CuNi-11 nanoflower at (**A**) 300 nm (in inset magnified image of flakes scale at 100 nm) and (**B**) 1 μm. (**C**) EDX pattern of CuNi-11 nanocatalyst, (**D**) elemental mapping of copper, and (**E**) nickel element.

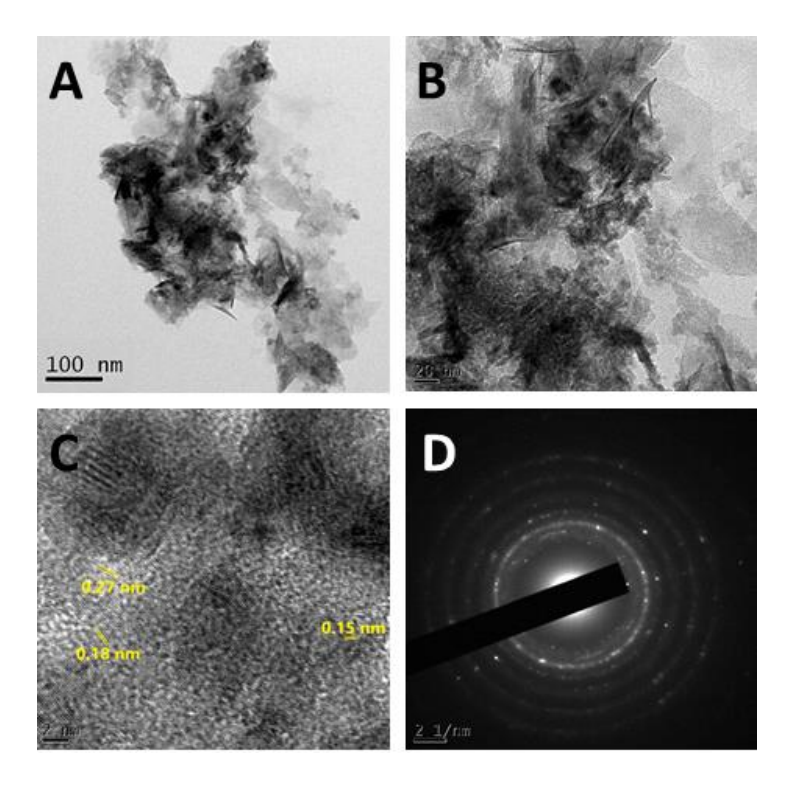


**Figure 5.6.** TEM images of CuNi-11 nanocatalyst at (**A**) 100 nm (**B**) 20 nm (**C**) 2 nm and (**D**) SAED pattern.

Furthermore, magnetic study of CuNi-11 nanocatalyst was performed using a vibrating-sample magnetometer (VSM), confirming the ferromagnetic nature of CuNi-11 (**Figure 5.7**). [74] Magnetic properties of CuNi-11 were studied at room temperature with an applied field of ±20.0 kOe. The values of saturation magnetization (M<sub>s</sub>), remanence (M<sub>r</sub>), remanence to saturation ratio (M<sub>r</sub>/M<sub>s</sub>), and coercivity (Hc) were calculated from the obtained M-H loop curve. These values were found to be 10.27 emu/g, 1.30 emu/g, 0.13, 75.48 Oe for M<sub>s</sub>, M<sub>r</sub>, M<sub>r</sub>/M<sub>s</sub>, and H<sub>c</sub>, respectively. Overall, these results highlight the ferromagnetic nature of bimetallic CuNi-11 nanocatalyst.[59,74]

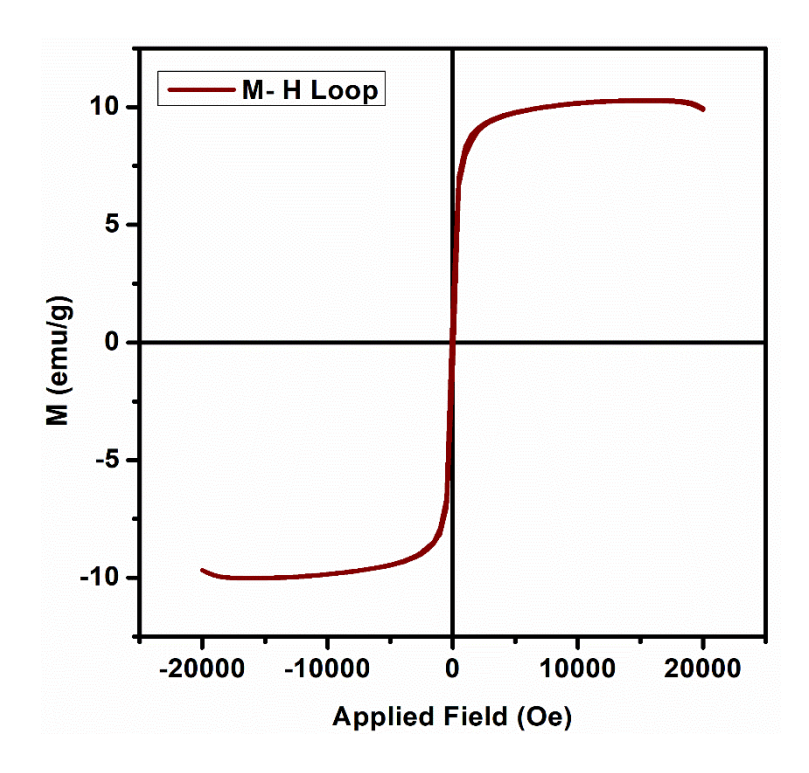
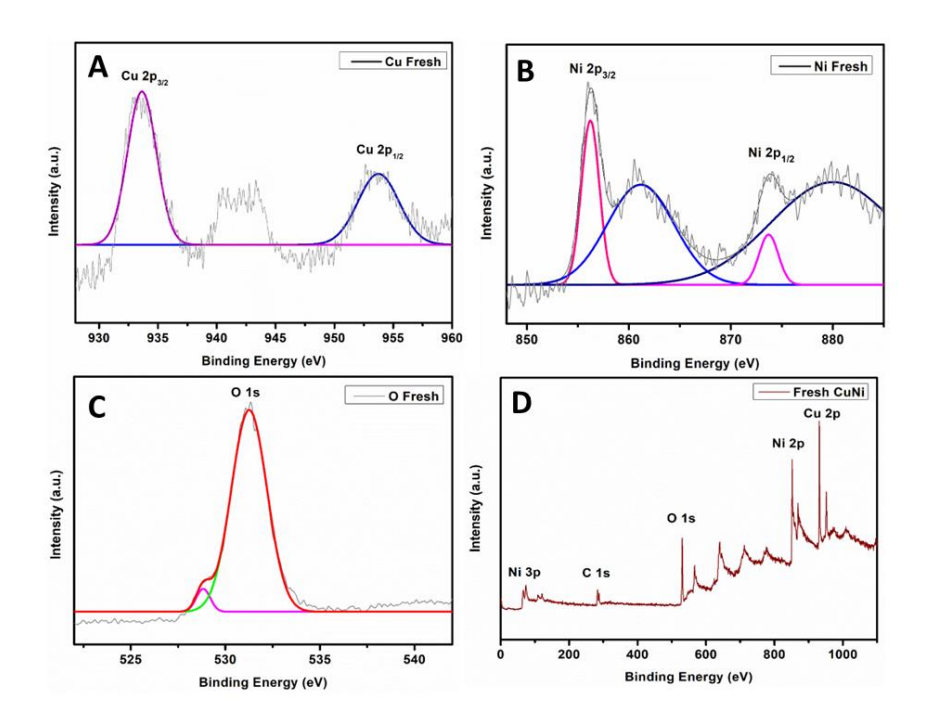


Figure 5.7. Magnetic hysteresis curve of CuNi-11 nanoparticle.

Finally, X-ray photoelectron spectroscopy (XPS) analysis was performed to confirm the chemical composition and the oxidation state of the catalyst (**Figure 5.8**). The XPS spectra of Cu 2p exhibited two broad peaks of Cu 2p<sub>3/2</sub> and Cu 2p<sub>1/2</sub> at 933.6 eV and 953.6 eV, respectively, for the presence of CuO (i.e. Cu<sup>2+</sup>) as a result of surface oxidation of metallic copper (**Figure 5.8A**). [75,76] On the other hand, the XPS spectra of Ni 2p exhibited two peaks of Ni 2p<sub>3/2</sub> and Ni 2p<sub>1/2</sub>

(**Figure 5.8B**). The peak at 855.7 eV and the satellite peak at 861.2 eV for Ni  $2p_{3/2}$  and at 873.3 eV and its satellite peak at 879.9 eV for Ni  $2p_{1/2}$  for Ni<sup>+2</sup> of Ni(OH)<sub>2</sub>.[77,78] The peak separation of 17.6 eV in Ni  $2p_{3/2}$  and Ni  $2p_{1/2}$  confirmed the formation of Ni(OH)<sub>2</sub> due to the spin-orbit coupling phenomenon.[79–81] Moreover, the O 1s peak observed at 531.2 eV confirmed the presence of hydroxide which supports the formation of nickel hydroxide in CuNi-11 nanocatalyst as shown in **Figure 5.8(C**). [82,83] The survey scan confirmed the presence of Cu, Ni, and O elements (**Figure 5.8D**).



**Figure 5.8.** XPS spectra of (**A**) Cu 2p, (**B**) Ni 2p, (**C**) O 1s and (**D**) survey scan of synthesized CuNi-11 nanocatalyst.

Furthermore, the XPS spectra of recovered catalyst were also performed, confirming the reduction of CuNi-11 nanocatalyst to Cu(0)/Ni(0) in presence of HCOOH (**Figure 5.9(A-C**)). The XPS spectra of copper Cu  $2p_{3/2}$  and Cu  $2p_{1/2}$  present at 932.7 eV and 953.2 eV for the formation of Cu(0).[84,85] Additionally, the XPS spectra of Ni  $2p_{3/2}$  and Ni  $2p_{1/2}$  observed at 852.1 eV and their satellite peaks shown in **Figure 5.9(B)** confirmed the presence of Ni metallic character.[86,87]

This is an important observation since the alloy Cu(0)/Ni(0) appears to be the active catalyst form during catalytic operation.

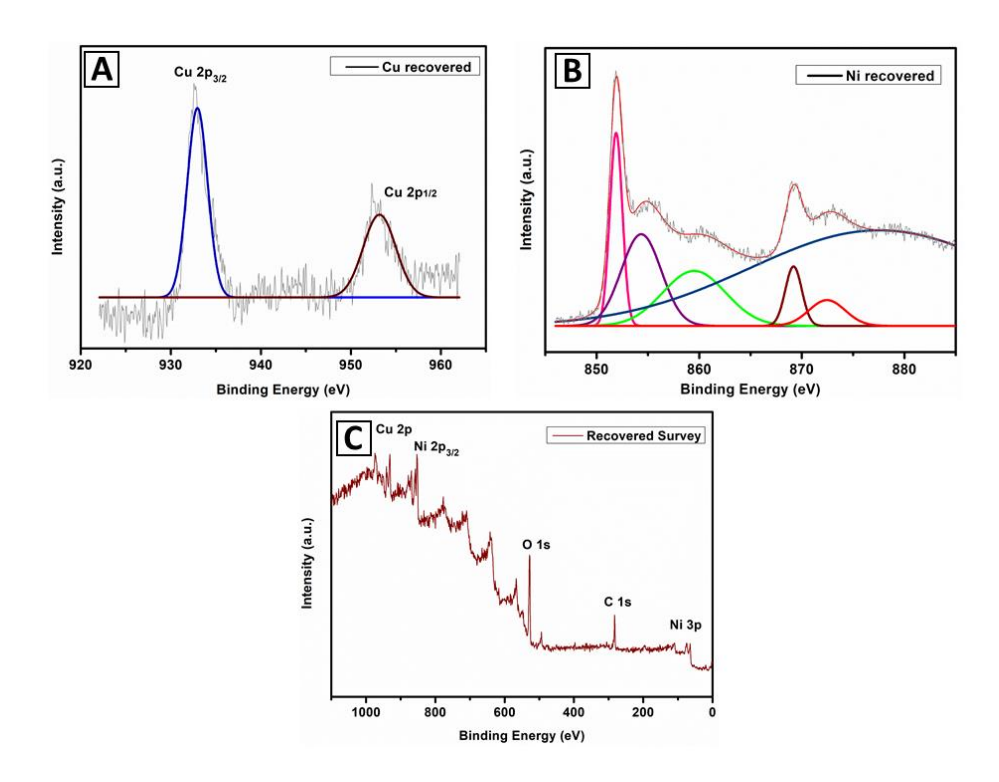


**Figure 5.9.** XPS spectra of **(A)** Cu 2p, **(B)** Ni 2p, **(C)** survey scan of recovered CuNi-11 nanocatalyst.

#### 5.3.2. Catalytic results

The catalytic carboxylation reaction of different substituted benzenes using the CuNi-11 nanocatalyst in the presence of formic acid as carboxylating agent and solvent-free conditions has been performed. Initially, several catalysts including monometallic Cu and Ni, CuCl, CuNi-11, CuNi-12, and CuNi-21 were screened for the direct carboxylation of benzene using 12 mmol of formic acid for 20 hours at 55 °C temperature (**Figure 5.10**). Based on previous reports,[88,89] the concept of a Lewis-acid mediated pathway was also explored by using CuCl which provided only 9% conversion and ruled out the possibility of that pathway. The reaction with monometallic Cu, monometallic Ni, CuNi-12, and CuNi-21 revealed that excess Cu and/or Ni suppress the catalytic activity, whereas an equimolar ratio of Cu and Ni species is essential for enhanced catalytic performance.[90] The synergistic effect

in between Cu and Ni metal enhances the catalytic activity and provides 100% conversion for the same reaction whereas monometallic Cu and Ni metal shows only 41% and 68% conversion of benzene into benzoic acid. The best result was obtained with CuNi-11 nanocatalyst with 100% conversion and 100% selectivity. The obtained data indicate the importance of bimetallic CuNi nanocatalyst for the catalytic conversion of benzene. Therefore, all catalytic reactions were carried out with CuNi-11 nanocatalyst.

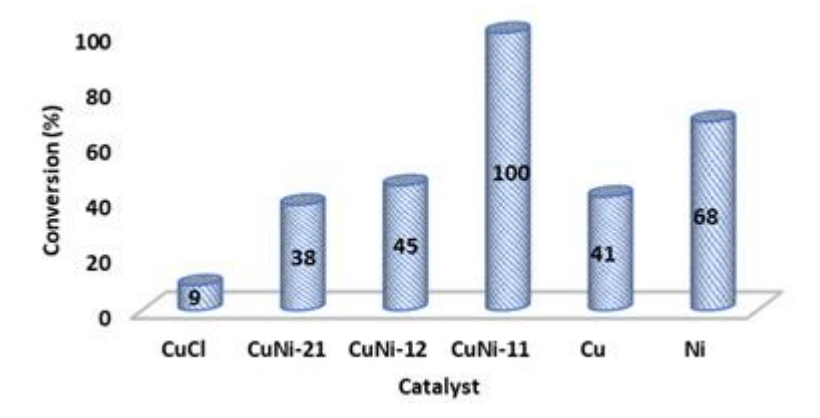


**Figure 5.10.** Effect of different catalysts on the conversion of benzene to benzoic acid. **Reaction conditions:** Substrate (benzene) = 1 mmol, catalyst (CuNi-11) = 15 mg, formic acid = 12 mmol, solvent = 2 mL, time = 20 h, temperature =  $55 \, ^{\circ}\text{C}$ .

The systematic investigation of carboxylation reactions was performed using benzene as a model substrate to efficiently select the optimal reaction conditions (e.g. loading of solvent, concentration of formic acid and substrate, reaction time and temperature). To examine the influence of solvent (2 mL), various solvents such as 2-propanol, methanol, water, and methanol-water mixture (1 mL each) were screened with HCOOH (12 mmol), catalyst (15 mg) for 20 hours. Remarkably, the highest conversion was obtained when the reaction was solvated with either water (100% conversion) or a water-methanol mixture (95% conversion) (**Table 5.1**). Surprisingly, a solvent-free carboxylation reaction also resulted in a maximum 100% benzene conversion and 100% selectivity to benzoic acid. Consequently, the

solvent-free reaction was preferred to avoid the post-work-up process of the reaction mixture.[40,91] It is to be noted that formic acid may play the role of the solvent medium in the reaction mixture as all reagents were present in the liquid form.

**Table 5.1**. Effect of solvent on the conversion of benzene into benzoic acid

Entry	Solvent (2 mL)	CuNi-11 (mg)	Formic acid (mmol)	Conversion (%)
1	H <sub>2</sub> O	15	15	100
2	МеОН	15	15	71
3	H <sub>2</sub> O:MeOH	15	15	95
4	2-Propanol	15	15	47
5	-	15	15	100

**Reaction conditions**: Substrate (benzene) = 1 mmol, catalyst (CuNi-11) = 15 mg, formic acid = 15 mmol, solvent = 2 mL, time = 20 h, temperature = 55 °C.

Furthermore, the reaction in solvent-free conditions was carried out by varying the formic acid amount between 5 to 15 mmol, with benzene (1 mmol) and CuNi-11 (15 mg) for 20 hours. It was observed that the conversion of benzene depends significantly on the amount of HCOOH, as shown in **Table 5.2**. As the formic acid amount decreases, the conversion of benzene decreases and with 5 mmol of formic acid no conversion was observed whereas the 100% conversion was observed with 12 and 15 mmol of formic acid. Hence, further all the reactions were carried out with 12 mmol of formic acid.

**Table 5.2.** Effect of amount of formic acid on carboxylation of benzene

Entry	Formic acid (mmol)	CuNi-11 (mg)	Conversion (%)
1	5	15	-
2	8	15	17
3	10	15	77
4	12	15	100
5	15	15	100

**Reaction conditions**: Substrate (benzene) = 1 mmol, catalyst (CuNi-11) = 15 mg, formic acid = 5-15 mmol, time = 20 h, temperature = 55 °C.

Thereafter, the effect of benzene concentration (1-2.5 mmol) was carried out with HCOOH (12 mmol), CuNi-11 (15 mg) for 20 hours at 55 °C. A complete 100% conversion of benzene to benzoic acid was obtained using 1 mmol of benzene (**Table 5.3**). These results showed that as the substrate amount increases, the conversion decreases.

**Table 5.3.** Effect of substrate amount on carboxylation reaction of benzene

Entry	Substrate (mmol)	Formic acid (mmol)	Conversion (%)
1	1	12	100
2	1.5	12	47
3	2	12	33
4	2.5	12	15

**Reaction conditions:** Substrate (benzene) = 1-2.5 mmol, catalyst (CuNi-11) = 15 mg, formic acid = 12 mmol, time = 20 h, temperature =  $55 \, ^{\circ}$ C.

Moreover, a control experiment without catalyst resulted in only 17% conversion, whereas 100% conversion was obtained when 15 mg of CuNi-11 nanocatalyst was utilized (**Table 5.4**). This result showed the importance of the synthesized bimetallic CuNi-11 catalyst for the carboxylation of benzene to benzoic acid.

**Table 5.4**. Effect of catalyst amount loading on carboxylation of benzene

Entry	CuNi-11 (mg)	Formic acid (mmol)	Conversion (%)	
1	1	12	17	
2	3	12	36	
3	6	12	47	
4	9	12	58	
5	12	12	80	
6	15	12	100	

**Reaction conditions:** Substrate (benzene) = 1 mmol, catalyst (CuNi-11) = 0-15 mg, formic acid = 12 mmol, time = 20 h, temperature = 55 °C.

The influence of temperature was studied on the carboxylation reaction. When the reaction was carried out at either room temperature and 40 °C for 20 h, benzene conversion was 12% and 72%, respectively. A maximum 100% conversion with 100% selectivity was obtained at 55 °C in 20 hours (**Figure 5.11**). Hence, the final optimized reaction conditions for carboxylation of benzene were 1 mmol of benzene, 12 mmol of HCOOH, and 15 mg of CuNi-11 catalyst along with a reaction temperature of 55 °C and reaction time of 20 hours to achieve complete benzene conversion and selectivity.

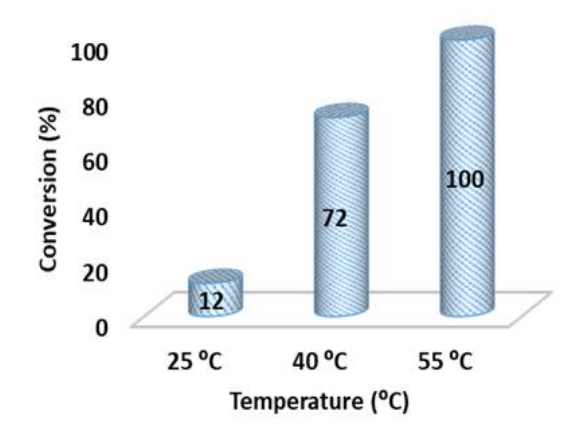


**Figure 5.11.** Effect of temperature on the carboxylation reaction of benzene. **Reaction conditions:** Substrate (benzene) = 1 mmol, catalyst

(CuNi-11) = 15 mg, formic acid = 12 mmol, temperature = 25-55  $^{\circ}$ C, time = 20 h.

Furthermore, to check the applicability of the reaction, carboxylation of some simple substituted arenes including toluene, haloarenes (-Br, -Cl, -F), phenol, aniline, naphthalene, and pyridine were explored under the identified optimized reaction conditions (**Table 5.5, Entry 1-9**). Additionally, the reaction is also applicable to solid arenes such as naphthalene, using methanol as solvent (2 mL), which requires a longer reaction time to achieve 100% conversion and 100% selectivity (**Table 5.5, Entry 5**). All products and conversions were confirmed by Shimadzu GC-MS and NMR analysis (**Section 5.5 and 5.6**). The general catalytic reaction for carboxylation reaction as shown in **Scheme 5.2**.

COOH

CuNi-11

HCOOH, 55 °C

$$R_1$$
 $R_1$ = -H, -Me, -Cl, -Br

 $R_1$ 

COOH

CuNi-11

HCOOH, 55 °C

**Scheme 5.2.** Catalytic conversion reaction scheme of substituted benzene to corresponding benzoic acids using CuNi-11 nanocatalyst.

**Table 5.5.** Carboxylation of selected substituted arenes into their corresponding acids.

Entry	Substrate	Product	Time (h)	Conv. (%)
1		СООН	20	100
2		СООН	30	100
3	Br	Вг	31	100
4	CI	СООН	31	100
5	F	ГСООН	30	100
6	H <sub>2</sub> N	H <sub>2</sub> N COOH	29	100
7	НО	НО	35	100
8		COOH	28	100
9 <sup>a</sup>		СООН	40	100

**Reaction conditions**: Substrate = 1 mmol, catalyst (CuNi-11) = 15 mg (0.0096 mol%), formic acid = 12 mmol, time = 20-40 h, temperature = 55 °C. <sup>a</sup>Methanol used as solvent due to solubility issue in water.

The kinetic study of the carboxylation reaction was performed using benzene as a model substrate by taking samples periodically at 4, 10, 15, and 20 hours and around 17, 47, 76, and 100% conversion was observed (**Figure 5.12A**). Furthermore, the recyclability of the catalyst has been studied with model substrate benzene. After each run, the reaction mixture was separated with a magnet, then washed and dried overnight at room temperature. The recycled catalyst was reused for up to six consecutive cycles (**Figure 5.12B**).

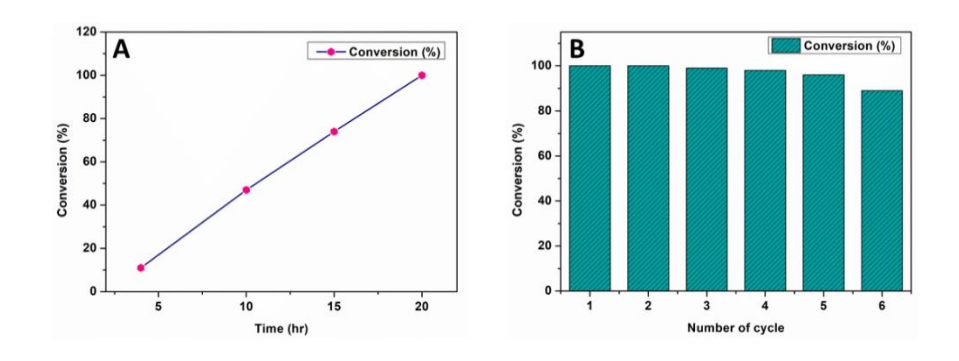


**Figure 5.12. (A)** Kinetic study and **(B)** Catalyst reusability of the carboxylation reaction of benzene for all the cyclic runs. **Reaction conditions:** Substrate (benzene) = 1 mmol, Catalyst (CuNi-11) = 15 mg, formic acid = 12 mmol, time = 4-20 h, temperature =  $55 \, ^{\circ}$ C.

To check the leaching of the catalyst, hot-filtration test was performed.[4,92] The reaction was stirred for 4 hours, and the catalyst was separated with a magnet. Then, the reaction mixture was filtered using a filter paper. Further, the supernatant was proceeded and stirred as reaction mixture to react without catalyst and the sample was taken for GC-MS analysis. There was no conversion observed after catalyst removal, indicating no leaching of the Cu and Ni metals. Also, the supernatant was characterized via ICP-OES and the analysis reveals no significant leaching of Cu and Ni metals (**Table 5.6**).

**Table 5.6.** ICP-OES analysis of reaction mixture for leaching of the bimetallic CuNi-11 nanocatalyst.

Sample	ICP-OES (ppm)		
CuNi-11	Cu	Ni	
	0.6466	0.8797	

Further, to check the morphological changes in the recovered catalyst, FE-SEM was performed in which no significant changes were observed in the structure of the recovered catalyst (**Figure 5.13**). These results reveal that the synthesized catalyst is recyclable, reusable, and robust in nature.

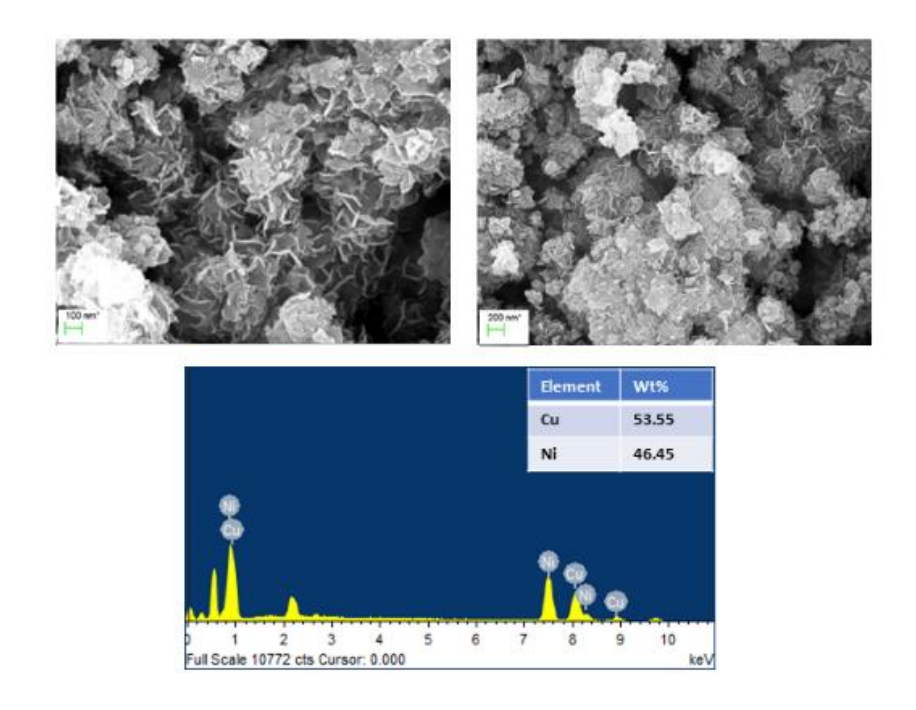


Figure 5.13. FE-SEM images of recovered CuNi-11 nanocatalyst.

Additionally, to get more evidence of the formation of benzoic acid, Fourier transformation infrared spectroscopy (FT-IR) was performed on the isolated product. The analysis showed absorbance peaks at 3073, 2827, 1682, 1288, and 933 cm<sup>-1</sup> for O-H, C-H, C=O and aryl C-H vibrations of benzoic acid (**Figure 5.14**).[93,94]

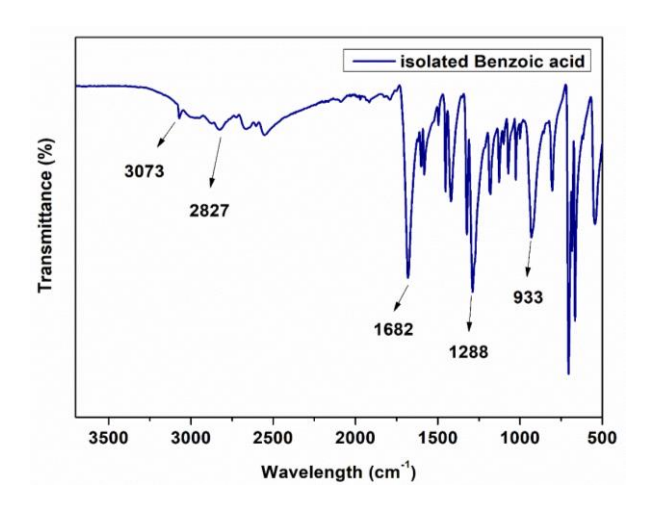
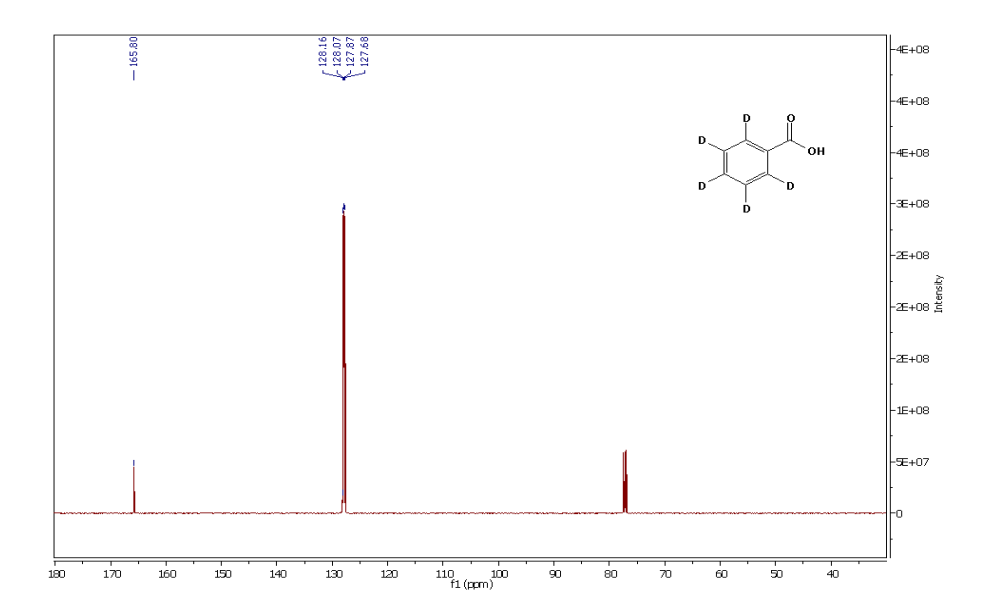


Figure 5.14. FT-IR spectra of isolated benzoic acid after reaction.

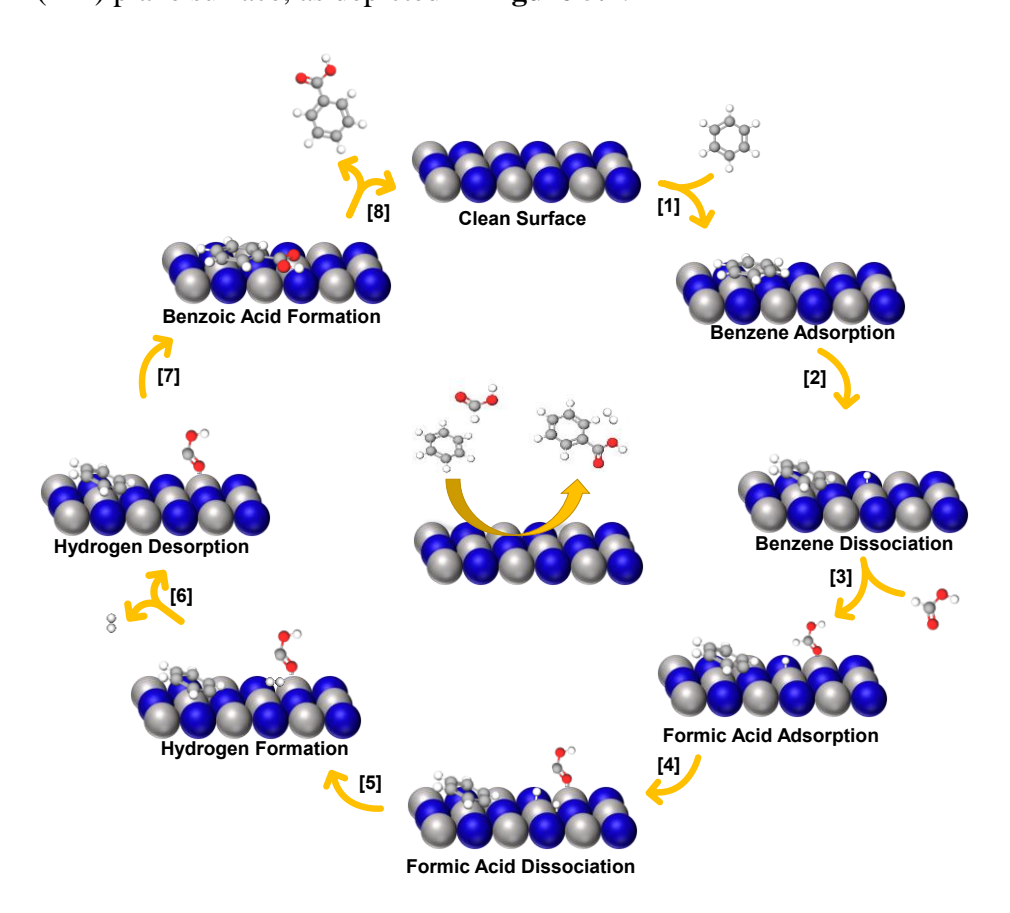
Furthermore, an isotopic-labelling experiment was performed under standard reaction conditions using  $C_6D_6$  as substrate and formic acid as carboxylating agent, and the corresponding expected deuterated acidic product was obtained (**Figure 5.15**).



**Figure 5.15**. Labelling experiment with benzene-d6:  $^{13}$ C NMR (400 MHz, CDCl<sub>3</sub>):  $\delta$  165.80, 128.16, 128.07, 127.87, 127.68.

To the best of our knowledge, the mechanistic aspects of the direct carboxylation of benzene with formic acid on CuNi-11 bimetallic catalyst remain unknown. In this regard, we performed DFT calculations to gain valuable insights into the potential reaction mechanism. We

considered the alloy Cu(0)/Ni(0) form of the catalyst as suggested by the XPS analysis of recovered catalyst (**Figure 5.16**). **Scheme 5.3** presents a proposed reaction mechanism for the carboxylation of benzene to benzoic acid with formic acid as carboxylating agent on the CuNi-11 nanocatalyst surface. The computed reaction energy profile and graphical snapshots of relevant reactants, intermediates, and transition states (TSs) for the reaction on (111) CuNi-11 surface are shown in **Figure 5.16**. Importantly, our PXRD analysis has authenticated the active sites of CuNi-11 nanocatalyst are located on the (111) plane surface, as depicted in **Figure 5.2**.



**Scheme 5.3**. Plausible mechanism of benzene carboxylation with formic acid on bimetallic nanoparticles.

In the first step of the cycle, benzene chemisorbs through its  $\pi$  electron cloud with hexagonal close-packed (hcp) flat-lying orientation, involving the H-flipped configuration of the ring.[95] Generally, it is established that benzene adsorbs on transition metals with its aromatic

ring lying parallel to the surface, [96-99] similar to the adsorption of biomass derived rings on metal catalysts.[100] The computed binding energy of benzene on (111) of CuNi-11 three-fold hollow site is -137.7 kJ mol-1, whereas DFT-computed adsorption energy of benzene ranges between -54.0 to -103.2 and -84.0 to -101.3 kJ mol<sup>-1</sup> on three-fold hollow sites of (111) Cu[101-103] and Ni[96,104-106] metals, respectively. The stronger binding energy of benzene on CuNi-11 catalyst relative to Cu and Ni metals may be traced down to (i) a larger overlap of benzene  $\pi$  orbitals with the orbitals of the CuNi-11 surface than that with either Cu or Ni surface individually and (ii) better description of adsorbate-surface dispersion interactions by PBE-D3 method (see computational methods in supporting information). At the hcp adsorbed state (C<sub>6</sub>H<sub>6</sub>\*), the mechanism is initiated by activation of benzene C-H bond and formation of tilted phenyl (C<sub>6</sub>H<sub>5</sub>\*) intermediate with a neighboring H'\* species occupying the hcp site. The geometry structure for benzene C-H scission TS (TS1) exhibits the breaking of a σ bond, featuring a three-membered metallacycle C-Cu-H, with an activation energy barrier of 180.9 kJ mol<sup>-1</sup>. Formic acid then adsorbs nearly perpendicular with its carbonyl oxygen bonded atop on a Ni site and C-H bond pointing towards a bridge Cu-Ni site. The computed adsorption energy of formic acid is -60.1 kJ mol<sup>-1</sup>, indicating an energetically favorable process. Several theoretical studies have investigated formic acid adsorption and decomposition on Cu and Ni (111) surfaces and reported atop adsorption through the carbonyl oxygen, with binding energies of -46.3 and -34.7 kJ mol<sup>-1</sup> for Cu and Ni metals, respectively.[31,107,108] After adsorption, formic acid decomposes into adsorbed bidentate carboxyl intermediate (COOH\*) and atomic hcp-bounded H"\*. Furthermore, breaking the C-H bond in HCOOH (TS2) on CuNi bimetallic surface is exothermic (-65.4 kJ mol<sup>-</sup> 1), with an activation barrier of 46.3 kJ mol<sup>-1</sup>. Jiang and coworkers investigated the activation of the HCOOH C-H bond on the Cu (111) surface and reported an activation energy barrier of 36.7 kJ mol<sup>-1</sup>.[36] Dehydrogenation of **HCOOH** to the formate intermediate

(HCOO\*)[109] via the cleavage of the O-H bond, followed by C-H bond scission to produce CO<sub>2</sub>\* and 2H\* was not considered herein, as the liberation of CO<sub>2</sub> gas was not detected experimentally via lime water test. In the next step, the surface-bound hydrogens on adjacent hcp sites (H'\* + H"\*) recombine to form molecular hydrogen. The H-H bond formation (TS3) takes place on top of a Ni atom, with an activation barrier of 74.4 kJ mol<sup>-1</sup>. The atop adsorbed molecular hydrogen desorbs from the surface with an energetic penalty of 53.1 kJ mol<sup>-1</sup>. Liberation of H<sub>2</sub> gas was detected by the flame test, supporting the proposed reaction mechanism. Lastly, C<sub>7</sub>H<sub>6</sub>O<sub>2</sub> forms on the hcp site through the recombination of phenyl and carboxyl intermediates via TS4. The recombination step is exothermic with reaction and activation energy barriers of 80.7 and 36.2 kJ mol<sup>-1</sup>, respectively.

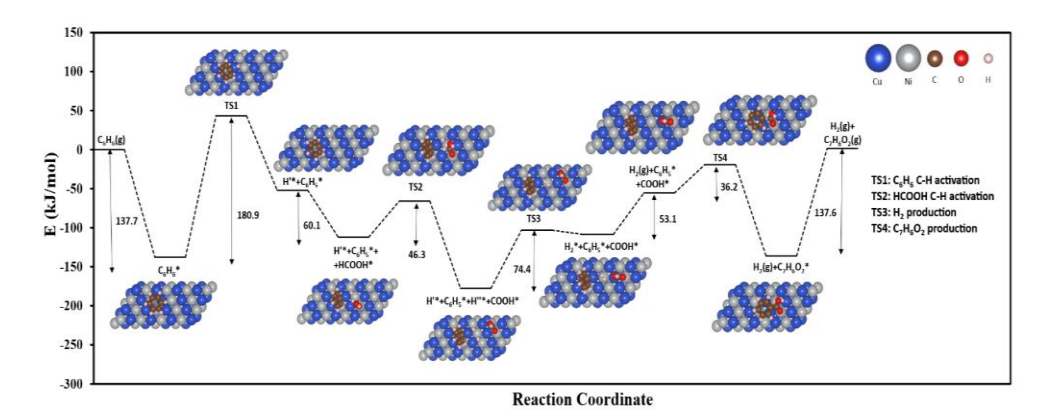


**Figure 5.16.** Potential energy surface of direct carboxylation of benzene to benzoic acid on close-packed fcc (111) CuNi-11 bimetallic surface. The detailed structures of reactants, transition states, intermediates, and products are schematically illustrated in insets.

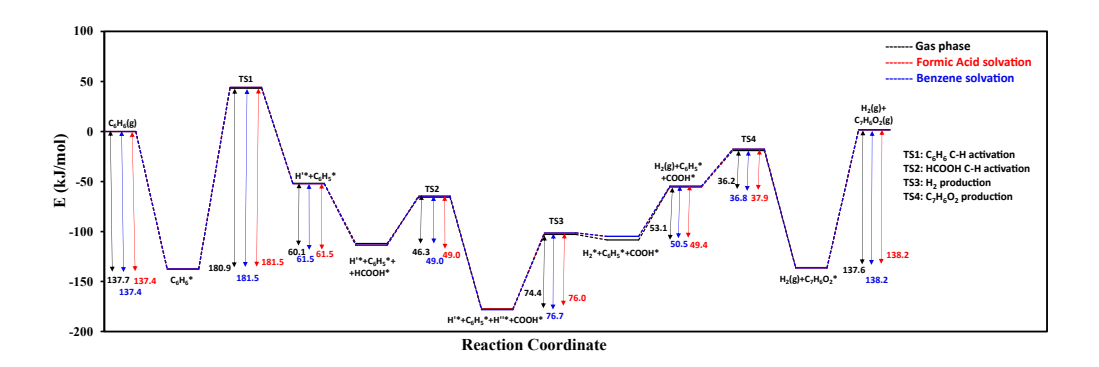


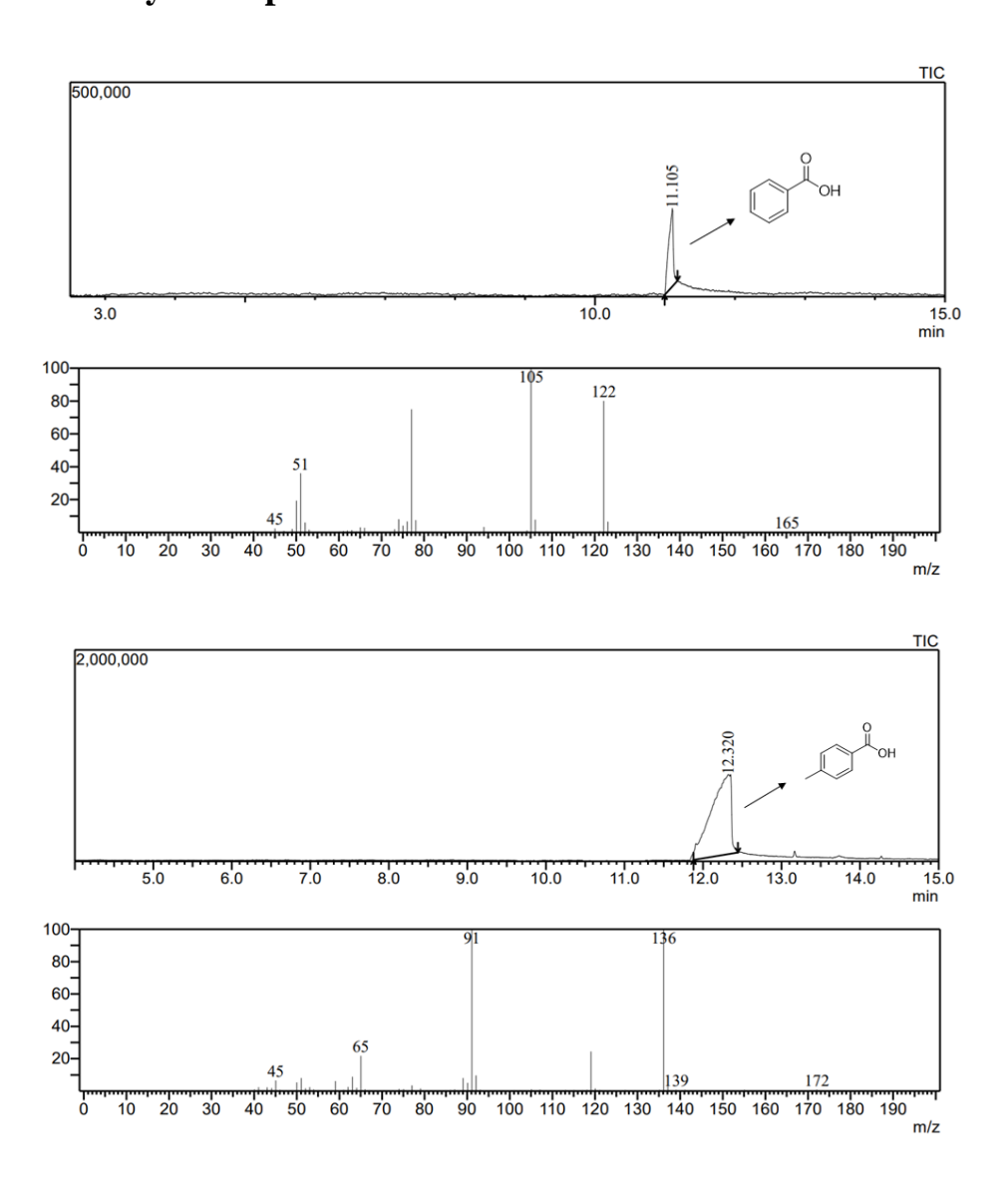
**Figure 5.17.** Potential energy surface of direct carboxylation of benzene to benzoic acid on close-packed fcc (111) CuNi-11 bimetallic surface on the gas phase (black) and in the presence of formic acid (red), and benzene (blue) as the solvation medium.

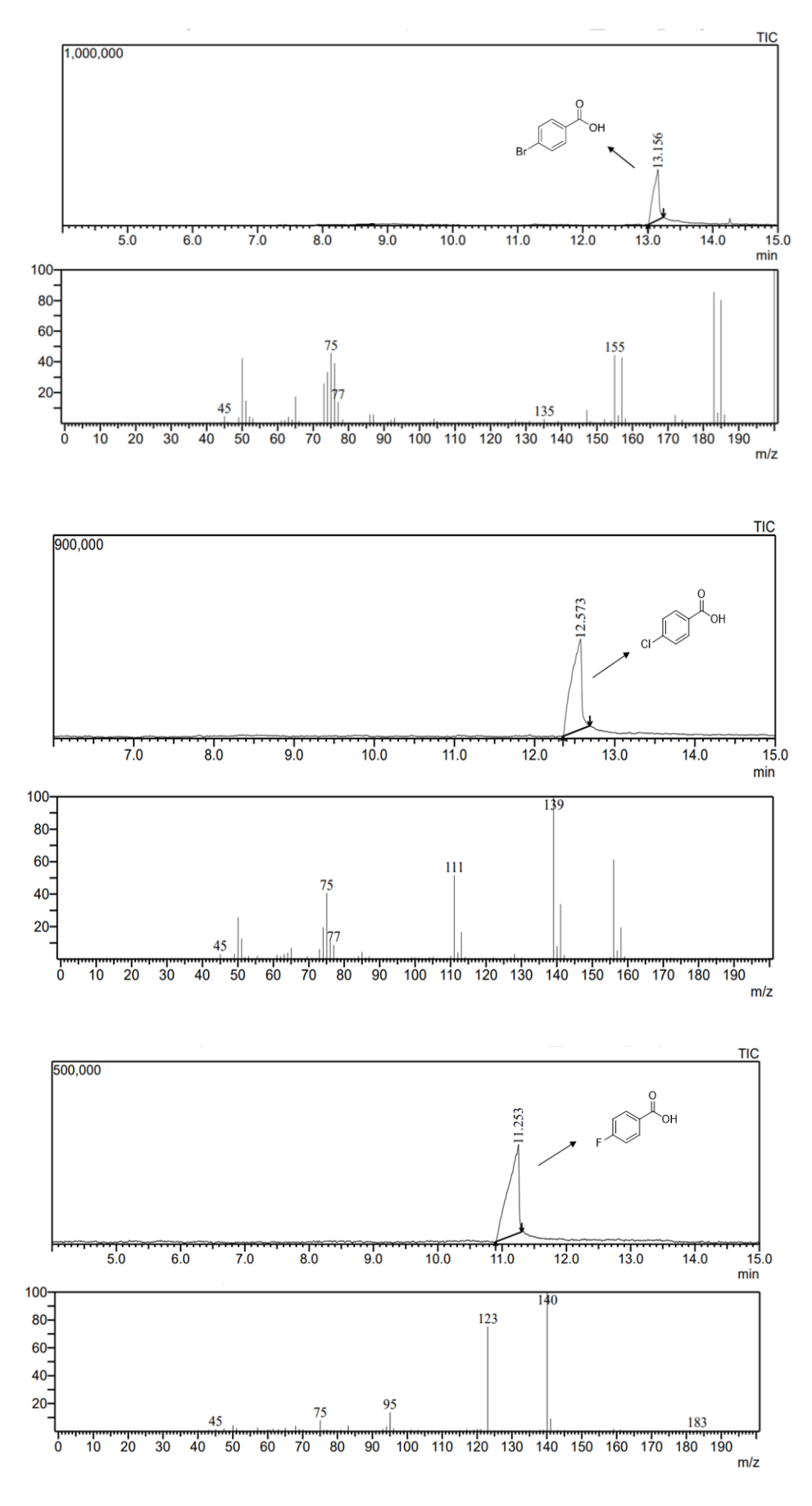
The catalytic cycle completes with benzoic acid desorbing to regenerate the catalyst, with desorption energy of 137.6 kJ mol<sup>-1</sup>. Overall, benzene C-H bond activation was found to be the rate-determining step in the carboxylation reaction. Finally, to demonstrate the solvation effects on the reaction mechanism, the self-consistent continuum solvation model was applied on the DFT optimized structures, as shown in **Figure 5.17** by utilizing both formic acid and benzene as the solvation medium for the reaction.[56] We showed that implicit solvation effects do not change the reaction pathway energetics.

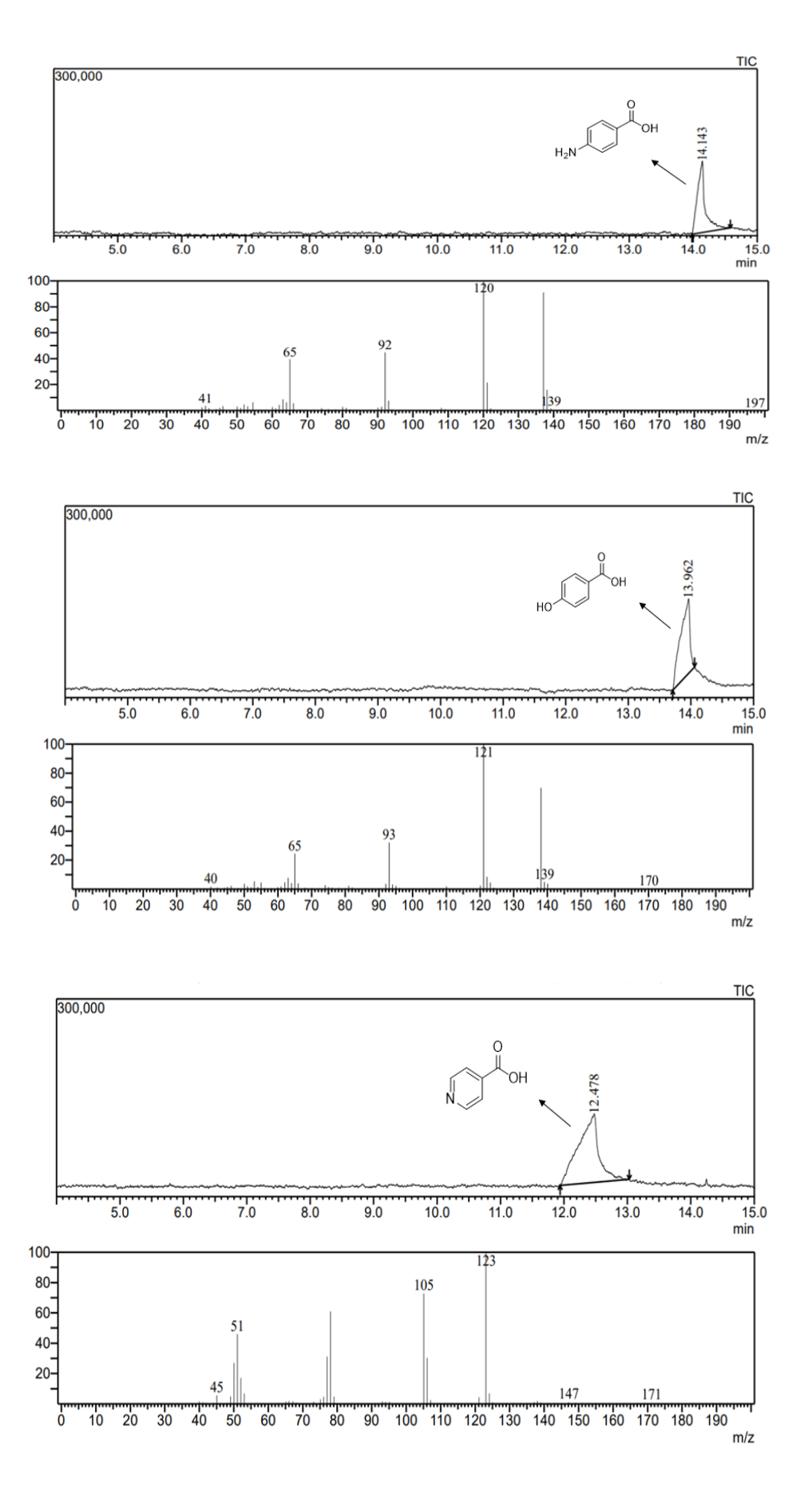
#### **5.4. Conclusions**

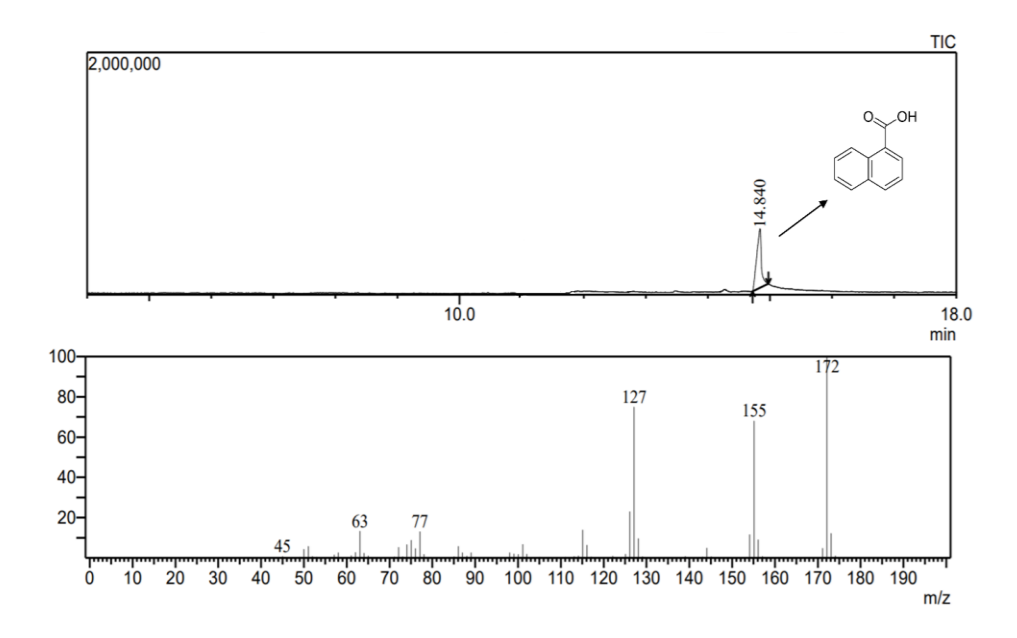
In summary, we utilize synthesis, characterization, and catalytic experiments together with first principles calculations to report the first example of direct carboxylation of benzene on bimetallic CuNi-11 nanocatalyst. The reaction proceeds through the activation of both benzene and formic acid with desorption of molecular H<sub>2</sub>. The CuNi-11 nanocatalyst is highly efficient, recyclable, and cost-effective. Our work advances the field of arene functionalization by introducing an activator, additive- and solvent-free carboxylation reaction at mild conditions using a recyclable bimetallic CuNi-11 catalyst, while providing a mechanistic understanding of the reaction.

## 5.5. GC-MS analysis of all substituted benzene carboxylation products





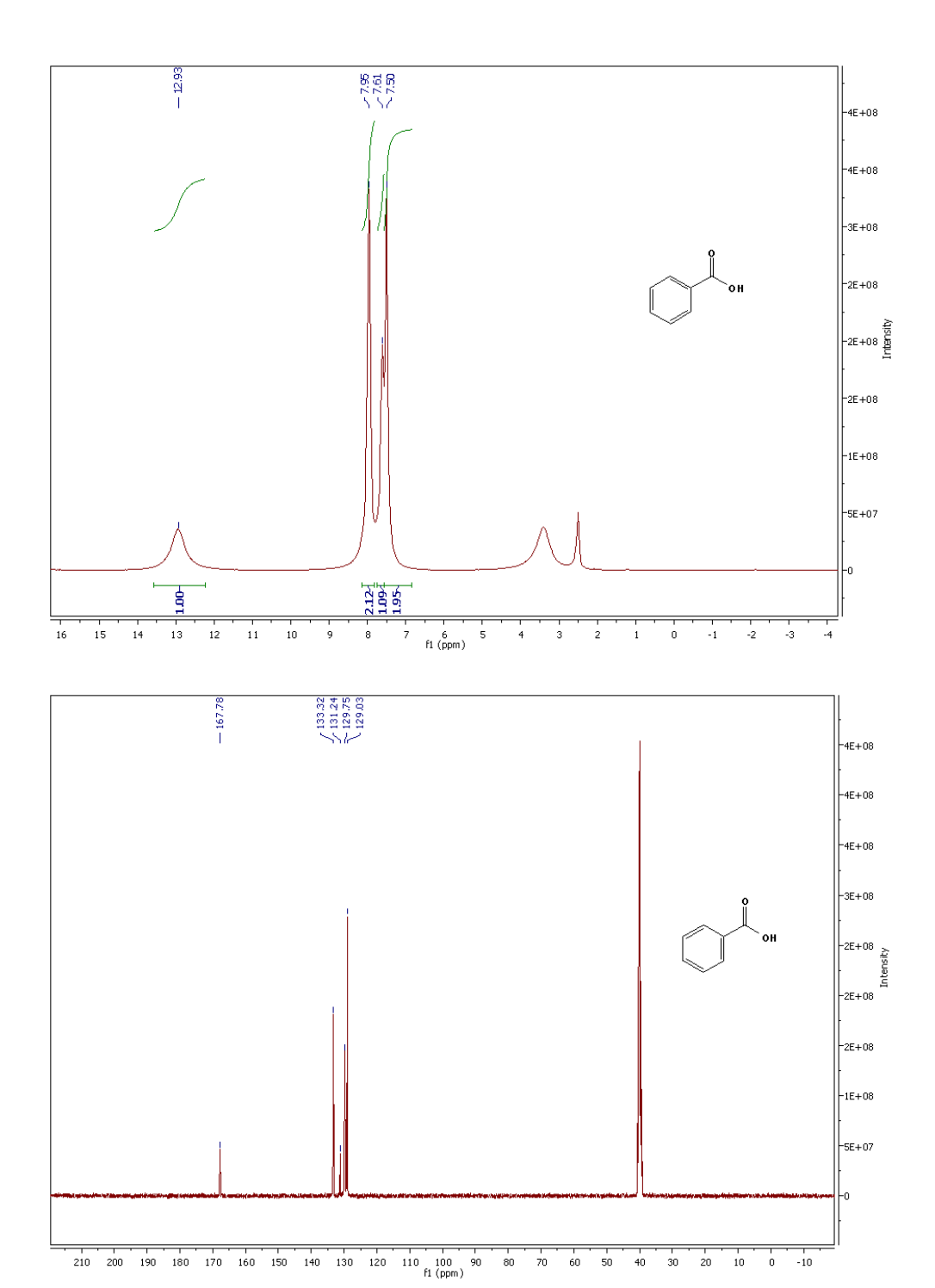




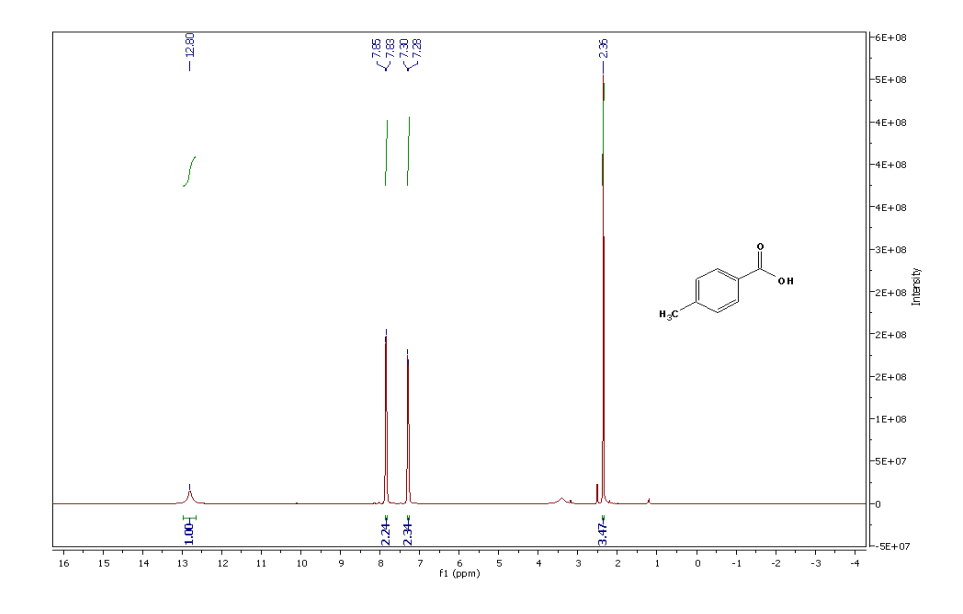
### 5.6. <sup>1</sup>H and <sup>13</sup>C-NMR data of all carboxylated benzene products

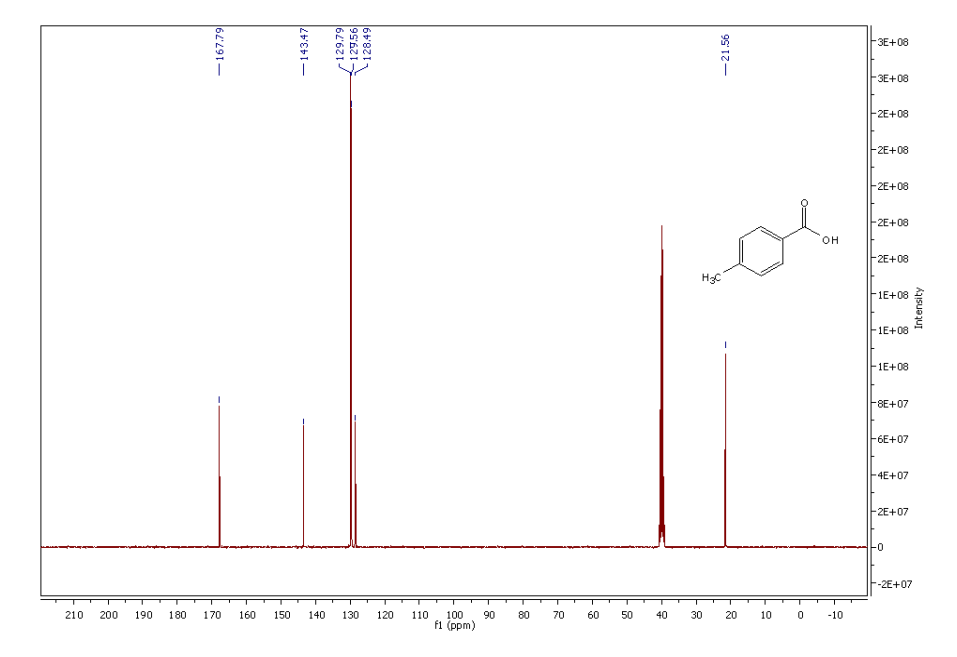
After completion of reaction all the products were cooled to room temperature and diluted with ethyl acetate and residue was purified with silica gel chromatography. The resulting product were then given for NMR analysis with DMSO-d6 and the data was analysed with the references.<sup>17–19</sup>

**Benzoic acid**: <sup>1</sup>H NMR (400 MHz, DMSO-d6): δ 12.93 (s, 1H), 7.95 (2H), 7.61 (1H), 7.50 (2H). <sup>13</sup>C NMR (400 MHz, DMSO-d6): δ 167.78, 133.32, 131.24, 129.75, 129.03.

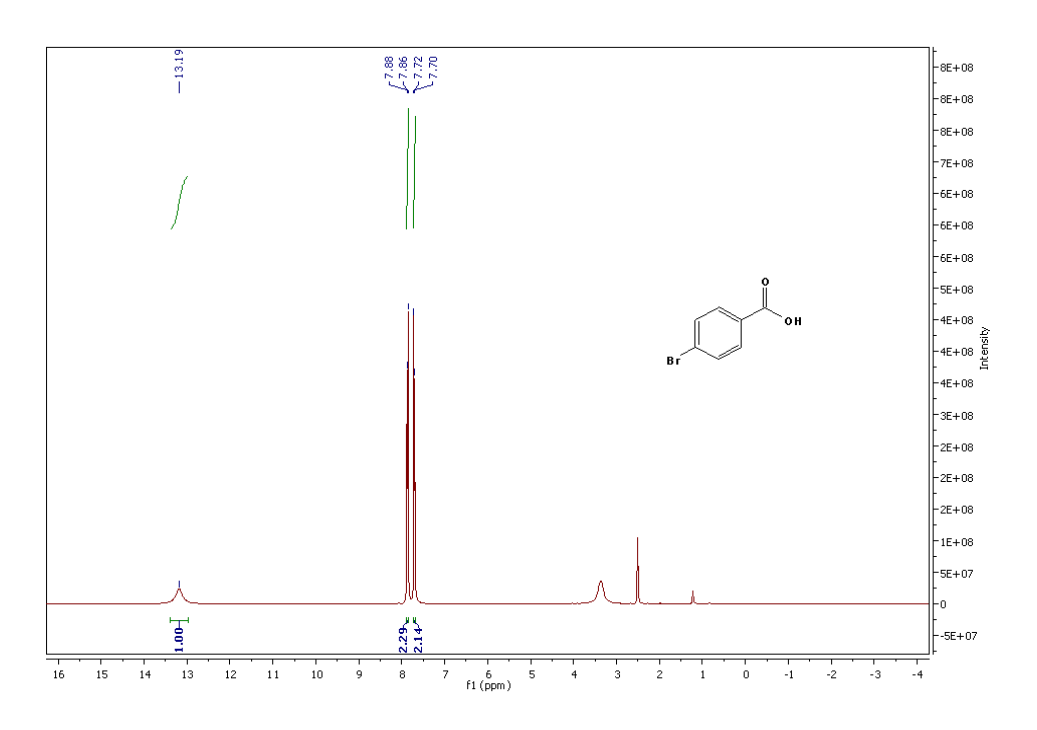


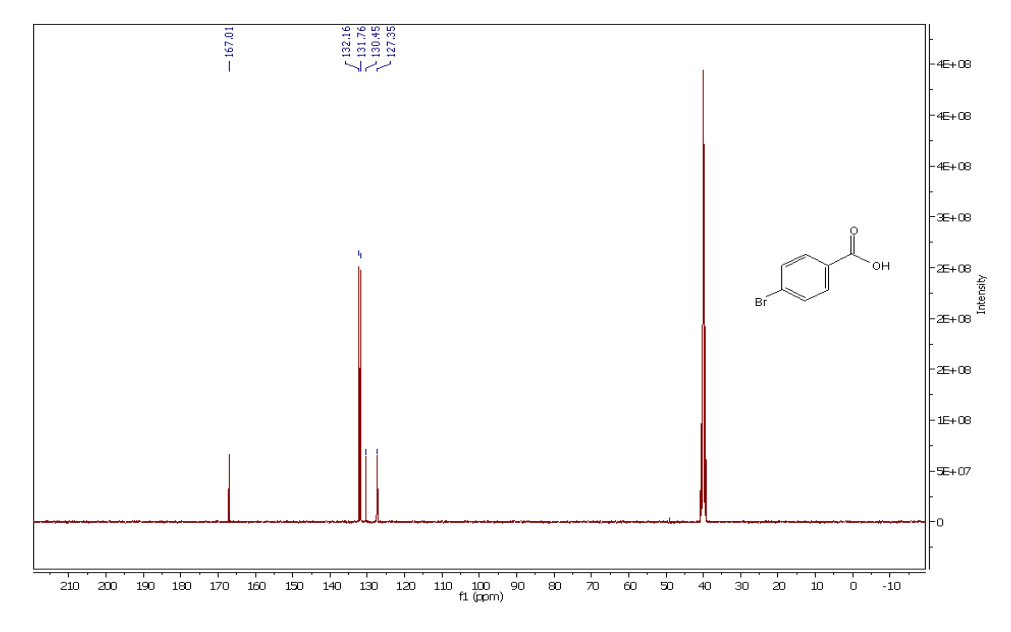
**4-methyl benzoic acid:**  $^{1}$ H NMR (400 MHz, DMSO-d6):  $\delta$  12.80 (s, 1H), 7.85 (d, 2H), 7.28 (d, 2H), 2.36 (s, 3H).  $^{13}$ C NMR (400 MHz, DMSO-d6):  $\delta$  167.79, 143.35, 129.79, 129.56, 128.49, 21.56.



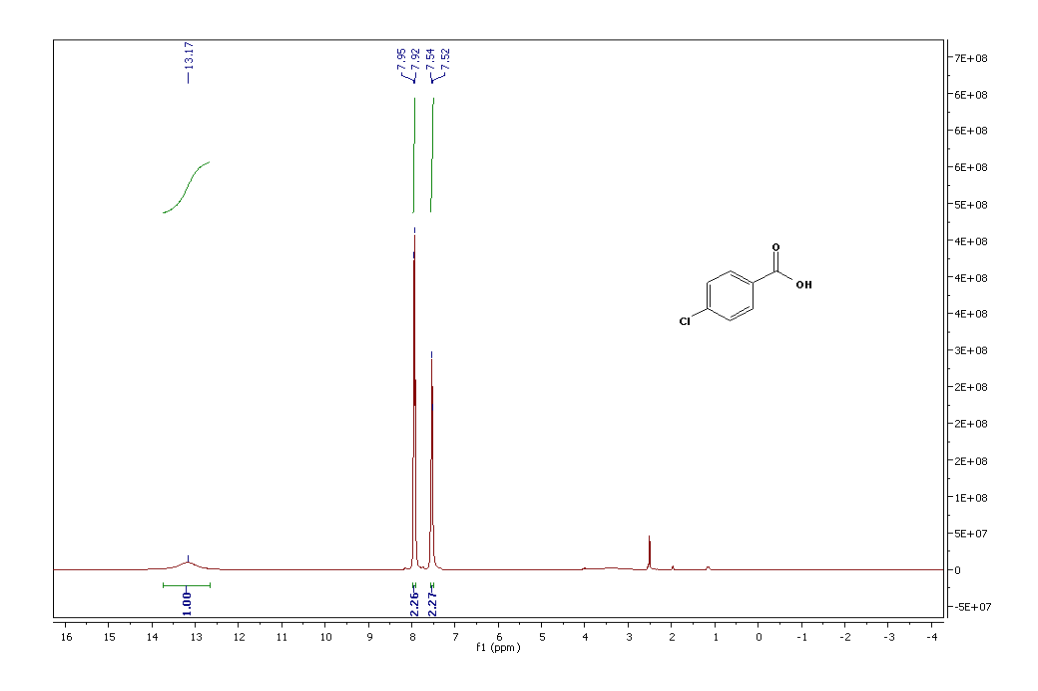


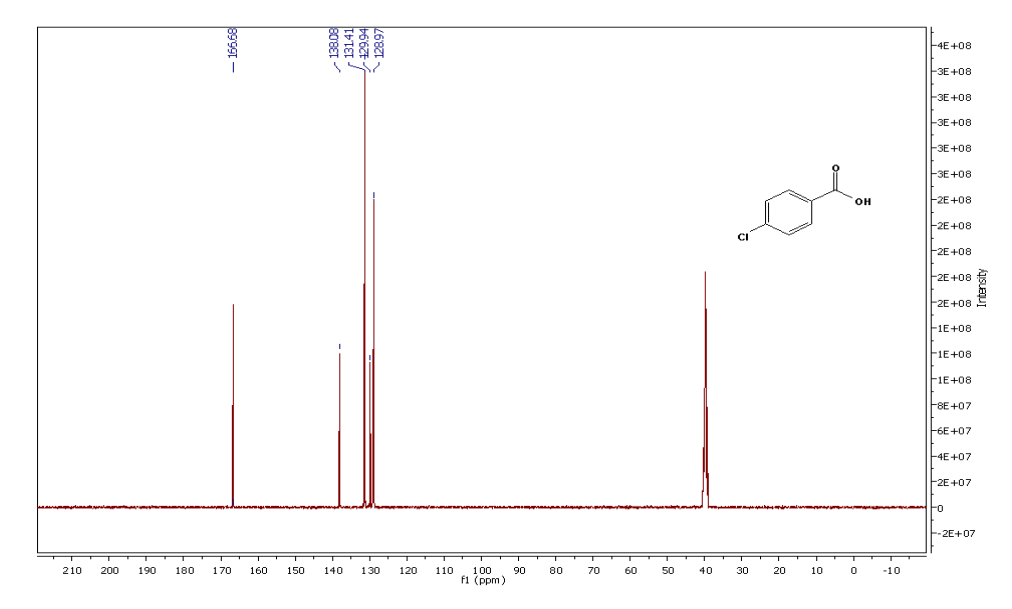
**4-bromo benzoic acid:**  $^{1}$ H NMR (400 MHz, DMSO-d6):  $\delta$  13.19 (s, 1H), 7.88 (d, 2H), 7.70 (d, 2H).  $^{13}$ C NMR (400 MHz, DMSO-d6):  $\delta$  167.01, 132.16, 131.76, 130.45, 127.35.



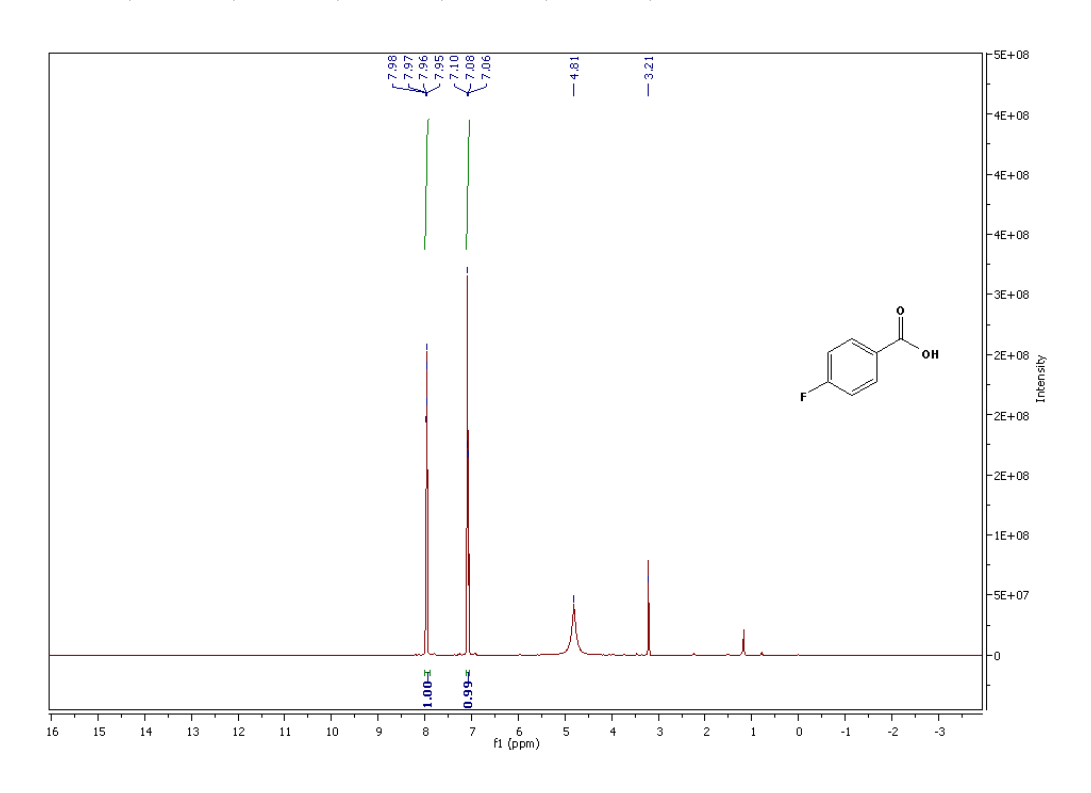


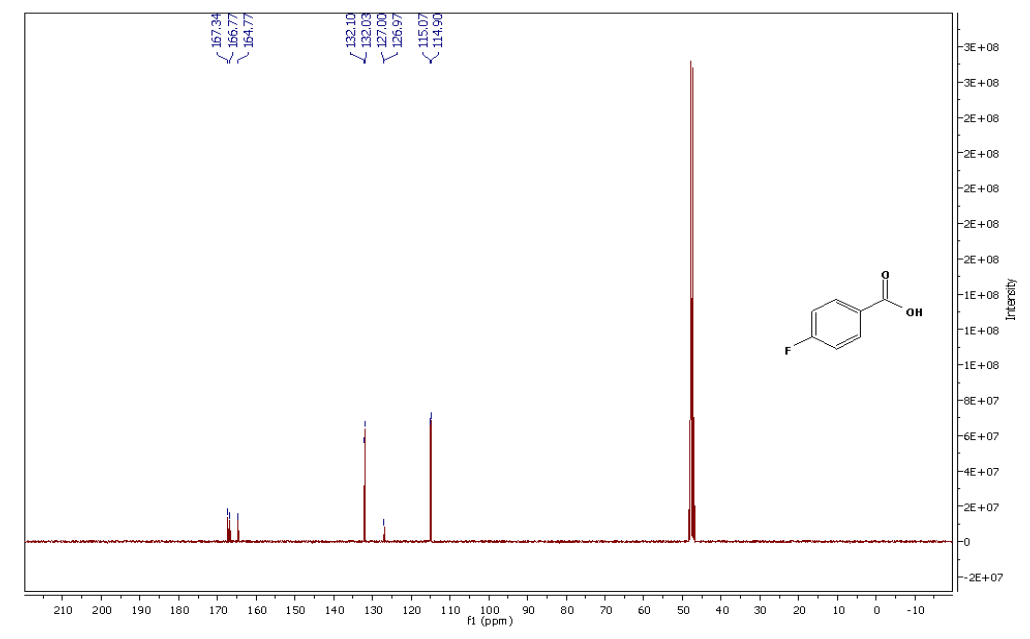
**4-chloro benzoic acid:**  $^{1}$ H NMR (400 MHz, DMSO-d6):  $\delta$ 13.17 (s, 1H), 7.95 (d, 2H), 7.54 (d, 2H).  $^{13}$ C NMR (400 MHz, DMSO-d6):  $\delta$  166.68, 138.08, 131.41, 129.94, 128.97.



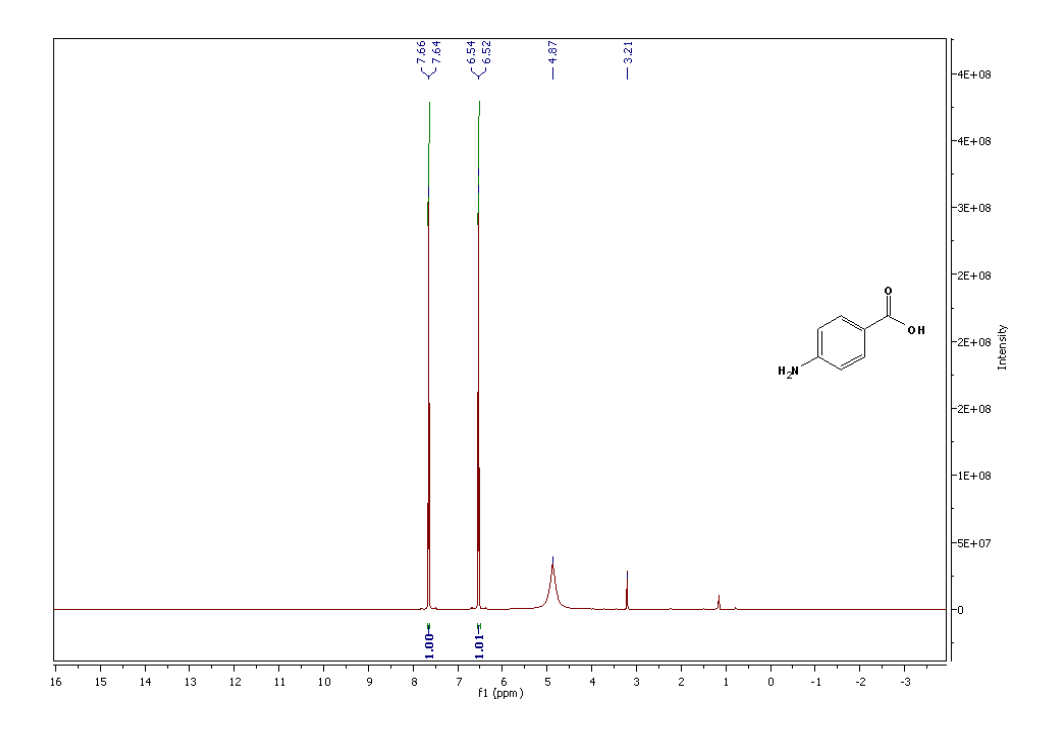


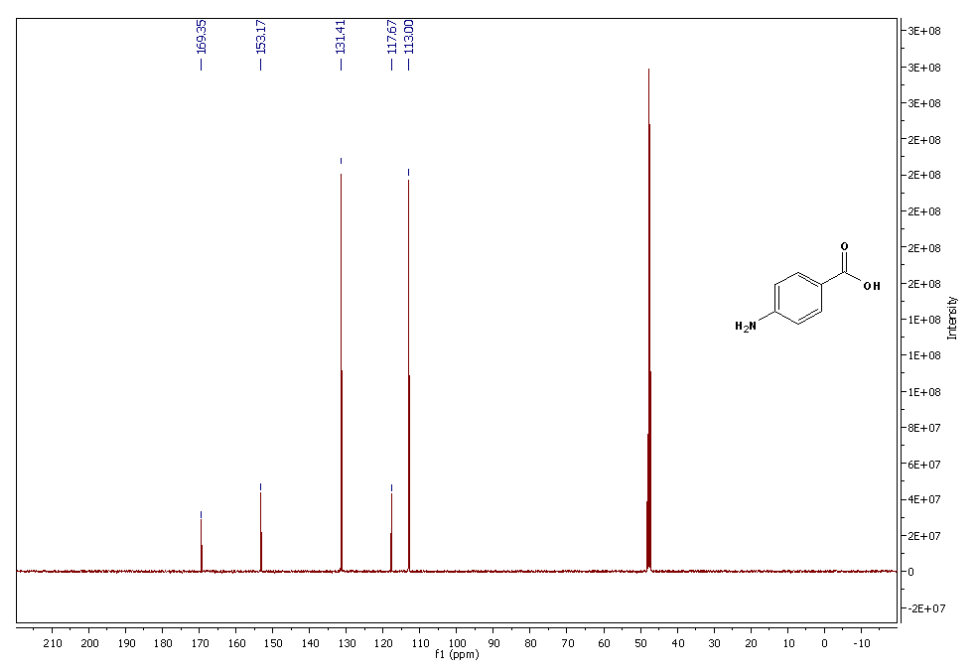
**4-fluoro benzoic acid:**  $^{1}$ H NMR (500 MHz, MeOH-d4):  $\delta$  7.98 (m, 2H), 7.06-7.10 (m, 2H).  $^{13}$ C NMR (500 MHz, MeOH-d4):  $\delta$  167.34, 166.77, 164.77, 132.10, 132.03, 127.00, 126.97, 115.07, 114.90.



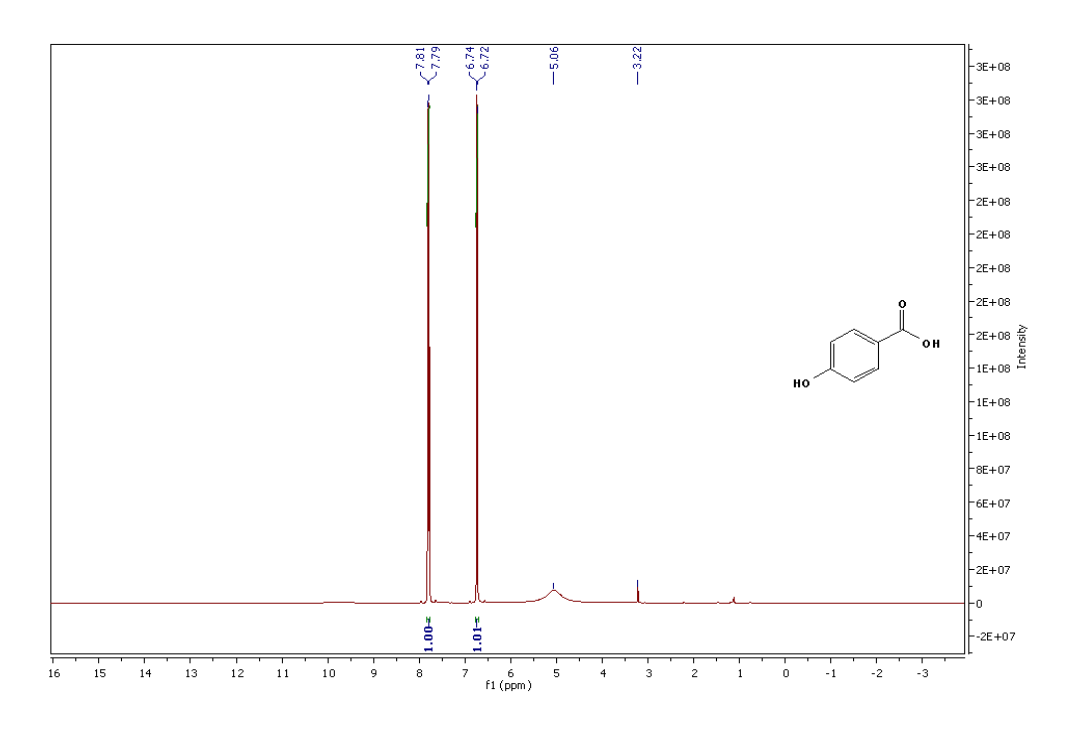


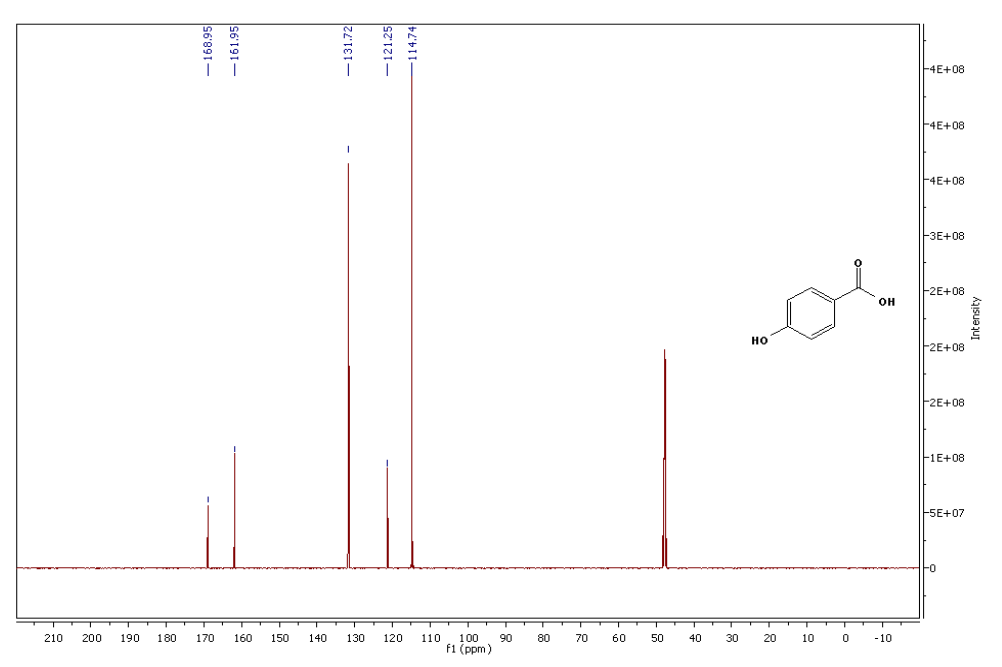
**4-amino benzoic acid:**  $^{1}$ H NMR (500 MHz, MeOH-d4):  $\delta$  7.66 (d, 2H), 6.54 (d, 2H).  $^{13}$ C NMR (500 MHz, MeOH-d4):  $\delta$  169.35, 153.17, 131.41, 117.67, 113.00.



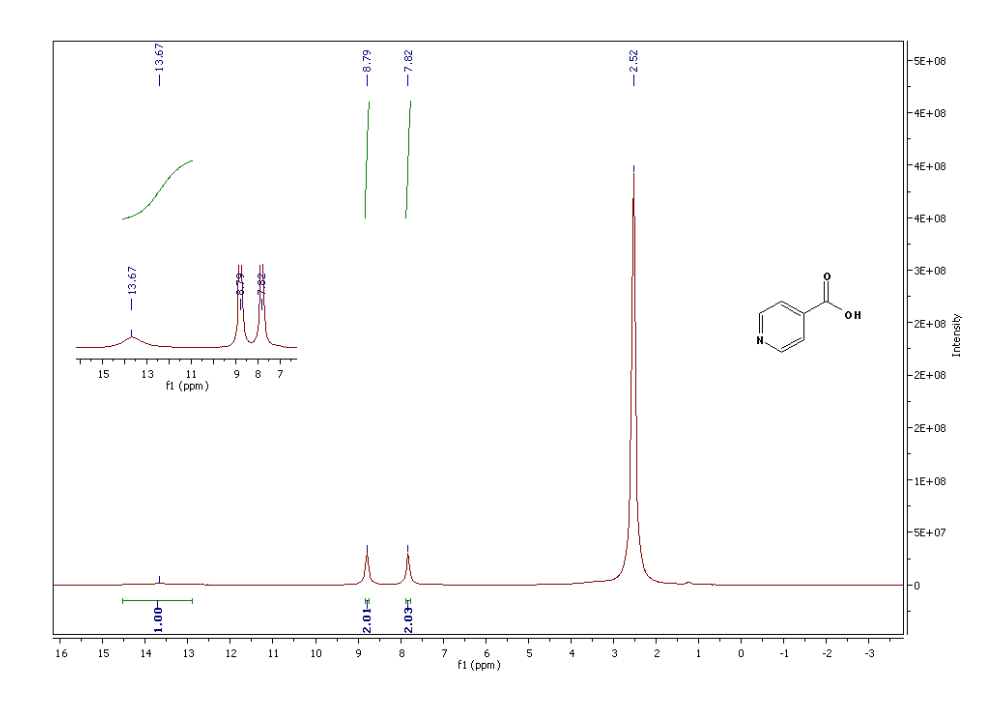


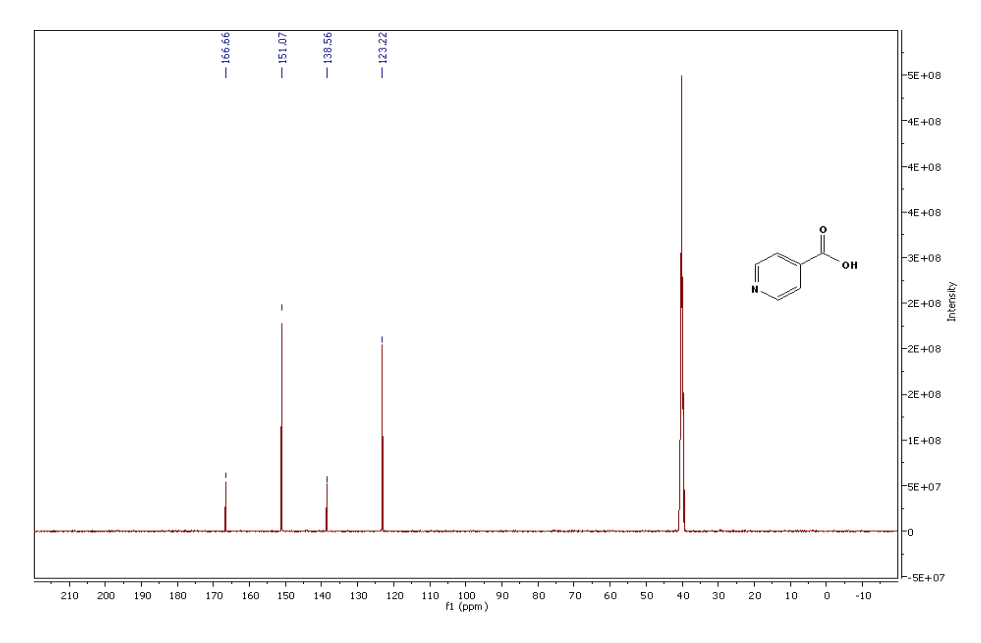
**4-hydroxy benzoic acid:**  $^{1}$ H NMR (500 MHz, MeOH-d4):  $\delta$  7.81 (d, 2H), 6.73 (d, 2H).  $^{13}$ C NMR (500 MHz, MeOH-d4):  $\delta$  168.95, 161.95, 131.72, 121.25, 114.74.



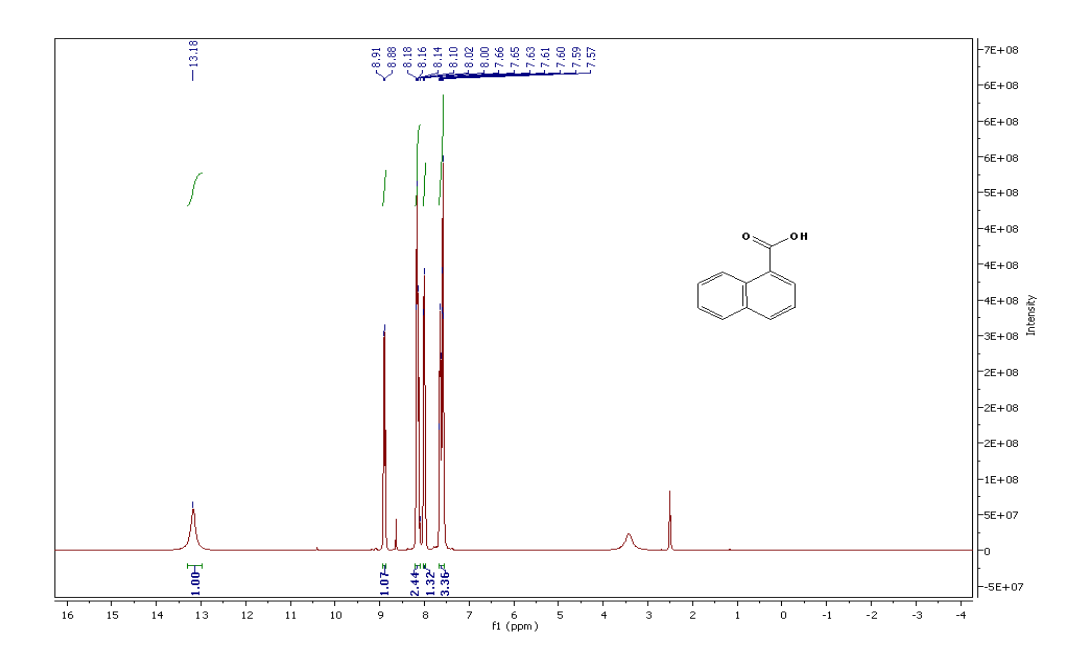


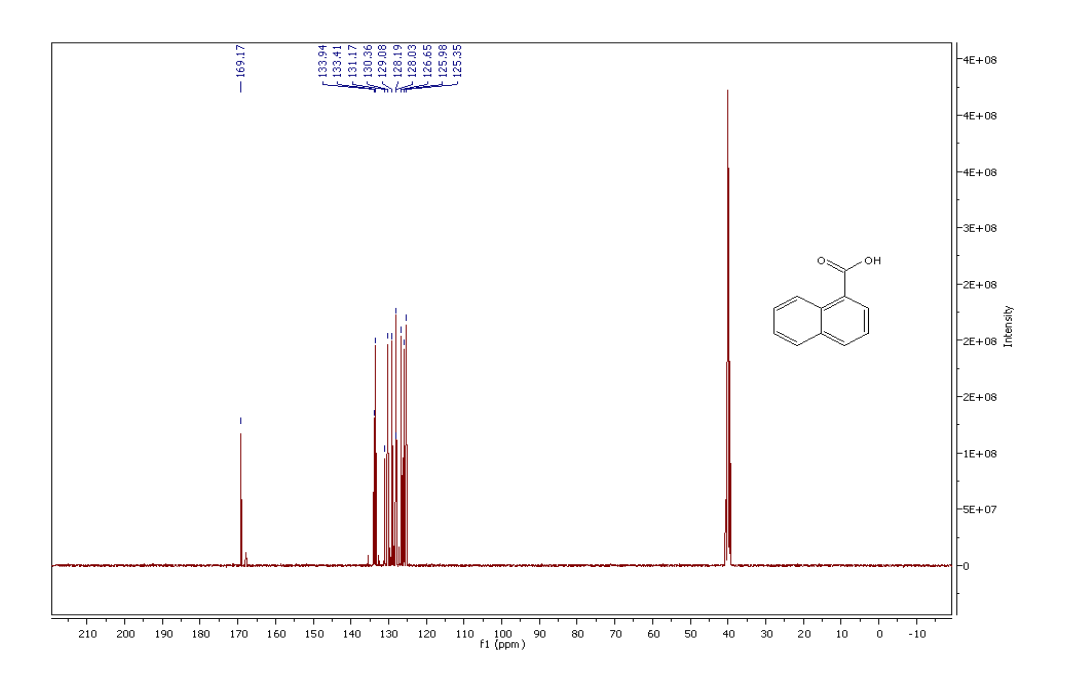
**4-pyridine carboxylic acid:**  $^{1}\text{H NMR}$  (500 MHz, DMSO-d6):  $\delta$  7.82 (s, 2H), 8.79 (s, 2H), 13.67 (s, 1H).  $^{13}\text{C NMR}$  (500 MHz, DMSO-d6):  $\delta$  166.66, 151.07, 138.56, 123.22.





**1-naphthoic acid:** <sup>1</sup>H NMR (400 MHz, DMSO-d6): δ 13.18 (s, 1H), 8.88 (d, 1H), 8.16 (m, 2H), 8.08-8.00 (m, 1H), 7.66-7.57 (m, 3H). 13C NMR (400 MHz, DMSO-d6): δ 169.17, 133.94, 133.41, 131.17, 130.36, 129.08, 129.08, 128.19, 128.03, 126.65, 125.98, 125.35.





#### 5.7. References

- [1] Y. Zhang, J. Yang, R. Ge, J. Zhang, J.M. Cairney, Y. Li, M. Zhu, S. Li, W. Li, The effect of coordination environment on the activity and selectivity of single-atom catalysts, Coord. Chem. Rev. 461 (2022) 214493. https://doi.org/10.1016/j.ccr.2022.214493.
- [2] R. Narayanan, M.A. El-Sayed, Catalysis with Transition Metal Nanoparticles in Colloidal Solution: Nanoparticle Shape Dependence and Stability, J. Phys. Chem. B. 109 (2005) 12663–12676. https://doi.org/10.1021/jp051066p.
- [3] X. Cui, W. Li, P. Ryabchuk, K. Junge, M. Beller, Bridging homogeneous and heterogeneous catalysis by heterogeneous single-metal-site catalysts, Nat. Catal. 1 (2018) 385–397. https://doi.org/10.1038/s41929-018-0090-9.
- [4] M. Ali Nasseri, Z. Rezazadeh, M. Kazemnejadi, A. Allahresani, A Co–Cu bimetallic magnetic nanocatalyst with synergistic and bifunctional performance for the base-free Suzuki, Sonogashira, and C–N cross-coupling reactions in water, Dalton Trans. 49 (2020) 10645–10660. https://doi.org/10.1039/D0DT01846E.
- [5] M.A. Nasseri, Z. Rezazadeh, M. Kazemnejadi, A. Allahresani, Cu-Mn Bimetallic Complex Immobilized on Magnetic NPs as an Efficient Catalyst for Domino One-Pot Preparation of Benzimidazole and Biginelli Reactions from Alcohols, Catal. Lett. 151 (2021) 1049–1067. https://doi.org/10.1007/s10562-020-03371-0.
- [6] M. Kazemnejadi, R. Omer Ahmed, B. Mahmoudi, Ni/Pd-catalyzed Suzuki–Miyaura cross-coupling of alcohols and aldehydes and C–N cross-coupling of nitro and amines via domino redox reactions: base-free, hydride acceptor-free, RSC Adv. 10 (2020) 43962–43974. https://doi.org/10.1039/D0RA08344E.
- [7] J. Govan, Y.K. Gun'ko, Recent Advances in the Application of Magnetic Nanoparticles as a Support for Homogeneous Catalysts, Nanomaterials. 4 (2014) 222–241. https://doi.org/10.3390/nano4020222.
- [8] I. Mustieles Marin, J.M. Asensio, B. Chaudret, Bimetallic Nanoparticles Associating Noble Metals and First-Row Transition Metals in Catalysis, ACS Nano. 15 (2021) 3550–3556. https://doi.org/10.1021/acsnano.0c09744.
- [9] Q. Zhang, X. Yang, J. Guan, Applications of Magnetic Nanomaterials in Heterogeneous Catalysis, ACS Appl. Nano Mater. 2 (2019) 4681–4697. https://doi.org/10.1021/acsanm.9b00976.
- [10] H. Yue, C. Zhu, L. Huang, A. Dewanji, M. Rueping, Advances in allylic and benzylic C–H bond functionalization enabled by metallaphotoredox catalysis, Chem. Commun. 58 (2022) 171–184. https://doi.org/10.1039/D1CC06285A.
- [11] A. del Olmo, J. Calzada, M. Nuñez, Benzoic acid and its derivatives as naturally occurring compounds in foods and as

- additives: Uses, exposure, and controversy, Crit. Rev. Food Sci. Nutr. 57 (2017) 3084–3103. https://doi.org/10.1080/10408398.2015.1087964.
- [12] A.N. Sarve, P.A. Ganeshpure, P. Munshi, Carboxylation of Toluene by CO2 Generating p-Toluic Acid: A Kinetic Look, Ind. Eng. Chem. Res. 51 (2012) 5174–5180. https://doi.org/10.1021/ie300014z.
- [13] C.-H. Jun, C.W. Moon, D.-Y. Lee, Chelation-Assisted Carbon—Hydrogen and Carbon—Carbon Bond Activation by Transition Metal Catalysts, Chem. Eur. J. 8 (2002) 2422–2428. https://doi.org/10.1002/1521-3765(20020603)8:11<2422::AID-CHEM2422>3.0.CO;2-B.
- [14] J. Luo, I. Larrosa, C-H Carboxylation of Aromatic Compounds through CO2 Fixation, ChemSusChem. 10 (2017) 3317–3332. https://doi.org/10.1002/cssc.201701058.
- [15] L. J, L. I, C-H Carboxylation of Aromatic Compounds through CO2 Fixation., Chemsuschem. 10 (2017) 3317–3332. https://doi.org/10.1002/cssc.201701058.
- [16] D. Liu, Z. Xu, M. Liu, Y. Fu, Mechanistic insights into the rhodium-catalyzed aryl C–H carboxylation, Org. Chem. Front. 9 (2022) 370–379. https://doi.org/10.1039/D1QO01560E.
- [17] A. Correa, R. Martín, Palladium-Catalyzed Direct Carboxylation of Aryl Bromides with Carbon Dioxide, J. Am. Chem. Soc. 131 (2009) 15974–15975. https://doi.org/10.1021/ja905264a.
- [18] S. Wang, G. Du, C. Xi, Copper-catalyzed carboxylation reactions using carbon dioxide, Org. Biomol. Chem. 14 (2016) 3666–3676. https://doi.org/10.1039/C6OB00199H.
- [19] C. Pei, J. Zong, S. Han, B. Li, B. Wang, Ni-Catalyzed Direct Carboxylation of an Unactivated C–H Bond with CO2, Org. Lett. 22 (2020) 6897–6902. https://doi.org/10.1021/acs.orglett.0c02429.
- [20] A. Gevorgyan, K.H. Hopmann, A. Bayer, Formal C–H Carboxylation of Unactivated Arenes, Chem. Eur. J. 26 (2020) 6064–6069. https://doi.org/10.1002/chem.202000515.
- [21] T. Suga, H. Mizuno, J. Takaya, N. Iwasawa, Direct carboxylation of simple arenes with CO2 through a rhodium-catalyzed C–H bond activation, Chem. Commun. 50 (2014) 14360–14363. https://doi.org/10.1039/C4CC06188H.
- [22] F.-P. Wu, J.-B. Peng, X. Qi, X.-F. Wu, Palladium-Catalyzed Carbonylative Transformation of Organic Halides with Formic Acid as the Coupling Partner and CO Source: Synthesis of Carboxylic Acids, J. Org. Chem. 82 (2017) 9710–9714. https://doi.org/10.1021/acs.joc.7b01808.
- [23] T. Morimoto, K. Kakiuchi, Evolution of Carbonylation Catalysis: No Need for Carbon Monoxide, Angew. Chem. Int. Ed. 43 (2004) 5580–5588. https://doi.org/10.1002/anie.200301736.
- [24] M.G. Mura, L.D. Luca, G. Giacomelli, A. Porcheddu, Formic Acid: A Promising Bio-Renewable Feedstock for Fine Chemicals, Adv. Synth. Catal. 354 (2012) 3180–3186. https://doi.org/10.1002/adsc.201200748.

- [25] D. Mellmann, P. Sponholz, H. Junge, M. Beller, Formic acid as a hydrogen storage material development of homogeneous catalysts for selective hydrogen release, Chem. Soc. Rev. 45 (2016) 3954–3988. https://doi.org/10.1039/C5CS00618J.
- [26] X. Qi, C.-L. Li, L.-B. Jiang, W.-Q. Zhang, X.-F. Wu, Palladium-catalyzed alkoxycarbonylation of aryl halides with phenols employing formic acid as the CO source, Catal. Sci. Technol. 6 (2016) 3099–3107. https://doi.org/10.1039/C5CY01957E.
- [27] J. Scaranto, M. Mavrikakis, HCOOH decomposition on Pt(111): A DFT study, Surf. Sci. 648 (2016) 201–211. https://doi.org/10.1016/j.susc.2015.09.023.
- [28] M. Rafiee, H. Bashiri, Catalytic decomposition of formic acid on Cu(100): Optimization and dynamic Monte Carlo simulation, Catal. Commun. 137 (2020) 105942. https://doi.org/10.1016/j.catcom.2020.105942.
- [29] B.W.J. Chen, S. Bhandari, M. Mavrikakis, Role of Hydrogen-bonded Bimolecular Formic Acid–Formate Complexes for Formic Acid Decomposition on Copper: A Combined First-Principles and Microkinetic Modeling Study, ACS Catal. 11 (2021) 4349–4361. https://doi.org/10.1021/acscatal.0c05695.
- [30] X. Li, K. Xuan, Y. Zhu, G. Chen, G. Yang, A mechanistic study on the decomposition of a model bio-oil compound for hydrogen production over a stepped Ni surface: Formic acid, Appl. Surf. Sci. 452 (2018) 87–95. https://doi.org/10.1016/j.apsusc.2018.05.049.
- [31] Q. Luo, G. Feng, M. Beller, H. Jiao, Formic Acid Dehydrogenation on Ni(111) and Comparison with Pd(111) and Pt(111), J. Phys. Chem. C. 116 (2012) 4149–4156. https://doi.org/10.1021/jp209998r.
- [32] B.W.J. Chen, M. Stamatakis, M. Mavrikakis, Kinetic Isolation between Turnovers on Au18 Nanoclusters: Formic Acid Decomposition One Molecule at a Time, ACS Catal. 9 (2019) 9446–9457. https://doi.org/10.1021/acscatal.9b02167.
- [33] S. Singh, S. Li, R. Carrasquillo-Flores, A.C. Alba-Rubio, J.A. Dumesic, M. Mavrikakis, Formic acid decomposition on Au catalysts: DFT, microkinetic modeling, and reaction kinetics experiments, AIChE J. 60 (2014) 1303–1319. https://doi.org/10.1002/aic.14401.
- [34] Y.-Y. Wang, Theoretical study of the oxidation of formic acid on a PtPd(111) surface, Prog. React. Kinet. Mech. 44 (2019) 67–73. https://doi.org/10.1177/1468678319830512.
- [35] Z. Jiang, N. Ye, T. Fang, Theoretical investigation on the effect of doped Pd on the Cu(1 1 1) surface for formic acid oxidation: Competing formation of CO2 and CO, Chem. Phys. Lett. 751 (2020) 137509. https://doi.org/10.1016/j.cplett.2020.137509.
- [36] F. He, K. Li, G. Xie, Y. Wang, M. Jiao, H. Tang, Z. Wu, Understanding the enhanced catalytic activity of Cu1@Pd3(111) in formic acid dissociation, a theoretical perspective, J. Power Sources. 316 (2016) 8–16. https://doi.org/10.1016/j.jpowsour.2016.03.062.

- [37] D. Wang, D. Astruc, The recent development of efficient Earthabundant transition-metal nanocatalysts, Chem. Soc. Rev. 46 (2017) 816–854. https://doi.org/10.1039/C6CS00629A.
- [38] H. Takeda, C. Cometto, O. Ishitani, M. Robert, Electrons, Photons, Protons and Earth-Abundant Metal Complexes for Molecular Catalysis of CO2 Reduction, ACS Catal. 7 (2017) 70–88. https://doi.org/10.1021/acscatal.6b02181.
- [39] K. Tanaka, F. Toda, Solvent-Free Organic Synthesis, Chem. Rev. 100 (2000) 1025–1074. https://doi.org/10.1021/cr940089p.
- [40] S. Ni, M. Hribersek, S.K. Baddigam, F.J.L. Ingner, A. Orthaber, P.J. Gates, L.T. Pilarski, Mechanochemical Solvent-Free Catalytic C–H Methylation, Angew. Chem. Int. Ed. 60 (2021) 6660–6666. https://doi.org/10.1002/anie.202010202.
- [41] P.H.K. Charan, G. Ranga Rao, Synthesis of CuNi and CuNi/SBA-15 by aqueous method at room temperature and their catalytic activity, Microporous Mesoporous Mater. 200 (2014) 101–109. https://doi.org/10.1016/j.micromeso.2014.08.029.
- [42] S.-H. Wu, D.-H. Chen, Synthesis and characterization of nickel nanoparticles by hydrazine reduction in ethylene glycol, J. Colloid Interface Sci. 259 (2003) 282–286. https://doi.org/10.1016/S0021-9797(02)00135-2.
- [43] J. VandeVondele, M. Krack, F. Mohamed, M. Parrinello, T. Chassaing, J. Hutter, Quickstep: Fast and accurate density functional calculations using a mixed Gaussian and plane waves approach, Comput. Phys. Commun. 167 (2005) 103–128. https://doi.org/10.1016/j.cpc.2004.12.014.
- [44] J.P. Perdew, K. Burke, M. Ernzerhof, Generalized Gradient Approximation Made Simple, Phys. Rev. Lett. 77 (1996) 3865–3868. https://doi.org/10.1103/PhysRevLett.77.3865.
- [45] S. Grimme, Semiempirical GGA-type density functional constructed with a long-range dispersion correction, J. Comput. Chem. 27 (2006) 1787–1799. https://doi.org/10.1002/jcc.20495.
- [46] S. Goedecker, M. Teter, J. Hutter, Separable dual-space Gaussian pseudopotentials, Phys. Rev. B. 54 (1996) 1703–1710. https://doi.org/10.1103/PhysRevB.54.1703.
- [47] M. Krack, Pseudopotentials for H to Kr optimized for gradient-corrected exchange-correlation functionals, Theor. Chem. Acc. 114 (2005) 145–152. https://doi.org/10.1007/s00214-005-0655-y.
- [48] C. Hartwigsen, S. Goedecker, J. Hutter, Relativistic separable dual-space Gaussian pseudopotentials from H to Rn, Phys. Rev. B. 58 (1998) 3641–3662. https://doi.org/10.1103/PhysRevB.58.3641.
- [49] J. VandeVondele, J. Hutter, Gaussian basis sets for accurate calculations on molecular systems in gas and condensed phases, J. Chem. Phys. 127 (2007) 114105. https://doi.org/10.1063/1.2770708.
- [50] G. Henkelman, B.P. Uberuaga, H. Jónsson, A climbing image nudged elastic band method for finding saddle points and minimum energy paths, J. Chem. Phys. 113 (2000) 9901–9904. https://doi.org/10.1063/1.1329672.

- [51] H. Liu, B. Wang, M. Fan, N. Henson, Y. Zhang, B.F. Towler, H. Gordon Harris, Study on carbon deposition associated with catalytic CH4 reforming by using density functional theory, Fuel. 113 (2013) 712–718. https://doi.org/10.1016/j.fuel.2013.06.022.
- [52] R. Zhang, X. Guo, B. Wang, L. Ling, Insight Into the Effect of CuNi(111) and FeNi(111) Surface Structure and Second Metal Composition on Surface Carbon Elimination by O or OH: A Comparison Study with Ni(111) Surface, J. Phys. Chem. C. 119 (2015) 14135–14144. https://doi.org/10.1021/acs.jpcc.5b03868.
- [53] H. Liu, R. Zhang, R. Yan, J. Li, B. Wang, K. Xie, Insight into CH4 dissociation on NiCu catalyst: A first-principles study, Appl. Surf. Sci. 258 (2012) 8177–8184. https://doi.org/10.1016/j.apsusc.2012.05.017.
- [54] S.-G. Wang, D.-B. Cao, Y.-W. Li, J. Wang, H. Jiao, Chemisorption of CO2 on Nickel Surfaces, J. Phys. Chem. B. 109 (2005) 18956–18963. https://doi.org/10.1021/jp052355g.
- [55] S.-G. Wang, D.-B. Cao, Y.-W. Li, J. Wang, H. Jiao, CO2 Reforming of CH4 on Ni(111): A Density Functional Theory Calculation, J. Phys. Chem. B. 110 (2006) 9976–9983. https://doi.org/10.1021/jp060992g.
- [56] O. Andreussi, I. Dabo, N. Marzari, Revised self-consistent continuum solvation in electronic-structure calculations, J. Chem. Phys. 136 (2012) 064102. https://doi.org/10.1063/1.3676407.
- [57] D.S. Hall, D.J. Lockwood, C. Bock, B.R. MacDougall, Nickel hydroxides and related materials: a review of their structures, synthesis and properties, Proc. R. Soc. Math. Phys. Eng. Sci. (2015). https://royalsocietypublishing.org/doi/abs/10.1098/rspa.2014.079 2 (accessed March 23, 2020).
- [58] J.A. Witt, D.R. Mumm, A. Mohraz, Microstructural tunability of co-continuous bijel-derived electrodes to provide high energy and power densities, J. Mater. Chem. A. 4 (2016) 1000–1007. https://doi.org/10.1039/C5TA06260H.
- [59] M. Biswas, A. Saha, M. Dule, T.K. Mandal, Polymer-Assisted Chain-like Organization of CuNi Alloy Nanoparticles: Solvent-Adoptable Pseudohomogeneous Catalysts for Alkyne–Azide Click Reactions with Magnetic Recyclability, J. Phys. Chem. C. 118 (2014) 22156–22165. https://doi.org/10.1021/jp5071874.
- [60] K. Xiao, X. Qi, Z. Bao, X. Wang, L. Zhong, K. Fang, M. Lin, Y. Sun, CuFe, CuCo and CuNi nanoparticles as catalysts for higher alcohol synthesis from syngas: a comparative study, Catal. Sci. Technol. 3 (2013) 1591–1602. https://doi.org/10.1039/C3CY00063J.
- [61] H. Keshavarz, A. Khavandi, S. Alamolhoda, M. Reza Naimi-Jamal, pH-Sensitive magnetite mesoporous silica nanocomposites for controlled drug delivery and hyperthermia, RSC Adv. 10 (2020) 39008–39016. https://doi.org/10.1039/D0RA06916G.
- [62] G. Su, C. Yang, J.-J. Zhu, Fabrication of Gold Nanorods with Tunable Longitudinal Surface Plasmon Resonance Peaks by

- Reductive Dopamine, Langmuir. 31 (2015) 817–823. https://doi.org/10.1021/la504041f.
- [63] J. Ahmed, K.V. Ramanujachary, S.E. Lofland, A. Furiato, G. Gupta, S.M. Shivaprasad, A.K. Ganguli, Bimetallic Cu–Ni nanoparticles of varying composition (CuNi3, CuNi, Cu3Ni), Colloids Surf. Physicochem. Eng. Asp. 331 (2008) 206–212. https://doi.org/10.1016/j.colsurfa.2008.08.007.
- [64] N. Choudhary, T. Ghosh, S.M. Mobin, Ketone Hydrogenation by Using ZnO–Cu(OH)Cl/MCM-41 with a Splash of Water: An Environmentally Benign Approach, Chem. Asian J. 15 (2020) 1339–1348. https://doi.org/10.1002/asia.201901610.
- [65] K.S.W. Sing, Reporting physisorption data for gas/solid systems with special reference to the determination of surface area and porosity (Recommendations 1984), Pure Appl. Chem. 57 (1985) 603–619. https://doi.org/10.1351/pac198557040603.
- [66] G. Mayakrishnan, V. Elayappan, I.S. Kim, I.-M. Chung, Sea-Island-Like Morphology of CuNi Bimetallic Nanoparticles Uniformly Anchored on Single Layer Graphene Oxide as a Highly Efficient and Noble-Metal-Free Catalyst for Cyanation of Aryl Halides, Sci. Rep. 10 (2020) 1–15. https://doi.org/10.1038/s41598-020-57483-z.
- [67] S.N. Ansari, P. Kumar, A.K. Gupta, P. Mathur, S.M. Mobin, Catalytic CO2 Fixation over a Robust Lactam-Functionalized Cu(II) Metal Organic Framework, Inorg. Chem. 58 (2019) 9723–9732. https://doi.org/10.1021/acs.inorgchem.9b00684.
- [68] N. Austin, B. Butina, G. Mpourmpakis, CO2 activation on bimetallic CuNi nanoparticles, Prog. Nat. Sci. Mater. Int. 26 (2016) 487–492. https://doi.org/10.1016/j.pnsc.2016.08.007.
- [69] R. Cheula, M. Maestri, G. Mpourmpakis, Modeling Morphology and Catalytic Activity of Nanoparticle Ensembles Under Reaction Conditions, ACS Catal. 10 (2020) 6149–6158. https://doi.org/10.1021/acscatal.0c01005.
- [70] Y. Luo, L. Tang, U. Khan, Q. Yu, H.-M. Cheng, X. Zou, B. Liu, Morphology and surface chemistry engineering toward pH-universal catalysts for hydrogen evolution at high current density, Nat. Commun. 10 (2019) 269. https://doi.org/10.1038/s41467-018-07792-9.
- [71] B. Deka Boruah, A. Misra, Energy-Efficient Hydrogenated Zinc Oxide Nanoflakes for High-Performance Self-Powered Ultraviolet Photodetector, ACS Appl. Mater. Interfaces. 8 (2016) 18182–18188. https://doi.org/10.1021/acsami.6b04954.
- [72] X. Xiao, D. Huang, Y. Fu, M. Wen, X. Jiang, X. Lv, M. Li, L. Gao, S. Liu, M. Wang, C. Zhao, Y. Shen, Engineering NiS/Ni2P Heterostructures for Efficient Electrocatalytic Water Splitting, ACS Appl. Mater. Interfaces. 10 (2018) 4689–4696. https://doi.org/10.1021/acsami.7b16430.
- [73] G.-X. Tong, F.-T. Liu, W.-H. Wu, J.-P. Shen, X. Hu, Y. Liang, Polymorphous  $\alpha$  and  $\beta$ -Ni(OH)2 complex architectures: morphological and phasal evolution mechanisms and enhanced

- catalytic activity as non-enzymatic glucose sensors, CrystEngComm. 14 (2012) 5963–5973. https://doi.org/10.1039/C2CE25622C.
- [74] M. Raula, Md.H. Rashid, S. Lai, M. Roy, T.K. Mandal, Solvent-Adoptable Polymer Ni/NiCo Alloy Nanochains: Highly Active and Versatile Catalysts for Various Organic Reactions in both Aqueous and Nonaqueous Media, ACS Appl. Mater. Interfaces. 4 (2012) 878–889. https://doi.org/10.1021/am201549a.
- [75] C.-K. Wu, M. Yin, S. O'Brien, J.T. Koberstein, Quantitative Analysis of Copper Oxide Nanoparticle Composition and Structure by X-ray Photoelectron Spectroscopy, Chem. Mater. 18 (2006) 6054–6058. https://doi.org/10.1021/cm061596d.
- [76] S.D. Jones, L.M. Neal, H.E. Hagelin-Weaver, Steam reforming of methanol using Cu-ZnO catalysts supported on nanoparticle alumina, Appl. Catal. B Environ. 84 (2008) 631–642. https://doi.org/10.1016/j.apcatb.2008.05.023.
- [77] S.-Q. Liu, H.-R. Wen, Ying-Guo, Y.-W. Zhu, X.-Z. Fu, R. Sun, C.-P. Wong, Amorphous Ni(OH)2 encounter with crystalline CuS in hollow spheres: A mesoporous nano-shelled heterostructure for hydrogen evolution electrocatalysis, Nano Energy. 44 (2018) 7–14. https://doi.org/10.1016/j.nanoen.2017.11.063.
- [78] M. Chhetri, S. Sultan, C.N.R. Rao, Electrocatalytic hydrogen evolution reaction activity comparable to platinum exhibited by the Ni/Ni(OH)2/graphite electrode, Proc. Natl. Acad. Sci. 114 (2017) 8986–8990. https://doi.org/10.1073/pnas.1710443114.
- [79] S. Anantharaj, P. E. Karthik, S. Kundu, Petal-like hierarchical array of ultrathin Ni(OH) 2 nanosheets decorated with Ni(OH) 2 nanoburls: a highly efficient OER electrocatalyst, Catal. Sci. Technol. 7 (2017) 882–893. https://doi.org/10.1039/C6CY02282K.
- [80] N. Weidler, J. Schuch, F. Knaus, P. Stenner, S. Hoch, A. Maljusch, R. Schäfer, B. Kaiser, W. Jaegermann, X-ray Photoelectron Spectroscopic Investigation of Plasma-Enhanced Chemical Vapor Deposited NiOx, NiOx(OH)y, and CoNiOx(OH)y: Influence of the Chemical Composition on the Catalytic Activity for the Oxygen Evolution Reaction, J. Phys. Chem. C. 121 (2017) 6455–6463. https://doi.org/10.1021/acs.jpcc.6b12652.
- [81] L.M. Vicente-Arche, J. Bréhin, S. Varotto, M. Cosset-Cheneau, S. Mallik, R. Salazar, P. Noël, D.C. Vaz, F. Trier, S. Bhattacharya, A. Sander, P.L. Fèvre, F. Bertran, G. Saiz, G. Ménard, N. Bergeal, A. Barthélémy, H. Li, C.-C. Lin, D.E. Nikonov, I.A. Young, J.E. Rault, L. Vila, J.-P. Attané, M. Bibes, Spin-Charge Interconversion in KTaO3 2D Electron Gases, Adv. Mater. n/a (n.d.) 2102102. https://doi.org/10.1002/adma.202102102.
- [82] S. Dutta, A. Indra, Y. Feng, T. Song, U. Paik, Self-Supported Nickel Iron Layered Double Hydroxide-Nickel Selenide Electrocatalyst for Superior Water Splitting Activity, ACS Appl. Mater. Interfaces. 9 (2017) 33766–33774. https://doi.org/10.1021/acsami.7b07984.

- [83] Y.-Z. Su, K. Xiao, N. Li, Z.-Q. Liu, S.-Z. Qiao, Amorphous Ni(OH)2 @ three-dimensional Ni core—shell nanostructures for high capacitance pseudocapacitors and asymmetric supercapacitors, J. Mater. Chem. A. 2 (2014) 13845–13853. https://doi.org/10.1039/C4TA02486A.
- [84] Y. Yu, R. Jin, J. Easa, W. Lu, M. Yang, X. Liu, Y. Xing, Z. Shi, Highly active and stable copper catalysts derived from copper silicate double-shell nanofibers with strong metal–support interactions for the RWGS reaction, Chem. Commun. 55 (2019) 4178–4181. https://doi.org/10.1039/C9CC00297A.
- [85] M. Li, F. Cárdenas-Lizana, M.A. Keane, Combined catalytic action of supported Cu and Au in imine production from coupled benzyl alcohol and nitrobenzene reactions, Appl. Catal. Gen. 557 (2018) 145–153. https://doi.org/10.1016/j.apcata.2018.03.024.
- [86] E.L. Ratcliff, J. Meyer, K.X. Steirer, A. Garcia, J.J. Berry, D.S. Ginley, D.C. Olson, A. Kahn, N.R. Armstrong, Evidence for near-Surface NiOOH Species in Solution-Processed NiOx Selective Interlayer Materials: Impact on Energetics and the Performance of Polymer Bulk Heterojunction Photovoltaics, Chem. Mater. 23 (2011) 4988–5000. https://doi.org/10.1021/cm202296p.
- [87] O.U. Valdés-Martínez, C.E. Santolalla-Vargas, V. Santes, J.A. de los Reyes, B. Pawelec, J.L.G. Fierro, Influence of calcination on metallic dispersion and support interactions for NiRu/TiO2 catalyst in the hydrodeoxygenation of phenol, Catal. Today. 329 (2019) 149–155. https://doi.org/10.1016/j.cattod.2018.11.007.
- [88] Y. Suzuki, T. Hattori, T. Okuzawa, S. Miyano, Lewis Acid-Mediated Carboxylation of Fused Aromatic Compounds with Carbon Dioxide, Chem. Lett. 31 (2002) 102–103. https://doi.org/10.1246/cl.2002.102.
- [89] G.A. Olah, B. Török, J.P. Joschek, I. Bucsi, P.M. Esteves, G. Rasul, G.K. Surya Prakash, Efficient Chemoselective Carboxylation of Aromatics to Arylcarboxylic Acids with a Superelectrophilically Activated Carbon Dioxide—Al2Cl6/Al System, J. Am. Chem. Soc. 124 (2002) 11379–11391. https://doi.org/10.1021/ja020787o.
- [90] Y. Fujiwara, K. Tabaki, Y. Taniguchi, Exploitation of Synthetic Reactions via C-H Bond Activation by Transition Metal Catalysts. Carboxylation and Aminomethylation of Alkanes or Arenes, Synlett. 1996 (1996) 591–599. https://doi.org/10.1055/s-1996-5541.
- [91] D. Fildes, V. Caignaert, D. Villemin, P.-A. Jaffrès, Potassium exchanged zirconium hydrogen phosphate Zr(O3POK)2: a heterogeneous basic catalyst for Knoevenagel reaction without solvent, Green Chem. 3 (2001) 52–56. https://doi.org/10.1039/B009199P.
- [92] H. Gruber-Woelfler, P.F. Radaschitz, P.W. Feenstra, W. Haas, J.G. Khinast, Synthesis, catalytic activity, and leaching studies of a heterogeneous Pd-catalyst including an immobilized

- bis(oxazoline) ligand, J. Catal. 286 (2012) 30–40. https://doi.org/10.1016/j.jcat.2011.10.013.
- [93] W.A. Rodríguez-Rodríguez, J. Colón, R. Guzmán, H. Rivera, M.B. Santiago-Berríos, Synthesis, characterization and electrochemical characterization of lead selenide sub-micron particles capped with a benzoate ligand and prepared at different temperatures, Mater. Res. Express. 1 (2014) 035906. https://doi.org/10.1088/2053-1591/1/3/035906.
- [94] G.B. Tolstorozhev, M.V. Bel'kov, I.V. Skornyakov, O.K. Bazyl, V.Ya. Artyukhov, G.V. Mayer, O.I. Shadyro, P.V. Kuzovkov, S.D. Brinkevich, S.N. Samovich, Infrared Spectroscopy of Hydrogen Bonds in Benzoic Acid Derivatives, J. Appl. Spectrosc. 81 (2014) 109–117. https://doi.org/10.1007/s10812-014-9895-8.
- [95] A. Bilić, J.R. Reimers, N.S. Hush, R.C. Hoft, M.J. Ford, Adsorption of Benzene on Copper, Silver, and Gold Surfaces, J. Chem. Theory Comput. 2 (2006) 1093–1105. https://doi.org/10.1021/ct050237r.
- [96] S.J. Carey, W. Zhao, C.T. Campbell, Energetics of adsorbed benzene on Ni(111) and Pt(111) by calorimetry, Surf. Sci. 676 (2018) 9–16. https://doi.org/10.1016/j.susc.2018.02.014.
- [97] M. Saeys, M.-F. Reyniers, G.B. Marin, M. Neurock, Density Functional Study of Benzene Adsorption on Pt(111), J. Phys. Chem. B. 106 (2002) 7489–7498. https://doi.org/10.1021/jp0201231.
- [98] C. Morin, D. Simon, P. Sautet, Chemisorption of Benzene on Pt(111), Pd(111), and Rh(111) Metal Surfaces: A Structural and Vibrational Comparison from First Principles, J. Phys. Chem. B. 108 (2004) 5653–5665. https://doi.org/10.1021/jp0373503.
- [99] M. Sacchi, P. Singh, D.M. Chisnall, D.J. Ward, A.P. Jardine, W. Allison, J. Ellis, H. Hedgeland, The dynamics of benzene on Cu(111): a combined helium spin echo and dispersion-corrected DFT study into the diffusion of physisorbed aromatics on metal surfaces, Faraday Discuss. 204 (2017) 471–485. https://doi.org/10.1039/C7FD00095B.
- [100] V. Vorotnikov, G. Mpourmpakis, D.G. Vlachos, DFT Study of Furfural Conversion to Furan, Furfuryl Alcohol, and 2-Methylfuran on Pd(111), ACS Catal. 2 (2012) 2496–2504. https://doi.org/10.1021/cs300395a.
- [101] J.-H. Choi, Z. Li, P. Cui, X. Fan, H. Zhang, C. Zeng, Z. Zhang, Drastic reduction in the growth temperature of graphene on copper via enhanced London dispersion force, Sci. Rep. 3 (2013) 1925. https://doi.org/10.1038/srep01925.
- [102] W. Liu, V.G. Ruiz, G.-X. Zhang, B. Santra, X. Ren, M. Scheffler, A. Tkatchenko, Structure and energetics of benzene adsorbed on transition-metal surfaces: density-functional theory with van der Waals interactions including collective substrate response, New J. Phys. 15 (2013) 053046. https://doi.org/10.1088/1367-2630/15/5/053046.

- [103] T.W. White, N. Martsinovich, A. Troisi, G. Costantini, Quantifying the "Subtle Interplay" between Intermolecular and Molecule–Substrate Interactions in Molecular Assembly on Surfaces, J. Phys. Chem. C. 122 (2018) 17954–17962. https://doi.org/10.1021/acs.jpcc.8b06797.
- [104] A.K. Myers, G.R. Schoofs, J.B. Benziger, Comparison of benzene adsorption on nickel(111) and nickel(100), ACS Publ. (2002). https://doi.org/10.1021/j100293a002.
- [105] L. Delle Site, A. Alavi, C.F. Abrams, Adsorption energies and geometries of phenol on the (111) surface of nickel: An ab initio study, Phys. Rev. B. 67 (2003) 193406. https://doi.org/10.1103/PhysRevB.67.193406.
- [106] F. Mittendorfer, J. Hafner, Density-functional study of the adsorption of benzene on the (111), (100) and (110) surfaces of nickel, Surf. Sci. 472 (2001) 133–153. https://doi.org/10.1016/S0039-6028(00)00929-8.
- [107] Z. Jiang, P. Qin, T. Fang, Decomposition mechanism of formic acid on Cu (111) surface: A theoretical study, Appl. Surf. Sci. 396 (2017) 857–864. https://doi.org/10.1016/j.apsusc.2016.11.042.
- [108] J.A. Herron, J. Scaranto, P. Ferrin, S. Li, M. Mavrikakis, Trends in Formic Acid Decomposition on Model Transition Metal Surfaces: A Density Functional Theory study, ACS Catal. 4 (2014) 4434–4445. https://doi.org/10.1021/cs500737p.
- [109] T.C. Lin, U. De La Torre, A. Hejazi, S. Kwon, E. Iglesia, Unimolecular and bimolecular formic acid decomposition routes on dispersed Cu nanoparticles, J. Catal. 404 (2021) 814–831. https://doi.org/10.1016/j.jcat.2021.08.049.

### **CHAPTER 6**

# Precisely Designed Cobalt Single Atom on ZrO<sub>2</sub> Support for Chemical CO<sub>2</sub> Fixation

#### 6.1. Introduction

Heterogeneous catalysis has entered a new phase with the development of single-atom catalysts (SACs), in which the isolated active metal atoms are anchored to supports. 1-4 In SACs, every surface atomic site is accessible which delivers superior catalytic performance and the highest atom utilization efficiency.<sup>5,6</sup> SACs act as a bridge homogeneous and heterogeneous catalysts as they posesses properties of both type of materials i.e. recyclability and easy recoverability, thermal stability and better exposure of active sites.<sup>7,8</sup> For industrial applications, recyclability and cost-effectiveness and catalytic performance are the key requirements. In comparison to nano particle catalysts, SACs have demonstrated impressive enhancements in catalytic activity in various catalytic processes due to their distinct structural characteristics and fully exposed active sites. <sup>7–10</sup> However, the synthesis and stabilization of SACs is a challenging task due to the high surface energy of the isolated atoms, resulting in agrregation of SACs and decrease in catalytic activity. 11-13 For synthesizing SACs, various stratagies like doping, utilization of defects and spatial confinement have been utilized to stabilize the single atom over different supports. 11,14,15 Moreover, characterization of SACs remains a daunting task since it requires atomic level high resolution in techniques like STEM-HAADF and EELS. The conventional transmission electron mircoscopes are unable to observe single atoms on supported materials owing to their contrast mechanisms.<sup>16</sup> Aberration-corrected HAADF-STEM is extremely sensitive to atomic number of the atoms present in the sample. However, it is still challenging to observe single atoms when the difference in atomic numbers of the isolated atoms and the support is not enough to provide sufficient contrast. <sup>17</sup> Since AC-STEM is a local technique, it is necessary to combine information with techniques that provide an average over the entire sample, like EXAFS, and XANES while also yielding information on oxidation states and bond distances for nearest neighbors for the supported single atoms.<sup>18</sup>

Recently, SACs were explored for electrocatalytic, thermal and photocatalytic CO<sub>2</sub> hydrogenation and valorization reactions due to their enhanced catalytic performance. 4,19-23 SACs provide more exposure to active sites and result in product selectivity and enhancement in catalytic activity. An ideal catalyst would have a low energy barrier, selectivity towards the desired product, easy synthesis, recoverability and costeffectiveness.<sup>24</sup> SACs of non-noble metals have all these advantanges, which can reduce the process cost while increasing the catalytic performance without compromising selectivity towards desired products. 25,26 Hence, SACs of non-noble metals are the best choice for CO<sub>2</sub> conversion into value-added products. Carbon dioxide is the major greenhouse gas which leads to climate change and global warming. Thus, the conversion of CO<sub>2</sub> into value-added products can help achieve sustainablity and carbon neutrality. Previous efforts to utilize or capture CO<sub>2</sub> have explored the production of value added products like cyclic caronates, urea, methanol, etc.. However, owing to its high thermodynamic stability, the conversion of CO<sub>2</sub> requires high pressure and temperture. Also, achieving selectivity towards one product is a desirable goal for CO<sub>2</sub> conversion, otherwise in the case of CO<sub>2</sub> hydrogenation we can produce methanol, methane, formate, formic acid, etc.<sup>27,28</sup>

CO<sub>2</sub> fixation and reaction with epoxides to yield cyclic carbonates has potential to produce many commercial products since there are few undesirable side products.<sup>29</sup> The cycloaddition of CO<sub>2</sub> with epoxides is useful for the synthesis of plastics, cosmetics and adhesives.<sup>30,31</sup> These are useful as intermiadiates for various synthetic processes and also as electrolytes in lithium-ion batteries.Cyclic carbonates have also been utilized to synthesize commercially significant compounds including polycarbonates, polyurethanes, and

dialkyl carbonates etc.<sup>32</sup> Traditionally cyclic carbonates were synthesized using highly toxic phosgene, which is banned in many countries. Hence, the synthesis of cyclic carbonates from cycloaddition reaction of epoxides and carbon dioxide is a promising pathway.

Recently, various metal organic frameworks (MOFs) of Cu<sup>33</sup>, Pd@Eu<sup>34</sup>, Ca based<sup>35</sup>, Yttrium<sup>36</sup>, thulium<sup>37</sup>, Zn<sup>38,39</sup> and Ln based coordinated polymers<sup>40</sup> have been explored for the CO<sub>2</sub> fixation of expoxides with tetrabuthylammonium halogen containing reagent (TBAX) at 70-100°C for 4-24 hours and under solvent-free reaction conditions. Furthermore, CuCo<sub>2</sub>O<sub>4</sub> spinel<sup>30</sup>, phenolated lignin NPs<sup>41</sup>, ligated Ti coated Bi-oxo cores<sup>42</sup>, PABA@α-Fe<sub>2</sub>O<sub>3</sub><sup>43</sup> and N,S co-doped bifunctional carbon catalyst<sup>44</sup> were also explored using TBAX at room temperature to 105 °C for 3-24 hours. In all cases moderate to good yield was obtained but the reaction time and TBAX amount required was reatively high even at high reaction temperature. However, ionic liquidbased and halide-free reactions were also reported at 60-90 °C and 12-48 hours reaction times with poor substrate scopes. <sup>29,45,46</sup> Several SACs were recently reported for cycloaddition of CO<sub>2</sub> into epoxides;<sup>47–50</sup> however, these all showed narrow substrate scope or required solvents like DCM and DMF.

Herein, we synthesized a Co/ZrO<sub>2</sub> SAC via a facile coprecicipitation method and characterized extensively it with EXAFS, STEM, HAADF and XANES techniques to confirm the presence of single atoms and utilized it for catalytic conversion of epoxides into cyclic carbonates. The single atom catalyst showed superior catalytic activity compared to undoped ZrO<sub>2</sub> and Co<sub>3</sub>O<sub>4</sub>/ZrO<sub>2</sub> catalyst. The Co/ZrO<sub>2</sub> SAC showed 100% conversion with 100% selectivity towards cyclic carbonate product with minimal amount of TBAB (0.06 mmol) in solvent-free conditions which makes it cost-effective, greener, and environmentally benign<sup>43,51</sup>, whereas undoped ZrO<sub>2</sub> and Co<sub>3</sub>O<sub>4</sub>/ZrO<sub>2</sub> catalyst showed less than 50% conversion, confirming that the single atom catalyst provides more active sites. The catalyst showed broad substrate scope with excellent yield in all the cases with recyclability of up to six cycles.

### **6.2.** Experimental section

#### 6.2.1. Materials

Cobalt nitrate hexahydrate ( $Co(NO_{3)2}$ .  $6H_2O$ )  $\geq 99\%$  pure and zirconyl nitrate hydrate ( $ZrO(NO_3)_2$ .  $xH_2O$ ) anhydrous  $\geq 99.99\%$  pure were purchased from SRL chemicals, India. Ammonia solution was purchased from Merck, India. Reagents and epoxides compounds  $\geq 98-100\%$  pure were purchased from Sigma-Aldrich and TCI, India. All solvents were used as received.

#### **6.2.2.** Catalyst preparation

#### 6.2.2.1 Synthesis of Co doped ZrO<sub>2</sub>

For synthesizing Co doped ZrO<sub>2</sub>, firstly Cobalt nitrate hexahydrate and Zirconyl nitrates hydrates (1:9 molar ratio) were taken in round bottom flask in 50 mL water and stirred the mixture for 20 minutes. To maintain the pH ~ 9, ammonia solution was added dropwise with continuous stirring. During this addition of ammonia solution colour changes from light pink to bluish pink colour. After stirring the mixture for next 1 hour, the solution was centrifuged and washed several times with water till pH~7 and then dried overnight at 100 °C. Thereafter, the solid precipitate was calcined at 500 °C for 3 hours with ramping temperature 2 °C/min. The synthesized catalyst is named as Co/ZrO<sub>2</sub> single atom catalyst.

### 6.2.2.2. Synthesis of undoped ZrO<sub>2</sub>

The undoped ZrO<sub>2</sub> catalyst was synthesized using zirconyl nitrate with above mentioned method without using cobalt nitrate.

### 6.2.2.3. Synthesis of Co<sub>3</sub>O<sub>4</sub> supported on ZrO<sub>2</sub>

For synthesizing cobalt impregnated  $ZrO_2$  catalyst, as synthesized  $ZrO_2$  was initially taken in round bottom flask and stirred it into water for 20 minutes at room temperature. In another beaker,  $Co(NO_3)_2$ .  $6H_2O$  was dissolved in 10 mL water and added dropwise to the above dispersed solution of  $ZrO_2$  and allowed to stir the mixture for another 1 hour. After

1 hour, the solution was evaporated under reduced pressure and the precipitates were dried overnight at 100 °C and then calcined at 500 °C for 3 hours with ramping temperature 2 °C/min. The synthesized catalyst is named as Co<sub>3</sub>O<sub>4</sub>/ZrO<sub>2</sub> catalyst.

### 6.2.3. General catalytic reaction

In a general CO<sub>2</sub> fixation reaction, epoxides substrates (10 mmol) were added with catalyst (15 mg), TBAB (0.06 mmol) in stainless steel containing teflon reaction vessel pressure reactor attached with thermocouple at magnetic stirring bar. After closing the reactor, the reaction vessel was flushed three times with CO<sub>2</sub> to replace the existing air and then pressurized with 2 bar pressure and keep it for stirring at 80 °C for required reaction time. After completion of reaction, the reactor was cooled down to room temperature and pressure was released. The reaction mixture was centrifuged for catalyst separation and then catalyst was washed, dried and used for next cycle. The reaction mixture was diluted with ethyl acetate and dried under rota evaporator and given for GC-Ms and NMR analysis.

### 6.2.4. Physicochemical characterization

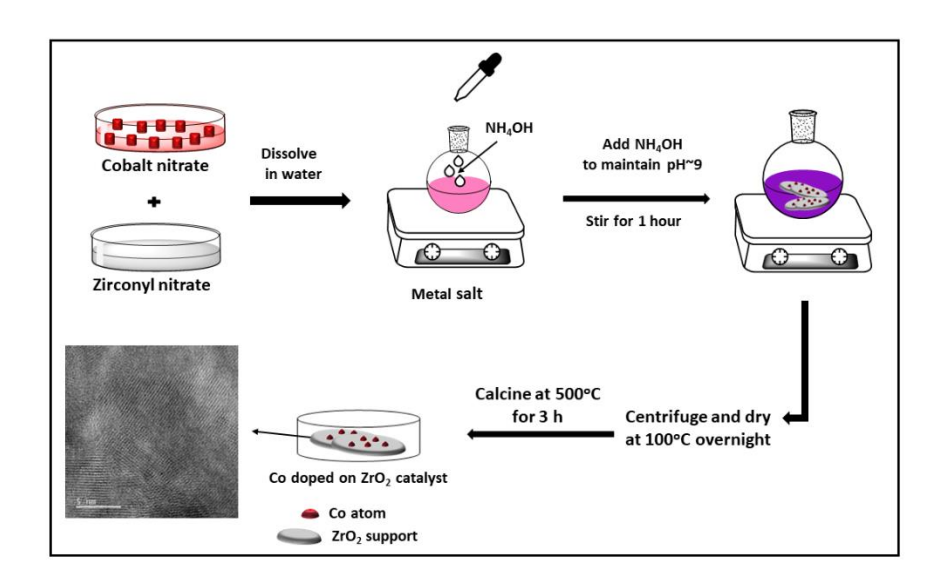
The details about the PXRD, FE-SEM, HR-TEM, BET characterization and utilized instruments have been discussed in Chapter 2 in physicochemical measurements section. The details about TGA, XPS and VSM analysis were discussed already in Chapter 3 in physicochemical measurements section and the details about ICP-AES, GC-MS was discussed in Chapter 4, physicochemical section. The formation of substituted products was confirmed by <sup>1</sup>H and <sup>13</sup>C NMR analysis using NMR Spectrometer, Model AVANCE NEO Ascend 500 Bruker BioSpin International AG. Samples were dispersed in ethanol and mounted on holey carbon grids for examination in a JEOL NEOARM 200CF transmission electron microscope equipped with spherical aberration correction to allow atomic resolution imaging, and an Oxford Aztec Energy Dispersive System (EDS) for elemental analysis. The microscope is equipped with two large area JEOL EDS

detectors for higher throughput in acquisition of x-ray fluorescence signals. Images were recorded in annular dark field (ADF) mode and in annular bright field (ABF) mode. XAS experiments were performed at 5BM-D beamline of DND-CAT at beamline 5 BM-D (DND-CAT) of the Advanced Photon Source (APS) of Argonne National Laboratory, at Co K (7709 eV) edge. Co/ZrO2 and Co3O4/ZrO2 samples were ground to a fine powder by using a pestle and mortar, then evenly spread on long Scotch tape (3M Corp) to form a uniform sample layer. The tape was folded to create a uniform surface to produce adequate absorption. The sample was mounted vertically on a sample holder with its surface normal bisecting the 90 angles between the X-ray incidence and photon detecting directions. A double crystal Si (111) monochromator was used for energy selection. Both Co K-edge XANES and EXAFS were measured under fluorescence mode by a Vortex ME4 detector. Metal Co foil transmission spectrum for energy calibration was collected along with each sample. XAS data were processed using WinXAS software.<sup>52</sup> Simulated phase and amplitude functions for Co-O scattering were extracted using Feff6.<sup>53</sup> The extracted *chi* was  $k^2$ -weighted and Fourier transformed over a k range of 2.5 to 10 Å<sup>-1</sup> for the samples. The  $S_0^2$  value was determined by fitting the Co foil reference compound. Fitting was performed in q-space to determine the Debye-Waller factor,  $\Delta \sigma^2$ . The final EXAFS fits were conducted in *R*-space.

### 6.3. Results and discussion

### **6.3.1.** Characterization of catalyst

The single-atom catalyst  $Co/ZrO_2$  was synthesized via coprecipitation method as shown in **Scheme 6.1.** For comparison, undoped  $ZrO_2$  and  $Co_3O_4$  impregnated  $ZrO_2$  was synthesized via incipent wetness impregnation (See supporting information).



**Scheme 6.1.** Schematic representation of the synthesis of Co/ZrO<sub>2</sub> catalyst.

All three catalysts i.e., single atom Co/ZrO<sub>2</sub> catalyst, undoped ZrO<sub>2</sub> and Co<sub>3</sub>O<sub>4</sub>/ZrO<sub>2</sub> catalyst were characterized using powder X-ray diffraction as shown in Figure 6.1. As shown in Figure 6.1A, undoped ZrO<sub>2</sub> catalyst showed peaks at 30.31°, 35.29°, 50.40°, 60.36° and 63.11° corresponding to the (101), (110), (200), (211) and (202) reflections of tetragonal ZrO<sub>2</sub> in agreement with JCPDS# 01-080-0965. 54,55 In contrast, the cobalt doped catalyst was analysed and there was no peak corresponding to any cobalt phase, which confirms that the Co was doped into the ZrO<sub>2</sub> surface. The XRD pattern shows that there is shift in the (101) plane of  $ZrO_2$  to higher  $2\theta$  value, further confirming the doping of cobalt as shown in **Figure 6.1B**. This peak shift is observed due to a decrease in the interplanar spacing in ZrO2 due to cobalt doping. 56,57 The ionic radii of Co<sup>+2</sup> is 0.74 Å, less than the ionic radius of 0.84 Å for Zr<sup>+4</sup> and which leads to change in lattice constant and results in shift of t-ZrO<sub>2</sub> plane to a higher 2θ value.<sup>58</sup> In the cobalt doped catalyst, no peak of Co<sub>3</sub>O<sub>4</sub> was observed.<sup>59</sup> This absence of cobalt and cobalt oxide peaks in the Co/ZrO<sub>2</sub>, supports the inference of doping of cobalt on the zirconia support. For comparison, Co<sub>3</sub>O<sub>4</sub> impregnated ZrO<sub>2</sub> was also synthesized and analysed, showing sharp peaks at 36.88°, 44.95°, 59.51° and 65.11° corresponding to the (311), (400), (511) and (440) planes of Co<sub>3</sub>O<sub>4</sub> in agreement with JCPDS# 043-1003 as shown in **Figure 6.1A**. $^{60,61}$  When compared with the Co/ZrO<sub>2</sub> catalyst, the powder XRD peak of Co<sub>3</sub>O<sub>4</sub> for (311) plane was absent in case of Co/ZrO<sub>2</sub> suggesting the absence of nanoparticles in Co/ZrO<sub>2</sub> catalyst. $^{62}$ The average crystallite size was calculated using the Scherrer equation $^{63}$  and it was found to be 17 nm, 20 nm and 12 nm for Co/ZrO<sub>2</sub>, undoped ZrO<sub>2</sub> and Co<sub>3</sub>O<sub>4</sub>/ZrO<sub>2</sub> respectively.

The thermal stability of Co doped ZrO<sub>2</sub> catalyst was analyzed by heating from 30 °C to 700 °C temperature under a nitrogen atmosphere. The thermogravimetric analysis indicates only 4% weight loss, which confirm the high thermal stability of the Co doped ZrO<sub>2</sub> catalyst as shown in **Figure 6.2**. There was initial weight loss up to 200 °C due to removal of adsorbed water and further weight loss was observed due to removal of trapped organic species inside the pores of ZrO<sub>2</sub> support material.<sup>51</sup>

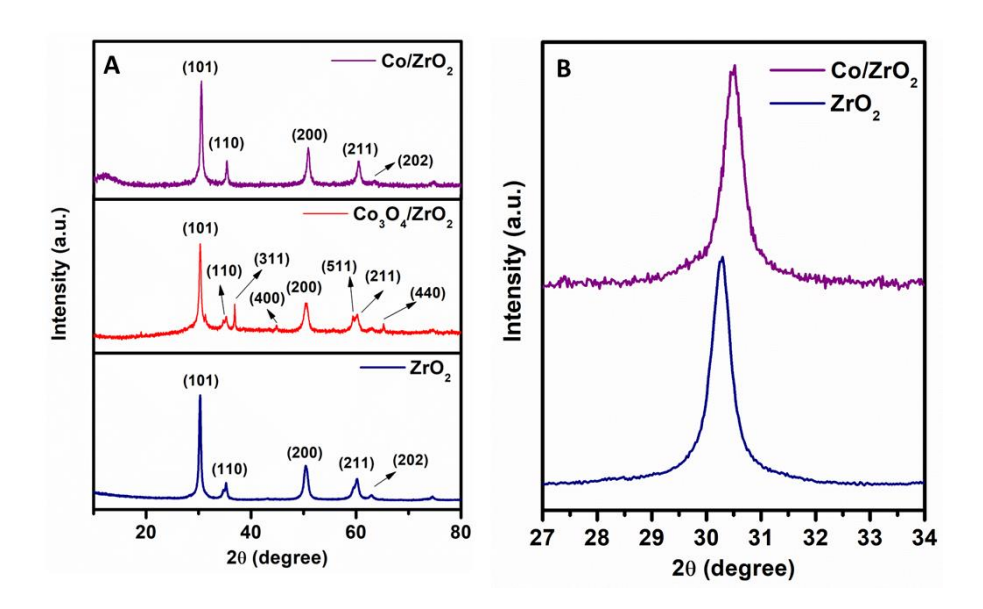


**Figure 6.1.** (**A**) PXRD of Co/ZrO<sub>2</sub> single atom catalyst, Co<sub>3</sub>O<sub>4</sub> supported on ZrO<sub>2</sub> and undoped ZrO<sub>2</sub> and (**B**) shifting of (101) plane of ZrO<sub>2</sub> with doping of cobalt.

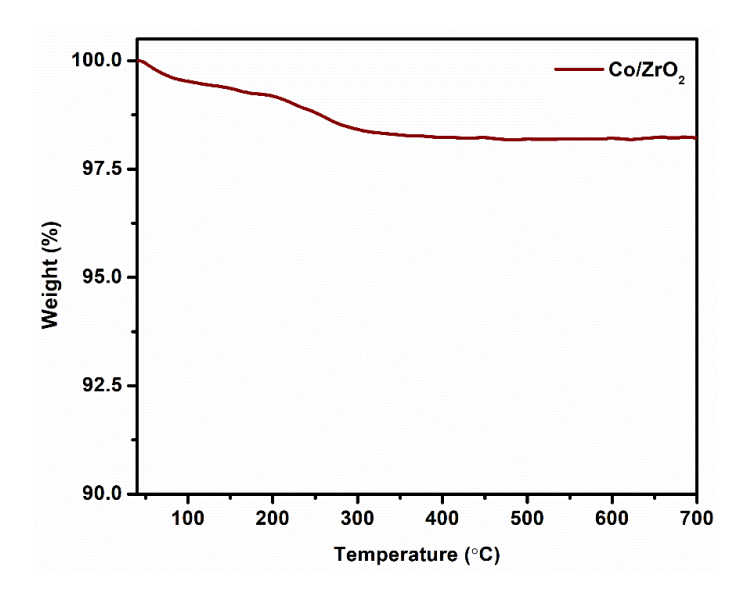


**Figure 6.2.** Thermogravimetric analysis of Co/ZrO<sub>2</sub> single atom catalyst.

N<sub>2</sub> adsorption-desorption was performed at 1 bar pressure at 77 K temperature after degassing at 300 °C temperature to determine surface area, pore size and pore volume (**Figure 6.3**). Cobalt doped ZrO<sub>2</sub> catalyst has a high surface area of 76 m<sup>2</sup>/g with pore size and pore volume of 3.4 nm, and 0.061 cm<sup>3</sup>/g respectively. The N<sub>2</sub> adsorption-desorption curve followed a type IV isotherm suggesting the formation of mesopores, which is in good agreement with the Barrett-Joyner-Halenda (BJH) pore size calculated value.

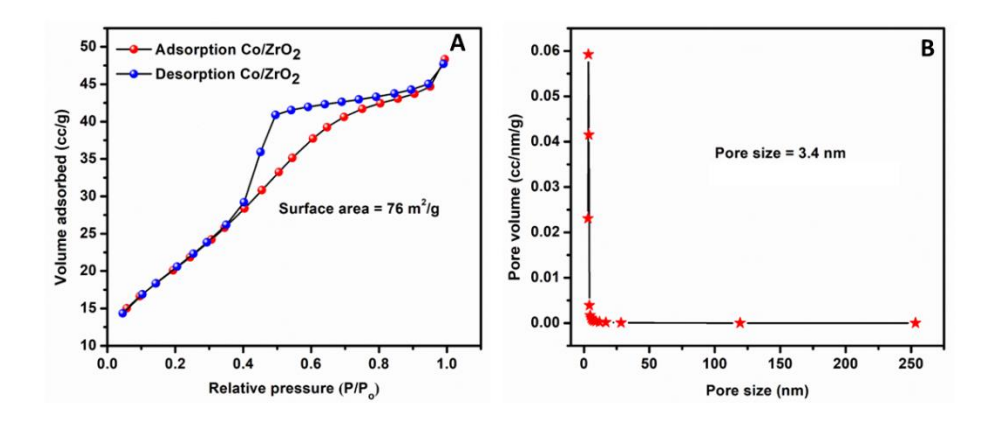


**Figure 6.3**. N<sub>2</sub> adsorption-desorption study for (**A**) surface area and (**B**) Pore size distribution of Co/ZrO<sub>2</sub> single atom catalyst.

Moreover, the undoped ZrO<sub>2</sub> and Co<sub>3</sub>O<sub>4</sub> impregnated ZrO<sub>2</sub> was also analyzed, and all three-catalysts showed the same type of isotherm.

Moreover, the calculated surface area, pore size and pore volume were found to be 69 m<sup>2</sup>/g, 3.4 nm and 0.061 cc/g respectively for undoped  $ZrO_2$  (see **Figure 6.4(A-B)**). Additionally, the specific surface area of  $Co_3O_4/ZrO_2$  catalyst was also calculated using the BET equation and was estimated as 46 m<sup>2</sup>/g with a pore size and pore volume of 3.4 nm and 0.057 cc/g respectively (see **Figure 6.4(C-D)**).

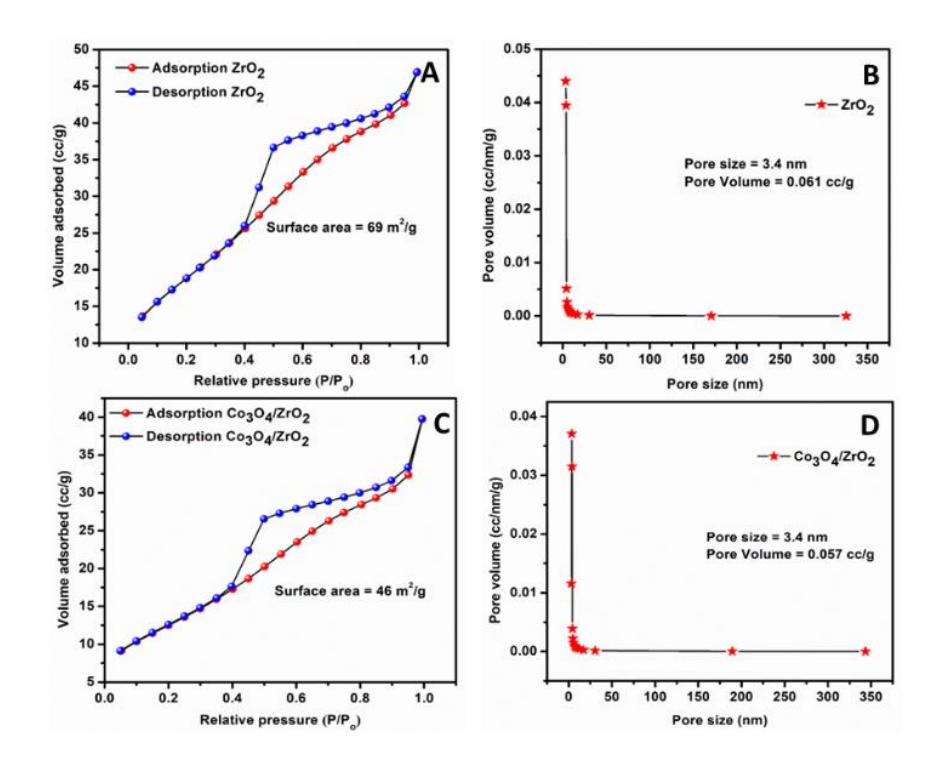


**Figure 6.4.** N<sub>2</sub> adsorption-desorption study for (**A-C**) surface area and (**B-D**) Pore size distribution of undoped ZrO<sub>2</sub> and Co<sub>3</sub>O<sub>4</sub>/ZrO<sub>2</sub> catalyst.

To confirm the atomic dispersion of cobalt atom on zirconia, aberration corrected scanning transmission electron microscopy (AC-STEM) was performed. Annular dark field (ADF) and simultaneous annular bright field (ABF) STEM images were recorded as shown in **Figure 6.5.** In ABF mode, the crystalline morphology of ZrO<sub>2</sub> can be seen clearly as indicated by the lattice fringes (**Figure 6.5(A-B)**). In ADF mode, there were no identifiable single Co atoms on ZrO<sub>2</sub> as shown in **Figure 6.5(C-D)** as a result of the lower atomic number of Co relative to Zr. It is important to note that no clusters of cobalt oxide were observed anywhere in the Co doped catalyst.

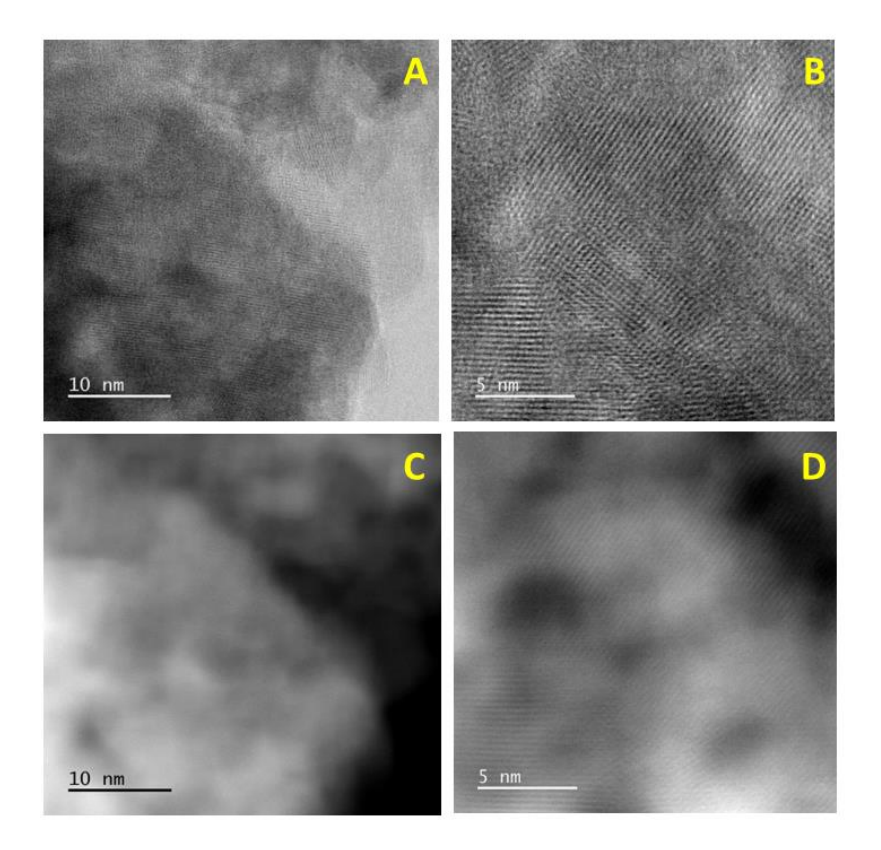


**Figure 6.5.** (**A-B**) STEM images in ABF mode and (**C-D**) STEM images in ADF mode of Co/ZO<sub>2</sub> single atom catalyst.

Further, to confirm the dispersion of Co, Energy-dispersive X-ray spectroscopy (EDS) was performed in different regions of Co/ZrO<sub>2</sub> at various magnifications, as shown in **Figure 6.6.** 

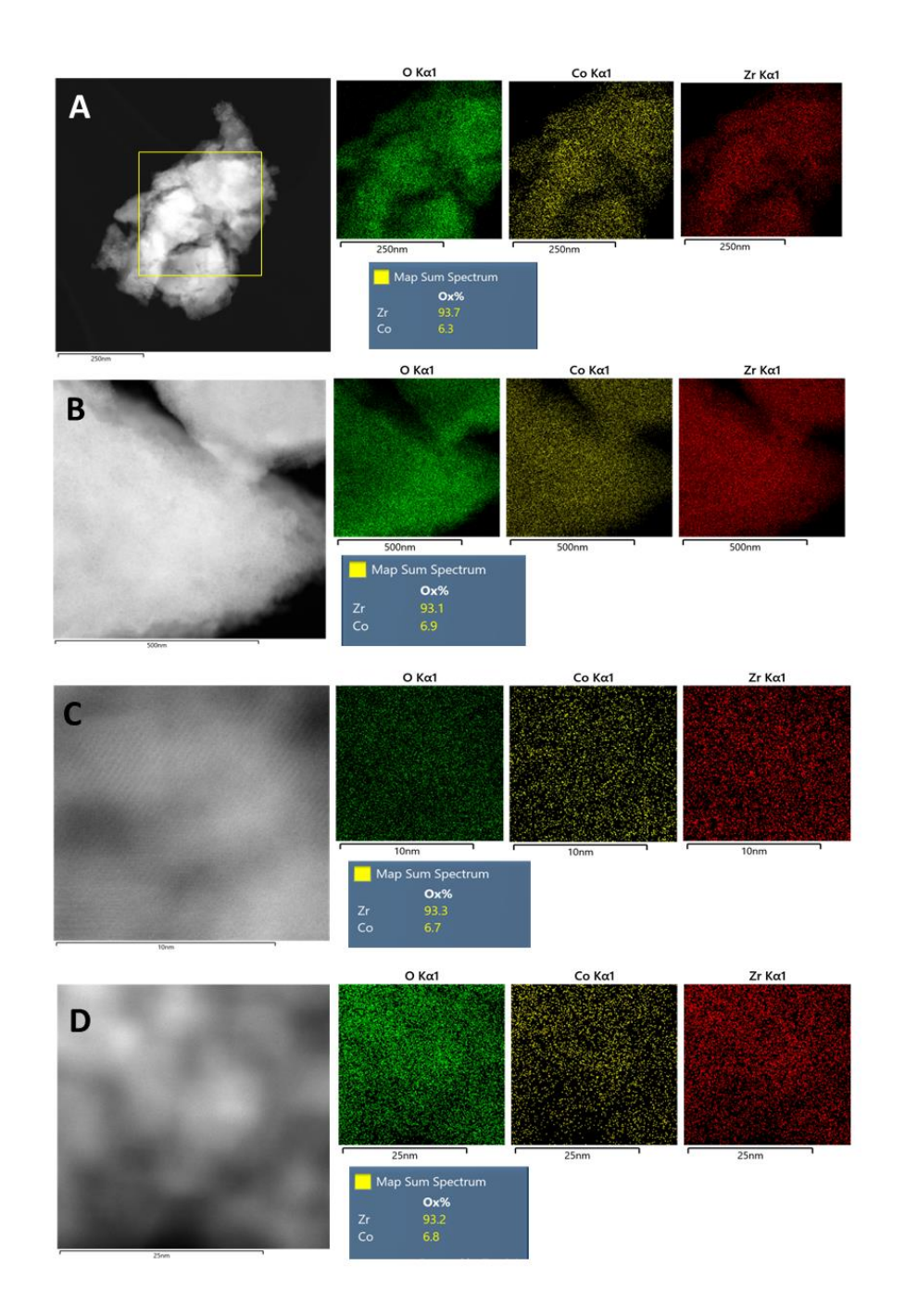


**Figure 6.6.** STEM mapping of Zirconium, Cobalt, and Oxygen element of Co doped ZrO<sub>2</sub> catalyst at different regions at higher magnifications with scale bars of (**A**) 250 nm, (**B**) 500 nm, (**C**) 10 nm and (**D**) 25 nm.

In each elemental mapping, the cobalt distribution was uniform (i.e., ~7 wt%) on ZrO<sub>2</sub> and no detectable Co particles on ZrO<sub>2</sub> were observed in the cobalt map. Similarly, the EDS results of HR-TEM and FE-SEM analysis were consistent for Co distribution on ZrO<sub>2</sub> as shown in **Figure 6.7** and **Figure 6.8** respectively, which suggests the atomic dispersion of cobalt on the ZrO<sub>2</sub> support. The lattice fringe of 0.287 nm

corresponding to the (101) planes of t-ZrO<sub>2</sub> are shown in **Figure 6.7B**, which is in agreement with PXRD spectra of the Co single atom catalyst (**Figure 6.1**). The colour mapping of Co doped ZrO<sub>2</sub> catalyst showed uniform distribution of Co on ZrO<sub>2</sub> catalyst as shown in **Figure 6.7C**. The SAED pattern of the Co/ZrO<sub>2</sub> catalyst show the concentric rings expected from the crystalline zirconia support as shown in **Figure 6.7D** inset.

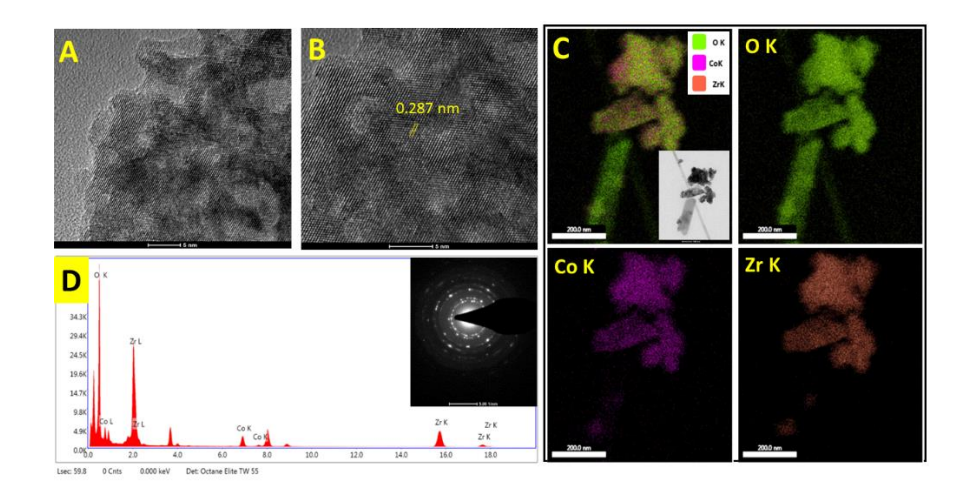


**Figure 6.7.** HR-TEM images of single atom Co/ZrO<sub>2</sub> catalyst at (**A-B**) 5 nm, (**C**) Elemental mapping and (**D**) EDS spectra (inset selected area electron diffraction (SAED) pattern at 5 1/nm).

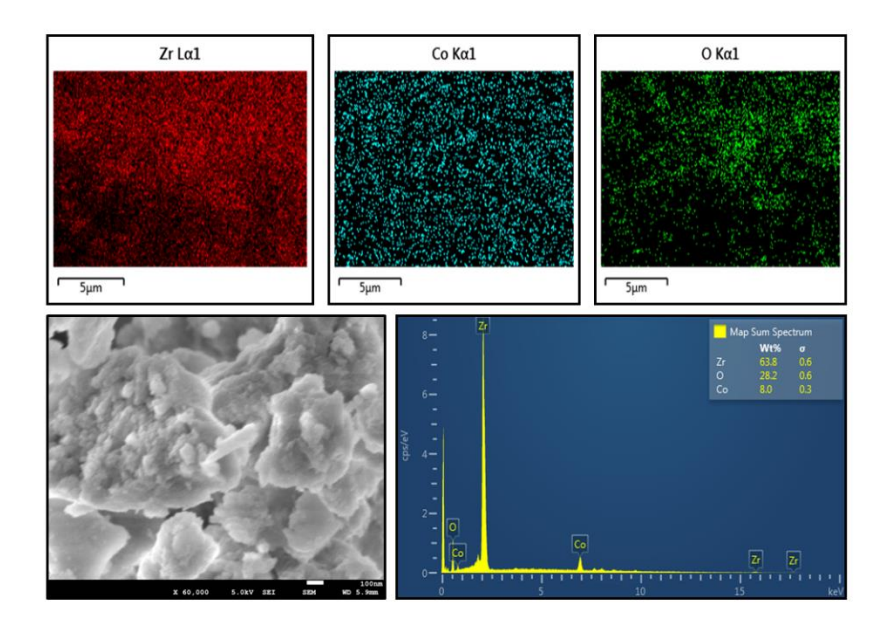


**Figure 6.8.** FE-SEM mapping and elemental analysis of Zirconium, Cobalt, and Oxygen of Co doped ZrO<sub>2</sub> catalyst.

For comparison, STEM images of Co<sub>3</sub>O<sub>4</sub> impregnated ZrO<sub>2</sub> were also recorded, which revealed that the catalyst has two types of morphology: one with small pores and the other with more open pore structures as shown in **Figure 6.9A**. The morphology is quite distinct as seen in this figure and in some cases the two phases are joined to each other, as shown in **Figure 6.9B**. The EDS analysis shows that the open pore structure comes from the Co<sub>3</sub>O<sub>4</sub> phase since its concentration increases as we zoom into the open pore structure (Figure 6.3C and **6.3D**). The particles of Co<sub>3</sub>O<sub>4</sub> can be as large as the ZrO<sub>2</sub> particles (Figure 6.10A). However, EDS analysis shows that smaller Co<sub>3</sub>O<sub>4</sub> aggregates could be dispersed on the ZrO<sub>2</sub> (Figure 6.10C). Also, in some regions of ZrO<sub>2</sub> there were regions suggestive of atomically dispersed Co (**Figure 6.10D**). In summary, while the cobalt doped ZrO<sub>2</sub> catalyst contains exclusively atomically dispersed Co, whereas in the impregnated catalyst we see phase separation of Co<sub>3</sub>O<sub>4</sub> and ZrO<sub>2</sub>. Additionally, we also see atomically dispersed Co on the ZrO<sub>2</sub> in the impregnated catalyst These results are in good agreement with PXRD data where the sharp (311) peak corresponding to large Co<sub>3</sub>O<sub>4</sub> particles in  $Co_3O_4/ZrO_2$  is not seen in case of the Co doped on  $ZrO_2$ .

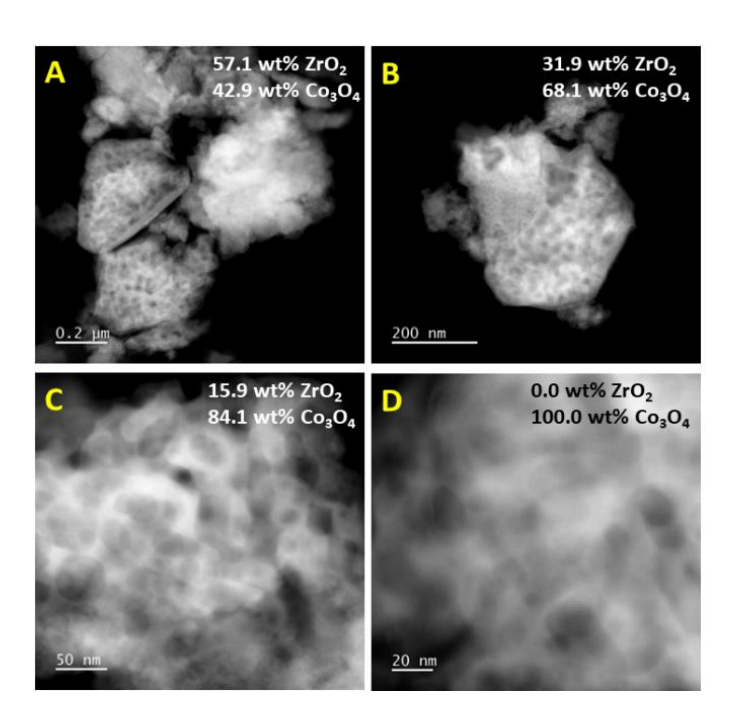


**Figure 6.9.** (**A-B**) STEM images of impregnated Co<sub>3</sub>O<sub>4</sub>/ZrO<sub>2</sub> catalyst at different magnifications as indicated by the scale bars of (**A-B**) 200 nm,

(C) 50 nm, and (D) 20 nm with elemental analysis of each field of view listed on the image.

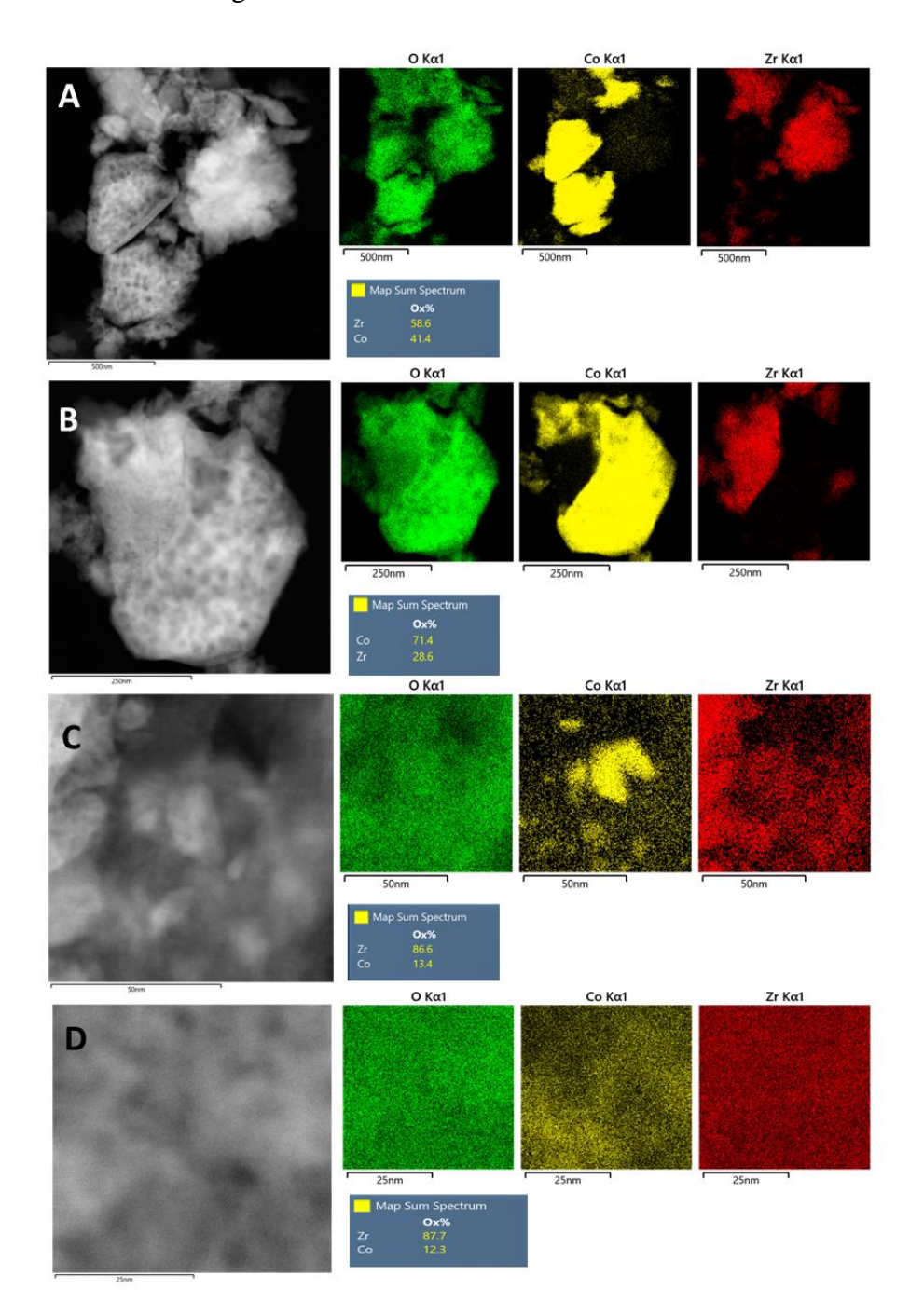


**Figure 6.10.** STEM mapping of Zirconium, Cobalt, and Oxygen element of  $Co_3O_4$  impregnated  $ZrO_2$  catalyst at different regions at higher magnifications with scale bar (**A**) 500 nm, (**B**) 250 nm, (**C**) 50 nm and (**D**) 25 nm.

The local Co coordination and oxidation state were analyzed via Co K-edge X-ray absorption near-edge structure (XANES) and

extended X-ray absorption fine structure (EXAFS) spectroscopy, as shown in **Figure 6.11**. The XANES energy corresponds to the dipole allowed electromagnetic transition for ionization of a 1s electron to the 4p vacant orbitals and is taken as the first inflection point of the leading edge. For 3d compounds, the 1s to 3d dipole forbidden transition gives a pre-edge peak. The energy of the pre-edge peak can be used to determine the oxidation state. <sup>64</sup> The XANES spectra of Co foil (metallic Co) show no obvious pre-edge peak and the leading edge represents the XANES energy at 7709 eV as shown in **Figure 6.11A**. The Co<sub>3</sub>O<sub>4</sub>/ZrO<sub>2</sub> reference XANES spectra shows the peak for both Co<sup>+2</sup> and Co<sup>+3</sup> ions. Co<sup>+2</sup> is resolved in the spectrum, while Co<sup>+3</sup> pre-edge peak overlaps with the Co<sup>+2</sup> pre-edge peak and the leading edge of the XANES spectrum as indicated in **Figure 6.11A**. For Co/ZrO<sub>2</sub>, the pre-edge peak has the same energy as Co<sup>+2</sup> with no evidence of a Co<sup>+3</sup> pre-edge peak. Also, the XANES spectrum of Co/ZrO<sub>2</sub> is shifted to lower energy i.e. 7724 eV consistent with Co<sup>+2</sup> ions present on isolated Co<sup>+2</sup> on ZrO<sub>2</sub>.<sup>65,66</sup> Further. Co K-edge EXAFS spectra for Co doped ZrO<sub>2</sub> and Co<sub>3</sub>O<sub>4</sub> impregnated ZrO<sub>2</sub> catalyst were derived as shown in Figure 6.11B and Figure 6.12 and the Fourier transform first shell fitting results of Co doped ZrO<sub>2</sub> catalyst along with Co<sub>3</sub>O<sub>4</sub>/ZrO<sub>2</sub> and Co foil are described in **Table 6.1**.

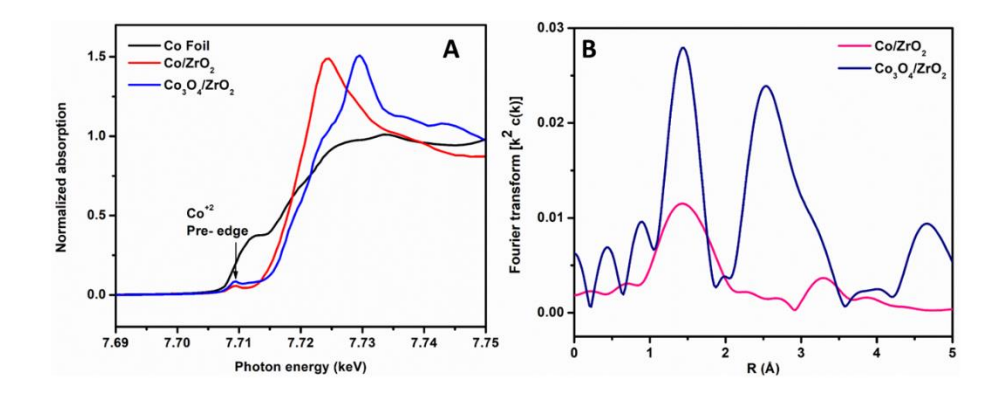


**Figure 6.11.** (**A**) Co K-edge XANES spectrum of Co/ZrO<sub>2</sub> single atom catalyst (red),  $Co_3O_4/ZrO_2$  impregnated catalyst (blue) along with Co foil (black) as references and (**B**) Fourier transform of Co K-edge EXAFS spectra of Co/ZrO<sub>2</sub> single atom catalyst where  $k^2$ :  $\Delta k = 2.55$  to  $10.0 \text{ Å}^{-1}$  and  $Co_3O_4/ZrO_2$  catalyst where  $k^2$ :  $\Delta k = 2.7$  to  $10.2 \text{ Å}^{-1}$  in R-space.

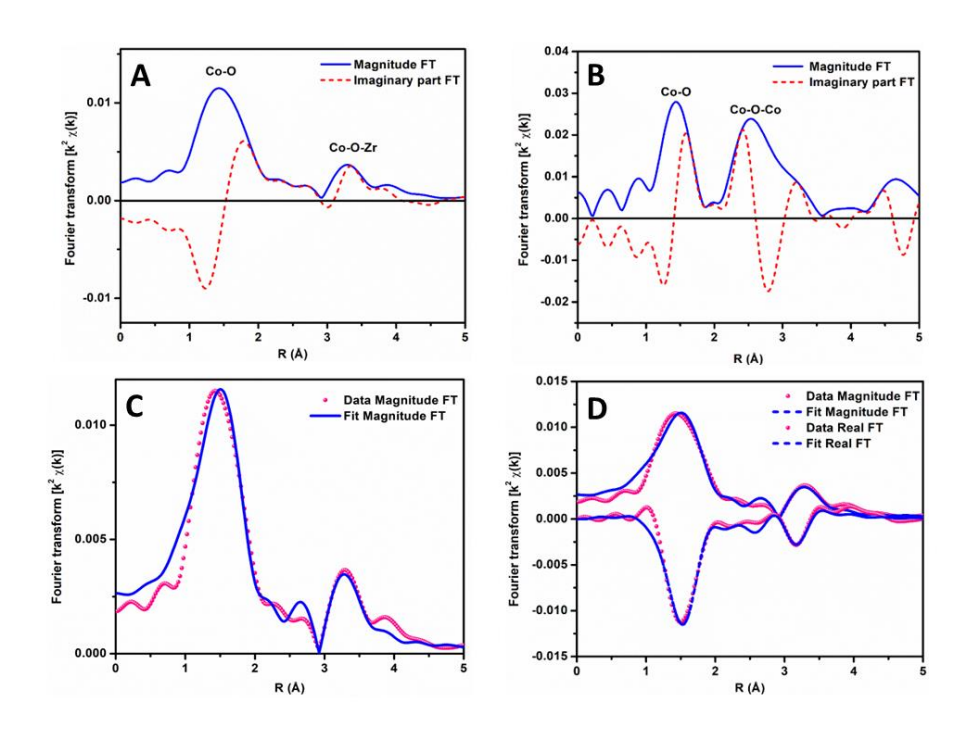


**Figure 6.12**. Fourier transform of Co K-edge EXAFS spectra of (**A**) Co/ZrO<sub>2</sub> single atom catalyst where  $k^2$ :  $\Delta k = 2.55$  to 10.0 Å<sup>-1</sup>, (**B**) Co<sub>3</sub>O<sub>4</sub>/ZrO<sub>2</sub> catalyst where  $k^2$ :  $\Delta k = 2.7$  to 10.2 Å<sup>-1</sup>, and (**C-D**) Fourier transform of Co K-edge EXAFS spectra with corresponding fitting in R-space.

EXAFS first-shell fitting results indicate 4 Co-O bonds at 2.03 Å of Co/ZrO<sub>2</sub>. For comparison, there are 6 Co-O bonds at 2.13 Å in the CoO reference, while half of the Cobalt in Co<sub>3</sub>O<sub>4</sub> has 4 Co-O at 1.94 Å and 6 Co-O at 1.92 Å with higher shell Co-O-Co peaks at 2.86 and 3.31 Å. Thus, the Co-O bond distance in Co/ZrO<sub>2</sub> is shorter and number of bonds is smaller than those in the CoO reference. In Co/ZrO<sub>2</sub>, there is also a very small second-shell Co-O-Zr peak at 3.42 Å indicating isolated Co<sup>+2</sup> ions. Co<sub>3</sub>O<sub>4</sub>/ZrO<sub>2</sub> has 50% Co with 4 bonds and 50% Co with 6 bonds for an average Co-O coordination of 5 at 1.91 Å. In addition, there are two Co-O-Co higher shell bond distances at 2.87 Å and 3.38 Å consistent with Co<sub>3</sub>O<sub>4</sub> oxide nanoparticles. The EXAFS fits are given in **Table 6.1**. These results confirmed that Co/ZrO<sub>2</sub> catalysts have no structure reminiscent of CoO and Co<sub>3</sub>O<sub>4</sub> confirming the presence of isolated Co<sup>+2</sup> in the Co doped ZrO<sub>2</sub> single atom catalyst.

**Table 6.1.** Co K-edge first shell EXAFS fitting results for Co/ZrO<sub>2</sub>, Co<sub>3</sub>O<sub>4</sub>/ZrO<sub>2</sub> and reference Co foil where ( $k^2$ :  $\Delta k = 2.5 - 9.7 \text{ Å}^{-1}$  and  $\Delta R = 0.9 - 2.1 \text{ Å}$ ) and  $^*S_o = 0.80$ .

Sample	XANES	Edge	Scatter	CN	R	ΔΕο	$\sigma^2$
	Pre-	Energy			(Å)	(eV)	
	Edge	(eV)					
	Energy						
	(eV)						
Co foil*	-	7709.0	Co-Co	12.0	2.49	5.7	0.0065
			Со-О	4.8	1.91	5.0	0.005
C03O4/ZrO2	7709.3	7717.6	Co-O-	4.0	2.87	3.5	0.004
203242132	7705.5	7717.0	Co				
			Со-О-	4.0	3.38	3.5	0.004
			Co				
Co/7::0	7700.2	77164	Со-О	3.9	2.04	-1.3	0.012
Co/ZrO <sub>2</sub>	7709.3	7716.4	Co-O-	3.7	3.42	1.2	0.016
			Zr				

Additionally, the X-ray photoelectron spectra (XPS) of the  $Co/ZrO_2$  catalyst were obtained. The XPS spectra of Co 2p, Zr 3d and O 1s is shown in **Figure 6.13**. The Co 2p spectra displays two peaks at 781.4 eV and 796.6 eV for Co 2p<sub>3/2</sub> and Co 2p<sub>1/2</sub> respectively indicating the presence of  $Co^{+2}$  shown in **Figure 6.13A**.<sup>67–69</sup> The Zr 3d spectra exhibited two peaks at 182.4 eV and 184.7 eV for Zr 3d<sub>5/2</sub> and Zr 3d<sub>3/2</sub> for tetragonal Zr<sup>+4</sup> as shown in **Figure 6.13B**.<sup>25</sup>

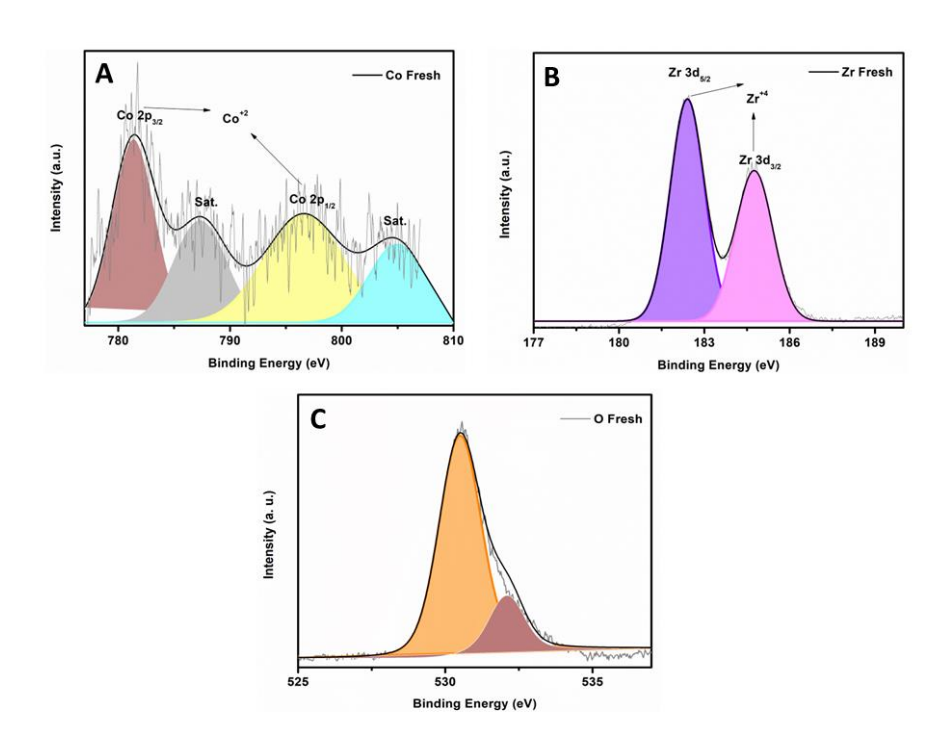


**Figure 6.13.** XPS analysis of fresh single atom Co/ZrO<sub>2</sub> catalyst (**A**) Co 2p spectrum and (**B**) Zr 2p spectrum and (**C**) O 1s spectrum.

All characterization results are therefore consistent with the Co doped  $ZrO_2$  being a single atom catalyst with uniform isolated  $Co^{+2}$  ions with no of  $Co_3O_4$  or CoO clusters. The impregnated catalyst has a mixed structure with non-uniform dispersion of  $Co_3O_4$  on  $ZrO_2$ .

### 6.3.2. Catalytic CO<sub>2</sub> fixation

The undoped ZrO<sub>2</sub> along with Co/ZrO<sub>2</sub> and Co<sub>3</sub>O<sub>4</sub>/ZrO<sub>2</sub> catalysts were tested for catalytic CO<sub>2</sub> fixation of epoxides to yield cyclic carbonates using tetrabutylammonium bromide (TBAB) as a co-catalyst under solvent-free conditions. The reaction conditions were optimized by varying temperature, substrate, TBAB and catalyst amounts and type of TBA halide ion. The effect on conversion is shown in **Figure 6.14**. For the CO<sub>2</sub> fixation reaction, epichlorohydrin was utilized as model substrate. Initially, the reaction was performed using 10 mmol of epichlorohydrin with 0.25 mmol of TBAB with using 15 mg of Co/ZrO<sub>2</sub> catalyst at 80 °C temperature for different reaction times from 1-6 hours as shown in **Figure 6.14A**. With decreasing the reaction time, the conversion decreases from 100 to 55%, respectively. Additional

reactions performed different were using reagents i.e. tetrabutylammonium iodide (TBAI), tetrabutylammonium fluoride (TBAF), tetrabutylammonium bromide (TBAB) and 4-Dimethylaminopyridine (DMAP) for 4 hours as shown in Figure 6.14B. In absence of TBAB, there was no conversion observed indicating that TBAB is essential for the reaction and can be considered as co-catalyst for the reaction. TBAB gave the highest epichlorohydrin conversion, e.g., 100% into its cyclic carbonate. Hence, further optimizations were conducted using TBAB. The amount of TBAB was optimized by varying the concentration from 0.25 mmol to 0.04 mmol. At 0.04 mmol, conversion was 94% while at 0.06 mmol, the conversion 100%, see Figure 6.14C. Therefore, 0.06 mmol is the optimum amount for the conversion for 10 mmol of epichlorohydrin into its cyclic carbonate. Addition of DMAP gave 65% epichlorohydrin conversion, which may be due to stronger affinity of nitrogen than that of oxygen with epoxide substrate resulting in lower conversion. It appears that DMAP coordinates with catalyst's acidic sites inhibiting the adsorption of epoxide substrate. 44,70 The amount of catalyst and substrate were optimized for different reaction times as shown in Figure 6.14(D-F). As the catalyst amount decreases from 15 mg to 5 mg, the conversion decreases from 100% to 89%. While increasing the substrate amount from 10 mmol to 20 mmol, there is also a decrease in conversion. At room temperature, there is only 30% conversion indicating that higher reaction temperatures are required to affect epoxide, ring-opening and CO<sub>2</sub> fixation. The optimized reaction conditions were 10 mmol of epichlorohydrin, 12 mg of Co/ZrO<sub>2</sub> catalyst, 0.06 mmol of TBAB with 2 bar CO<sub>2</sub> at 80 °C with solvent-free reaction condition wherein 100% conversion was observed with 100% selectivity.

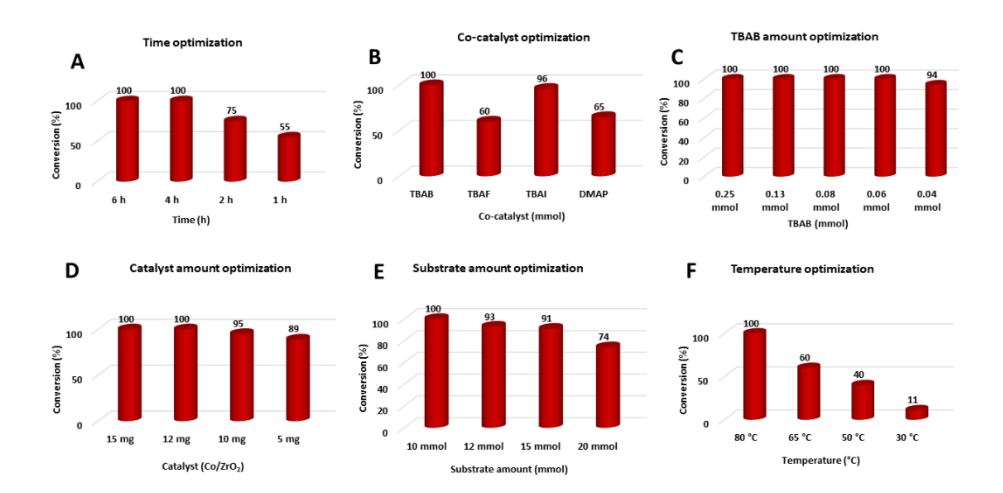


**Figure 6.14**. Catalytic optimization of  $CO_2$  fixation reaction at various reaction conditions. **Reaction conditions**: (**A**) substrate = 10 mmol, catalyst ( $Co/ZrO_2$ ) = 15 mg, TBAB = 0.25 mmol, temperature = 80 °C, time = 1-6 h,  $CO_2$  = 2 bar. (**B**) substrate = 10 mmol, catalyst ( $Co/ZrO_2$ ) = 15 mg, TBAB = 0.25 mmol, temp. = 80 °C, time = 4 h,  $CO_2$  = 2 bar. (**C**) substrate = 10 mmol, catalyst ( $Co/ZrO_2$ ) = 15 mg, TBAB = 0.25-0.04 mmol, temperature = 80 °C, time = 4 h,  $CO_2$  = 2 bar. (**D**) substrate = 10 mmol, catalyst ( $Co/ZrO_2$ ) = 5-15 mg, TBAB = 0.06 mmol, temperature = 80 °C, time = 4 h,  $CO_2$  = 2 bar. (**E**) substrate = 10-20 mmol, catalyst ( $Co/ZrO_2$ ) = 12 mg, TBAB = 0.06 mmol, temperature = 80 °C, time = 4 h,  $CO_2$  = 2 bar. (**F**) substrate = 10 mmol, catalyst ( $Co/ZrO_2$ ) = 12 mg, TBAB = 0.06 mmol, temperature = 30-80 °C, time = 4 h,  $CO_2$  = 2 bar.

The effect of catalyst composition, e.g., undoped ZrO<sub>2</sub> and Co<sub>3</sub>O<sub>4</sub> impregnated ZrO<sub>2</sub>, was also evaluated and is shown in **Figure 6.15.** For undoped ZrO<sub>2</sub>, the conversion was 38%; while for Co<sub>3</sub>O<sub>4</sub>/ZrO<sub>2</sub>, the conversion was 47%. The slightly higher conversion may be due to small fraction of single Co<sup>+2</sup> ions. However, Co doped ZrO<sub>2</sub> single atom catalyst showed superior catalytic activity over both undoped ZrO<sub>2</sub> and Co<sub>3</sub>O<sub>4</sub>/ZrO<sub>2</sub> catalysts. These results revealed that Co doped ZrO<sub>2</sub> single atom catalyst is most suitable catalyst for cycloaddition of CO<sub>2</sub> to cyclic epoxides to yield cyclic carbonate with minimal amount of TBAB under solvent-free conditions.

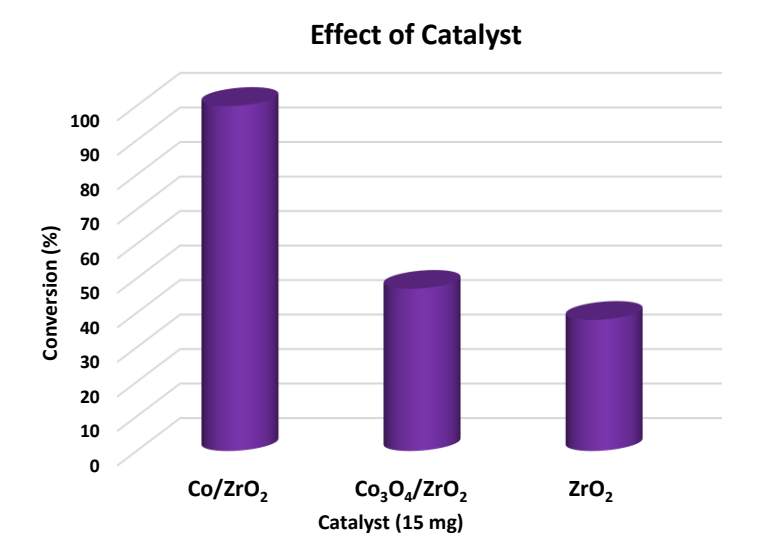


**Figure 6.15.** Effect of different catalysts on  $CO_2$  fixation of epichlorohydrin. **Reaction conditions:** Substrate = 10 mmol, catalyst  $(Co/ZrO_2) = 12$  mg,  $CO_2 = 2$  bar, TBAB = 0.06 mmol (20 mg), temperature = 80 °C, time = 4 h.

To check the scope of the reaction, various substituted epoxides were utilized for the  $CO_2$  fixation reaction as shown in **Table 6.2**. All substrates were converted into their corresponding cyclic carbonates at 100% conversion and 100% selectivity under mild reaction conditions with minimal amount of TBAB. Both -chloro and -bromo substituted epoxides gave 100% conversion and selectivity towards cyclic carbonates in 4 hours (Table 6.2, Entry 1-2). Similarly, aliphatic substituted epoxides gave 100% conversion into their corresponding carbonates in 4-6 hours (Table 6.2, Entry 3-7). However, as the aliphatic chain size increases from epoxypropane (propylene oxide) to epoxy hexane, the reaction time increases, perhaps, due to steric hindrance near the epoxide ring.<sup>71</sup> Hydroxide substituted epoxide took longer reaction times than that of aliphatic and halide substituted epoxides (**Table 6.2, Entry 8**). 40,71 Finally, styrene oxide, allyl glycidyl ether, tert-Butyl glycidyl ether and phenyl glycidyl ether and other aromatic epoxides i.e. 3,6-Dioxabicyclo[3.1.0]hexane were also converted 100% into corresponding carbonates (**Table 6.2, Entry 9-14**). As the bulky substitute increases, the reaction time increases with decreasing catalytic activity. The effect of the bulky group was observed, in all the substrates, but complete conversions were obtained with 100% selectivity. All the conversion and selectivity were determined using <sup>1</sup>H and <sup>13</sup>C NMR (**Section 6.5**). The general catalytic reaction of conversion of epoxides into cyclic carbonates shown as **Scheme 6.2**.

$$\begin{array}{c} O \\ R \\ R = -\text{CI, -Br, -H, -Me,} \\ -\text{CH}_2\text{CH}_3, -\text{CH}_2\text{CH}_2\text{CH}_3,} \\ -\text{OH, -CH}_2\text{CH}_2 = \text{CH}_2, -\text{Ph} \\ \end{array}$$

 $R = t-Bu, -Ph, -CH_2CH_2=CH_2$ 

**Scheme 6.2.** General catalytic reaction of cycloaddition of CO<sub>2</sub> to epoxides.

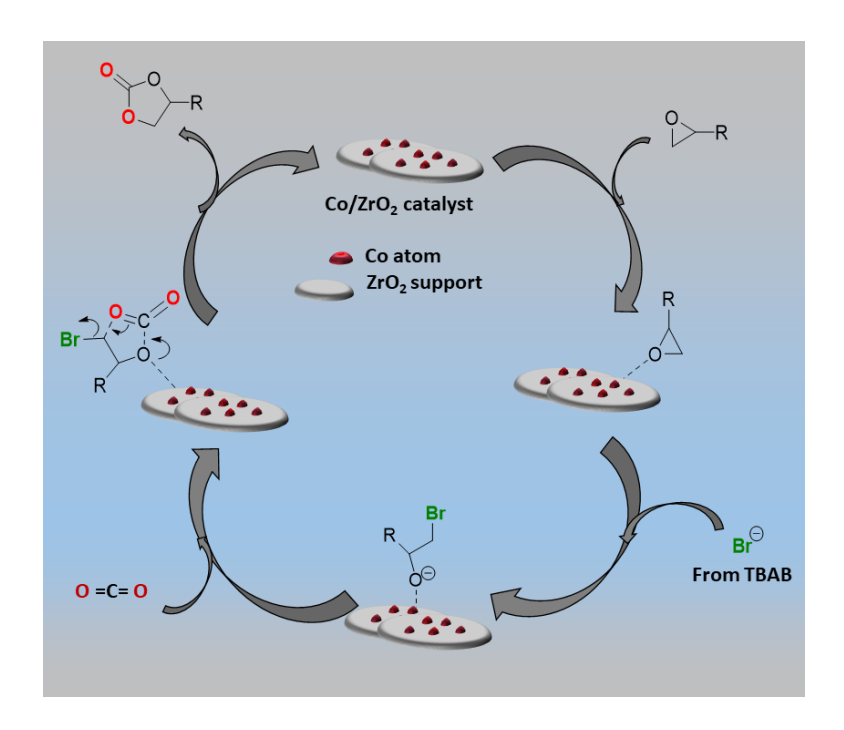
Table 6.2. Substrate scope on CO<sub>2</sub> fixation of epichlorohydrin

Entry	Substrate	Product	Time	Conv
			( <b>h</b> )	(%)
1	O CI	O CI	4	100
2	O Br	O O O Br	4	100
3		0	4	100
4	0		4	100
5	0		5	100

6			6	100
7			7	100
8	OH	O O OH	9	100
9	Ph	O Ph	5	100
10			8	100
11		0,0,0	10	100
12	Ph	Ph	10	100
13	0	0>0	13	100
14	000	0 0 0	15	100

**Reaction conditions:** Substrate = 10 mmol, Catalyst (Co/ZrO<sub>2</sub>) = 12 mg,  $CO_2$  = 2 bar, TBAB = 0.06 mmol (20 mg), temperature = 80 °C, time = 4-15 h,  $CO_2$  = 2 bar. All the conversion and selectivity were analysed from  $^1H$  and  $^{13}C$  NMR.

Based on previous literature studies, the reaction mechanism of  $CO_2$  fixation is shown in **Scheme 6.3**.  $^{30,33,42,46,72-74}$  Initially, the epoxide substrate adsorbs on the Lewis acidic site with oxygen atom of the epoxide. Here, in  $Co/ZrO_2$ , the single  $Co^{+2}$  ion is the active site. Subsequently, nucleophilic attack of bromide ion occurs, which leads to ring opening of epoxide substrate. Adsorbed  $CO_2$  reacts with the epoxy intermediate forming the cyclic carbonate product with loss of bromide ion and completing the catalytic cycle.



**Scheme 6.3.** A plausible mechanism of CO<sub>2</sub> fixation of epoxides into cyclic carbonates.

### 6.3.3. Recycle study and leaching test

To study the recyclability of the catalyst for CO<sub>2</sub> fixation of epichlorohydrin, after completion of reaction, the reactor was cooled to room temperature and reaction mixture was centrifuged and filtered. The filtrate was sent for GC-MS analysis and the solid residue was washed several times and dried overnight at room temperature. This solid residue or catalyst was then utilized for the next catalytic cycle. The catalyst was recyclable up to six cycles as shown in **Figure 6.16**. The small loss in conversion with each regeneration is likely due to small losses in the amount of catalyst during the separation and washing of the catalyst.

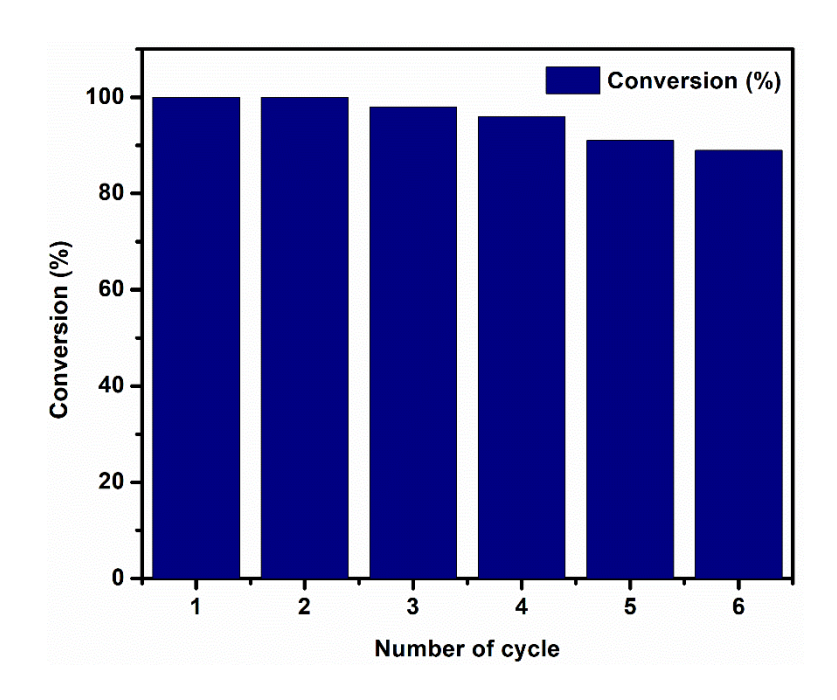


**Figure 6.16.** Catalyst reusability of the  $CO_2$  fixation in epichlorohydrin for all the cyclic runs. **Reaction conditions:** Substrate = 10 mmol, catalyst  $(Co/ZrO_2) = 12$  mg,  $CO_2 = 2$  bar, TBAB = 0.06 mmol (20 mg), temperature = 80°C, time = 4 h,  $CO_2 = 2$  bar.

Leaching tests of the catalyst were also performed using hot filtration in which the reaction was conducted for 1 hour. After that, reaction mixture was filtered, and the filtrate was allowed to proceed further in presence of CO<sub>2</sub> without catalyst.<sup>51</sup> After completion, the conversion and selectivity were determined and confirmed that there was no significant conversion after removal of catalyst. The amount of Co in the filtrate was determined by Inductively Coupled Plasma Atomic Emission Spectroscopy (ICP-AES) and was less than 1 ppm, **Table 6.3.** These studies confirm that the Co doped ZrO<sub>2</sub> single atom catalyst is recyclable for the cycloaddition reaction of CO<sub>2</sub> to epoxides.

**Table 6.3.** ICP-AES analysis for leaching of Co doped single atom catalyst.

Sample	ICP-AES (ppm)		
Co/ZrO <sub>2</sub>	Со	Zr	
	0.996	0.103	

In **Table 6.4**, we compare our results on CO<sub>2</sub> fixation of epoxides with those previously reported in the literature. Cui et al. reported zinc single atoms on N-doped carbon via simple pyrolysis of active-carbon-supported phenanthroline-ligated Zn(OAc)2 complex procedure for cycloaddition of CO<sub>2</sub> and epoxides.<sup>47</sup> The reaction was performed in solvent-free conditions at comparatively high pressure and temperature i.e. 5 bar and 100°C using TBAB as additive. All the substrates (16 substrates) were converted in good to excellent yield, however only 5 mmol of substrate was utilized for the reaction (**Table 6.4, Entry 1**). Yang et al. synthesized a ZIF-8 metal organic framework and derived hollow porous carbon (HPC) with uniform N-doping and loading of Zn SACs via pyrolysis.<sup>48</sup> The reaction was performed with epibromohydrin as substrate under light irradiation at RT, however, reaction was performed in DMF solvent and required 10 hours to achieve 94% conversion (Table 6.4, Entry 2). Li et al. synthesized  $Au_{19}Ag_4(S-Adm)_{15}$  clusters,  $Au_{20}Ag_1(S-Adm)_{15}$  cluster and  $Au_{21}(S-Adm)_{15}$ Adm)<sub>15</sub> with 1-adamantanethiolate (S-Adm).<sup>49</sup> In Au<sub>19</sub>Ag<sub>4</sub>(S-Adm)<sub>15</sub>, all Ag sites are open on surface, in Au<sub>20</sub>Ag<sub>1</sub>(S-Adm)<sub>15</sub> partially open Ag sites and in Au<sub>21</sub>(S-Adm)<sub>15</sub> no Ag sites are present. Based on present Ag sites, their catalytic activity was in order of Au<sub>19</sub>Ag<sub>4</sub>(S-Adm)<sub>15</sub> >  $Au_{20}Ag_1(S-Adm)_{15} > Au_{21}(S-Adm)_{15}$ . The reaction was performed with 0.3 mmol of substrates (3 substrates) using DCM/DMF solvent mixture and all three substrates showed ~80% conversion in 24 hours with 10 mol% of TBAB. The reaction involved harmful solvent and involved high reaction time despite the lower amount of substrate (Table 6.4, Entry 3-5). Xu et al. explored the strong electronic metal-support interaction in iridium single atom catalyst supported on WO<sub>3</sub> for CO<sub>2</sub> cycloaddition reaction.<sup>50</sup> The reaction was performed in neat condition for 1 mmol of substrate at 40 °C with 10 mg of TBAB. All substrate (6 substrates) were showed moderate to excellent yield (40-100%) in high reaction time i.e. 15 hours (**Table 6.4, Entry 6**).

Previous literature results utilized either low amounts of substrate with high amount of TBAB and high reaction time or utilized

toxic solvents like DCM and DMF. Also, the synthesis process of previous SACs involved multistep procedures whereas our catalyst was synthesized at room temperature with using much simpler methods. Based on this, our results indicate superior catalytic performance with balanced reaction condition for chemical fixation reaction. The Co/ZrO<sub>2</sub> SAC is capable to convert 10 mmol of substrates (14 substrate) with trace amount of TBAB (0.06 mmol) with 100% conversion under solvent-free conditions.

**Table 6.4.** Comparative results of some earlier reported single-atom catalysts

S. No.	Catalyst	Substrate	TBAB	Temp (°C)	Time (h)	Solvent- free	Conv (%)	Ref.
1	Zn- SAC@N C-700	Epichloroh ydrin (5 mmol)	2 mol%	100	2	Yes	97	47
2	HPC-800 (Zn SACs)	Epibromoh ydrin (0.15 mmol)	0.1 mmol	300 mW/c m <sup>2</sup>	10	No	94	48
3	Au <sub>19</sub> Ag <sub>4</sub> ( S- Adm) <sub>15</sub> c luster	Epichloroh ydrin (0.3 mmol)	10 mol%	60	24	No	78	49
4	Au <sub>20</sub> Ag <sub>1</sub> ( S- Adm) <sub>15</sub> c luster	Epichloroh ydrin (0.3 mmol)	10 mol%	60	24	No	30	49
5	Au <sub>21</sub> (S- Adm) <sub>15</sub> c luster	Epichloroh ydrin (0.3 mmol)	10 mol%	60	24	No	50	49
6	Ir/WO <sub>3</sub> SAC	Epichloroh ydrin (1 mmol)	0.03 mmol	40	15	Yes	100	50
7	Co/ZrO <sub>2</sub>	Epichloroh ydrin (10 mmol)	0.06 mmol	80	4	Yes	100	This work

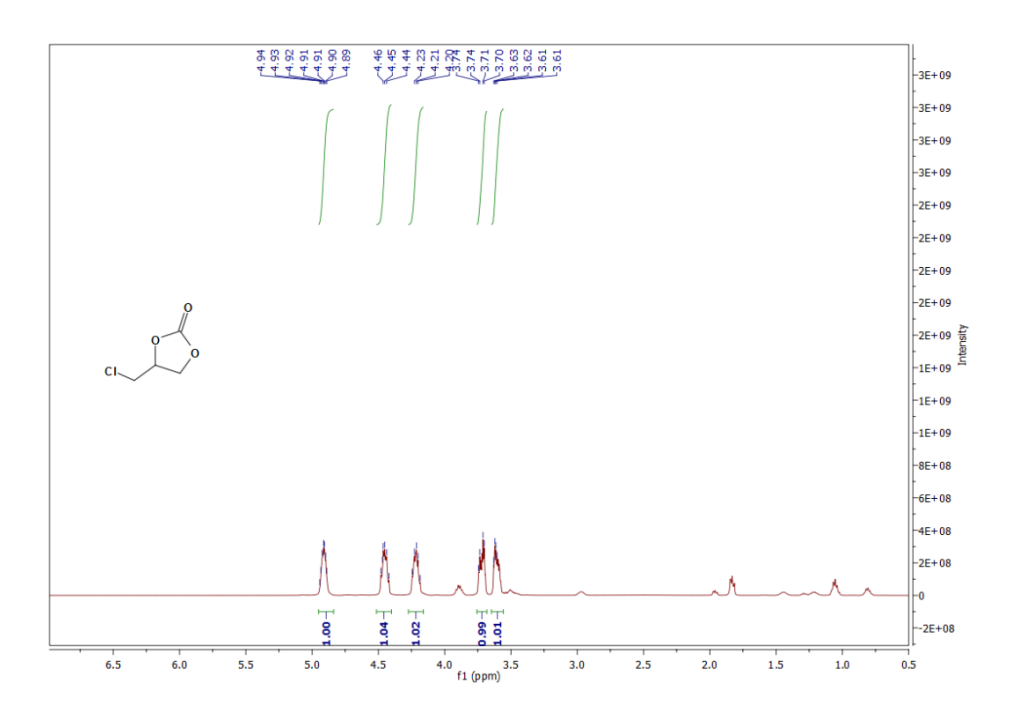
### 6.4. Conclusions

We have successfully synthesized Co doped ZrO<sub>2</sub> single atom catalyst via co-precipitation and characterized via STEM, XANES and EXAFS to confirm the Co is present in the form of single atoms. The EXAFS data revealed the presence of isolated Co<sup>+2</sup> ions with 4 Co-O bonds at 2.04 Å. EDS elemental mapping confirmed the uniform dispersion of Co on ZrO<sub>2</sub> support. The as synthesized single atom catalyst was utilized for CO<sub>2</sub> fixation into epoxides in solvent-free condition to give high rates and selectivity of cyclic carbonates. For comparison, undoped ZrO<sub>2</sub> and Co<sub>3</sub>O<sub>4</sub>/ZrO<sub>2</sub> catalyst were utilized which were much less active for CO<sub>2</sub> fixation. These results suggest that the single atom Co<sup>+2</sup> catalyst is superior to other reported single atom CO<sub>2</sub> fixation catalysts.

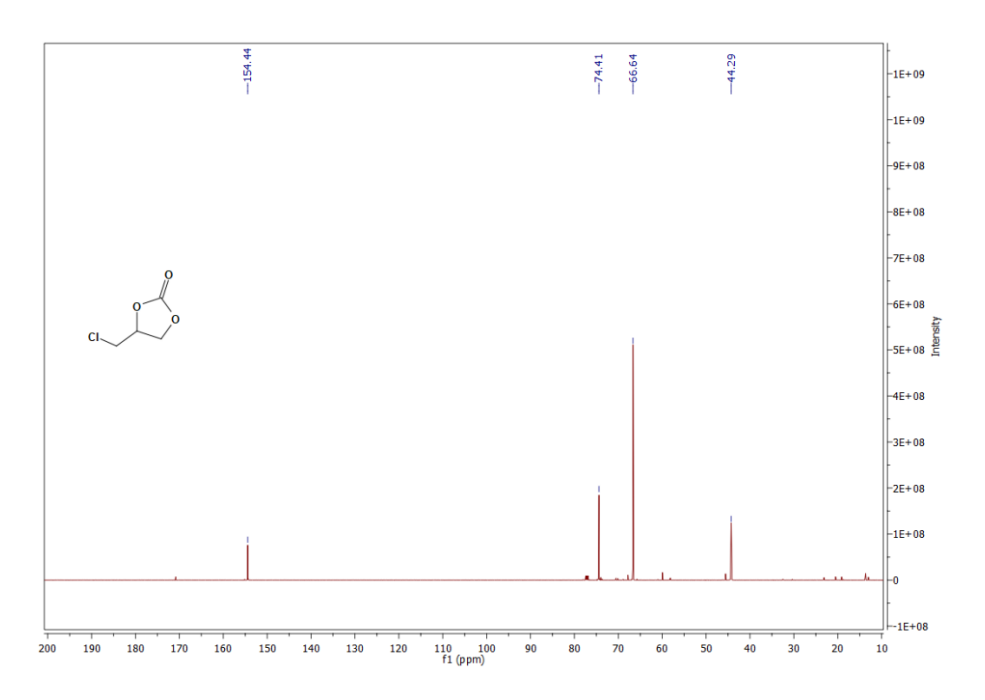
## 6.5. <sup>1</sup>H and <sup>13</sup>C-NMR data of all cyclic carbonate products

After completion of reaction all the products were cooled to room temperature and diluted with ethyl acetate and residue was purified with silica gel chromatography. The resulting product were then given for NMR analysis with CDCl<sub>3</sub> and the data was analysed with the references. <sup>29,33,35,43,75,76</sup>

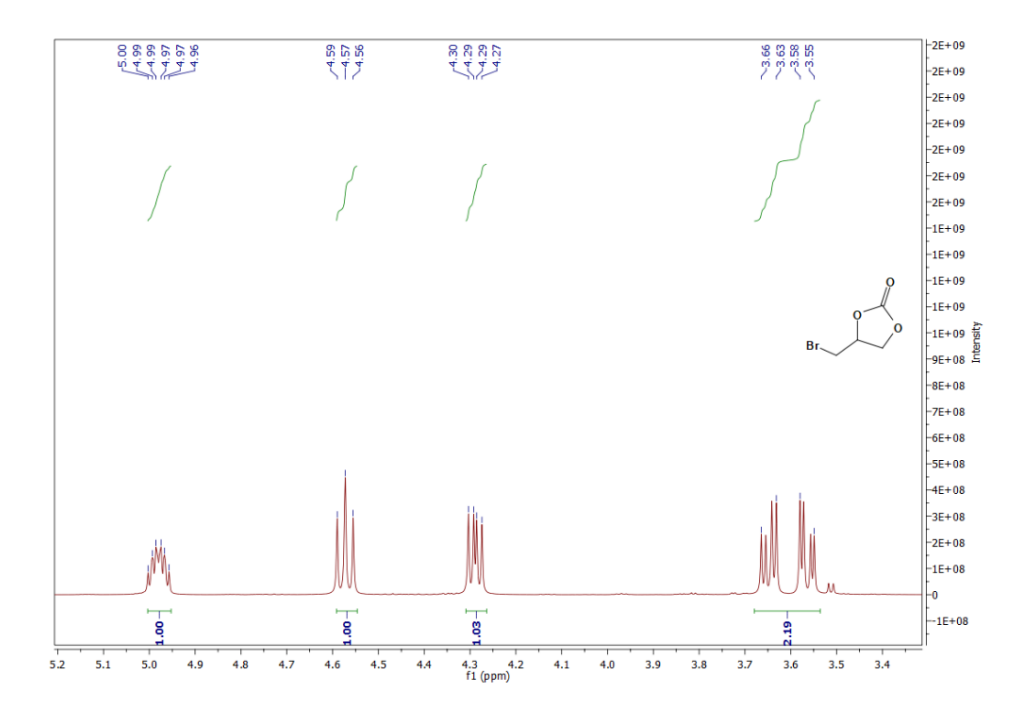
# <sup>1</sup>H NMR of 4-(chloromethyl)-1,3-dioxolan-2-one:



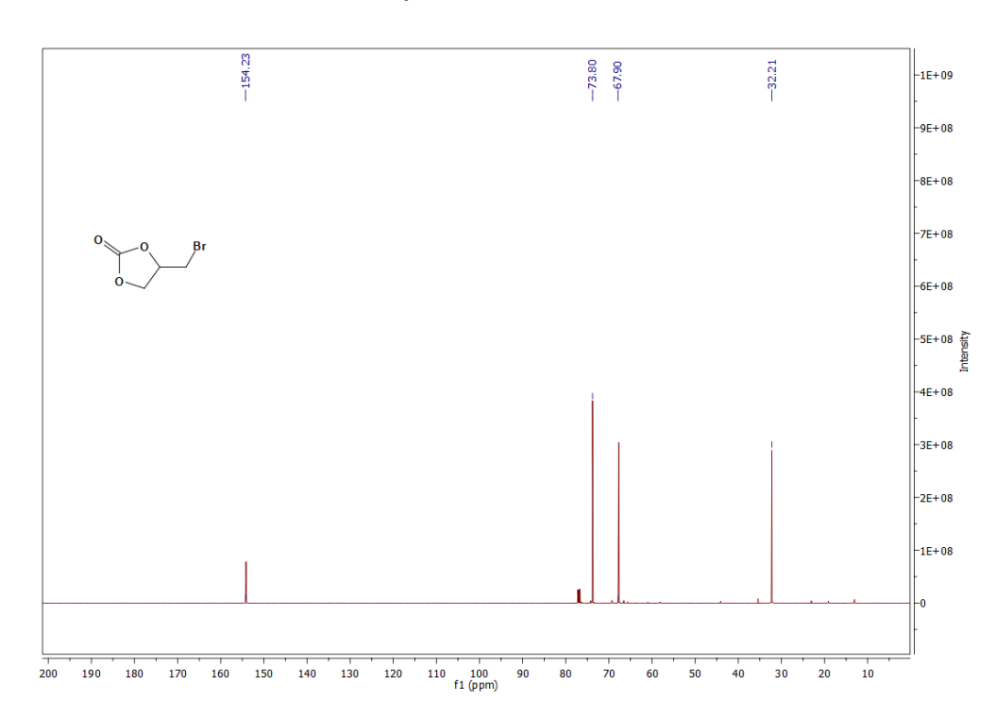
## <sup>13</sup>C NMR of 4-(chloromethyl)-1,3-dioxolan-2-one:



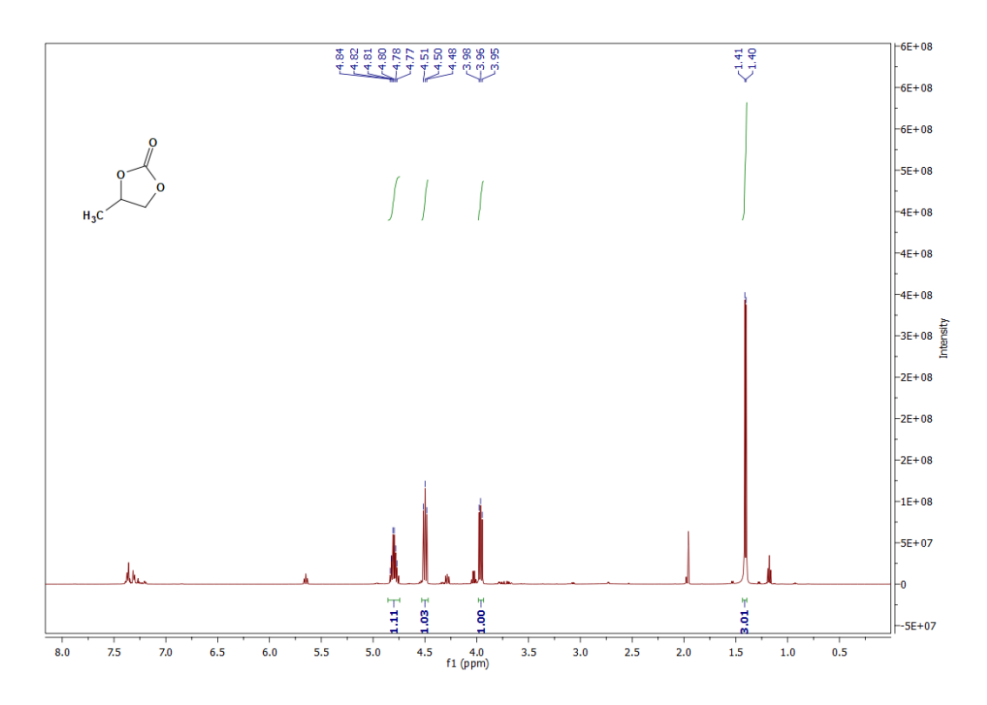
## <sup>1</sup>H NMR of 4-(bromomethyl)-1,3-dioxolan-2-one:



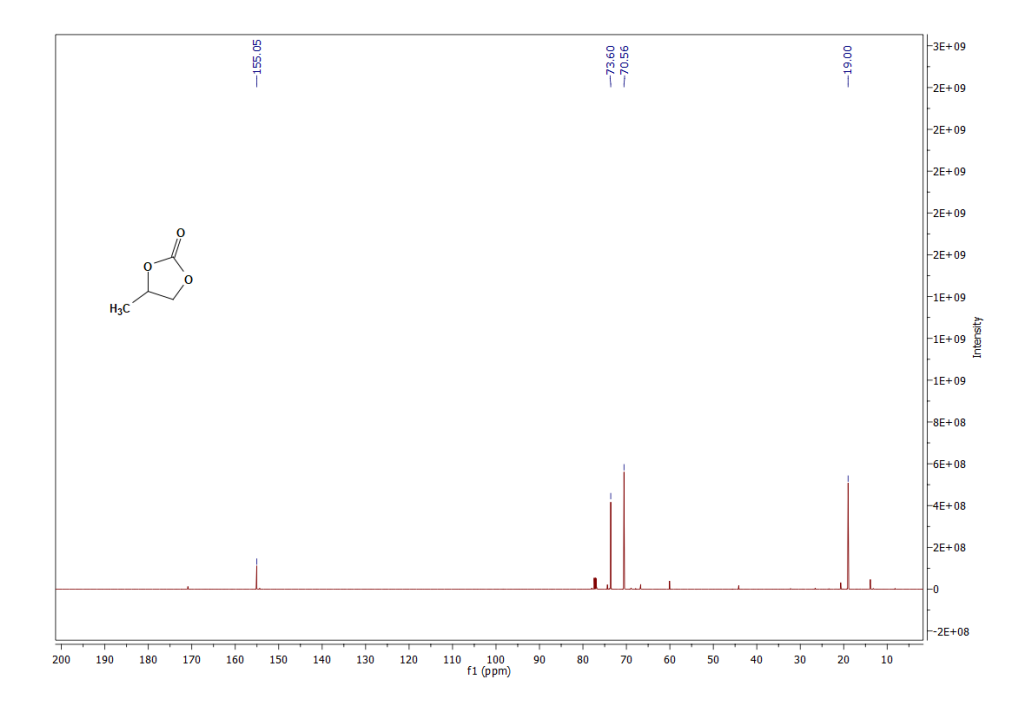
## $^{13}\mathrm{C}\ \mathrm{NMR}\ \mathrm{of}\ 4\text{-(bromomethyl)-1,3-dioxolan-2-one:}$



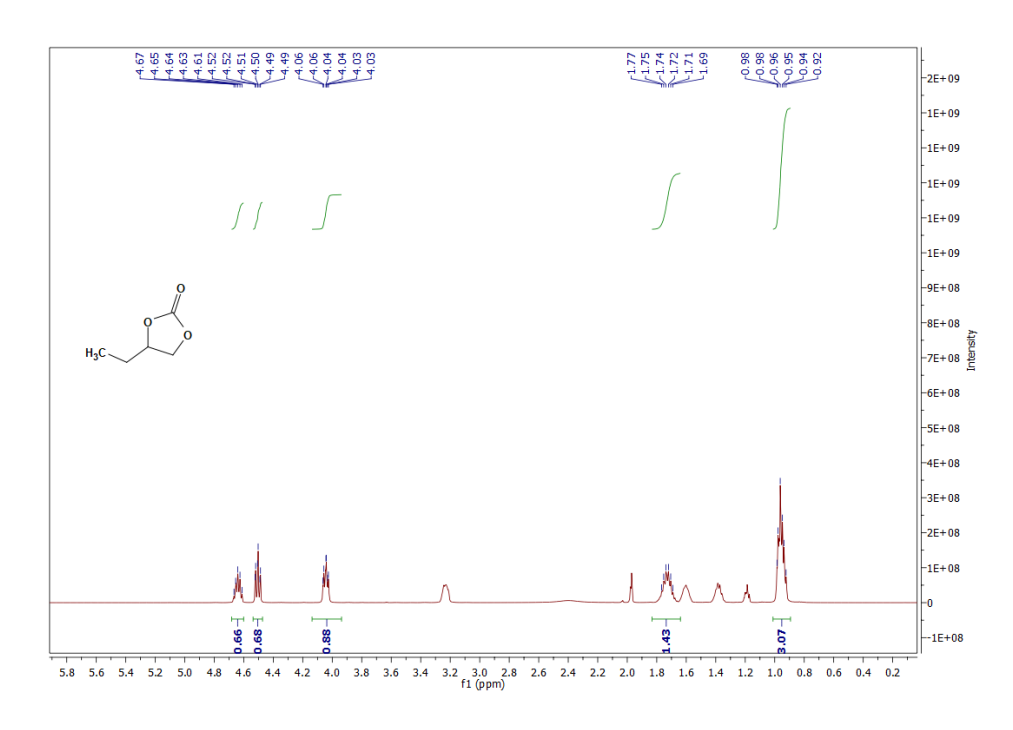
## <sup>1</sup>H NMR of 4-methyl-1,3-dioxolan-2-one:



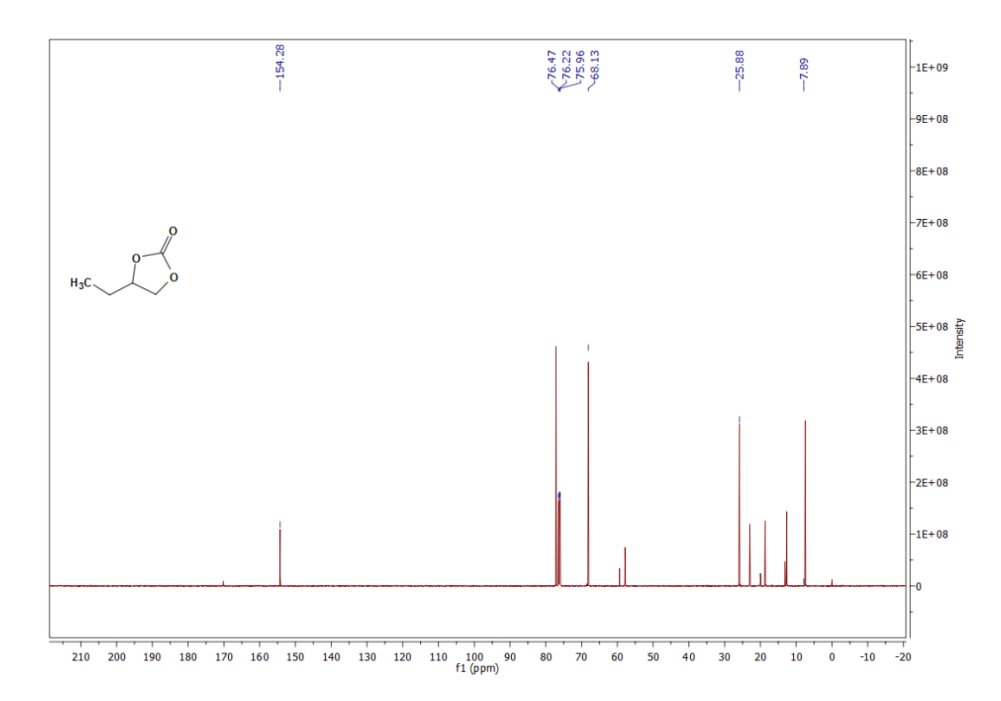
## <sup>13</sup>C NMR of 4-methyl-1,3-dioxolan-2-one:



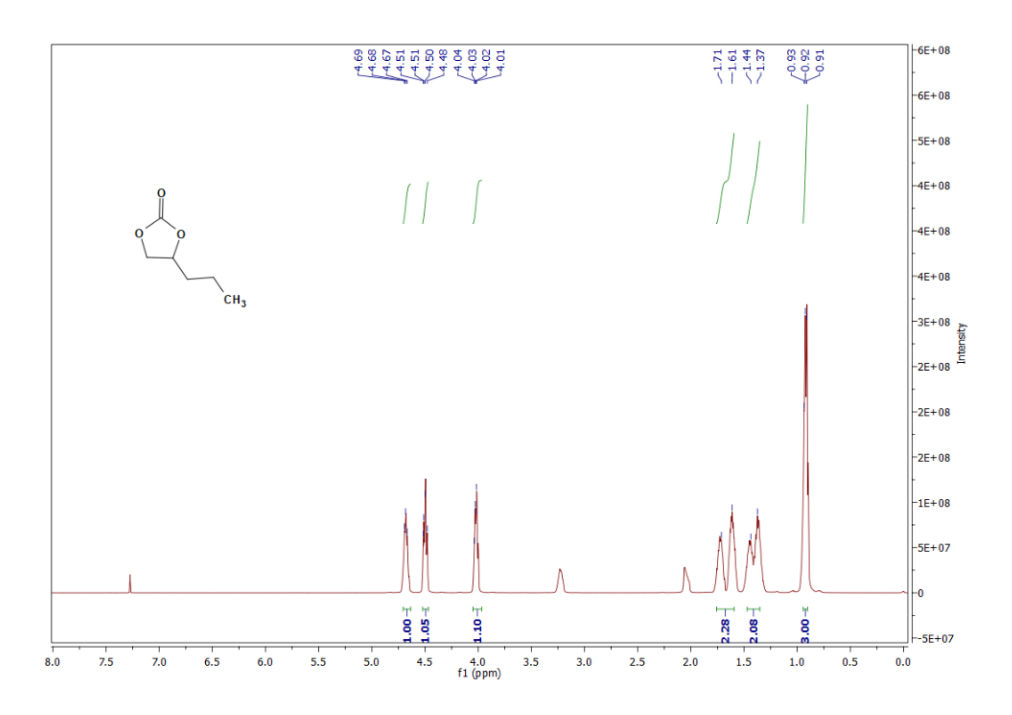
## <sup>1</sup>H NMR of 4-ethyl-1,3-dioxolan-2-one:



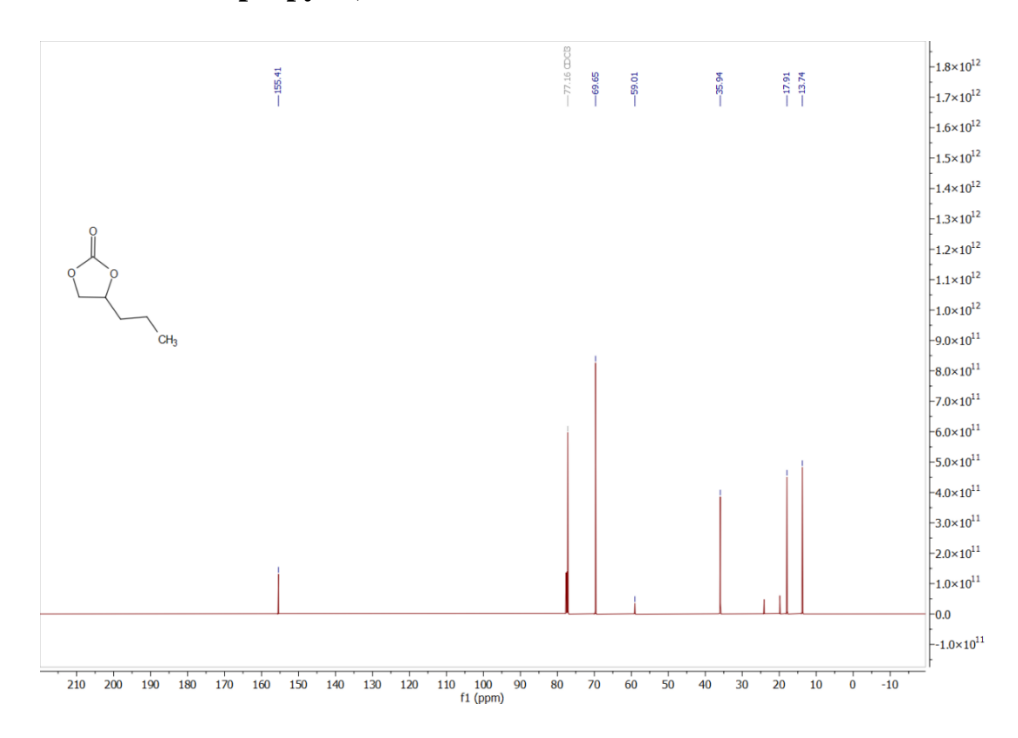
## <sup>13</sup>C NMR of 4-ethyl-1,3-dioxolan-2-one:



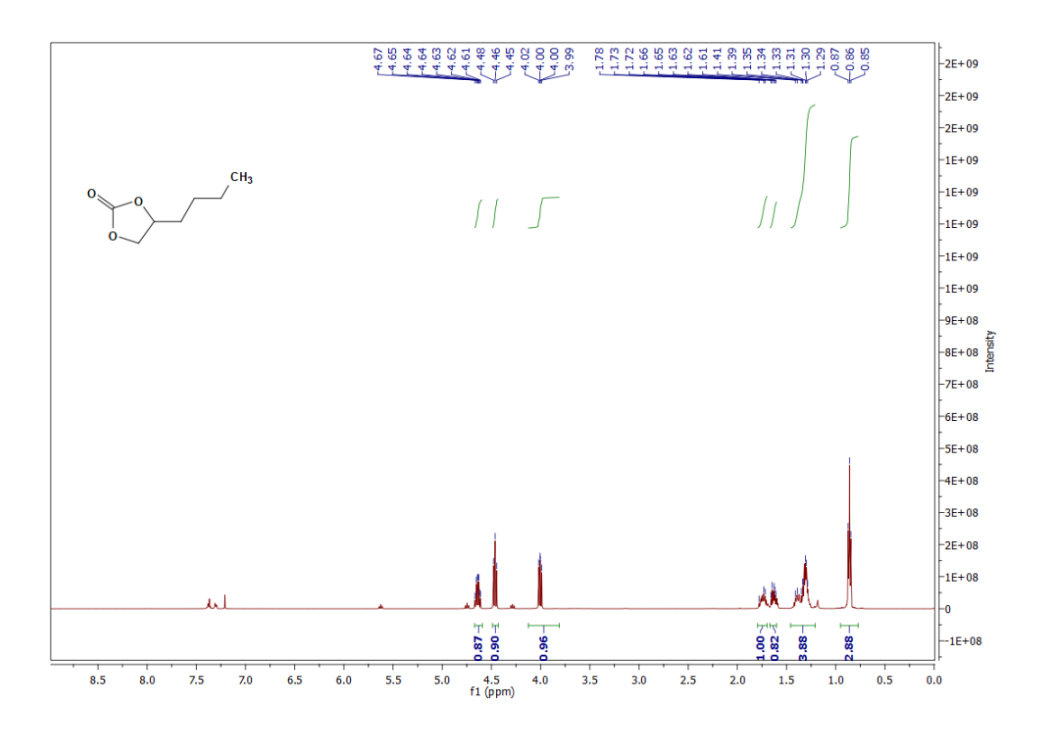
### <sup>1</sup>H NMR of 4-propyl-1,3-dioxolan-2-one:



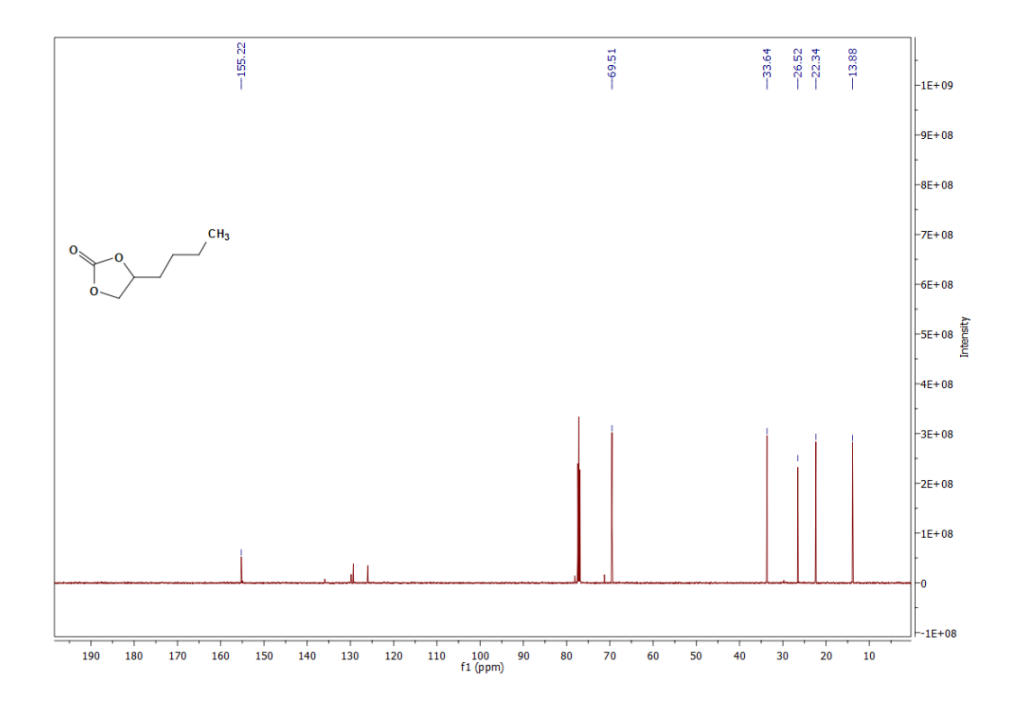
## <sup>13</sup>C NMR of 4-propyl-1,3-dioxolan-2-one:



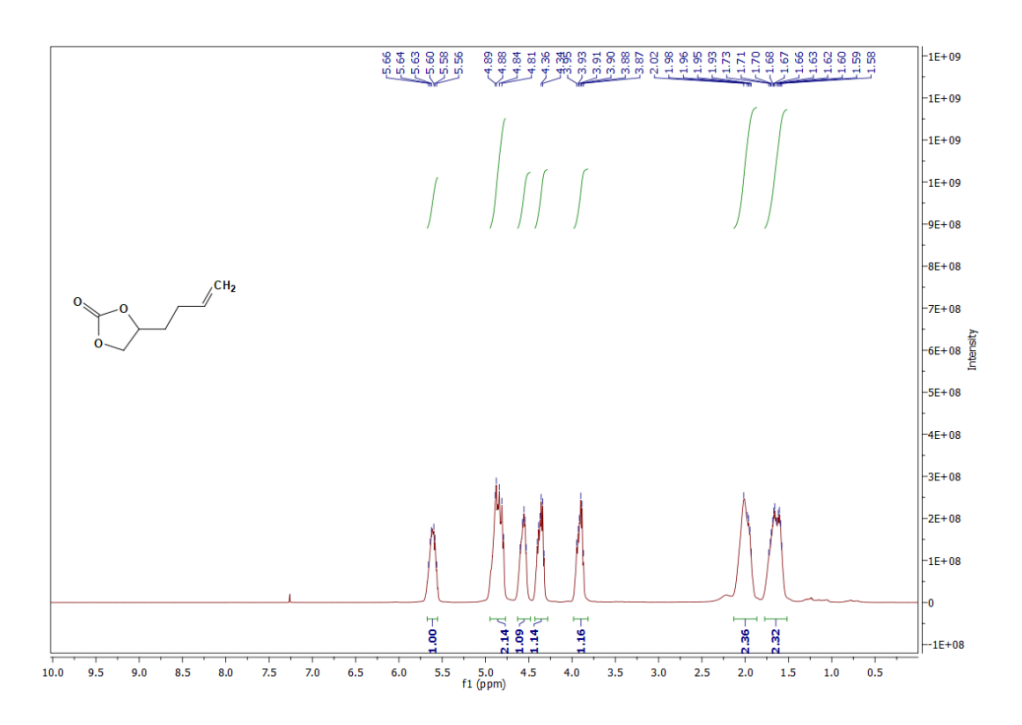
## <sup>1</sup>H NMR of 4-butyl-1,3-dioxolan-2-one:



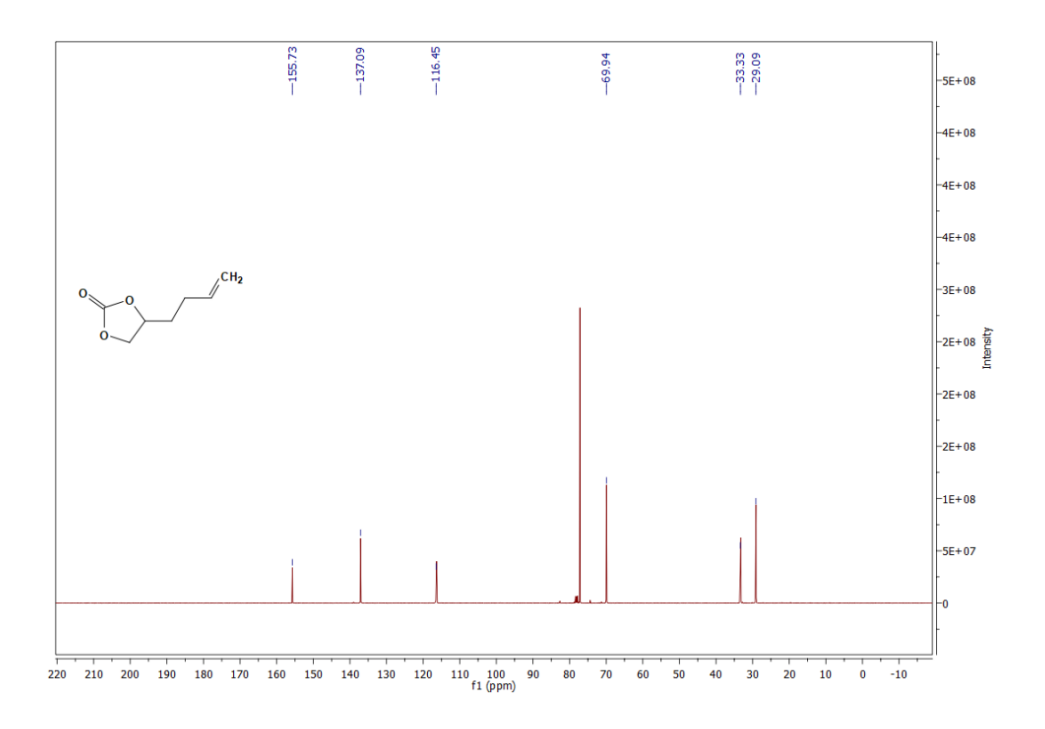
## <sup>13</sup>C NMR of 4-butyl-1,3-dioxolan-2-one:



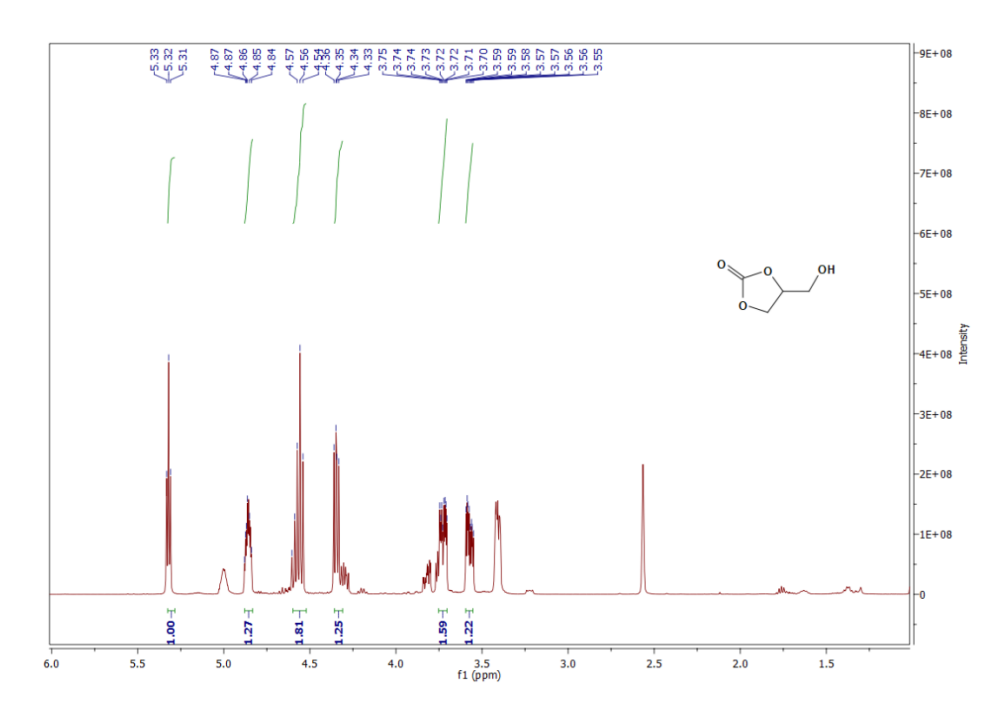
### <sup>1</sup>H NMR of 4-(but-3-en-1-yl)-1,3-dioxolan-2-one:



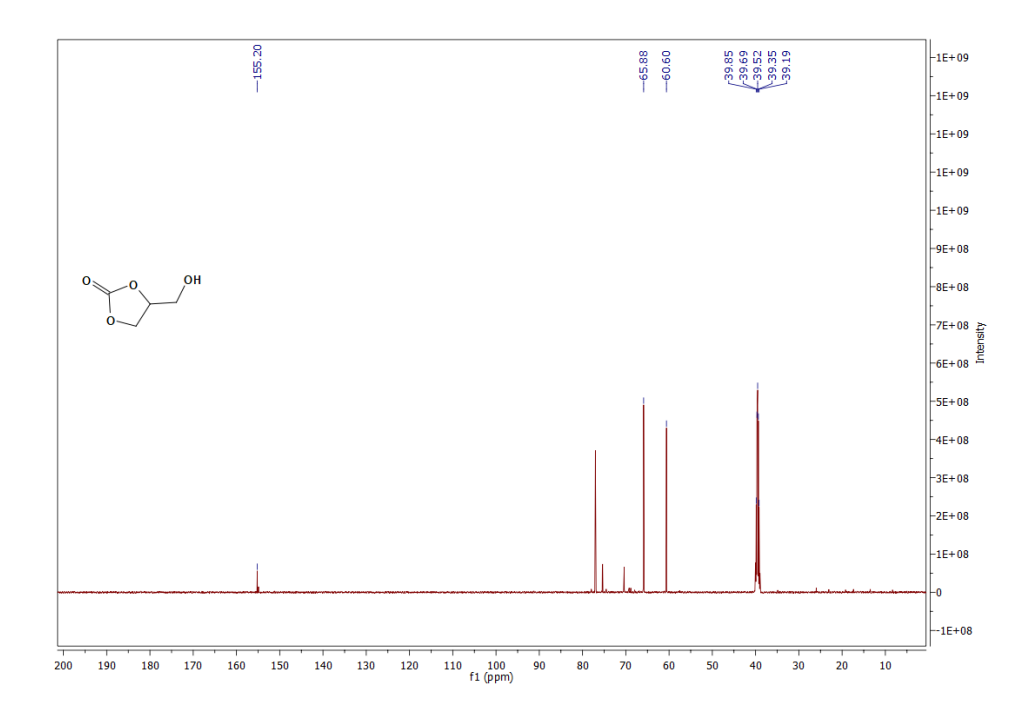
# $^{13}\mathrm{C}$ NMR of 4-(but-3-en-1-yl)-1,3-dioxolan-2-one:



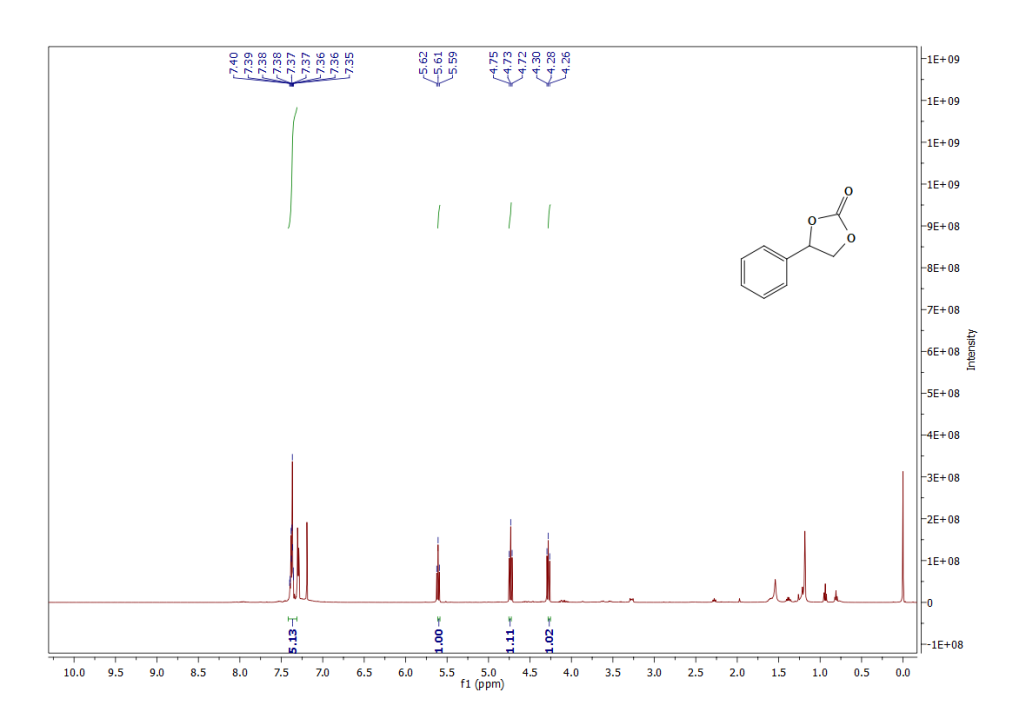
 $^{1}H$  NMR of 4-(hydroxymethyl)-1,3-dioxolan-2-one



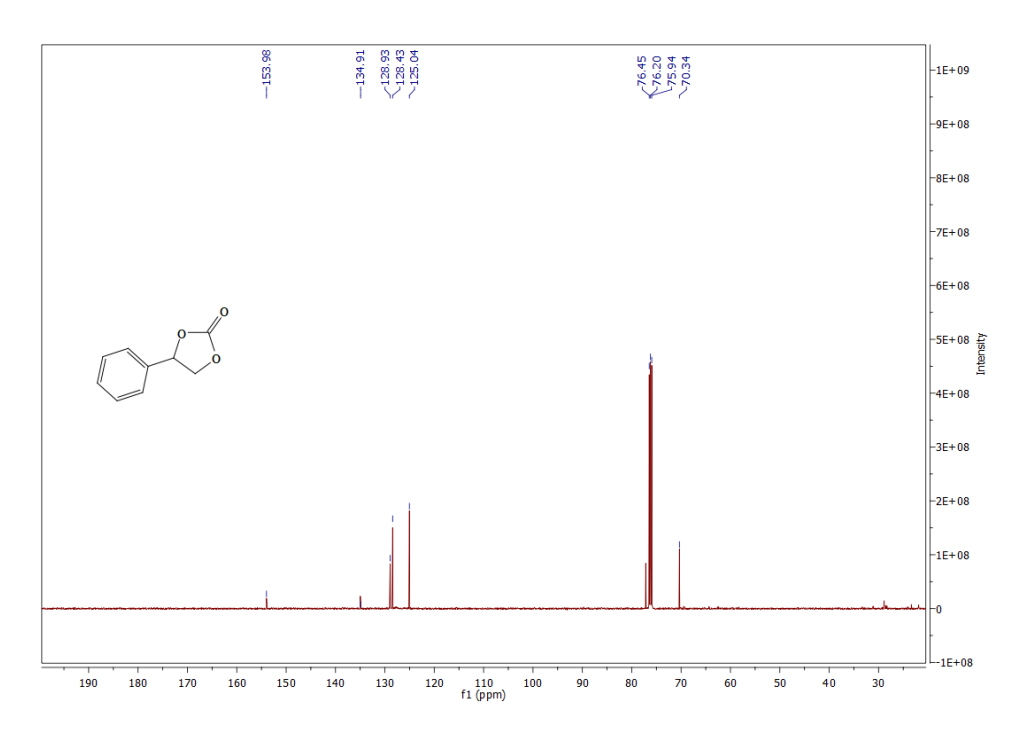
### <sup>13</sup>C NMR of 4-(hydroxymethyl)-1,3-dioxolan-2-one:



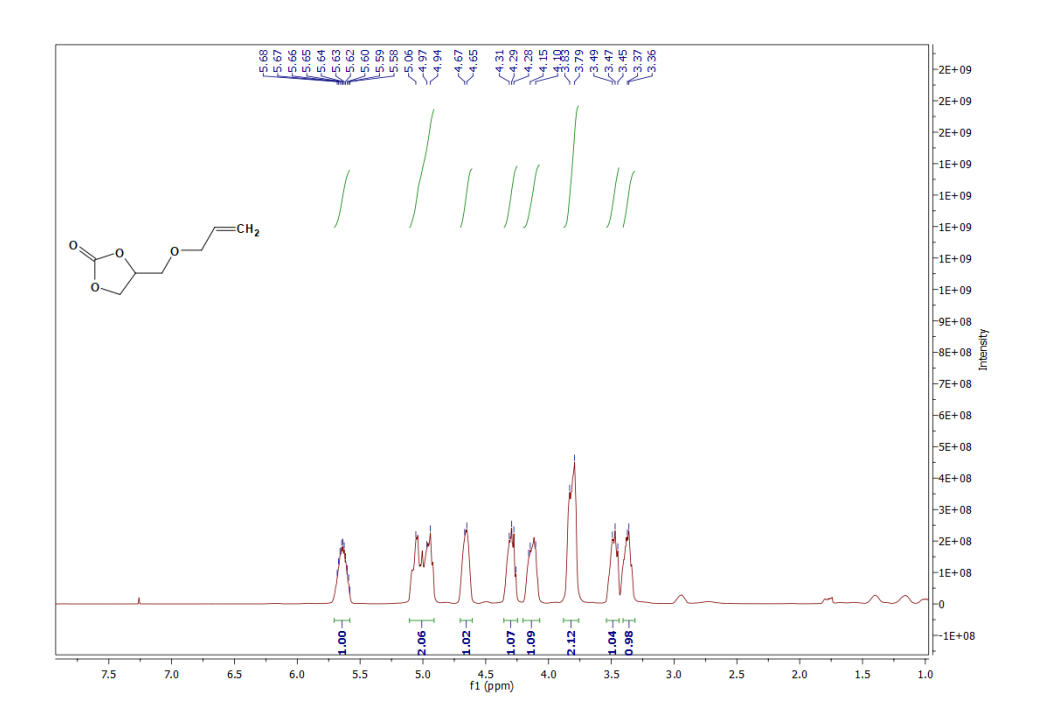
### <sup>1</sup>H NMR of 4-phenyl-1,3-dioxolan-2-one:



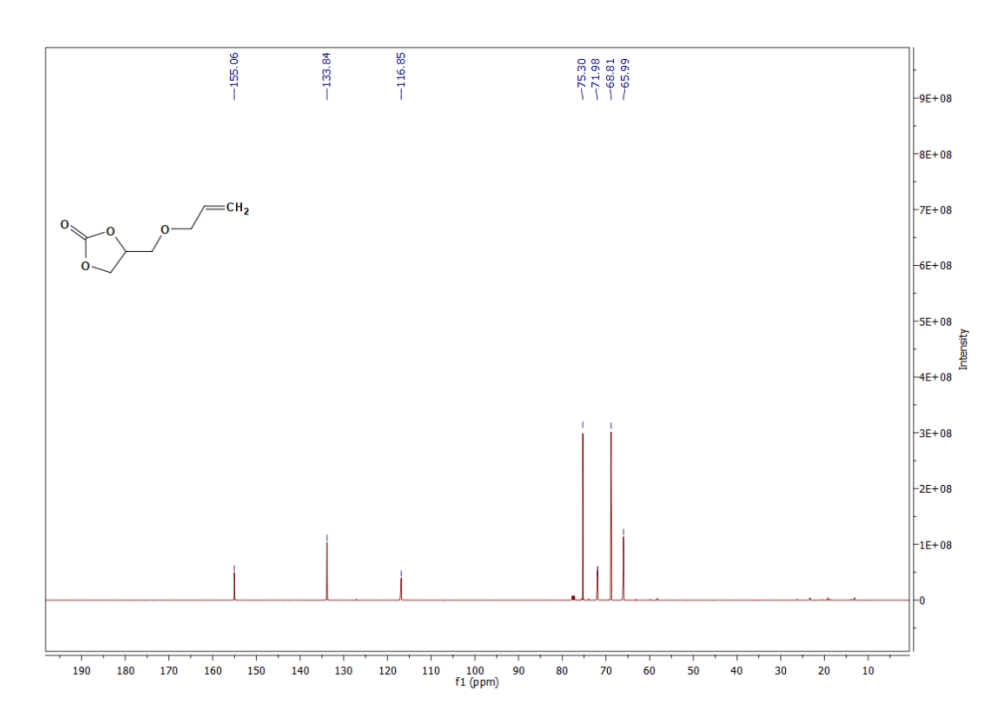
# $^{13}\mathrm{C}$ NMR of 4-phenyl-1,3-dioxolan-2-one:



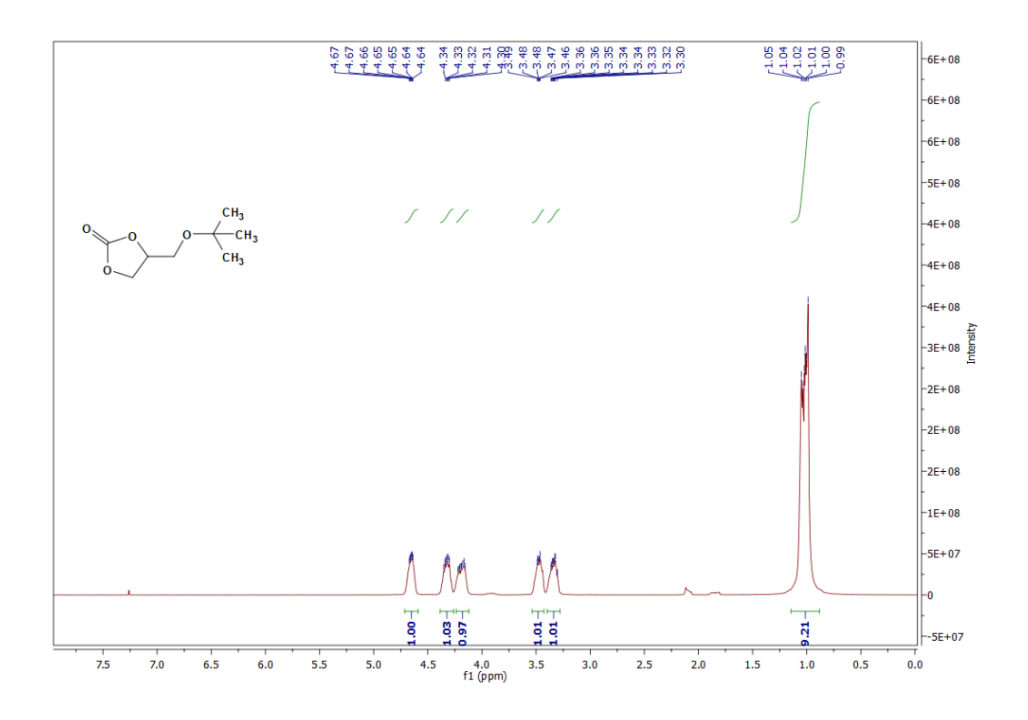
## $^1H\ NMR\ of\ 4-((allyloxy)methyl)-1,3-dioxolan-2-one$ :



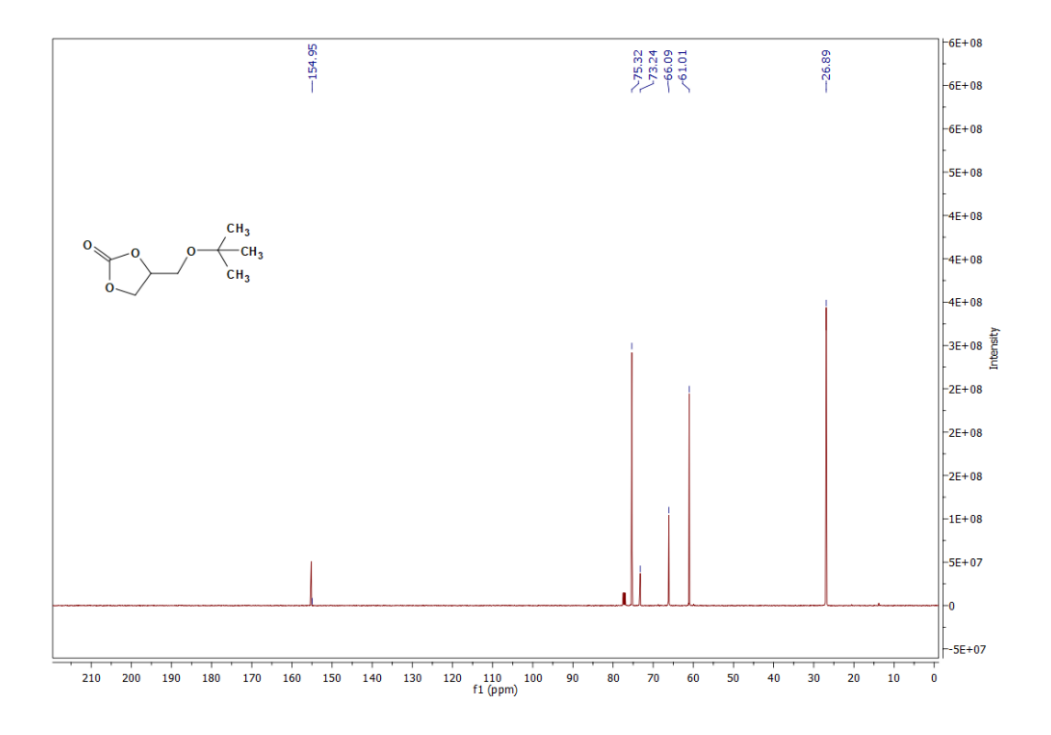
## <sup>13</sup>C NMR of 4-((allyloxy)methyl)-1,3-dioxolan-2-one:



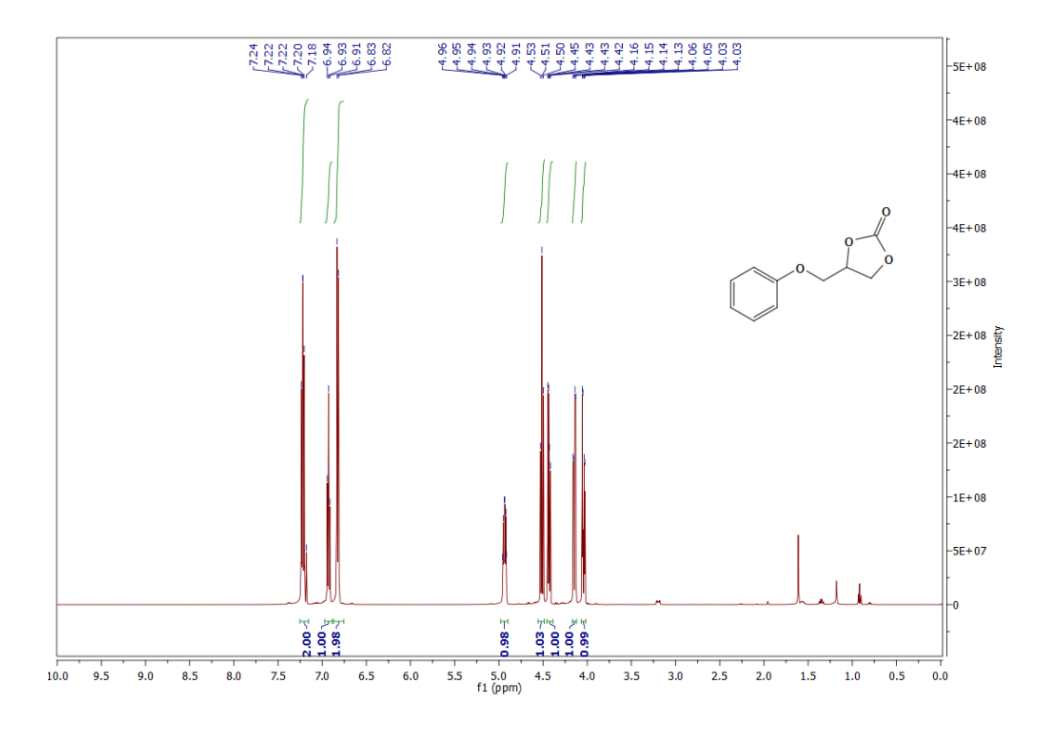
# $^1\mathrm{H}$ NMR of 4-(tert-butoxymethyl)-1,3-dioxolan-2-one:



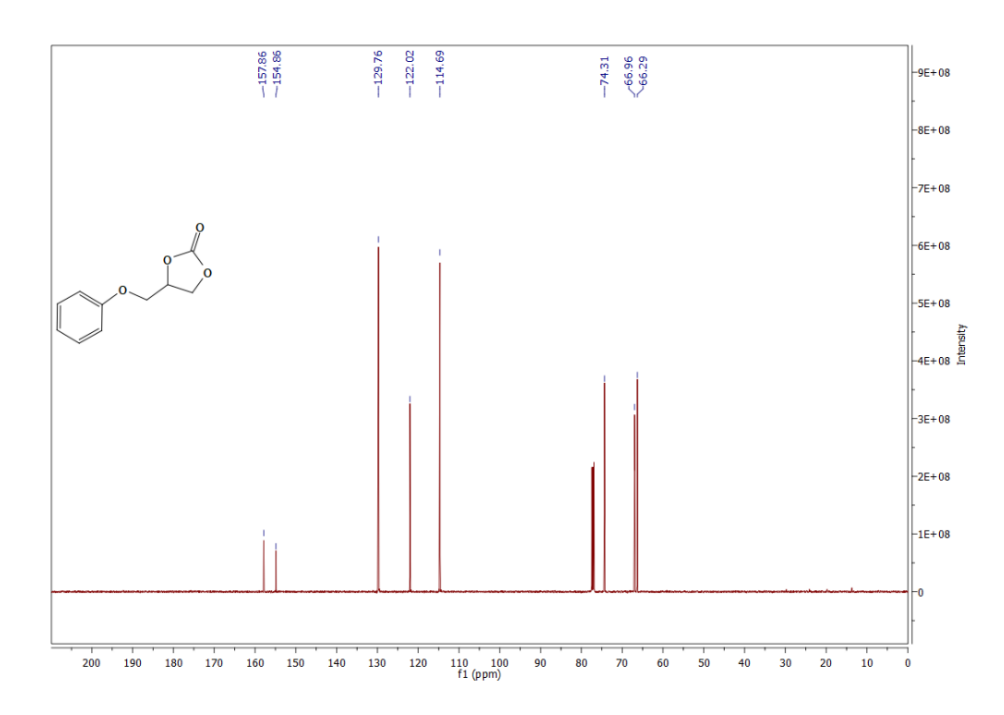
## <sup>13</sup>C NMR of 4-(tert-butoxymethyl)-1,3-dioxolan-2-one:



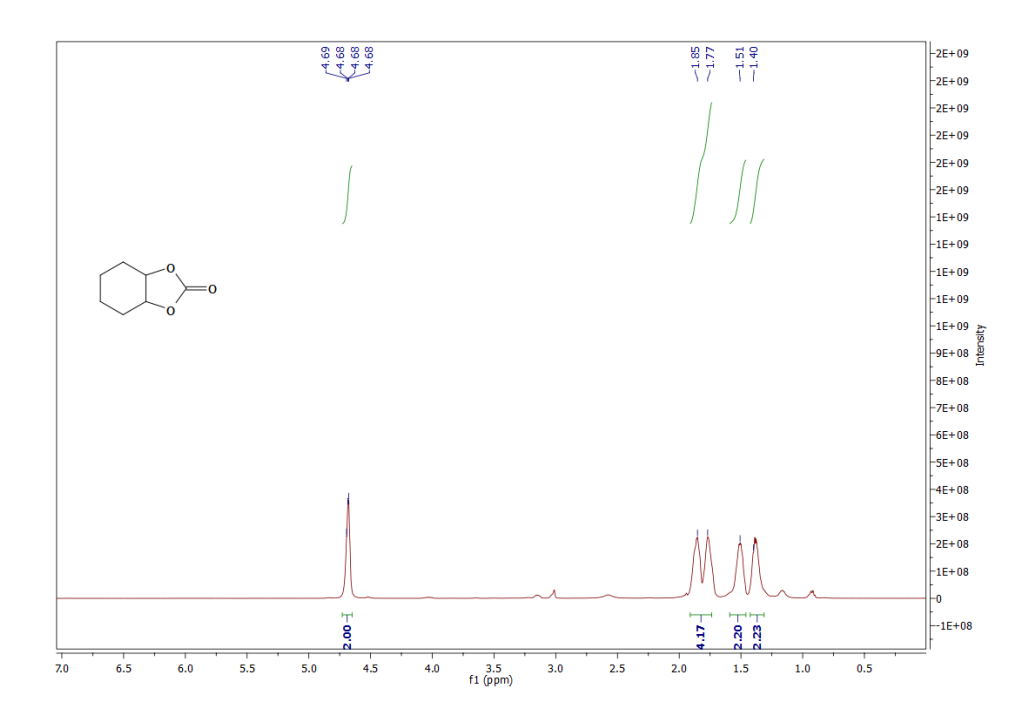
# $^1H$ NMR of 4-(phenoxymethyl)-1,3-dioxolan-2-one:



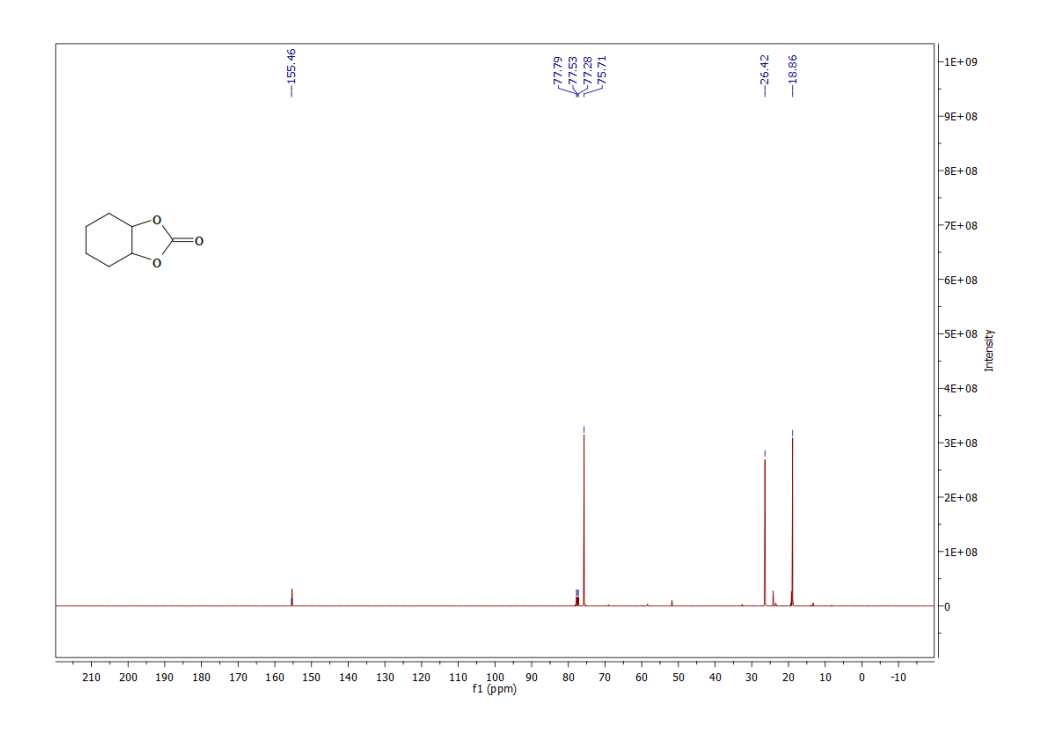
# <sup>13</sup>C NMR of 4-(phenoxymethyl)-1,3-dioxolan-2-one:



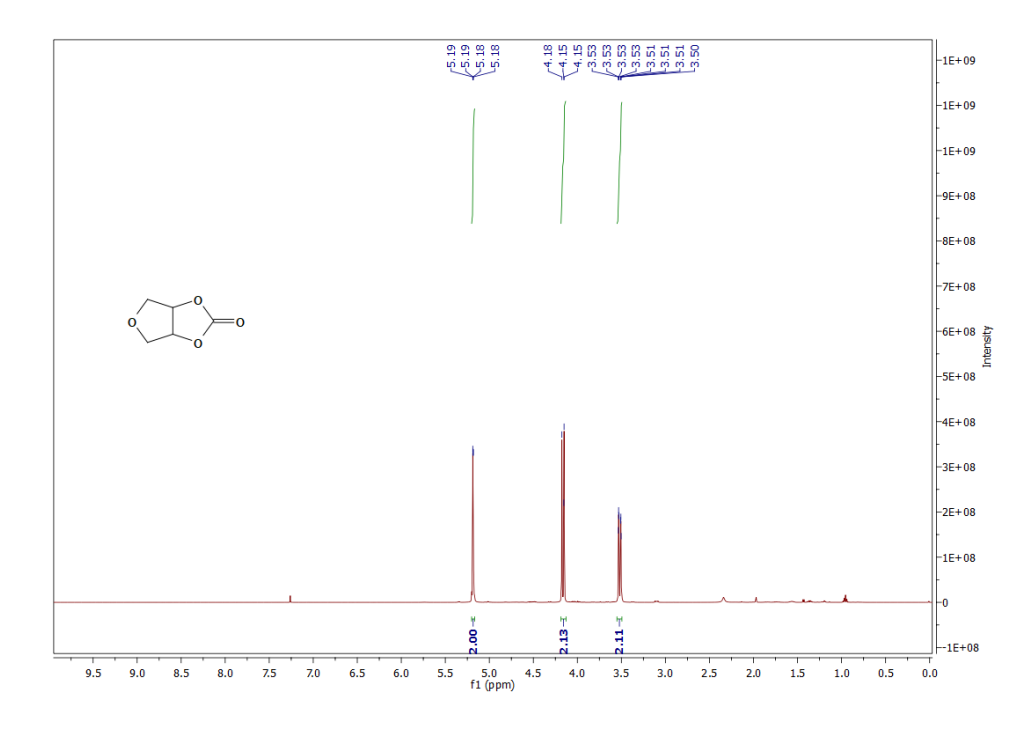
# $^1H$ NMR of Hexahydro benzo[d][1,3]dioxol-2-one



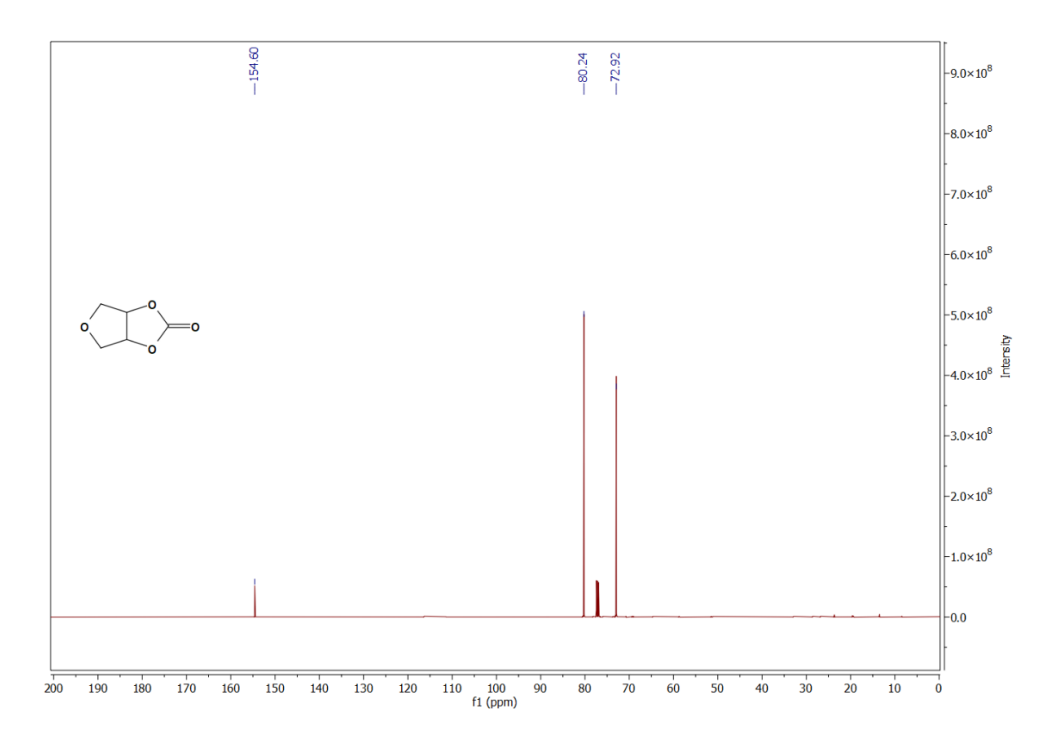
# $^{13}\mathrm{C}\ \mathrm{NMR}$ of Hexahydrobenzo[d][1,3]dioxol-2-one



## <sup>1</sup>H NMR of Tetrahydrofuro[3,4-d][1,3]dioxol-2-one:



# $^{13}\mathrm{C}\ NMR\ of\ Tetrahydrofuro[3,4-d][1,3]dioxol-2-one:$



#### 6.6. References

- (1) Zhang, H.; Zhou, W.; Chen, T.; Guan, B. Y.; Li, Z.; Lou, X. W. (David). A Modular Strategy for Decorating Isolated Cobalt Atoms into Multichannel Carbon Matrix for Electrocatalytic Oxygen Reduction. *Energy Environ. Sci.* **2018**, *11* (8), 1980–1984. https://doi.org/10.1039/C8EE00901E.
- (2) Guo, Y.; Mei, S.; Yuan, K.; Wang, D.-J.; Liu, H.-C.; Yan, C.-H.; Zhang, Y.-W. Low-Temperature CO2 Methanation over CeO2-Supported Ru Single Atoms, Nanoclusters, and Nanoparticles Competitively Tuned by Strong Metal–Support Interactions and H-Spillover Effect. *ACS Catal.* **2018**, 8 (7), 6203–6215. https://doi.org/10.1021/acscatal.7b04469.
- (3) Kwon, Y.; Kim, T. Y.; Kwon, G.; Yi, J.; Lee, H. Selective Activation of Methane on Single-Atom Catalyst of Rhodium Dispersed on Zirconia for Direct Conversion. *J. Am. Chem. Soc.* **2017**, 139 (48), 17694–17699. https://doi.org/10.1021/jacs.7b11010.
- (4) Qi, R.; Zhu, B.; Han, Z.; Gao, Y. High-Throughput Screening of Stable Single-Atom Catalysts in CO2 Reduction Reactions. *ACS Catal.* **2022**, *12* (14), 8269–8278. https://doi.org/10.1021/acscatal.2c02149.
- (5) Li, Y.; Hao, J.; Song, H.; Zhang, F.; Bai, X.; Meng, X.; Zhang, H.; Wang, S.; Hu, Y.; Ye, J. Selective Light Absorber-Assisted Single Nickel Atom Catalysts for Ambient Sunlight-Driven CO2 Methanation. *Nat Commun* **2019**, *10* (1), 2359. https://doi.org/10.1038/s41467-019-10304-y.
- (6) Lu, Y.; Zhang, Z.; Wang, H.; Wang, Y. Toward Efficient Single-Atom Catalysts for Renewable Fuels and Chemicals Production from Biomass and CO2. *Applied Catalysis B: Environmental* **2021**, 292, 120162. https://doi.org/10.1016/j.apcatb.2021.120162.
- (7) Zhang, W.; Zheng, W. Single Atom Excels as the Smallest Functional Material. *Advanced Functional Materials* **2016**, *26* (18), 2988–2993. https://doi.org/10.1002/adfm.201600240.
- (8) Liu, J. Catalysis by Supported Single Metal Atoms. *ACS Catal.* **2017**, 7 (1), 34–59. https://doi.org/10.1021/acscatal.6b01534.
- (9) Mitchell, S.; Vorobyeva, E.; Pérez-Ramírez, J. The Multifaceted Reactivity of Single-Atom Heterogeneous Catalysts. *Angewandte Chemie International Edition* **2018**, *57* (47), 15316–15329. https://doi.org/10.1002/anie.201806936.
- (10) Peng, Y.; Lu, B.; Chen, S. Carbon-Supported Single Atom Catalysts for Electrochemical Energy Conversion and Storage. *Advanced Materials* **2018**, *30* (48), 1801995. https://doi.org/10.1002/adma.201801995.
- (11) Vasconcelos, S. C.; Marchini, L.; Lima, C. G. S.; Madriaga, V. G. C.; Ribeiro, R. S. A.; Rossa, V.; Ferreira, L. E. M.; Silva, F. de C. da; Ferreira, V. F.; Passos, F. B.; Varma, R. S.; Paixão, M. W.; Lima, T. M. Single-Atom Catalysts for the Upgrading of Biomass-Derived Molecules: An Overview of Their Preparation, Properties

- and Applications. *Green Chem.* **2022**, *24* (7), 2722–2751. https://doi.org/10.1039/D1GC03809E.
- (12) Wang, A.; Li, J.; Zhang, T. Heterogeneous Single-Atom Catalysis. *Nat Rev Chem* **2018**, 2 (6), 65–81. https://doi.org/10.1038/s41570-018-0010-1.
- (13) Singh, B.; Gawande, M. B.; Kute, A. D.; Varma, R. S.; Fornasiero, P.; McNeice, P.; Jagadeesh, R. V.; Beller, M.; Zbořil, R. Single-Atom (Iron-Based) Catalysts: Synthesis and Applications. *Chem. Rev.* **2021**, *121* (21), 13620–13697. https://doi.org/10.1021/acs.chemrev.1c00158.
- (14) Wu, Q.; Wu, C. Mechanism Insights on Single-Atom Catalysts for CO2 Conversion. *J. Mater. Chem. A* **2023**, *11* (10), 4876–4906. https://doi.org/10.1039/D2TA06949K.
- (15) Ji, S.; Chen, Y.; Wang, X.; Zhang, Z.; Wang, D.; Li, Y. Chemical Synthesis of Single Atomic Site Catalysts. *Chem. Rev.* **2020**, *120* (21), 11900–11955. https://doi.org/10.1021/acs.chemrev.9b00818.
- (16) Liu, Q.; Zhang, Z. Platinum Single-Atom Catalysts: A Comparative Review towards Effective Characterization. *Catalysis Science & Technology* **2019**, *9* (18), 4821–4834. https://doi.org/10.1039/C9CY01028A.
- (17) Lin, L.; Yao, S.; Gao, R.; Liang, X.; Yu, Q.; Deng, Y.; Liu, J.; Peng, M.; Jiang, Z.; Li, S.; Li, Y.-W.; Wen, X.-D.; Zhou, W.; Ma, D. A Highly CO-Tolerant Atomically Dispersed Pt Catalyst for Chemoselective Hydrogenation. *Nat. Nanotechnol.* **2019**, *14* (4), 354–361. https://doi.org/10.1038/s41565-019-0366-5.
- (18) Qi, P.; Wang, J.; Djitcheu, X.; He, D.; Liu, H.; Zhang, Q. Techniques for the Characterization of Single Atom Catalysts. *RSC Adv.* **2021**, *12* (2), 1216–1227. https://doi.org/10.1039/D1RA07799F.
- (19) Gong, L.; Zhang, D.; Lin, C.-Y.; Zhu, Y.; Shen, Y.; Zhang, J.; Han, X.; Zhang, L.; Xia, Z. Catalytic Mechanisms and Design Principles for Single-Atom Catalysts in Highly Efficient CO2 Conversion. *Advanced Energy Materials* **2019**, *9* (44), 1902625. https://doi.org/10.1002/aenm.201902625.
- (20) Millet, M.-M.; Algara-Siller, G.; Wrabetz, S.; Mazheika, A.; Girgsdies, F.; Teschner, D.; Seitz, F.; Tarasov, A.; Levchenko, S. V.; Schlögl, R.; Frei, E. Ni Single Atom Catalysts for CO2 Activation. *J. Am. Chem. Soc.* **2019**, *141* (6), 2451–2461. https://doi.org/10.1021/jacs.8b11729.
- (21) Zhang, N.; Zhang, X.; Tao, L.; Jiang, P.; Ye, C.; Lin, R.; Huang, Z.; Li, A.; Pang, D.; Yan, H.; Wang, Y.; Xu, P.; An, S.; Zhang, Q.; Liu, L.; Du, S.; Han, X.; Wang, D.; Li, Y. Silver Single-Atom Catalyst for Efficient Electrochemical CO2 Reduction Synthesized from Thermal Transformation and Surface Reconstruction. *Angewandte Chemie International Edition* **2021**, *60* (11), 6170–6176. https://doi.org/10.1002/anie.202014718.
- (22) Gao, C.; Chen, S.; Wang, Y.; Wang, J.; Zheng, X.; Zhu, J.; Song, L.; Zhang, W.; Xiong, Y. Heterogeneous Single-Atom Catalyst for Visible-Light-Driven High-Turnover CO2 Reduction: The Role of

- Electron Transfer. *Advanced Materials* **2018**, *30* (13), 1704624. https://doi.org/10.1002/adma.201704624.
- (23) Zhu, C.; Fu, S.; Shi, Q.; Du, D.; Lin, Y. Single-Atom Electrocatalysts. *Angewandte Chemie International Edition* **2017**, 56 (45), 13944–13960. https://doi.org/10.1002/anie.201703864.
- (24) Ling, C.; Li, Q.; Du, A.; Wang, J. Computation-Aided Design of Single-Atom Catalysts for One-Pot CO2 Capture, Activation, and Conversion. *ACS Appl. Mater. Interfaces* **2018**, *10* (43), 36866–36872. https://doi.org/10.1021/acsami.8b10394.
- (25) Xiong, X.; Mao, C.; Yang, Z.; Zhang, Q.; Waterhouse, G. I. N.; Gu, L.; Zhang, T. Photocatalytic CO2 Reduction to CO over Ni Single Atoms Supported on Defect-Rich Zirconia. *Advanced Energy Materials* **2020**, *10* (46), 2002928. https://doi.org/10.1002/aenm.202002928.
- (26) Li, X.; Surkus, A.-E.; Rabeah, J.; Anwar, M.; Dastigir, S.; Junge, H.; Brückner, A.; Beller, M. Cobalt Single-Atom Catalysts with High Stability for Selective Dehydrogenation of Formic Acid. *Angewandte Chemie International Edition* **2020**, *59* (37), 15849–15854. https://doi.org/10.1002/anie.202004125.
- (27) Abdel-Mageed, A. M.; Wohlrab, S. Review of CO2 Reduction on Supported Metals (Alloys) and Single-Atom Catalysts (SACs) for the Use of Green Hydrogen in Power-to-Gas Concepts. *Catalysts* **2022**, *12* (1), 16. https://doi.org/10.3390/catal12010016.
- (28) Rohmann, K.; Kothe, J.; Haenel, M. W.; Englert, U.; Hölscher, M.; Leitner, W. Hydrogenation of CO2 to Formic Acid with a Highly Active Ruthenium Acriphos Complex in DMSO and DMSO/Water. *Angewandte Chemie International Edition* **2016**, *55* (31), 8966–8969. https://doi.org/10.1002/anie.201603878.
- (29) Liu, K.; Xu, Z.; Huang, H.; Zhang, Y.; Liu, Y.; Qiu, Z.; Tong, M.; Long, Z.; Chen, G. In Situ Synthesis of Pyridinium-Based Ionic Porous Organic Polymers with Hydroxide Anions and Pyridinyl Radicals for Halogen-Free Catalytic Fixation of Atmospheric CO 2. *Green Chemistry* **2022**, 24 (1), 136–141. https://doi.org/10.1039/D1GC03465K.
- (30) Prasad, D.; Patil, K. N.; Bhanushali, J. T.; Nagaraja, B. M.; Jadhav, A. H. Sustainable Fixation of CO2 into Epoxides to Form Cyclic Carbonates Using Hollow Marigold CuCo2O4 Spinel Microspheres as a Robust Catalyst. *Catal. Sci. Technol.* **2019**, *9* (16), 4393–4412. https://doi.org/10.1039/C9CY00945K.
- (31) Lu, X.-B.; Darensbourg, D. J. Cobalt Catalysts for the Coupling of CO2 and Epoxides to Provide Polycarbonates and Cyclic Carbonates. *Chem. Soc. Rev.* **2012**, *41* (4), 1462–1484. https://doi.org/10.1039/C1CS15142H.
- (32) Mitra, A.; Biswas, T.; Ghosh, S.; Tudu, G.; S. Paliwal, K.; Ghosh, S.; Mahalingam, V. Halide-Free Catalytic Carbon Dioxide Fixation of Epoxides to Cyclic Carbonates under Atmospheric Pressure. *Sustainable Energy & Fuels* **2022**, *6* (2), 420–429. https://doi.org/10.1039/D1SE01513C.
- (33) Ansari, S. N.; Kumar, P.; Gupta, A. K.; Mathur, P.; Mobin, S. M. Catalytic CO2 Fixation over a Robust Lactam-Functionalized

- Cu(II) Metal Organic Framework. *Inorg. Chem.* **2019**, *58* (15), 9723–9732. https://doi.org/10.1021/acs.inorgchem.9b00684.
- (34) You, L.-X.; Yao, S.-X.; Zhao, B.-B.; Xiong, G.; Dragutan, I.; Dragutan, V.; Liu, X.-G.; Ding, F.; Sun, Y.-G. Striking Dual Functionality of a Novel Pd@Eu-MOF Nanocatalyst in C(Sp 2)—C(Sp 2) Bond-Forming and CO 2 Fixation Reactions. *Dalton Transactions* **2020**, *49* (19), 6368–6376. https://doi.org/10.1039/D0DT00770F.
- (35) Wang, Y.-X.; Wang, H.-M.; Meng, P.; Song, D.-X.; Hou, J.-J.; Zhang, X.-M. An Uncoordinated Tertiary Nitrogen Based Tricarboxylate Calcium Network with Lewis Acid—Base Dual Catalytic Sites for Cyanosilylation of Aldehydes. *Dalton Trans.* **2021**, *50* (5), 1740–1745. https://doi.org/10.1039/D0DT03747H.
- (36) Ye, Y.; Ge, B.; Meng, X.; Liu, Y.; Wang, S.; Song, X.; Liang, Z. An Yttrium-Organic Framework Based on a Hexagonal Prism Second Building Unit for Luminescent Sensing of Antibiotics and Highly Effective CO2 Fixation. *Inorg. Chem. Front.* **2022**, *9* (2), 391–400. https://doi.org/10.1039/D1QI01352A.
- (37) Chen, H.; Zhang, Z.; Lv, H.; Liu, S.; Zhang, X. Investigation on the Catalytic Behavior of a Novel Thulium-Organic Framework with a Planar Tetranuclear {Tm4} Cluster as the Active Center for Chemical CO2 Fixation. *Dalton Trans.* **2022**, *51* (2), 532–540. https://doi.org/10.1039/D1DT03646G.
- (38) Ma, F.-X.; Mi, F.-Q.; Sun, M.-J.; Huang, T.; Wang, Z.-A.; Zhang, T.; Cao, R. A Highly Stable Zn9-Pyrazolate Metal–Organic Framework with Metallosalen Ligands as a Carbon Dioxide Cycloaddition Catalyst. *Inorg. Chem. Front.* **2022**, *9* (8), 1812–1818. https://doi.org/10.1039/D1QI01555A.
- (39) Kong, L.; Li, Z.; Hu, H.; Zhu, J.; Chen, Z.; Deng, M.; Ling, Y.; Li, P.; Jia, Y.; Zhou, Y. Reticular Chemistry Approach to Explore the Catalytic CO2-Epoxide Cycloaddition Reaction over Tetrahedral Coordination Lewis Acidic Sites in a Rutile-Type Zinc-Phosphonocarboxylate Framework. *Chemical Engineering Journal* **2022**, 427, 131759. https://doi.org/10.1016/j.cej.2021.131759.
- (40) Sinchow, M.; Semakul, N.; Konno, T.; Rujiwatra, A. Lanthanide Coordination Polymers through Design for Exceptional Catalytic Performances in CO2 Cycloaddition Reactions. *ACS Sustainable Chem. Eng.* **2021**, *9* (25), 8581–8591. https://doi.org/10.1021/acssuschemeng.1c01955.
- (41) Jaroonwatana, W.; Theerathanagorn, T.; Theerasilp, M.; Gobbo, S. D.; Yiamsawas, D.; D'Elia, V.; Crespy, D. Nanoparticles of Aromatic Biopolymers Catalyze CO 2 Cycloaddition to Epoxides under Atmospheric Conditions. *Sustainable Energy & Fuels* **2021**, *5* (21), 5431–5444. https://doi.org/10.1039/D1SE01305J.
- (42) Ding, Q.-R.; Yu, Y.; Cao, C.; Zhang, J.; Zhang, L. Stepwise Assembly and Reversible Structural Transformation of Ligated Titanium Coated Bismuth-Oxo Cores: Shell Morphology Engineering for Enhanced Chemical Fixation of CO2. *Chem. Sci.* **2022**, *13* (12), 3395–3401. https://doi.org/10.1039/D1SC06847D.

- (43) Tudu, G.; Paliwal, K. S.; Ghosh, S.; Biswas, T.; Koppisetti, H. V. S. R. M.; Mitra, A.; Mahalingam, V. Para-Aminobenzoic Acid-Capped Hematite as an Efficient Nanocatalyst for Solvent-Free CO2 Fixation under Atmospheric Pressure. *Dalton Trans.* **2022**, *51* (5), 1918–1926. https://doi.org/10.1039/D1DT03821D.
- (44) Ghosh, A.; Reddy, G. N.; K, M. S. P.; Chatterjee, S.; Bhattacharjee, S.; Maitra, R.; Lyubimov, S. E.; Arzumanyan, A. V.; Naumkin, A.; Bhaumik, A.; Chowdhury, B. Fabrication of a Hollow Sphere N,S Co-Doped Bifunctional Carbon Catalyst for Sustainable Fixation of CO2 to Cyclic Carbonates. *Green Chem.* **2022**, *24* (4), 1673–1692. https://doi.org/10.1039/D1GC04153C.
- (45) Sun, Y.; Huang, H.; Vardhan, H.; Aguila, B.; Zhong, C.; Perman, J. A.; Al-Enizi, A. M.; Nafady, A.; Ma, S. Facile Approach to Graft Ionic Liquid into MOF for Improving the Efficiency of CO2 Chemical Fixation. *ACS Appl. Mater. Interfaces* **2018**, *10* (32), 27124–27130. https://doi.org/10.1021/acsami.8b08914.
- (46) Liang, J.; Xie, Y.-Q.; Wang, X.-S.; Wang, Q.; Liu, T.-T.; Huang, Y.-B.; Cao, R. An Imidazolium-Functionalized Mesoporous Cationic Metal–Organic Framework for Cooperative CO2 Fixation into Cyclic Carbonate. *Chem. Commun.* **2018**, *54* (4), 342–345. https://doi.org/10.1039/C7CC08630J.
- (47) Cui, X.; Dai, X.; Surkus, A.-E.; Junge, K.; Kreyenschulte, C.; Agostini, G.; Rockstroh, N.; Beller, M. Zinc Single Atoms on N-Doped Carbon: An Efficient and Stable Catalyst for CO2 Fixation and Conversion. *Chinese Journal of Catalysis* **2019**, *40* (11), 1679–1685. https://doi.org/10.1016/S1872-2067(19)63316-4.
- (48) Yang, Q.; Yang, C.-C.; Lin, C.-H.; Jiang, H.-L. Metal–Organic-Framework-Derived Hollow N-Doped Porous Carbon with Ultrahigh Concentrations of Single Zn Atoms for Efficient Carbon Dioxide Conversion. *Angewandte Chemie International Edition* **2019**, 58 (11), 3511–3515. https://doi.org/10.1002/anie.201813494.
- (49) Li, G.; Sui, X.; Cai, X.; Hu, W.; Liu, X.; Chen, M.; Zhu, Y. Precisely Constructed Silver Active Sites in Gold Nanoclusters for Chemical Fixation of CO2. *Angewandte Chemie* **2021**, *133* (19), 10667–10670. https://doi.org/10.1002/ange.202100071.
- (50) Xu et al.. Strong Electronic Metal—Support Interaction between Iridium Single Atoms and a WO3 Support Promotes Highly Efficient and Robust CO2 Cycloaddition. *Advanced Materials* **2022**, *34* (44), 2206991. https://doi.org/10.1002/adma.202206991.
- (51) Choudhary, N.; Abdelgaid, M.; Mpourmpakis, G.; Mobin, S. M. CuNi Bimetallic Nanocatalyst Enables Sustainable Direct Carboxylation Reactions. *Molecular Catalysis* **2022**, *530*, 112620. https://doi.org/10.1016/j.mcat.2022.112620.
- (52) Ressler, T. WinXAS: A Program for X-Ray Absorption Spectroscopy Data Analysis under MS-Windows. *J Synchrotron Rad* **1998**, 5 (2), 118–122. https://doi.org/10.1107/S0909049597019298.
- (53) Rehr, J. J.; Booth, C. H.; Bridges, F.; Zabinsky, S. I. X-Ray-Absorption Fine Structure in Embedded Atoms. *Phys. Rev. B* **1994**,

- 49 (17), 12347–12350. https://doi.org/10.1103/PhysRevB.49.12347.
- (54) Vrijburg, W. L.; Helden, J. W. A. van; Parastaev, A.; Groeneveld, E.; Pidko, E. A.; Hensen, E. J. M. Ceria–Zirconia Encapsulated Ni Nanoparticles for CO2 Methanation. *Catal. Sci. Technol.* **2019**, *9* (18), 5001–5010. https://doi.org/10.1039/C9CY01428D.
- (55) Ramírez-García, G.; Rosa, E. D. la; López-Luke, T.; S. Panikar, S.; Salas, P. Controlling Trapping States on Selective Theranostic Core@shell (NaYF 4:Yb,Tm@TiO 2-ZrO 2) Nanocomplexes for Enhanced NIR-Activated Photodynamic Therapy against Breast Cancer Cells. *Dalton Transactions* **2019**, *48* (27), 9962–9973. https://doi.org/10.1039/C9DT00482C.
- (56) Yu, S.; Jin Yun, H.; Minzae Lee, D.; Yi, J. Preparation and Characterization of Fe-Doped TiO 2 Nanoparticles as a Support for a High Performance CO Oxidation Catalyst. *Journal of Materials Chemistry* 2012, 22 (25), 12629–12635. https://doi.org/10.1039/C2JM30360D.
- (57) Li, J.; Shen, B.; Hong, Z.; Lin, B.; Gao, B.; Chen, Y. A Facile Approach to Synthesize Novel Oxygen-Doped g -C 3 N 4 with Superior Visible-Light Photoreactivity. *Chemical Communications* **2012**, 48 (98), 12017–12019. https://doi.org/10.1039/C2CC35862J.
- (58) Radovanovic, P. V.; Gamelin, D. R. Electronic Absorption Spectroscopy of Cobalt Ions in Diluted Magnetic Semiconductor Quantum Dots: Demonstration of an Isocrystalline Core/Shell Synthetic Method. *J. Am. Chem. Soc.* **2001**, *123* (49), 12207–12214. https://doi.org/10.1021/ja0115215.
- (59) Sheng Chua, C.; Ansovini, D.; Jun Lee, C. J.; Ting Teng, Y.; Ting Ong, L.; Chi, D.; Andy Hor, T. S.; Raja, R.; Lim, Y.-F. The Effect of Crystallinity on Photocatalytic Performance of Co 3 O 4 Water-Splitting Cocatalysts. *Physical Chemistry Chemical Physics* **2016**, *18* (7), 5172–5178. https://doi.org/10.1039/C5CP07589K.
- (60) Yan, X.; Tian, L.; He, M.; Chen, X. Three-Dimensional Crystalline/Amorphous Co/Co3O4 Core/Shell Nanosheets as Efficient Electrocatalysts for the Hydrogen Evolution Reaction. *Nano Lett.* **2015**, *15* (9), 6015–6021. https://doi.org/10.1021/acs.nanolett.5b02205.
- (61) Zhou, Y.-X.; Chen, Y.-Z.; Cao, L.; Lu, J.; Jiang, H.-L. Conversion of a Metal–Organic Framework to N-Doped Porous Carbon Incorporating Co and CoO Nanoparticles: Direct Oxidation of Alcohols to Esters. *Chem. Commun.* **2015**, *51* (39), 8292–8295. https://doi.org/10.1039/C5CC01588J.
- (62) Cao, Y.; Ge, J.; Jiang, M.; Zhang, F.; Lei, X. Acid-Etched Co3O4 Nanoparticles on Nickel Foam: The Highly Reactive (311) Facet and Enriched Defects for Boosting Methanol Oxidation Electrocatalysis. *ACS Appl. Mater. Interfaces* **2021**, *13* (25), 29491–29499. https://doi.org/10.1021/acsami.1c04045.
- (63) Choudhary, N.; Ghosh, T.; Mobin, S. M. Ketone Hydrogenation by Using ZnO-Cu(OH)Cl/MCM-41 with a Splash of Water: An

- Environmentally Benign Approach. *Chemistry An Asian Journal* **2020**, *15* (8), 1339–1348. https://doi.org/10.1002/asia.201901610.
- (64) Krogman, J. P.; Gallagher, J. R.; Zhang, G.; Hock, A. S.; Miller, J. T.; Thomas, C. M. Assignment of the Oxidation States of Zr and Co in a Highly Reactive Heterobimetallic Zr/Co Complex Using X-Ray Absorption Spectroscopy (XANES). *Dalton Trans.* **2014**, *43* (37), 13852–13857. https://doi.org/10.1039/C4DT01534G.
- (65) Liu, Z.; Xiao, Z.; Luo, G.; Chen, R.; Dong, C.-L.; Chen, X.; Cen, J.; Yang, H.; Wang, Y.; Su, D.; Li, Y.; Wang, S. Defects-Induced In-Plane Heterophase in Cobalt Oxide Nanosheets for Oxygen Evolution Reaction. *Small* 2019, 15 (50), 1904903. https://doi.org/10.1002/smll.201904903.
- (66) Reith, L.; Triana, C. A.; Pazoki, F.; Amiri, M.; Nyman, M.; Patzke, G. R. Unraveling Nanoscale Cobalt Oxide Catalysts for the Oxygen Evolution Reaction: Maximum Performance, Minimum Effort. *J. Am. Chem. Soc.* **2021**, *143* (37), 15022–15038. https://doi.org/10.1021/jacs.1c03375.
- (67) Zhou, P.; Zhang, S.; Ren, Z.; Tang, X.; Zhang, K.; Zhou, R.; Wu, D.; Liao, J.; Zhang, Y.; Huang, C. In Situ Cutting of Ammonium Perchlorate Particles by Co-Bipy "Scalpel" for High Efficiency Thermal Decomposition. *Advanced Science* **2022**, *9* (35), 2204109. https://doi.org/10.1002/advs.202204109.
- (68) Mia, S.; P. Varapragasam, S. J.; Baride, A.; Balasanthiran, C.; Balasubramanian, B.; M. Rioux, R.; D. Hoefelmeyer, J. Diffusion Doping of Cobalt in Rod-Shape Anatase TiO 2 Nanocrystals Leads to Antiferromagnetism. *Nanoscale Advances* **2020**, *2* (10), 4853–4862. https://doi.org/10.1039/D0NA00640H.
- (69) Ahmed, M. S.; Choi, B.; Kim, Y.-B. Development of Highly Active Bifunctional Electrocatalyst Using Co3O4 on Carbon Nanotubes for Oxygen Reduction and Oxygen Evolution. *Sci Rep* **2018**, *8* (1), 2543. https://doi.org/10.1038/s41598-018-20974-1.
- (70) Klenov, O. P.; Chumakova, N. A.; Pokrovskaya, S. A.; Noskov, A. S. Modeling of Heat Transfer in a Porous Monolith Catalyst with Square Channels. *Ind. Eng. Chem. Res.* **2016**, *55* (14), 3879–3889. https://doi.org/10.1021/acs.iecr.5b04804.
- (71) Chen, X.; Wei, M.; Yang, A.; Jiang, F.; Li, B.; Kholdeeva, O. A.; Wu, L. Near-Infrared Photothermal Catalysis for Enhanced Conversion of Carbon Dioxide under Mild Conditions. *ACS Appl. Mater. Interfaces* **2022**, *14* (4), 5194–5202. https://doi.org/10.1021/acsami.1c18889.
- (72) Liu, L.-H.; Liu, L.; Chi, H.-R.; Li, C.-N.; Han, Z.-B. A [(M 2 ) 6 L 8 ] Metal–Organic Polyhedron with High CO 2 Uptake and Efficient Chemical Conversion of CO 2 under Ambient Conditions. *Chemical Communications* **2022**, *58* (44), 6417–6420. https://doi.org/10.1039/D2CC01734B.
- (73) Zhai, G.; Liu, Y.; Lei, L.; Wang, J.; Wang, Z.; Zheng, Z.; Wang, P.; Cheng, H.; Dai, Y.; Huang, B. Light-Promoted CO2 Conversion from Epoxides to Cyclic Carbonates at Ambient Conditions over a Bi-Based Metal–Organic Framework. *ACS*

- *Catal.* **2021**, *11* (4), 1988–1994. https://doi.org/10.1021/acscatal.0c05145.
- (74) Ke, S.-C.; Luo, T.-T.; Chang, G.-G.; Huang, K.-X.; Li, J.-X.; Ma, X.-C.; Wu, J.; Chen, J.; Yang, X.-Y. Spatially Ordered Arrangement of Multifunctional Sites at Molecule Level in a Single Catalyst for Tandem Synthesis of Cyclic Carbonates. *Inorg. Chem.* **2020**, *59* (3), 1736–1745. https://doi.org/10.1021/acs.inorgchem.9b02952.
- (75) Ullah, H.; Mousavi, B.; Younus, H. A.; Khattak, Z. A. K.; Chaemchuen, S.; Suleman, S.; Verpoort, F. Chemical Fixation of Carbon Dioxide Catalyzed via Cobalt (III) ONO Pincer Ligated Complexes. *Commun Chem* **2019**, 2 (1), 1–9. https://doi.org/10.1038/s42004-019-0139-y.
- (76) Ding, Q.-R.; Yu, Y.; Cao, C.; Zhang, J.; Zhang, L. Stepwise Assembly and Reversible Structural Transformation of Ligated Titanium Coated Bismuth-Oxo Cores: Shell Morphology Engineering for Enhanced Chemical Fixation of CO2. *Chem. Sci.* **2022**, *13* (12), 3395–3401. https://doi.org/10.1039/D1SC06847D.

#### CHAPTER 7

### **Conclusions and Future Outlook**

This thesis focuses on design and synthesis of heterogeneous bimetallic, recyclable catalysts for various organic transformations. Initially, ZnO-Cu(OH)Cl/MCM-41 was synthesized via wetness impregnated method at room temperature. As synthesized catalysts has MCM-41 as silica support where Zn and Cu are incorporated. The synthesized catalyst was utilized for ketone hydrogenation with using water as solvent with mild reaction conditions. The catalyst showed high surface area with high catalytic activity with recyclability up to five cycles. Furthermore, bimetallic CoNi nanoflower was synthesized via liquid phase reduction method and morphological study confirmed the formation of flower like structure. As synthesized catalyst showed excellent catalytic activity for the conversion of terminal alkynes with 100% conversion and 100% selectivity towards alkane product. The catalyst is magnetically separable and recyclable up to six cycles. After this, bimetallic, magnetically separable CuNi nanocatalysts were synthesized with three molar ratios (1:1, 1:2 and 2:1) and their catalytic activity have been compared for biomass derived aldehydes and CuNi-12 showed higher catalytic activity. Also, the synergistic effect in between existing metals was observed when compared with monometallic Cu and Ni catalyst. The catalyst is recyclable up to seven cycles. Furthermore, all three catalysts were utilized for direct carboxylation of arenes and CuNi-11 catalysts showed high conversion in comparison to other composites and monometallic systems. This again confirm that bimetallic system showed superior catalytic activity over monometallic systems. The catalytic reaction involved the use of formic acid and showed unique mechanism with C-H activation of benzene and formic acid with gasfree, activator-free and solvent-free conditions. After this work, Co doped ZrO<sub>2</sub> SAC as synthesized and utilized for CO<sub>2</sub> fixation into epoxides. Also, for comparison undoped ZrO<sub>2</sub> and Co<sub>3</sub>O<sub>4</sub> impregnated ZrO<sub>2</sub> catalyst was utilized, and the results confirmed that SACs showed greater catalytic activity over other catalysts in solvent-free conditions and recyclability up to six cycles.

Above utilized all catalysts can be modified further by varying their synthesis parameters to tune their surface area, particle size, morphology, and properties for the utilization in various catalytic applications. All the catalysts are bimetallic, cost-effective, easy to synthesize, reusable and recyclable and hence, can be utilized for bulk scale applications. Likewise, these bimetallic materials can be utilized in several other applications like supercapacitor, sensing, photocatalysis, water splitting or electrocatalysis.

# **APPENDIX 1**

Table A1

**Table A1.** Permissions for re-producing the materials

Figure 1.2	Representation of bimetallic alloys	Reproduced from Ref. [7]: Chapter 1,
	and intermetallics.	with permission from the American
		Chemical Society
Figure 1.3	Comparative results of	Reproduced from Ref. [18]: Chapter
	monometallic and bimetallic	1, with permission from the American
	catalyst for deoxygenation	Chemical Society
	reaction.	
Figure 1.4	Representation of (a) supported	Reproduced from Ref. [7]: Chapter 1,
	nanocatalyst and (b) modified	with permission from the American
	nanocatalyst	Chemical Society
Figure 1.5	Bimetallic catalyst separations	Reproduced from Ref. [31]: Chapter
	using external magnet.	1, with permission from the Royal
		Society of Chemistry
Figure 1.6	Applications of supported and	Reproduced from Ref. [33]: Chapter
	unsupported nanoparticles in	1, with permission from the American
	catalysis.	Chemical Society
Figure 1.7	Comparative geometrical and	Reproduced from Ref. [33]: Chapter
	electronic structures of	1, with permission from the American
	nanoparticles, cluster, and single	Chemical Society
	atom catalyst.	
Figure 1.8	The effects of support on	Reproduced from Ref. [43]: Chapter
	stabilizing single atoms and	1, with permission from the American
	changes in surface free energy and	Chemical Society
	specific activity per metal atom	
	with metal particle size.	
Figure 1.9	Different types of SACs are	Reproduced from Ref. [43]: Chapter
	illustrated by schematic diagrams:	1, with permission from the American
	(A) Metal single atoms anchored to	Chemical Society
	graphene, (B) metal surfaces, and	
	(C) metal oxides, respectively.	

Figure 1.10	Characterization techniques for	Reproduced from Ref. [46]: Chapter
	analyzing single atom catalysis.	1, with permission from the American
		Chemical Society
Figure 1.11	Chemoselectivity pattern from	Reproduced from Ref. [7]: Chapter 1,
	nanocatalysts to single atom	with permission from the American
	catalysts.	Chemical Society